



UNIVERSITY OF GENOA

DEPARTMENT OF ELECTRICAL, ELECTRONIC AND  
TELECOMMUNICATION ENGINEERING AND NAVAL ARCHITECTURE  
(DITEN)

PHD IN SCIENCE AND TECHNOLOGY FOR ELECTRONIC AND  
TELECOMMUNICATION ENGINEERING

# **Novel Inverse-Scattering Methods in Banach Spaces**

PhD Thesis

Emanuele Tavanti

February 2019

*TUTOR:* Prof. Andrea Randazzo

*SUPERVISOR:* Prof. Mirco Raffetto

*Coordinator of the PhD Course:* Prof. Mario Marchese

# Abstract

The scientific community is presently strongly interested in the research of new microwave imaging methods, in order to develop reliable, safe, portable, and cost-effective tools for the non-invasive/non-destructive diagnostic in many fields (such as medicine, civil and industrial engineering, ...). In this framework, microwave imaging techniques addressing the full three-dimensional nature of the inspected bodies are still very challenging, since they need to cope with significant computational complexity. Moreover, non-linearity and ill-posedness issues, which usually affects the related inverse scattering problems, need to be faced, too. Another promising topic is the development of phaseless methods, in which only the amplitude of the electric field is assumed to be measurable. This leads to a significant complexity reduction and lower cost for the experimental apparatuses, but the missing information on the phase of the electric field samples exacerbates the ill-posedness problems. In the present Thesis, a novel inexact-Newton inversion algorithm is proposed, in which the iteratively linearized problems are solved in a regularized sense by using a truncated Landweber or a conjugate gradient method developed in the framework of the  $l^p$  Banach spaces. This is an improvement that allows to generalize the classic framework of the  $l^2$  Hilbert spaces in which the inexact-Newton approaches are usually defined. The applicability of the proposed imaging method in both the 3D full-vector and 2D phaseless scenarios at microwave frequencies is assessed in this Thesis, and an extensive validation of the proposed imaging method against both synthetic and experimental data is presented, highlighting the advantages over the inexact-Newton scheme developed in the classic framework of the  $l^2$  Hilbert spaces.

# **Acknowledgements**

I would like to thank my tutor Prof. Ing. Andrea Randazzo for his patience and professionalism.

I would like to thank also the whole staff of the Applied Electromagnetics Group for their support and pleasant company.

Thanks to my parents and grandparents, which have let me to realize my dream.

Thanks to my little rabbit Gianluca and my dachshund Conny. I will carry them in my heart for all my life.

# Index

Chapter 1	Introduction .....	6
Chapter 2	Electromagnetic Scattering: Mathematical Formulation.....	11
2.1	Full-Vector 3D Scenario .....	11
2.2	Discretization of the 3D Full-Vector Scenario.....	15
2.3	2D Phaseless Scenario.....	20
2.4	Discretization of the 2D Phaseless Scenario .....	23
2.5	Multi-View Arrangement.....	26
Chapter 3	Inversion Procedure .....	29
3.1	Inexact-Newton .....	30
3.2	Discussion on the Regularization in Banach Spaces.....	31
3.3	Truncated Landweber Method in Banach Spaces .....	34
3.4	Conjugate Gradient Method in Banach Spaces.....	35
3.5	3D Full-Vector Scenario: Fréchet Derivative Computation .....	36
3.6	2D Phaseless Scenario: Fréchet Derivative Computation.....	38
3.7	Frequency Hopping .....	39
Chapter 4	Numerical and Experimental Validation: 3D Full-Vector Scenario .....	40
4.1	Numerical Validation: Landweber-based Method .....	41
4.2	Numerical Validation: Conjugate Gradient-based Method.....	57
4.3	Experimental Validation: Landweber-based Method .....	69
4.4	Experimental Validation: Conjugate Gradient-based Method.....	74
Chapter 5	Numerical and Experimental Validation: 2D Phaseless Scenario.....	78
5.1	Numerical Validation with Synthetic Data .....	79
5.2	Experimental Validation .....	100
Conclusions.....		115

## Appendix A: Automatic Detection of Circular Cylinders in Reconstructed Contrast

Function .....	116
References.....	118

# Chapter 1 Introduction

Non-invasive/non-destructive diagnostic systems play a key role in several applicative fields, such as subsurface prospecting and biomedical imaging. In the last three decades, a particular focus has been dedicated by the scientific community to microwave imaging techniques [1]–[12]. Such techniques aim at providing information on the internal structure of the body to be inspected, whose interior is not accessible, by processing a set of electromagnetic field samples gathered outside the body by an active illuminating/measurement apparatus. These systems offer mainly two advantages over its popular competitors based on harmful x-rays emissions (e.g., computerized tomography) [13] or expensive magnetic resonance tools: They employ non-ionizing radiations that are safe for the users (provided that the devices fulfill the proper electromagnetic compatibility requirements [14]) and can be largely made by using off-the-shelf components commonly available in consumer electronics to limit the costs. Thanks to these benefits, recently microwave imaging systems are being considered as powerful tools in different applications, such as the development of portable biomedical devices for early brain stroke diagnosis [15]–[17], breast screening [18]–[20], early failure detection in civil buildings [21], [22], and wood inspection [23].

Many microwave imaging algorithms developed in the past in the scientific literature refer to two-dimensional (2D) scenarios and, in particular, tomographic configurations [8], [24]–[28]. This is often due to the high computational resources that are required to work in the three-dimensional (3D) setting. Some of the first attempts in 3D electromagnetic imaging can be found in [29]–[31], but only recently, essentially due to the increased computational power available also in common personal computers, much work has been made in order to extend existing 2D procedures to inspect 3D targets. The proposed approaches can be mainly grouped into two categories: the quantitative methods, which aims at retrieving an as much as possible accurate distribution of the dielectric properties of the object under test, and the qualitative ones, whose outputs consist in some kind of indicator function about the estimated internal structure of the target or some other simplified information (such as position and size of the inclusions). The techniques belonging to the latter class usually provide a fast response, although the reconstructed information of the object to be inspected

are limited (e.g., position, shape, ...) [3]. The synthetic focusing techniques have an important role in the class of qualitative methods. These approaches allow to generate an image of the reflection properties of the inspected region by a proper processing of the signals used to illuminate the target and of the corresponding received ones; in particular, by focusing on one pixel at a time, this processing aims to constructively sum the contributes arriving from the pixel of interest and to destructively sum the contributes of the remaining ones. Examples of this kind of approaches applied to the 3D setting can be found in [32] and [33], where the Delay And Sum (DAS) technique is investigated for the localization of breast tumors and hemorrhagic brain injuries, respectively. Also in [34], [35] synthetic focusing techniques are presented for 3D breast cancer detection. Finally, in [36] and [37] artefacts removal techniques for synthetic focusing are reported again in the context of breast screening. Another important sub-class of the qualitative methods is made of the holographic microwave imaging techniques, in which the knowledge on a planar aperture of the electric field, generated by illuminating the target, is processed through direct and inverse Fourier transforms in order to get a map of reflectivity of the inspected domain. Applications of this kind of methods in the 3D setting have been reported in [38], where a reflectometer working in the millimeter-wave band is presented, and in [39]–[41]. The Linear Sampling Method (LSM) is another deeply investigated kind of qualitative method. Several versions of the original LSM exist; however, generally they allow to detect the positions and shapes of inclusions in a known background medium by evaluating the norm of a complex function defined for each pixel of the inspected region. Among the various application of the LSM in the 3D setting [10], the hybridization reported in [42] can be cited, in which the output of the LSM is processed by the level set method in order to extract the compact support of the target. Others particular approaches to the 3D qualitative microwave imaging can be found in [43], where diffraction tomography and Singular Value Decomposition (SVD) in a multi-frequency setting are evaluated on synthetic data, in [44], where the recovery of sparse solutions is investigated, in [45], where a forward-propagating waves algorithm based on the Huygens principle is validated in an Ultra Wide Band (UWB) frequency range on experimental data, and in [46], where an inverse source-based approach is employed to detect moving objects in a through-the-wall configuration.

Differently from qualitative methods, quantitative approaches aim at providing an approximation of the dielectric properties distribution, although they can be significantly

more time-consuming especially in 3D scenarios. In this framework, the Distorted Born Iterative Method (DBIM) [12] has been generalized to the 3D setting in various ways [18], [20], [47]. Also Newton-type approaches have been adopted for quantitative 3D imaging [48]–[51]. Moreover, multi-scaling approaches, in which the reconstruction procedure is iteratively focused in localized areas of the investigated domain, can be of particular interest and have been reported in [52]–[54], with this last employing a particle swarm stochastic optimizer. Concerning stochastic methods, an interesting application in the 3D setting is proposed in [55], in which firstly the LSM is used to detect the supports of the targets, and then the stochastic algorithm Ant Colony Optimization (ACO) is used to retrieve the related dielectric properties. Generally, the stochastic methods better cope with the false minima issue, which usually affects the non-linear inverse electromagnetic scattering problems, with respect to the deterministic methods [56]. However, they can lead to unfeasible computational burdens in practice. Others particular approaches to the 3D quantitative microwave imaging can be found in [57], where a 3D time-domain method based on Born-type iterations and constrained minimization is described, in [58], in which a differential imaging algorithm is applied for breast imaging, in [59], where the Bayesian framework is considered to image 3D aggregates of low-contrast objects, and in [60], where the dual-mesh scheme, the iterative block solver, and the adjoint Jacobian method have been extended to 3D reconstructions to evaluate their viability for medical imaging. Beyond the numerical algorithms employed to reconstruct the spatial distribution of dielectric properties, also particular experimental setups have been investigated in order to enhance the 3D microwave imaging. For example, in [61], [62] a metallic resonant chamber, in which the target is enclosed, has been proven to provide some advantages over the more common free-space configuration.

Most of the microwave imaging algorithms existing in literature (both for 3D and 2D configurations) assume the availability of full-data measurements, that is both the real and imaginary parts of the measured electric field phasor are recorded. This requires a quite complex and expensive experimental apparatus due to the need of a coherent detection, which involves the need of a reference channel (a vector network analyzer (VNA) can be used for this purpose). The imaging configuration would be significantly simplified if only the amplitudes of the measured fields were considered. Such scenario is known as phaseless microwave imaging. In the past, these kind of approaches were proposed mainly in the



framework of antennas diagnostic or source reconstruction [63]–[66] and only in a limited manner for imaging of materials [67]–[69]. More recently the phaseless setting has gained a higher consideration for the imaging of quite complex targets. For example, two-step strategies consisting in a phase retrieval step followed by a full-data inverse scattering one are described in [70], [71], and an improved three-step procedure, in which a further phase retrieval task on the illuminating electric field is accomplished, is discussed in [72]. A one-step technique, without a phase retrieval problem to be solved explicitly, is presented in [73]. In [74] an application of the compressive sensing theory is proposed for the imaging of point-like targets. An iterative multi-scaling algorithm employing a particle swarm stochastic optimizer is adopted in [75]. In [76] an adapted subspace-based optimization method is introduced. The contrast source inversion (CSI) and multiplicative regularized CSI methods are used in [77]. In [78] the distorted Rytov iterative method is modified for the phaseless setup. An hybrid method known as memetic algorithm is adopted in [79]. In [80] a phase retrieval step [81] followed by an inexact-Newton inversion scheme is proposed. Finally, the use of metasurface antennas has been evaluated for phaseless microwave imaging [82], [83], and the differential evolution stochastic method was considered, too [84].

In any case, i.e., for 3D or 2D and full-data or phaseless scenarios, the underlying electromagnetic inverse scattering problems are usually ill-posed in the Hadamard sense, since their solutions are not unique and do not depend continuously on the data [85], [86]. Moreover, when the target to be inspected represents a strong inhomogeneity in the propagation medium, the linearization such as the Born approximation [87] cannot be used, and the full non-linear problem must be considered. Consequently, it is necessary to develop strategies able to perform an efficient regularization of the involved non-linear inverse problems. Although significant advancements have been attained in this field by using both deterministic and stochastic inversion procedures, as reported in this Introduction, there is still the need to develop novel approaches able to address the limitations of the existing ones. In the present Thesis, a non-linear regularizing scheme belonging to the class of deterministic local quantitative methods is proposed and applied to the 3D full-vector and 2D phaseless scenarios. As most of the previously mentioned microwave imaging techniques, it is devoted to the near-field inspection of targets in the resonant regime, i.e., the objects under test exhibits dimensions that are comparable with the wavelength of the incident radiation. The involved electromagnetic phenomena are described by means of the

Electric Field Integral Equations (EFIE) [2], which lead to the non-linear and ill-posed operator equation to be inverted. The proposed algorithm belongs to the inexact-Newton class [88]–[90] and is defined in the framework of the  $l^p$  Banach spaces [91], with  $p > 1$ , differently from conventional quantitative imaging approaches that are usually based on the minimization of a least square residual (between the actual and predicted data) in the standard  $l^2$  Hilbert spaces. In particular, the inner linear problems that are defined in each Newton iteration are approximately solved by two alternative linear solvers: the truncated Landweber method [91]–[93] and the conjugate gradient one [94], [95], both developed in the new Banach framework. The chosen mathematical setting is more general with respect to the one adopted in classic Newton-type algorithms, and also much more involving, since the absence of a scalar product when  $p \neq 2$  denies the possibility to define spectral decompositions of the linear operators, and so advanced concepts of convex functional analysis are needed [91], [92]. The gained generality introduces novel and non-standard minimization strategies potentially able to provide reconstructions endowed with lower over-smoothing and ringing effects, which often characterize the least square-based approaches in  $l^2$ . Moreover, for  $p$  values close to one the method promotes sparsity in the retrieved solution, which is very useful for reconstructing small dielectric objects that may be more affected by the oversmoothing problems. This method has been initially proposed with success in [96]–[98] for solving the 2D full-data scalar problem related to tomographic imaging and it is extended in this Thesis to 3D full-vector and 2D phaseless settings.

The Thesis is organized as follows. In Chapter 2, the electromagnetic mathematical models for both the 3D full-vector and 2D phaseless scenarios are reported. Chapter 3 describes the developed inversion algorithms. Extensive validations against both synthetic and experimental data for the 3D full-vector and 2D phaseless scenarios are reported in Chapter 4 and 5, respectively. Finally, conclusions are drawn in Chapter 6.

## Chapter 2 Electromagnetic Scattering: Mathematical Formulation

In this Chapter, the equations that fully describe the classical electromagnetic scattering phenomena in the frequency domain will be derived starting from a limited and quite common set of hypotheses. Firstly, the 3D full-vector scenario will be developed. Thereafter, the 2D phaseless setting will be derived as a special case.

### 2.1 Full-Vector 3D Scenario

Let us consider the imaging setup sketched in Figure 1.

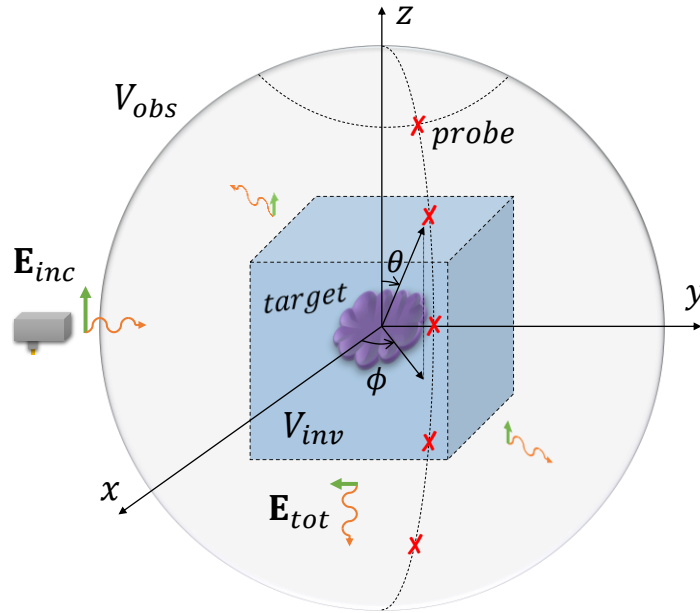


Figure 1. Schematic representation of the considered imaging setup.

The unknown target is located in an investigation volume  $V_{inv}$  of known geometry and it is embedded in an unbounded background medium. A time-harmonic source (physically realized by an antenna) generates a field impinging on the inspected scenario. This source is electromagnetically decoupled with respect to the target; such hypothesis allows to model the active source by a current density  $\mathbf{J}_o(\mathbf{r})$ , with  $\mathbf{r}$  position vector, independent from the

target dielectric properties. The sinusoidal nature of the involved fields is expressed by a multiplicative term  $e^{j\omega t}$ , with  $\omega$  angular frequency; however, in order to make the notation more compact, this term will be omitted in the following. When the source radiates in presence of no target, the resulting electric field is known as incident electric field  $\mathbf{E}_{inc}$ . Instead, when a target is present in  $V_{inv}$ , the interaction between the incident field and the object gives rise to the total electric field  $\mathbf{E}_{tot}$ . This is measured in a given observation (or measurement) domain  $V_{obs}$ , which surrounds the investigation one, by means of a set of receiving antennas. It is fundamental that the domain  $V_{obs}$  lies outside  $V_{inv}$  entirely in order to make feasible a non-destructive testing [4]. Let us now make some assumptions on the propagation mediums constituting the target and the background. Generally, their effects on the electromagnetic fields are described by the known constitutive relations [99], [100]

$$\begin{aligned}\mathbf{D}_{tot} &= \mathbf{f}_D(\mathbf{E}_{tot}, \mathbf{H}_{tot}) \\ \mathbf{B}_{tot} &= \mathbf{f}_B(\mathbf{E}_{tot}, \mathbf{H}_{tot})\end{aligned}\tag{1}$$

where  $\mathbf{D}_{tot}$  is the total electric displacement field,  $\mathbf{H}_{tot}$  is the total magnetic field, and  $\mathbf{B}_{tot}$  is the total magnetic induction field. Additionally, for conducting media there is the generalized Ohm law [99]

$$\mathbf{J} = \mathbf{f}_J(\mathbf{E}_{tot}, \mathbf{H}_{tot})\tag{2}$$

where  $\mathbf{J}$  is the current density. In the present context of interest, the propagation mediums are assumed to be inhomogeneous, linear, isotropic, temporal dispersive, spatially non-dispersive, and non-magnetic. Under these hypotheses, the general equations in (1) and (2) reduce to the following ones [99], [100]

$$\begin{aligned}\mathbf{D}_{tot} &= \epsilon(\mathbf{r}, \omega)\mathbf{E}_{tot} \\ \mathbf{B}_{tot} &= \mu_0\mathbf{H}_{tot} \\ \mathbf{J} &= \sigma(\mathbf{r}, \omega)\mathbf{E}_{tot}\end{aligned}\tag{3}$$

where  $\epsilon(\mathbf{r}, \omega) = \epsilon'(\mathbf{r}, \omega) - j\epsilon''(\mathbf{r}, \omega)$  is the complex dielectric permittivity, with  $\epsilon'$  and  $\epsilon''$  real and (opposed) imaginary parts of the dielectric permittivity, respectively,  $\sigma$  electric conductivity, and  $\mu_0$  vacuum magnetic permeability. The background media is considered

non-magnetic and simply characterized by the homogeneous complex dielectric permittivity  $\epsilon_b$ . Given this introduction, now the mathematical description of the electromagnetic phenomena of interest can be presented. First of all, when the target is not present in  $V_{inv}$ , namely it is filled with the background medium only, the following inhomogeneous wave equation is involved [99]

$$\nabla_{\mathbf{r}} \times \nabla_{\mathbf{r}} \times \mathbf{E}_{inc}(\mathbf{r}) - k_b^2 \mathbf{E}_{inc}(\mathbf{r}) = -j\omega\mu_0 \mathbf{J}_o(\mathbf{r}) \quad (4)$$

where  $k_b = \omega\sqrt{\epsilon_b\mu_0}$  is the background propagation constant. When an object is inserted in the investigated region, it causes phenomena of reflection, transmission, diffraction, and absorption, generally grouped under the term *scattering* phenomenon. The resulting total electric field  $\mathbf{E}_{tot}$ , under the aforementioned electromagnetic decoupling of source and target, can be written as follows [1], [2]

$$\mathbf{E}_{tot}(\mathbf{r}) = \mathbf{E}_{inc}(\mathbf{r}) + \mathbf{E}_{scat}(\mathbf{r}) \quad (5)$$

where  $\mathbf{E}_{scat}$  is known as scattering electric field and is an additive contribution due to the object presence. Let us note that if the scattering component is null, that is the object is not present,  $\mathbf{E}_{tot}$  turns back to be  $\mathbf{E}_{inc}$ . Because the target breaks the homogeneity of the propagation medium, the electric field volumetric equivalency principle [1], [2] is employed to get an equivalent problem in which an equivalent source radiates in the homogeneous background medium only and generates the same field scattered by the real target. The application of this principle starts by noting that the total electric field satisfies the following inhomogeneous wave equation

$$\begin{aligned} \nabla_{\mathbf{r}} \times \nabla_{\mathbf{r}} \times \mathbf{E}_{tot}(\mathbf{r}) - k^2(\mathbf{r})\mathbf{E}_{tot}(\mathbf{r}) &= -j\omega\mu_0 \mathbf{J}_o(\mathbf{r}) \\ k(\mathbf{r}) &= \begin{cases} k_b, & \mathbf{r} \notin V_{obj} \\ \omega\sqrt{\mu_0\epsilon(\mathbf{r})}, & \mathbf{r} \in V_{obj} \end{cases} \end{aligned} \quad (6)$$

where  $V_{obj}$  is the object's support. Subtracting (4) from (6), and by using (5), the following inhomogeneous wave equation is obtained

$$\nabla_{\mathbf{r}} \times \nabla_{\mathbf{r}} \times \mathbf{E}_{scat}(\mathbf{r}) - k_b^2 \mathbf{E}_{scat}(\mathbf{r}) = -j\omega\mu_0 \mathbf{J}_{eq}(\mathbf{r}) \quad (7)$$

$$\mathbf{J}_{eq}(\mathbf{r}) = \frac{j}{\omega\mu_0} [k^2(\mathbf{r}) - k_b^2] \mathbf{E}_{tot}(\mathbf{r}) \quad (8)$$

The quantity  $\mathbf{J}_{eq}$  is the wanted equivalent current density. Let us note that the equivalent current density's support coincides with the object's one ( $V_{eq} \equiv V_{obj}$ ), since  $\mathbf{J}_{eq} = \mathbf{0}$  for  $\mathbf{r} \notin V_{obj}$ . Now it is possible to define the following vector potential

$$\mathbf{A}_{scat}(\mathbf{r}) = -\mu_0 \iiint_{V_{eq}} \mathbf{J}_{eq}(\mathbf{r}') g_b(\mathbf{r}, \mathbf{r}') d\mathbf{r}' \quad (9)$$

where  $g_b(\mathbf{r}, \mathbf{r}') = -\frac{1}{4\pi} \frac{e^{-jk_b|\mathbf{r}-\mathbf{r}'|}}{|\mathbf{r}-\mathbf{r}'|}$  is the Green function for background [101]. Therefore, the scattering electric field is given by

$$\mathbf{E}_{scat}(\mathbf{r}) = -j\omega\mathbf{A}_{scat}(\mathbf{r}) - \frac{j}{\omega\mu_0\epsilon_b} \nabla_{\mathbf{r}} [\nabla_{\mathbf{r}} \cdot \mathbf{A}_{scat}(\mathbf{r})] \quad (10)$$

and substituting (9) in (10) we get

$$\begin{aligned} \mathbf{E}_{scat}(\mathbf{r}) = j\omega\mu_0 \iiint_{V_{eq}} \mathbf{J}_{eq}(\mathbf{r}') g_b(\mathbf{r}, \mathbf{r}') d\mathbf{r}' \\ + \frac{j}{\omega\epsilon_b} \nabla_{\mathbf{r}} \left[ \nabla_{\mathbf{r}} \cdot \iiint_{V_{eq}} \mathbf{J}_{eq}(\mathbf{r}') g_b(\mathbf{r}, \mathbf{r}') d\mathbf{r}' \right] \end{aligned} \quad (11)$$

By exploiting the integral's linearity, the scattered electric field can be written as

$$\mathbf{E}_{scat}(\mathbf{r}) = j\omega\mu_0 \iiint_{V_{eq}} \bar{\bar{\mathbf{G}}}_b(\mathbf{r}, \mathbf{r}') \cdot \mathbf{J}_{eq}(\mathbf{r}') d\mathbf{r}' \quad (12)$$

where  $\bar{\bar{\mathbf{G}}}_b$  is the Green dyadic tensor for background [102]

$$\bar{\bar{\mathbf{G}}}_b(\mathbf{r}, \mathbf{r}') = \left( \bar{\bar{\mathbf{I}}} + \frac{\nabla_{\mathbf{r}} \nabla_{\mathbf{r}}}{k_b^2} \right) g_b(\mathbf{r}, \mathbf{r}') \quad (13)$$

and  $\bar{\bar{\mathbf{I}}}$  is the dyadic identity. Moreover, by defining the contrast function

$$c(\mathbf{r}) = \frac{\epsilon(\mathbf{r})}{\epsilon_b} - 1 \quad (14)$$

the previous scattering equation can be formulated as

$$\mathbf{E}_{scat}(\mathbf{r}) = -k_b^2 \iiint_{V_{eq}} \bar{\bar{\mathbf{G}}}_b(\mathbf{r}, \mathbf{r}') \cdot c(\mathbf{r}') \mathbf{E}_{tot}(\mathbf{r}') d\mathbf{r}' \quad (15)$$

By noting that the integral in (15) can be equivalently defined on  $V_{inv}$ , since  $c(\mathbf{r}') = 0$  when  $\mathbf{r}' \notin V_{eq}$ , the following system of equations can be outlined

$$\begin{aligned} \mathbf{E}_{scat}(\mathbf{r}) &= -k_b^2 \iiint_{V_{inv}} \bar{\bar{\mathbf{G}}}_b(\mathbf{r}, \mathbf{r}') \cdot c(\mathbf{r}') \mathbf{E}_{tot}(\mathbf{r}') d\mathbf{r}', \quad \mathbf{r} \in V_{obs} \\ \mathbf{E}_{inc}(\mathbf{r}) &= \mathbf{E}_{tot}(\mathbf{r}) + k_b^2 \iiint_{V_{inv}} \bar{\bar{\mathbf{G}}}_b(\mathbf{r}, \mathbf{r}') \cdot c(\mathbf{r}') \mathbf{E}_{tot}(\mathbf{r}') d\mathbf{r}', \quad \mathbf{r} \in V_{inv} \end{aligned} \quad (16)$$

The former equation in (16) is called data equation, because it involves the scattering data gathered in  $V_{obs}$ , whereas the second one is known as state equation, since  $\mathbf{r}$  is restricted to the internal domain  $V_{inv}$ .

## 2.2 Discretization of the 3D Full-Vector Scenario

In order to develop numerical algorithms able to solve forward and inverse electromagnetics problems, the scattering equations described in the previous Section are discretized by means of the Method of Moments (MoM) [103], [104]. In this view, a cube-based mesh of  $V_{inv}$  given by  $N$  voxels  $\{V_n^{inv}\}_{n=1}^N$  with centers  $\{\mathbf{r}_n^{inv}\}_{n=1}^N$  is considered. Each voxel has volume  $v$  and side  $\Delta$ . Moreover,  $M$  observation points (where the antennas collect the scattered electric field) belonging to  $V_{obs}$  are selected and identified with  $\{\mathbf{r}_m^{obs}\}_{m=1}^M$ . A schematic representation of the considered discretized problem is shown in Figure 2.

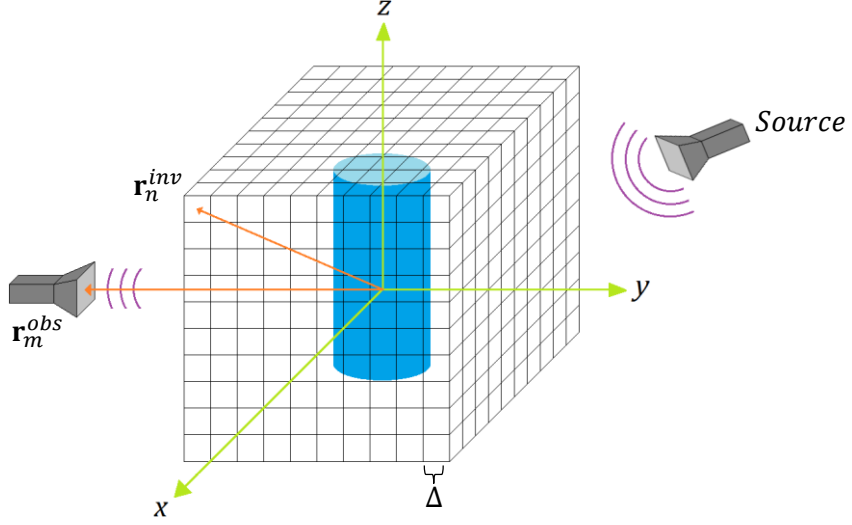


Figure 2. Schematic representation of the considered discretized problem.

On the mesh of  $V_{inv}$  the following pulse basis functions are defined

$$b_n(\mathbf{r}) = \begin{cases} 1, & \|\mathbf{r} - \mathbf{r}_n^{inv}\|_\infty \leq \frac{\Delta}{2} \\ 0, & \text{otherwise} \end{cases} \quad n = 1, \dots, N \quad (17)$$

Now the quantity  $c\mathbf{E}_{tot}$  in  $V_{inv}$  can be approximated through these basis as

$$c(\mathbf{r})\mathbf{E}_{tot}(\mathbf{r}) \cong \sum_{l=1}^N c(\mathbf{r}_l^{inv})\mathbf{E}_{tot}(\mathbf{r}_l^{inv})b_l(\mathbf{r}), \quad \mathbf{r} \in V_{inv} \quad (18)$$

This means that  $c\mathbf{E}_{tot}$  is approximated by a piece-wise constant (PWC) function, where the constant levels are given by the values that  $c\mathbf{E}_{tot}$  assumes in the voxels centers. The following system is obtained by introducing the approximation (18) in (16)

$$\begin{aligned} \mathbf{E}_{scat}(\mathbf{r}) &= -k_b^2 \sum_{l=1}^N \iiint_{V_l^{inv}} \bar{\mathbf{G}}_b(\mathbf{r}, \mathbf{r}') d\mathbf{r}' \cdot c(\mathbf{r}_l^{inv})\mathbf{E}_{tot}(\mathbf{r}_l^{inv}), \quad \mathbf{r} \in V_{obs} \\ \mathbf{E}_{inc}(\mathbf{r}) &= \mathbf{E}_{tot}(\mathbf{r}) + k_b^2 \sum_{l=1}^N \iiint_{V_l^{inv}} \bar{\mathbf{G}}_b(\mathbf{r}, \mathbf{r}') d\mathbf{r}' \cdot c(\mathbf{r}_l^{inv})\mathbf{E}_{tot}(\mathbf{r}_l^{inv}), \quad \mathbf{r} \in V_{inv} \end{aligned} \quad (19)$$

Thereafter, by adopting the so-called point-matching (or collocation) approach, the Dirac's delta  $\delta$  are considered as testing functions, and the following operators are defined



$$\mathbf{T}_m^{obs}(\cdot)(\mathbf{r}) = \iiint_{\mathbb{R}^3} (\cdot)(\mathbf{r}) \delta(|\mathbf{r} - \mathbf{r}_m^{obs}|) d\mathbf{r}, \quad m = 1, \dots, M \quad (20)$$

$$\mathbf{T}_n^{inv}(\cdot)(\mathbf{r}) = \iiint_{\mathbb{R}^3} (\cdot)(\mathbf{r}) \delta(|\mathbf{r} - \mathbf{r}_n^{inv}|) d\mathbf{r}, \quad n = 1, \dots, N \quad (21)$$

The operators (20) perform a sampling of a complex vector field in the measurement points, whereas the ones in (21) sample in the voxels centers. Now the operators in (20) and (21) are applied to the 3D full-vector data and state equations obtaining

$$\begin{aligned} \mathbf{E}_{scat}(\mathbf{r}_m^{obs}) &= -k_b^2 \sum_{l=1}^N \iiint_{V_l^{inv}} \bar{\mathbf{G}}_b(\mathbf{r}_m^{obs}, \mathbf{r}') d\mathbf{r}' \cdot c(\mathbf{r}_l^{inv}) \mathbf{E}_{tot}(\mathbf{r}_l^{inv}) \\ \mathbf{E}_{inc}(\mathbf{r}_n^{inv}) &= \mathbf{E}_{tot}(\mathbf{r}_n^{inv}) + k_b^2 \sum_{l=1}^N \iiint_{V_l^{inv}} \bar{\mathbf{G}}_b(\mathbf{r}_n^{inv}, \mathbf{r}') d\mathbf{r}' \cdot c(\mathbf{r}_l^{inv}) \mathbf{E}_{tot}(\mathbf{r}_l^{inv}) \end{aligned} \quad (22)$$

The Dyadic Green's function occurs in a singularity when  $\mathbf{r}_n^{inv} \equiv \mathbf{r}'$  [102], [105], [106]. In order to take care of such singularity, the state equation in (22) is rewritten as

$$\begin{aligned} \mathbf{E}_{inc}(\mathbf{r}_n^{inv}) &= \hat{c}(\mathbf{r}_n^{inv}) \mathbf{E}_{tot}(\mathbf{r}_n^{inv}) \\ &+ k_b^2 \sum_{l=1}^N PV \iiint_{V_l^{inv}} \bar{\mathbf{G}}_b(\mathbf{r}_n^{inv}, \mathbf{r}') d\mathbf{r}' \cdot c(\mathbf{r}_l^{inv}) \mathbf{E}_{tot}(\mathbf{r}_l^{inv}) \end{aligned} \quad (23)$$

where  $\hat{c} = 1 + \frac{j\omega\mu_0}{3}c$  and  $PV$  is the integral's principal value. By using the  $\mathbb{R}^3$  Euclidean space's canonical basis, the dyadic Green function (pre-multiplied by  $k_b^2$ ) can be represented in matrix form as

$$\mathbf{G}_b(\mathbf{r}, \mathbf{r}') = \begin{bmatrix} k_b^2 + \frac{\partial^2}{\partial x^2} & \frac{\partial^2}{\partial x \partial y} & \frac{\partial^2}{\partial x \partial z} \\ \frac{\partial^2}{\partial y \partial x} & k_b^2 + \frac{\partial^2}{\partial y^2} & \frac{\partial^2}{\partial y \partial z} \\ \frac{\partial^2}{\partial z \partial x} & \frac{\partial^2}{\partial z \partial y} & k_b^2 + \frac{\partial^2}{\partial z^2} \end{bmatrix} g_b(\mathbf{r}, \mathbf{r}') \quad (24)$$

The matrix is symmetric since the derivatives order can be exchanged. Moreover, the following quantities are defined [105]

$$\begin{aligned}
\mathbf{E}_{tot}^{ext} &= \begin{bmatrix} E_{tot}^x(\mathbf{r}_1^{obs}) \\ \vdots \\ E_{tot}^x(\mathbf{r}_M^{obs}) \\ E_{tot}^y(\mathbf{r}_1^{obs}) \\ \vdots \\ E_{tot}^y(\mathbf{r}_M^{obs}) \\ E_{tot}^z(\mathbf{r}_1^{obs}) \\ \vdots \\ E_{tot}^z(\mathbf{r}_M^{obs}) \end{bmatrix} & \mathbf{E}_{inc}^{ext} &= \begin{bmatrix} E_{inc}^x(\mathbf{r}_1^{obs}) \\ \vdots \\ E_{inc}^x(\mathbf{r}_M^{obs}) \\ E_{inc}^y(\mathbf{r}_1^{obs}) \\ \vdots \\ E_{inc}^y(\mathbf{r}_M^{obs}) \\ E_{inc}^z(\mathbf{r}_1^{obs}) \\ \vdots \\ E_{inc}^z(\mathbf{r}_M^{obs}) \end{bmatrix} & \mathbf{E}_{scat}^{ext} &= \begin{bmatrix} E_{scat}^x(\mathbf{r}_1^{obs}) \\ \vdots \\ E_{scat}^x(\mathbf{r}_M^{obs}) \\ E_{scat}^y(\mathbf{r}_1^{obs}) \\ \vdots \\ E_{scat}^y(\mathbf{r}_M^{obs}) \\ E_{scat}^z(\mathbf{r}_1^{obs}) \\ \vdots \\ E_{scat}^z(\mathbf{r}_M^{obs}) \end{bmatrix} \\
\mathbf{E}_{tot}^{int} &= \begin{bmatrix} E_{tot}^x(\mathbf{r}_1^{inv}) \\ \vdots \\ E_{tot}^x(\mathbf{r}_N^{inv}) \\ E_{tot}^y(\mathbf{r}_1^{inv}) \\ \vdots \\ E_{tot}^y(\mathbf{r}_N^{inv}) \\ E_{tot}^z(\mathbf{r}_1^{inv}) \\ \vdots \\ E_{tot}^z(\mathbf{r}_N^{inv}) \end{bmatrix} & \mathbf{E}_{inc}^{int} &= \begin{bmatrix} E_{inc}^x(\mathbf{r}_1^{inv}) \\ \vdots \\ E_{inc}^x(\mathbf{r}_N^{inv}) \\ E_{inc}^y(\mathbf{r}_1^{inv}) \\ \vdots \\ E_{inc}^y(\mathbf{r}_N^{inv}) \\ E_{inc}^z(\mathbf{r}_1^{inv}) \\ \vdots \\ E_{inc}^z(\mathbf{r}_N^{inv}) \end{bmatrix} & \mathbf{c} &= \begin{bmatrix} c(\mathbf{r}_1^{inv}) \\ \vdots \\ c(\mathbf{r}_N^{inv}) \end{bmatrix} & \hat{\mathbf{c}} &= \begin{bmatrix} \hat{c}(\mathbf{r}_1^{inv}) \\ \vdots \\ \hat{c}(\mathbf{r}_N^{inv}) \end{bmatrix} \\
\mathbf{G}_b^{ext} &= - \begin{bmatrix} \mathbf{G}_{b,xx}^{ext} & \mathbf{G}_{b,xy}^{ext} & \mathbf{G}_{b,xz}^{ext} \\ \mathbf{G}_{b,yx}^{ext} & \mathbf{G}_{b,yy}^{ext} & \mathbf{G}_{b,yz}^{ext} \\ \mathbf{G}_{b,zx}^{ext} & \mathbf{G}_{b,zy}^{ext} & \mathbf{G}_{b,zz}^{ext} \end{bmatrix} \\
\mathbf{G}_b^{int} &= -\frac{j\omega\mu_0}{3} \mathbf{I} - \begin{bmatrix} \mathbf{G}_{b,xx}^{int} & \mathbf{G}_{b,xy}^{int} & \mathbf{G}_{b,xz}^{int} \\ \mathbf{G}_{b,yx}^{int} & \mathbf{G}_{b,yy}^{int} & \mathbf{G}_{b,yz}^{int} \\ \mathbf{G}_{b,zx}^{int} & \mathbf{G}_{b,zy}^{int} & \mathbf{G}_{b,zz}^{int} \end{bmatrix} \\
\mathbf{G}_{b,x_\alpha x_\beta}^{ext} &= \begin{bmatrix} \iiint_{V_1^{inv}} G_b^{x_\alpha x_\beta}(\mathbf{r}_1^{obs}, \mathbf{r}') d\mathbf{r}' & \dots & \iiint_{V_N^{inv}} G_b^{x_\alpha x_\beta}(\mathbf{r}_1^{obs}, \mathbf{r}') d\mathbf{r}' \\ \vdots & \ddots & \vdots \\ \iiint_{V_1^{inv}} G_b^{x_\alpha x_\beta}(\mathbf{r}_M^{obs}, \mathbf{r}') d\mathbf{r}' & \dots & \iiint_{V_N^{inv}} G_b^{x_\alpha x_\beta}(\mathbf{r}_M^{obs}, \mathbf{r}') d\mathbf{r}' \end{bmatrix}
\end{aligned} \tag{25}$$

$$\mathbf{G}_{b,x_\alpha x_\beta}^{int} = \begin{bmatrix} \iiint_{V_1^{inv}} G_b^{x_\alpha x_\beta}(\mathbf{r}_1^{inv}, \mathbf{r}') d\mathbf{r}' & \dots & \iiint_{V_N^{inv}} G_b^{x_\alpha x_\beta}(\mathbf{r}_1^{inv}, \mathbf{r}') d\mathbf{r}' \\ \vdots & \ddots & \vdots \\ \iiint_{V_1^{inv}} G_b^{x_\alpha x_\beta}(\mathbf{r}_N^{inv}, \mathbf{r}') d\mathbf{r}' & \dots & \iiint_{V_N^{inv}} G_b^{x_\alpha x_\beta}(\mathbf{r}_N^{inv}, \mathbf{r}') d\mathbf{r}' \end{bmatrix}$$

$$G_b^{x_\alpha x_\beta}(\mathbf{r}, \mathbf{r}') = \left( k_b^2 \delta_{\alpha\beta} + \frac{\partial^2}{\partial x_\alpha \partial x_\beta} \right) g_b(\mathbf{r}, \mathbf{r}')$$

where  $\delta_{\alpha\beta}$  is the Kronecker delta,  $\alpha, \beta \in \{1,2,3\}$ , and  $x_1 = x$ ,  $x_2 = y$ ,  $x_3 = z$ . The scalar functions  $E_{tot}^x(\cdot)$ ,  $E_{tot}^y(\cdot)$ ,  $E_{tot}^z(\cdot)$  are the Cartesian components of the vector-valued function  $\mathbf{E}_{tot}(\cdot)$ , and analogous definitions are used for  $\mathbf{E}_{inc}(\cdot)$  and  $\mathbf{E}_{scat}(\cdot)$ .  $\mathbf{G}_b^{ext}$  and  $\mathbf{G}_b^{int}$  are the external and internal Green matrices for background, respectively, and it is worth noting that  $\mathbf{G}_b^{int}$  is symmetric. The integrals in  $\mathbf{G}_b^{ext}$  can be approximated by [107]

$$\iiint_{V_l^{inv}} G_b^{x_\alpha x_\beta}(\mathbf{r}_m^{obs}, \mathbf{r}') d\mathbf{r}' \cong -4\pi a \left[ \frac{\sin(k_b a)}{k_b a} - \cos(k_b a) \right] G_b^{x_\alpha x_\beta}(\mathbf{r}_m^{obs}, \mathbf{r}_l^{inv}) \quad (26)$$

with

$$G_b^{x_\alpha x_\beta}(\mathbf{r}_m^{obs}, \mathbf{r}_l^{inv}) = -\frac{e^{-jk_b R_{ml}}}{4\pi k_b^2 R_{ml}^3} [(k_b^2 R_{ml}^2 - 1 - jk_b R_{ml}) \delta_{\alpha\beta} + (3 - k_b^2 R_{ml}^2 + 3jk_b R_{ml}) \left( \frac{x_m^{obs} - x_l^{inv}}{R_{ml}} \right) \left( \frac{x_\beta^{obs} - x_\beta^{inv}}{R_{ml}} \right)] \quad (27)$$

where  $a = \sqrt[3]{\frac{3}{4\pi} v}$ ,  $R_{ml} = |\mathbf{r}_m^{obs} - \mathbf{r}_l^{inv}|$ ,  $\mathbf{r}_m^{obs} = [x_m^{obs} \ y_m^{obs} \ z_m^{obs}]^T$ , and  $\mathbf{r}_l^{inv} = [x_l^{inv} \ y_l^{inv} \ z_l^{inv}]^T$ . Let us note that  $a$  is the radius of a sphere with center in  $\mathbf{r}_l^{inv}$  and volume  $v$  (the voxel's volume). Concerning  $\mathbf{G}_b^{int}$ , when  $\mathbf{r}_n^{inv} \notin V_l^{inv}$  it is possible to use the same approximation adopted for  $\mathbf{G}_b^{ext}$ . On the contrary, when  $\mathbf{r}_n^{inv} \in V_l^{inv}$  the principal value can be approximated as [107]

$$PV \iiint_{V_n^{inv}} G_b^{x_\alpha x_\beta}(\mathbf{r}_n^{inv}, \mathbf{r}') d\mathbf{r}' \cong \begin{cases} -\frac{2}{3}(1 + jk_b a)e^{-jk_b a} + 1, & \alpha = \beta \\ 0, & \alpha \neq \beta \end{cases} \quad (28)$$

With the previous definitions, the scattering equations in (22) and (23) can be rewritten in the following compact matrix form

$$\begin{aligned} \mathbf{E}_{scat}^{ext} &= \mathbf{G}_b^{ext} \text{diag}_3(\mathbf{c}) \mathbf{E}_{tot}^{int} \\ \mathbf{E}_{inc}^{int} &= [\mathbf{I} - \mathbf{G}_b^{int} \text{diag}_3(\mathbf{c})] \mathbf{E}_{tot}^{int} \end{aligned} \quad (29)$$

where

$$\text{diag}_3(\mathbf{c}) = \begin{bmatrix} \text{diag}(\mathbf{c}) & \mathbf{0}_{N \times N} & \mathbf{0}_{N \times N} \\ \mathbf{0}_{N \times N} & \text{diag}(\mathbf{c}) & \mathbf{0}_{N \times N} \\ \mathbf{0}_{N \times N} & \mathbf{0}_{N \times N} & \text{diag}(\mathbf{c}) \end{bmatrix} \quad (30)$$

with  $\text{diag}(\mathbf{c})$  diagonal matrix having the elements of  $\mathbf{c}$  as diagonal entries, and  $\mathbf{0}_{N \times N}$  null matrix of dimension  $N \times N$ . Since the matrix  $\mathbf{I} - \mathbf{G}_b^{int} \text{diag}_3(\mathbf{c})$  is usually well-conditioned and invertible [1], [2], the two equations can be combined together in order to obtain the following relationship

$$\mathbf{E}_{scat}^{ext} = \mathbf{G}_b^{ext} \text{diag}_3(\mathbf{c}) [\mathbf{I} - \mathbf{G}_b^{int} \text{diag}_3(\mathbf{c})]^{-1} \mathbf{E}_{inc}^{int} = \mathbf{F}^{3D}(\mathbf{c}) \quad (31)$$

which describes the mapping between the contrast function and the scattered electric field in the measurement points.

### 2.3 2D Phaseless Scenario

The 3D full-vector setting usually requires a large amount of memory to store the involved Green matrices, and consequently it leads to a considerable computational burden to execute the imaging algorithm presented in Chapter 3. Moreover, assuming a cubic investigation domain, by denoting with  $N_x$  the number of subdivision in which each Cartesian axis is partitioned by the cube-based mesh, it results that the number of voxels  $N$  grows as  $N_x^3$  and so the computational requirements increase very rapidly with a finer discretization.

Therefore, the tomographic hypothesis [1], [2], [27], [28] is often adopted. This consists in considering the target as infinitely extended along the  $z$ -axis and with dielectric properties varying on the transversal plane only, i.e.  $\epsilon(\mathbf{r}) = \epsilon(x, y) = \epsilon(\mathbf{r}_t)$ . Consequently, the focus can be reduced to a target's cross-section of  $V_{eq}$  only, indicated as  $D_{eq}$ . This assumption is valid when the antenna main lobe is narrow in the elevation direction and the wavelength is sufficiently small with respect to the target's height. Moreover, a Transverse Magnetic  $z$ -polarized (TM $_z$ ) incident electric field is adopted, i.e.  $\mathbf{E}_{inc}(\mathbf{r}) = E_{inc}(\mathbf{r}_t)\hat{\mathbf{z}}$ . The described configuration is sketched in Figure 3, in which  $D_{inv}$  is the investigation domain and  $D_{obs}$  is the observation one (both coplanar to  $D_{eq}$ ).

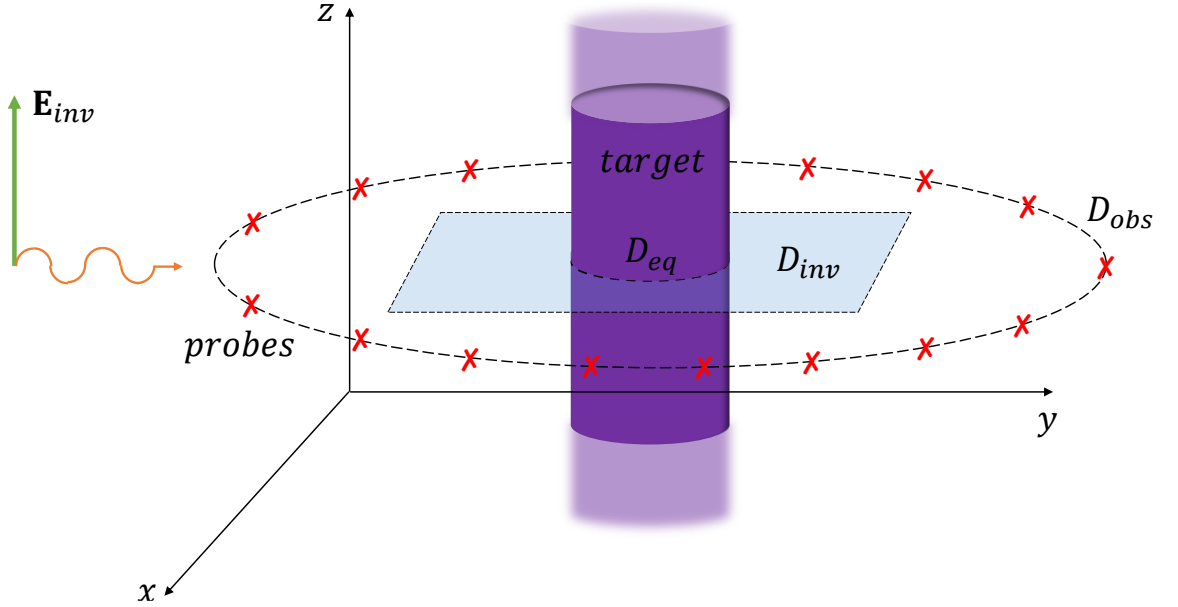


Figure 3. Schematic representation of the tomographic setup.

Under these hypotheses, thanks to the symmetry of the configuration, it can be demonstrated that  $\mathbf{E}_{tot}(\mathbf{r}) = E_{tot}(\mathbf{r}_t)\hat{\mathbf{z}}$  and  $\mathbf{E}_{scat}(\mathbf{r}) = E_{scat}(\mathbf{r}_t)\hat{\mathbf{z}}$ . Therefore, the scattering equation in (15) reduces to

$$E_{scat}(\mathbf{r}_t)\hat{\mathbf{z}} = -k_b^2 \iint_{D_{eq}} \left[ \int_{-\infty}^{+\infty} \bar{\mathbf{G}}_b(\mathbf{r}_t, \mathbf{r}') dz' \right] \cdot c(\mathbf{r}') E_{tot}(\mathbf{r}') \hat{\mathbf{z}} d\mathbf{r}' \quad (32)$$

The following equalities hold for the inner integral on  $z'$  [108]

$$\int_{-\infty}^{+\infty} \bar{\mathbf{G}}_b(\mathbf{r}_t, \mathbf{r}') dz' = \left( \bar{\mathbf{I}} + \frac{\nabla_{\mathbf{r}} \nabla_{\mathbf{r}}}{k_b^2} \right) \int_{-\infty}^{+\infty} g_b(\mathbf{r}_t, \mathbf{r}') dz' = \left( \bar{\mathbf{I}} + \frac{\nabla_{\mathbf{r}} \nabla_{\mathbf{r}}}{k_b^2} \right) G_b^{2D}(\mathbf{r}_t, \mathbf{r}_t') \quad (33)$$

where

$$G_b^{2D}(\mathbf{r}_t, \mathbf{r}_t') = \frac{j}{4} H_0^{(2)}(k_b |\mathbf{r}_t - \mathbf{r}_t'|) \quad (34)$$

is the 2D Green function for background and  $H_0^{(2)}$  is the zero-order and second kind Hankel function [109]. Then, considering that  $\nabla_{\mathbf{r}} \cdot f(\mathbf{r}_t) \hat{\mathbf{z}} = 0$ , (32) reduces to the following Lippmann-Schwinger [110] scalar equation

$$E_{scat}(\mathbf{r}_t) = -k_b^2 \iint_{D_{eq}} c(\mathbf{r}_t') E_{tot}(\mathbf{r}_t') G_b^{2D}(\mathbf{r}_t, \mathbf{r}_t') d\mathbf{r}_t' \quad (35)$$

Analogously to the 3D scenario, the equation (35) can be applied on both  $D_{obs}$  and  $D_{inv}$  to get the data and state equations, respectively, i.e.,

$$\begin{aligned} E_{scat}(\mathbf{r}_t) &= -k_b^2 \iint_{D_{inv}} c(\mathbf{r}_t') E_{tot}(\mathbf{r}_t') G_b^{2D}(\mathbf{r}_t, \mathbf{r}_t') d\mathbf{r}_t', \quad \mathbf{r}_t \in D_{obs} \\ E_{inc}(\mathbf{r}_t) &= E_{tot}(\mathbf{r}_t) + k_b^2 \iint_{D_{inv}} c(\mathbf{r}_t') E_{tot}(\mathbf{r}_t') G_b^{2D}(\mathbf{r}_t, \mathbf{r}_t') d\mathbf{r}_t', \quad \mathbf{r}_t \in D_{inv} \end{aligned} \quad (36)$$

Differently from the full-data situation, here only the incident electric field is assumed to be known in both its amplitude and phase components, whereas only the amplitude of the measured total electric field is available [73], [74], [78]. In particular, the data of the considered phaseless problem is the square modulus of the total electric field. Therefore, (36) is modified accordingly, obtaining

$$P_{tot}(\mathbf{r}_t) = \left| -k_b^2 \iint_{D_{inv}} c(\mathbf{r}_t') E_{tot}(\mathbf{r}_t') G_b^{2D}(\mathbf{r}_t, \mathbf{r}_t') d\mathbf{r}_t' + E_{inc}(\mathbf{r}_t) \right|^2, \quad \mathbf{r}_t \in D_{obs} \quad (37)$$

$$E_{inc}(\mathbf{r}_t) = E_{tot}(\mathbf{r}_t) + k_b^2 \iint_{D_{inv}} c(\mathbf{r}') E_{tot}(\mathbf{r}') G_b^{2D}(\mathbf{r}_t, \mathbf{r}') d\mathbf{r}', \quad \mathbf{r}_t \in D_{inv}$$

## 2.4 Discretization of the 2D Phaseless Scenario

Similarly to the 3D full-vector case, the 2D phaseless problem is discretized by means of a MoM with pulse basis functions and point-matching. A square-based mesh of  $D_{inv}$  given by  $N$  pixels  $\{D_n^{inv}\}_{n=1}^N$  with centers  $\{\mathbf{r}_{t_n}^{inv}\}_{n=1}^N$  is considered. Each pixel has area  $v = \Delta^2$  (being  $\Delta$  the pixel side). Moreover,  $M$  observation points  $\{\mathbf{r}_{t_m}^{obs}\}_{m=1}^M$  belonging to  $D_{obs}$  are selected. A schematic representation of the considered discretized problem is shown in Figure 4.

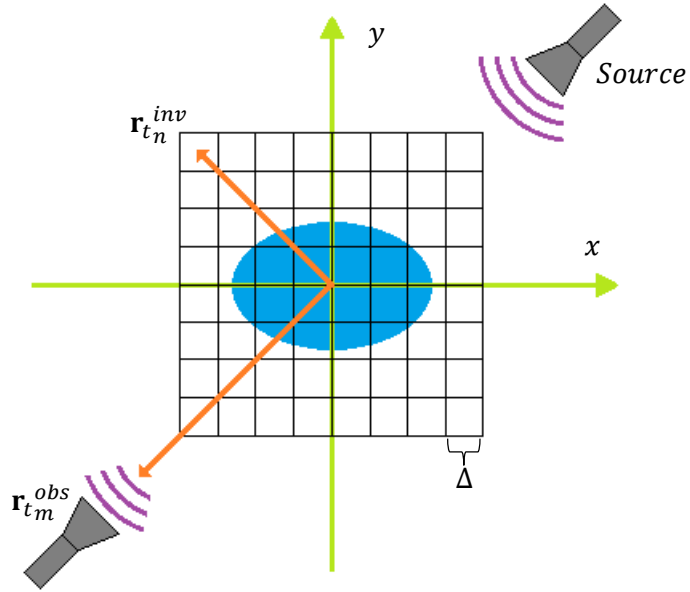


Figure 4. Schematic representation of the considered discretized problem.

The pulse basis functions are defined as

$$b_n(\mathbf{r}_t) = \begin{cases} 1, & \|\mathbf{r}_t - \mathbf{r}_{t_n}^{inv}\|_\infty \leq \frac{\Delta}{2} \\ 0, & \text{otherwise} \end{cases} \quad n = 1, \dots, N \quad (38)$$

Therefore, the quantity  $cE_{tot}$  in  $D_{inv}$  is PWC approximated as

$$c(\mathbf{r}_t)E_{tot}(\mathbf{r}_t) \cong \sum_{l=1}^N c(\mathbf{r}_{t_l}^{inv})E_{tot}(\mathbf{r}_{t_l}^{inv})b_l(\mathbf{r}_t), \quad \mathbf{r}_t \in D_{inv} \quad (39)$$

In accomplishment to the point-matching approach, the following testing operators are defined

$$t_m^{obs}(\cdot)(\mathbf{r}_t) = \iint_{\mathbb{R}^2} (\cdot)(\mathbf{r}_t) \delta(|\mathbf{r}_t - \mathbf{r}_{t_m}^{obs}|) d\mathbf{r}, \quad m = 1, \dots, M \quad (40)$$

$$t_n^{inv}(\cdot)(\mathbf{r}_t) = \iint_{\mathbb{R}^2} (\cdot)(\mathbf{r}_t) \delta(|\mathbf{r}_t - \mathbf{r}_{t_n}^{inv}|) d\mathbf{r}, \quad n = 1, \dots, N \quad (41)$$

The operators in (40), (41) have a meaning equivalent to their 3D counterparts in (20), (21). Introducing (39) in (36) and applying (40) and (41) to the data and state equations, respectively, we have

$$E_{scat}(\mathbf{r}_{t_m}^{obs}) = -k_b^2 \sum_{l=1}^N \iint_{D_l^{inv}} G_b^{2D}(\mathbf{r}_{t_m}^{obs}, \mathbf{r}_t') d\mathbf{r}_t' c(\mathbf{r}_{t_l}^{inv}) E_{tot}(\mathbf{r}_{t_l}^{inv}) \quad (42)$$

$$E_{inc}(\mathbf{r}_{t_n}^{inv}) = E_{tot}(\mathbf{r}_{t_n}^{inv}) + k_b^2 \sum_{l=1}^N \iint_{D_l^{inv}} G_b^{2D}(\mathbf{r}_{t_n}^{inv}, \mathbf{r}_t') d\mathbf{r}_t' c(\mathbf{r}_{t_l}^{inv}) E_{tot}(\mathbf{r}_{t_l}^{inv})$$

To get a compact matrix form, the following quantities are defined [1]

$$\mathbf{e}_{tot}^{ext} = \begin{bmatrix} E_{tot}(\mathbf{r}_{t_1}^{obs}) \\ \vdots \\ E_{tot}(\mathbf{r}_{t_M}^{obs}) \end{bmatrix} \quad \mathbf{e}_{inc}^{ext} = \begin{bmatrix} E_{inc}(\mathbf{r}_{t_1}^{obs}) \\ \vdots \\ E_{inc}(\mathbf{r}_{t_M}^{obs}) \end{bmatrix} \quad \mathbf{e}_{scat}^{ext} = \begin{bmatrix} E_{scat}(\mathbf{r}_{t_1}^{obs}) \\ \vdots \\ E_{scat}(\mathbf{r}_{t_M}^{obs}) \end{bmatrix} \quad (43)$$

$$\mathbf{e}_{tot}^{int} = \begin{bmatrix} E_{tot}(\mathbf{r}_{t_1}^{inv}) \\ \vdots \\ E_{tot}(\mathbf{r}_{t_N}^{inv}) \end{bmatrix} \quad \mathbf{e}_{inc}^{int} = \begin{bmatrix} E_{inc}(\mathbf{r}_{t_1}^{inv}) \\ \vdots \\ E_{inc}(\mathbf{r}_{t_N}^{inv}) \end{bmatrix} \quad \mathbf{c} = \begin{bmatrix} c(\mathbf{r}_{t_1}^{inv}) \\ \vdots \\ c(\mathbf{r}_{t_N}^{inv}) \end{bmatrix}$$



$$\mathbf{H}_b^{ext} = -k_b^2 \begin{bmatrix} \iint_{D_1^{inv}} G_b^{2D}(\mathbf{r}_{t_1}^{obs}, \mathbf{r}'_t) d\mathbf{r}'_t & \cdots & \iint_{D_N^{inv}} G_b^{2D}(\mathbf{r}_{t_1}^{obs}, \mathbf{r}'_t) d\mathbf{r}'_t \\ \vdots & \ddots & \vdots \\ \iint_{D_1^{inv}} G_b^{2D}(\mathbf{r}_{t_M}^{obs}, \mathbf{r}'_t) d\mathbf{r}'_t & \cdots & \iint_{D_N^{inv}} G_b^{2D}(\mathbf{r}_{t_M}^{obs}, \mathbf{r}'_t) d\mathbf{r}'_t \end{bmatrix}$$

$$\mathbf{H}_b^{int} = -k_b^2 \begin{bmatrix} \iint_{D_1^{inv}} G_b^{2D}(\mathbf{r}_{t_1}^{inv}, \mathbf{r}'_t) d\mathbf{r}'_t & \cdots & \iint_{D_N^{inv}} G_b^{2D}(\mathbf{r}_{t_1}^{inv}, \mathbf{r}'_t) d\mathbf{r}'_t \\ \vdots & \ddots & \vdots \\ \iint_{D_1^{inv}} G_b^{2D}(\mathbf{r}_{t_N}^{inv}, \mathbf{r}'_t) d\mathbf{r}'_t & \cdots & \iint_{D_N^{inv}} G_b^{2D}(\mathbf{r}_{t_N}^{inv}, \mathbf{r}'_t) d\mathbf{r}'_t \end{bmatrix}$$

where  $\mathbf{H}_b^{ext}$ ,  $\mathbf{H}_b^{int}$  are the external and internal Green matrices for background in the 2D case, respectively.  $\mathbf{H}_b^{int}$  is symmetric in this situation too. The elements in  $\mathbf{H}_b^{ext}$  are approximated as follows [111]

$$\begin{aligned} -k_b^2 \iint_{D_l^{inv}} G_b^{2D}(\mathbf{r}_{t_m}^{obs}, \mathbf{r}'_t) d\mathbf{r}'_t &\cong -k_b^2 \iint_{C_l^{inv}} G_b^{2D}(\mathbf{r}_{t_m}^{obs}, \mathbf{r}'_t) d\mathbf{r}'_t = \\ &= -\frac{j\pi k_b a}{2} J_1(k_b a) H_0^{(2)}(k_b |\mathbf{r}_{t_m}^{obs} - \mathbf{r}_{t_l}^{inv}|) \end{aligned} \quad (44)$$

where  $C_l^{inv}$  is a circular domain with center  $\mathbf{r}_{t_l}^{inv}$ , area  $v$ , and  $a = \sqrt{v/\pi}$  radius, and  $J_1$  is the first-order and first kind Bessel function [109]. Concerning the elements of  $\mathbf{H}_b^{int}$ , when  $\mathbf{r}_{t_n}^{inv} \notin D_l^{inv}$  equation (44) is used. In the other cases, when the Green function is singular, the elements are approximated as [111]

$$\begin{aligned} -k_b^2 \iint_{D_n^{inv}} G_b^{2D}(k_b |\mathbf{r}_{t_n}^{inv} - \mathbf{r}'_t|) d\mathbf{r}'_t &\cong -k_b^2 \iint_{C_n^{inv}} G_b^{2D}(k_b |\mathbf{r}_{t_n}^{inv} - \mathbf{r}'_t|) d\mathbf{r}'_t = \\ &= -\frac{j}{2} \left[ \pi k_b a H_1^{(2)}(k_b a) - 2j \right] \end{aligned} \quad (45)$$

where  $H_1^{(2)}$  is the Hankel function of first-order and second kind [109]. Finally, the data and state equations in (42) are written in compact matrix form as

$$\mathbf{e}_{scat}^{ext} = \mathbf{H}_b^{ext} \text{diag}(\mathbf{c}) \mathbf{e}_{tot}^{int} \quad (46)$$

$$\mathbf{e}_{inc}^{int} = [\mathbf{I} - \mathbf{H}_b^{int} \text{diag}(\mathbf{c})] \mathbf{e}_{tot}^{int}$$

By combining the previous equations, as in the 3D case, the following relationship between  $\mathbf{c}$  to  $\mathbf{e}_{scat}^{ext}$  is obtained

$$\mathbf{e}_{scat}^{ext} = \mathbf{H}_b^{ext} \text{diag}(\mathbf{c}) [\mathbf{I} - \mathbf{H}_b^{int} \text{diag}(\mathbf{c})]^{-1} \mathbf{e}_{inc}^{int} = \mathbf{F}^{2D}(\mathbf{c}) \quad (47)$$

Because in the phaseless setting only the amplitude of the total external electric field can be measured, the data vector is defined as follows

$$\mathbf{p}_{tot}^{ext} = \begin{bmatrix} P_{tot}(\mathbf{r}_{t_1}^{obs}) \\ \vdots \\ P_{tot}(\mathbf{r}_{t_M}^{obs}) \end{bmatrix} = (\mathbf{e}_{scat}^{ext} + \mathbf{e}_{inc}^{ext})^* \circ (\mathbf{e}_{scat}^{ext} + \mathbf{e}_{inc}^{ext}) \quad (48)$$

where  $\circ$  is the entry-wise product and  $()^*$  denotes the entry-wise complex-conjugate. Consequently, the relationship between  $\mathbf{c}$  and  $\mathbf{p}_{tot}^{ext}$  is

$$\mathbf{p}_{tot}^{ext} = [\mathbf{F}^{2D}(\mathbf{c}) + \mathbf{e}_{inc}^{ext}]^* \circ [\mathbf{F}^{2D}(\mathbf{c}) + \mathbf{e}_{inc}^{ext}] = \mathbf{F}_p^{2D}(\mathbf{c}) \quad (49)$$

It is important to note that the requirements in computational resources grow significantly slower than the 3D full-vector scenario, since now the number of voxels  $N$  grows as  $N_x^2$  for a square investigation domain.

## 2.5 Multi-View Arrangement

As it will be further highlighted in Chapter 3, the equations in (31) and (49) are non-linear and ill-posed with respect to the unknown contrast function. This implies that the inverse problem of interest suffers of false solutions, namely points in the contrast functions space that only locally minimize the residual between the measured and predicted data [112]. This puts a serious threat about the reliability of microwave imaging techniques. However, it has been found in [112] that the occurrence of this stationary points can be mitigated by keeping the ratio between the number of independent data and the number of unknowns  $N$  as high as possible. Regrettably, increasing the number of measurement points is not always a viable option, since the amount of independent collectable data is limited in accordance to the degrees of freedom theory of the scattered electric fields [113]. A feasible way to overcome

this issue consists in the adoption of a multi-view setup [114], namely the target is sequentially illuminated with  $S$  sources and the data for each one (or, as technically said, for each view) are collected. The observation domain may vary for each illumination, i.e.,  $D_{obs}^{(s)}$  with  $s = 1, \dots, S$ . In this setting,  $\mathbf{E}_{tot,(s)}$ ,  $\mathbf{E}_{inc,(s)}$ , and  $\mathbf{E}_{scat,(s)}$  are the total, incident, and scattered electric fields for the  $s$ th view, respectively. Moreover, the related symbols in (25) and (43) are modified as follows

- For the 3D full-vector scenario:  $\mathbf{E}_{tot}^{ext,(s)}$ ,  $\mathbf{E}_{inc}^{ext,(s)}$ ,  $\mathbf{E}_{scat}^{ext,(s)}$ ,  $\mathbf{E}_{inc}^{int,(s)}$ ,  $\mathbf{G}_{b,(s)}^{ext}$
- For the 2D phaseless scenario:  $\mathbf{e}_{tot}^{ext,(s)}$ ,  $\mathbf{e}_{inc}^{ext,(s)}$ ,  $\mathbf{e}_{scat}^{ext,(s)}$ ,  $\mathbf{p}_{tot}^{ext,(s)}$ ,  $\mathbf{e}_{inc}^{int,(s)}$ ,  $\mathbf{H}_{b,(s)}^{ext}$

with  $s = 1, \dots, S$ . Consequently, the single-view scattering equations reported in (31), (47), and (49) are rewritten as

$$\mathbf{E}_{scat}^{ext,(s)} = \mathbf{G}_{b,(s)}^{ext} \text{diag}_3(\mathbf{c}) [\mathbf{I} - \mathbf{G}_b^{int} \text{diag}_3(\mathbf{c})]^{-1} \mathbf{E}_{inc}^{int,(s)} = \mathbf{F}_{(s)}^{3D}(\mathbf{c}) \quad (50)$$

$$\mathbf{e}_{scat}^{ext,(s)} = \mathbf{H}_{b,(s)}^{ext} \text{diag}(\mathbf{c}) [\mathbf{I} - \mathbf{H}_b^{int} \text{diag}(\mathbf{c})]^{-1} \mathbf{e}_{inc}^{int,(s)} = \mathbf{F}_{(s)}^{2D}(\mathbf{c}) \quad (51)$$

$$\mathbf{p}_{tot}^{ext,(s)} = [\mathbf{F}_{(s)}^{2D}(\mathbf{c}) + \mathbf{e}_{inc}^{ext,(s)}]^* \circ [\mathbf{F}_{(s)}^{2D}(\mathbf{c}) + \mathbf{e}_{inc}^{ext,(s)}] = \mathbf{F}_{p,(s)}^{2D}(\mathbf{c}) \quad (52)$$

In order to get two operators able to map the contrast function to the multi-view data for the 3D full-vector and 2D phaseless scenarios, all the views are embedded in the following vectors

$$\hat{\mathbf{E}}_{scat}^{ext} = \begin{bmatrix} \mathbf{E}_{scat}^{ext,(1)} \\ \vdots \\ \mathbf{E}_{scat}^{ext,(S)} \end{bmatrix} \quad \hat{\mathbf{p}}_{tot}^{ext} = \begin{bmatrix} \mathbf{p}_{tot}^{ext,(1)} \\ \vdots \\ \mathbf{p}_{tot}^{ext,(S)} \end{bmatrix} \quad \hat{\mathbf{e}}_{scat}^{ext} = \begin{bmatrix} \mathbf{e}_{scat}^{ext,(1)} \\ \vdots \\ \mathbf{e}_{scat}^{ext,(S)} \end{bmatrix} \quad \hat{\mathbf{e}}_{inc}^{ext} = \begin{bmatrix} \mathbf{e}_{inc}^{ext,(1)} \\ \vdots \\ \mathbf{e}_{inc}^{ext,(S)} \end{bmatrix} \quad (53)$$

Now the multi-view scattering equations and the related scattering operators are obtained as follows

$$\hat{\mathbf{E}}_{scat}^{ext} = \begin{bmatrix} \mathbf{G}_{b,(1)}^{ext} \text{diag}_3(\mathbf{c}) [\mathbf{I} - \mathbf{G}_b^{int} \text{diag}_3(\mathbf{c})]^{-1} \mathbf{E}_{inc}^{int,(1)} \\ \vdots \\ \mathbf{G}_{b,(S)}^{ext} \text{diag}_3(\mathbf{c}) [\mathbf{I} - \mathbf{G}_b^{int} \text{diag}_3(\mathbf{c})]^{-1} \mathbf{E}_{inc}^{int,(S)} \end{bmatrix} = \begin{bmatrix} \mathbf{F}_{(1)}^{3D}(\mathbf{c}) \\ \vdots \\ \mathbf{F}_{(S)}^{3D}(\mathbf{c}) \end{bmatrix} = \hat{\mathbf{F}}^{3D}(\mathbf{c}) \quad (54)$$

$$\hat{\mathbf{e}}_{scat}^{ext} = \begin{bmatrix} \mathbf{H}_{b,(1)}^{ext} \text{diag}(\mathbf{c}) [\mathbf{I} - \mathbf{H}_b^{int} \text{diag}(\mathbf{c})]^{-1} \mathbf{e}_{inc}^{int,(1)} \\ \vdots \\ \mathbf{H}_{b,(S)}^{ext} \text{diag}(\mathbf{c}) [\mathbf{I} - \mathbf{H}_b^{int} \text{diag}(\mathbf{c})]^{-1} \mathbf{e}_{inc}^{int,(S)} \end{bmatrix} = \begin{bmatrix} \mathbf{F}_{(1)}^{2D}(\mathbf{c}) \\ \vdots \\ \mathbf{F}_{(S)}^{2D}(\mathbf{c}) \end{bmatrix} = \hat{\mathbf{F}}^{2D}(\mathbf{c}) \quad (55)$$

$$\hat{\mathbf{p}}_{tot}^{ext} = [\hat{\mathbf{F}}^{2D}(\mathbf{c}) + \hat{\mathbf{e}}_{inc}^{ext}]^* \circ [\hat{\mathbf{F}}^{2D}(\mathbf{c}) + \hat{\mathbf{e}}_{inc}^{ext}] = \begin{bmatrix} \mathbf{F}_{P,(1)}^{2D}(\mathbf{c}) \\ \vdots \\ \mathbf{F}_{P,(S)}^{2D}(\mathbf{c}) \end{bmatrix} = \hat{\mathbf{F}}_P^{2D}(\mathbf{c}) \quad (56)$$

## Chapter 3 Inversion Procedure

The imaging problems of interest consist in retrieving the unknown contrast functions starting from the available field measurements collected in the observation domain. In other words, (54) and (56) need to be solved with respect to the unknown  $\mathbf{c}$ . This implies the solution of an electromagnetic scattering inverse problem [1]–[3], [85], [86]. In both 3D full-vector and 2D phaseless scenarios, the data equation is a first-kind Fredholm equation, while the state one is a second-kind Fredholm equation. The last one is well-posed in the Hadamard sense, whereas the first one turns out to be ill-posed, since in our setting it is usually solvable but generally its solutions are not unique and do not depend continuously on the data [85], [86]. These awful properties found explanation in the analysis of the integral equation's kernel and in a Riemann lemma application [115]. Moreover, when the first-kind Fredholm equation of interest is turned in a numerical problem by means of a discretization process, it usually gives rise to an ill-conditioned problem [116]. Finally, from the structure of (54) and (56), we see that the relationship between the data and the unknown contrast function is non-linear. Therefore, in order to solve the involved inverse problem, a proper regularization approach able to cope with non-linearities is required. In the present Thesis, an inexact-Newton scheme [88]–[90] performing a regularization in the framework of the  $l^p$  Banach spaces [91]–[95] has been developed. It is composed by two nested loops: the outer one iteratively linearizes the scattering operators in (54) and (56), whereas, in the inner one, the obtained linear system is solved by a regularizing approach in  $l^p$  Banach spaces. Figure 5 provides the workflow of the considered inversion algorithm through a block diagram. In the following Section, a high-level description of the general inexact-Newton scheme is presented. Thereafter, an intuitive explanation of the  $l^p$  framework's benefits is presented and two inner linear solvers are introduced, namely the truncated Landweber method [91]–[93] and the conjugate gradient one [94], [95]. Finally, special insights in the computations of the needed Fréchet derivatives are furnished.

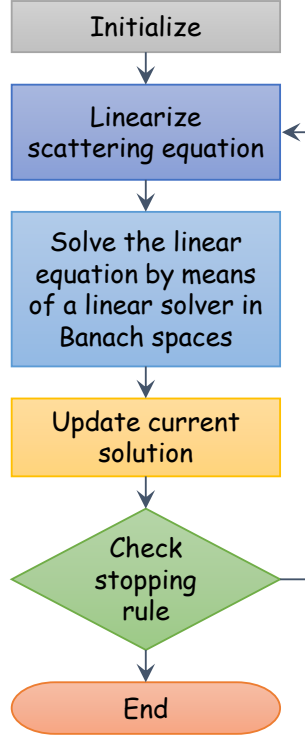


Figure 5. Block diagram representing the workflow of the proposed inexact-Newton inversion scheme.

### 3.1 Inexact-Newton

Generally, the equations in (54) and (56) can be written in compact form as

$$\mathbf{F}(\mathbf{c}) = \mathbf{d} \quad (57)$$

The unknown  $\mathbf{c}$  belongs to the linear space  $\mathcal{C}$ , which is the  $\mathbb{C}^N$  space endowed with the norm of  $l^p$ . The data  $\mathbf{d}$  belongs to the linear space  $\mathcal{D}$ : for the 2D phaseless scenario,  $\mathcal{D}$  is the  $\mathbb{R}^{SM}$  space endowed with the norm of  $l^p$ , whereas for the 3D full-vector case  $\mathcal{D}$  is the  $\mathbb{C}^{3SM}$  space endowed with the same kind of norm.  $\mathbf{F}$  is a non-linear operator so that  $\mathbf{F}: \mathcal{C} \rightarrow \mathcal{D}$ . The inexact-Newton algorithm [88], [89] inverts (57) by means of the following iterations

1. Set the initial guess  $\mathbf{c}_0$ . If no a-priori information is available,  $\mathbf{c}_0 = \mathbf{0}$  is used.
2. Compute a first-order Taylor expansion of (57) around the current solution  $\mathbf{c}_i$ . The following linear system is obtained [48]

$$\mathbf{F}'_{\mathbf{c}_i} \mathbf{h} = \mathbf{d} - \mathbf{F}(\mathbf{c}_i) = \mathbf{b}_i \quad (58)$$

where  $\mathbf{F}'_{\mathbf{c}_i}$  is the Fréchet derivative (or, more specifically, the Jacobian matrix) of  $\mathbf{F}$  in  $\mathbf{c}_i$ , and  $\mathbf{b}_i$  is the residual vector at the  $i$ th outer iteration.

3. Find a regularized solution  $\mathbf{h}$  of (58) by a regularizing linear solver defined in  $l^p$  Banach spaces.
4. Update the estimate

$$\mathbf{c}_{i+1} = \mathbf{c}_i + \mathbf{h} \quad (59)$$

2. Terminate when a given stopping rule is satisfied, otherwise repeat from step 2.

As previously mentioned, this algorithm belongs to the class of deterministic local methods, which can be trapped in local minima corresponding to false solutions of the inverse scattering problem [112]. To partially mitigate these drawback, beyond the multi-view setup introduced in Section 2.5, the eventually available a-priori information should be used to make the starting guess  $\mathbf{c}_0$  as close as possible to the actual solution [20], [112].

### 3.2 Discussion on the Regularization in Banach Spaces

The classic implementations of the inexact-Newton scheme use inner linear solvers that are defined in the framework of the  $l^2$  Hilbert spaces (the contrast functions space  $\mathcal{C}$  and the data one  $\mathcal{D}$  are both endowed with the  $l^2$  norm, and therefore both are Euclidean spaces). In this setting, the mathematical tools available in this kind of spaces allow a deep understanding of the regularization and convergence properties of the adopted linear solver [1], [85], [86], [117]. However, the imaging algorithms based on this framework are often characterized by problems of over-smoothness and ringing in the retrieved solutions, making difficult to recognize small dielectric discontinuities [96], [118], [119]. Such drawbacks of the classic approaches have lead the scientific community to consider new ways. Among these, one of the most interesting and promising is the generalization of the regularization framework in the  $l^p$  Banach spaces, with  $p > 1$  [91]. Their special feature is the new free parameter  $p$ , which characterizes the norm endowing the Banach space (and so its geometrical properties), and that can be tuned in order to mitigate the over-smoothness and ringing effects. Both the linear solvers that will be introduced in the following descend from classic iterative methods developed and studied in Hilbert spaces, and only recently revisited

and generalized in Banach spaces. In this framework, the lack of a dot product inducing a complete space for  $p \neq 2$  (as consequence of the Jordan-Von Neumann theorem [120]) denies the possibility to define a singular value decomposition of the linear operators, and so much more involving mathematical tools from complex convex analysis are needed. However, the key point at the base of the performance of linear solvers in  $l^p$  resides in the duality maps [91], [92]. These are nonlinear functions that associate an element of a generic Banach space  $\mathcal{B}$  to an element of its dual space  $\mathcal{B}^*$ , namely the space of the continuous linear functionals  $F: \mathcal{B} \rightarrow \mathbb{F}$ , where  $\mathbb{F}$  is the field on which  $\mathcal{B}$  is defined [121]. Beyond the tricky mathematical definition of the duality maps, a useful heuristic explanation of the duality maps role in the linear solvers presented in Sections 3.3 and 3.4 starts with the following theorem

*Asplund Theorem* [91], [92]. *Given a generic Banach space  $\mathcal{B}$  with norm  $\|\cdot\|_{\mathcal{B}}$ , its duality map  $J_{\mathcal{B}}$  is the subdifferential of the convex functional  $\frac{1}{r}\|\cdot\|_{\mathcal{B}}^r$  with  $r > 1$ , that is  $J_{\mathcal{B}} = \partial \left( \frac{1}{r} \|\cdot\|_{\mathcal{B}}^r \right)$ .*

In our problem of interest, the linear system in (58) is solved by finding a regularized solution that minimizes the following residual functional

$$\frac{1}{2} \|\mathbf{F}'_{\mathbf{c}_i} \mathbf{h} - \mathbf{b}_i\|_{\mathcal{D}}^2 \quad (60)$$

Applying the chain rule for subdifferentiation of composite functions and the Asplund theorem, it results that

$$\partial \left( \frac{1}{2} \|\mathbf{F}'_{\mathbf{c}_i} \mathbf{h} - \mathbf{b}_i\|_{\mathcal{D}}^2 \right) = \mathbf{F}'_{\mathbf{c}_i}{}^H \mathbf{J}_p^{\mathcal{D}} (\mathbf{F}'_{\mathbf{c}_i} \mathbf{h} - \mathbf{b}_i) \quad (61)$$

where  $\mathbf{F}'_{\mathbf{c}_i}{}^H$  is the adjoint operator of  $\mathbf{F}'_{\mathbf{c}_i}$ , and  $\mathbf{J}_p^{\mathcal{D}}: \mathcal{D} \rightarrow \mathcal{D}^*$ , with  $\mathcal{D}^*$  dual space of  $\mathcal{D}$ , is the duality map defined as [91], [92]

$$\mathbf{J}_p^{\mathcal{D}}(\mathbf{g}) = \|\mathbf{g}\|_{\mathcal{D}}^{2-p} \begin{bmatrix} |g_1|^{p-1} \text{sign}(g_1) \\ \vdots \\ |g_G|^{p-1} \text{sign}(g_G) \end{bmatrix} \quad (62)$$



where  $\mathbf{g} = [g_1 \ \cdots \ g_G]^T \in \mathcal{D}$  with  $G = 3SM$  in the 3D full-vector scenario and  $G = SM$  in the 2D phaseless one. As it will be seen in the following, the terms that the linear solvers in Sections 3.3 and 3.4 compute to iteratively update the estimated solution are based on the quantity at the right member of (61). In particular, we have that  $\mathbf{F}'_{\mathbf{c}_i^H}: \mathcal{D}^* \rightarrow \mathcal{C}^*$ , where  $\mathcal{C}^*$  is the dual space of  $\mathcal{C}$ , thus the update step is not executed in the contrast functions space  $\mathcal{C}$  but in its dual one. Once the new estimated solution is obtained in  $\mathcal{C}^*$ , the related approximated element of  $\mathcal{C}$  is obtained by applying the duality map  $\mathbf{J}_q^{\mathcal{C}^*}: \mathcal{C}^* \rightarrow (\mathcal{C}^*)^* \equiv \mathcal{C}$  (this last statement is due to the reflexivity of the considered spaces) defined as [91], [92]

$$\mathbf{J}_q^{\mathcal{C}^*}(\mathbf{f}) = \|\mathbf{f}\|_{\mathcal{C}^*}^{2-q} \begin{bmatrix} |f_1|^{q-1} \text{sign}(f_1) \\ \vdots \\ |f_N|^{q-1} \text{sign}(f_N) \end{bmatrix} \quad (63)$$

where  $q = p/(p-1)$  is the Hölder conjugate of  $p$  and  $\mathbf{f} = [f_1 \ \cdots \ f_N]^T \in \mathcal{C}^*$ . This highlights that the performed minimization is different from the conventional (i.e., Euclidean) one of the residual functional in (60). In fact, the classic Landweber and conjugate gradient methods iteratively update the estimated solution directly in  $\mathcal{C}$ . Therefore, the directions of minimization adopted by the linear solvers in Sections 3.3 and 3.4 are not the steepest descent ones of the Euclidean geometry, but non-standard ones conceived in the framework of the convex analysis in Banach spaces. The two frameworks are equal only when  $p = 2$ , namely when the data and unknowns spaces are endowed with the structure of the  $l^2$  Hilbert space; in fact, the duality maps in (62) and (63) reduce to identity ones when  $p = 2$ . Once this distinction has been understood, it is important to highlight how the new methods can overcome the limitations of the classic ones when  $1 < p < 2$ . To understand this fact from a heuristic point of view, we can notice that the duality map  $\mathbf{J}_p^{\mathcal{D}}$  emphasizes the smallest components of the residual vector and reduces the largest ones, since  $|u|^{p-1} > |u|$  for  $|u| < 1$ , and  $|u|^{p-1} < |u|$  for  $|u| > 1$ , because of  $0 < p-1 < 1$ . Therefore, the weak information in the residual vector (usually associated to high frequencies in the Fourier analysis) have now a stronger role in the reconstruction procedure, allowing for a better restoration of jump discontinuities. This can be interpreted as a lower filtering effect, and so a lower regularization, with respect to the Hilbert case. When the duality map  $\mathbf{J}_q^{\mathcal{C}^*}$  is applied to the updated estimated solution in  $\mathcal{C}^*$  to get the related approximated solution in  $\mathcal{C}$ , we see that it tends to make smaller the weak components of the element gained in  $\mathcal{C}^*$ , since

$|u|^{q-1} < |u|$  for  $|u| < 1$ , and  $|u|^{q-1} > |u|$  for  $|u| > 1$ , because of  $q - 1 > 1$ . This has the resulting effect of attenuating the ringing effects on the background and of reducing noise propagation.

### 3.3 Truncated Landweber Method in Banach Spaces

The algorithm considered in this Section is an iterative gradient method where the number of executed iterations plays the role of regularization parameter. In the particular case of the Hilbert spaces  $l^2$ , where the singular value decomposition can be defined, the algorithm is shown to perform a low-pass filtering of the spectral content of  $\mathbf{F}'_{\mathbf{c}_i}$  and the cut-off frequency is a non-decreasing function of the iteration number [1], [85], [86]. This behavior allows to filter out the high frequency components of  $\mathbf{F}'_{\mathbf{c}_i}$  responsible for the ill-conditioning of (58), given that a proper selection of the iteration number (i.e., the cut-off frequency) is performed. Recently, the method has been generalized to the  $l^p$  Banach spaces with  $p > 1$  and, in spite of the lack of the spectral theory when  $p \neq 2$  (see Section 3.2), the regularization capabilities associated to the iteration number can be still proved by arguments related to the continuity of the duality maps, as theoretically found in [92]. Its capability in mitigating the over-smoothness and ringing effects that often affect the solutions retrieved in the Hilbert spaces  $l^2$  has been shown in the context of 2D full-data microwave imaging in [96] for the first time. The algorithm is given by the following steps

1. Initialize  $\mathbf{h}_0 = \mathbf{0} \in \mathcal{C}$  and  $\hat{\mathbf{h}}_0 = \mathbf{0} \in \mathcal{C}^*$ .
2. Update the solution in  $\mathcal{C}^*$  by the following iterative rule

$$\hat{\mathbf{h}}_{k+1} = \hat{\mathbf{h}}_k - \beta \mathbf{F}'_{\mathbf{c}_i}{}^H \mathbf{J}_p^{\mathcal{D}}(\mathbf{F}'_{\mathbf{c}_i} \mathbf{h}_k - \mathbf{b}_i) \quad (64)$$

where  $\beta$  is the relaxation coefficient. In Hilbert space, it can be proven that the relaxation coefficient must be in the interval  $(0, 2\|\mathbf{F}'_{\mathbf{c}_i}\|_2^{-2})$  to guarantee the convergence of the method. By choosing  $\beta = \|\mathbf{F}'_{\mathbf{c}_i}\|_2^{-2}$ , namely the value in the middle of the admissible range, the convergence still holds in a neighbor of  $p = 2$  (this property can be proved by means of continuity arguments [92]).

3. Get the current approximated solution in  $\mathcal{C}$  with

$$\mathbf{h}_{k+1} = \mathbf{J}_q^{\mathcal{C}^*}(\hat{\mathbf{h}}_{k+1}) \quad (65)$$

4. Terminate when a given stopping rule is satisfied, otherwise repeat from step 2.

### 3.4 Conjugate Gradient Method in Banach Spaces

The classic conjugate gradient method is a minimization method based on the Krylov subspaces [117] that has been found to provide better performance than the steepest descent algorithm. As for the truncated Landweber method in  $l^2$ , the classic conjugate gradient can be shown to have regularizing properties, since it behaves as a spectral filter; however, as opposed to the Landweber approach, it is a non-linear method because its spectral input-output relation depends on the data [86]. The conjugate gradient has been generalized to the setting of the  $l^p$  Banach spaces (with  $p > 1$ ) too [94], [95], showing advantages on the retrieved solutions that are similar to the Landweber ones. Its superior performance with respect to the classic version of the algorithm has been shown in the context of 2D full-data microwave imaging in [16] for the first time. The method is composed by the following steps

1. Initialize  $\mathbf{h}_0 = \mathbf{0} \in \mathcal{C}$ ,  $\hat{\mathbf{h}}_0 = \mathbf{0} \in \mathcal{C}^*$  and  $\mathbf{p}_0 = \mathbf{F}'_{\mathbf{c}_i}{}^H \mathbf{J}_p^{\mathcal{D}}(\mathbf{b}_i) \in \mathcal{C}^*$ .
2. Solve the following single-variable minimization problem

$$\alpha_k = \arg \min_{\alpha > 0} \|\mathbf{F}'_{\mathbf{c}_i} \mathbf{J}_q^{\mathcal{C}^*}(\hat{\mathbf{h}}_k + \alpha \hat{\mathbf{p}}_k) - \mathbf{b}_i\|_p^2 \quad (66)$$

This can be solved by a simple one-dimensional optimizer (e.g., the secant method [122]).

3. Compute the following displacement in  $\mathcal{C}^*$

$$\begin{aligned} \hat{\mathbf{p}}_k &= -\mathbf{F}'_{\mathbf{c}_i}{}^H \mathbf{J}_p^{\mathcal{D}}(\mathbf{F}'_{\mathbf{c}_i} \mathbf{h}_k - \mathbf{b}_i) + \beta_k \hat{\mathbf{p}}_{k-1} \\ \beta_k &= \frac{\|\mathbf{F}'_{\mathbf{c}_i}{}^H \mathbf{J}_p^{\mathcal{D}}(\mathbf{F}'_{\mathbf{c}_i} \mathbf{h}_k - \mathbf{b}_i)\|_2^2}{\|\mathbf{F}'_{\mathbf{c}_i}{}^H \mathbf{J}_p^{\mathcal{D}}(\mathbf{F}'_{\mathbf{c}_i} \mathbf{h}_{k-1} - \mathbf{b}_i)\|_2^2} \end{aligned} \quad (67)$$

4. Update  $\hat{\mathbf{h}}$  with

$$\hat{\mathbf{h}}_{k+1} = \hat{\mathbf{h}}_k + \alpha_k \hat{\mathbf{p}}_k \quad (68)$$

where  $\alpha_k$  is obtained by solving (66).

5. Get the new current solution in  $\mathcal{C}$  by

$$\mathbf{h}_{k+1} = \mathbf{J}_q^{\mathcal{C}*}(\hat{\mathbf{h}}_{k+1}) \quad (69)$$

6. Terminate when a given stopping rule is satisfied, otherwise repeat from step 2.

### 3.5 3D Full-Vector Scenario: Fréchet Derivative Computation

The proposed non-linear solving scheme requires the determination of the Fréchet derivative, which reduces to the Jacobian matrix in our discrete setting. First, the Fréchet derivative for the single-view case is computed by introducing the following first-order Taylor expansion

$$(\mathbf{Y} - \mathbf{Z}\mathbf{X})^{-1} = \mathbf{Y}^{-1} + \mathbf{Y}^{-1}\mathbf{Z}\mathbf{X}\mathbf{Y}^{-1} + O(\mathbf{X}^2) \quad (70)$$

where  $\mathbf{X}, \mathbf{Y}, \mathbf{Z}$  are square matrices (with invertible  $\mathbf{Y}$  and  $\mathbf{Y} - \mathbf{Z}\mathbf{X}$ ). Moreover, the following identity holds

$$[\mathbf{I} - \text{diag}_3(\mathbf{c})\mathbf{G}_b^{\text{int}}]^{-1} = \mathbf{I} + \text{diag}_3(\mathbf{c})[\mathbf{I} - \mathbf{G}_b^{\text{int}}\text{diag}_3(\mathbf{c})]^{-1}\mathbf{G}_b^{\text{int}} \quad (71)$$

Using (70) and (71), now a Taylor expansion of  $\mathbf{F}^{3D}$  can be performed in a generic neighborhood of  $\tilde{\mathbf{c}}$  as [97]

$$\begin{aligned} \mathbf{F}^{3D}(\tilde{\mathbf{c}} + d\mathbf{c}) &= \mathbf{G}_b^{\text{ext}}\text{diag}_3(\tilde{\mathbf{c}} + d\mathbf{c})[\mathbf{I} - \mathbf{G}_b^{\text{int}}\text{diag}_3(\tilde{\mathbf{c}} + d\mathbf{c})]^{-1}\mathbf{E}_{\text{inc}}^{\text{int}} = \\ &= \mathbf{G}_b^{\text{ext}}\text{diag}_3(\tilde{\mathbf{c}})[\mathbf{I} - \mathbf{G}_b^{\text{int}}\text{diag}_3(\tilde{\mathbf{c}})]^{-1}\mathbf{E}_{\text{inc}}^{\text{int}} \\ &\quad + \mathbf{G}_b^{\text{ext}}[\mathbf{I} - \text{diag}_3(\tilde{\mathbf{c}})\mathbf{G}_b^{\text{int}}]^{-1}\text{diag}_3(d\mathbf{c})[\mathbf{I} - \mathbf{G}_b^{\text{int}}\text{diag}_3(\tilde{\mathbf{c}})]^{-1}\mathbf{E}_{\text{inc}}^{\text{int}} \\ &\quad + O[\text{diag}_3(d\mathbf{c})^2\mathbf{E}_{\text{inc}}^{\text{int}}] \end{aligned} \quad (72)$$

The linear term in  $\text{diag}_3(d\mathbf{c})$  is of our interest and, because of the state equation in (29), it can be rewritten as follows

$$\begin{aligned} \mathbf{G}_b^{ext} [\mathbf{I} - \text{diag}_3(\tilde{\mathbf{c}}) \mathbf{G}_b^{int}]^{-1} \text{diag}_3(d\mathbf{c}) [\mathbf{I} - \mathbf{G}_b^{int} \text{diag}_3(\tilde{\mathbf{c}})]^{-1} \mathbf{E}_{inc}^{int} = \\ = \mathbf{G}_b^{ext} [\mathbf{I} - \text{diag}_3(\tilde{\mathbf{c}}) \mathbf{G}_b^{int}]^{-1} \text{diag}(\mathbf{E}_{tot\tilde{\mathbf{c}}}^{int}) d\mathbf{c} \end{aligned} \quad (73)$$

where  $\mathbf{E}_{tot\tilde{\mathbf{c}}}^{int}$  is the total internal electric field in presence of the dielectric configuration  $\tilde{\mathbf{c}}$ . Therefore, the following desired Fréchet derivative is obtained

$$\mathbf{F}_{\tilde{\mathbf{c}}}^{3D'} = \mathbf{G}_b^{ext} [\mathbf{I} - \text{diag}_3(\tilde{\mathbf{c}}) \mathbf{G}_b^{int}]^{-1} \text{diag}(\mathbf{E}_{tot\tilde{\mathbf{c}}}^{int}) \quad (74)$$

Finally, the Fréchet derivative for the multi-view case is made by simply stacking the operator in (74) for each view as follows

$$\hat{\mathbf{F}}_{\tilde{\mathbf{c}}}^{3D'} = \begin{bmatrix} \mathbf{F}_{\tilde{\mathbf{c}},(1)}^{3D'} \\ \vdots \\ \mathbf{F}_{\tilde{\mathbf{c}},(S)}^{3D'} \end{bmatrix} = \begin{bmatrix} \mathbf{G}_{b,(1)}^{ext} [\mathbf{I} - \text{diag}_3(\tilde{\mathbf{c}}) \mathbf{G}_b^{int}]^{-1} \text{diag}(\mathbf{E}_{tot\tilde{\mathbf{c}},(1)}^{int}) \\ \vdots \\ \mathbf{G}_{b,(S)}^{ext} [\mathbf{I} - \text{diag}_3(\tilde{\mathbf{c}}) \mathbf{G}_b^{int}]^{-1} \text{diag}(\mathbf{E}_{tot\tilde{\mathbf{c}},(S)}^{int}) \end{bmatrix} \quad (75)$$

About our implementation,  $\mathbf{E}_{tot\tilde{\mathbf{c}},(s)}^{int}$  is efficiently computed by using the BiCGSTAB-FFT method [123], which has an asymptotical computational complexity  $O(I_E N \log N)$ , where  $I_E$  is the number of iterations in which the solution  $\mathbf{E}_{tot\tilde{\mathbf{c}},(s)}^{int}$  is reached. Moreover, the matrix inversion in (74) is not computed explicitly, since this task has a totally unfeasible computational workload. On the contrary, the matrix  $\mathbf{G}_{\tilde{\mathbf{c}},(s)}^{inh} = \mathbf{G}_{b,(s)}^{ext} [\mathbf{I} - \text{diag}_3(\tilde{\mathbf{c}}) \mathbf{G}_b^{int}]^{-1}$  is considered, which is known as inhomogeneous Green matrix for  $\tilde{\mathbf{c}}$  and sth view [18]. From  $\mathbf{G}_b^{int}$  symmetry and (29), the transpose  $\mathbf{G}_{\tilde{\mathbf{c}},(s)}^{inh T} = [\mathbf{I} - \mathbf{G}_b^{int} \text{diag}_3(\tilde{\mathbf{c}})]^{-1} \mathbf{G}_{b,(s)}^{ext T}$  results to have each column corresponding to the total internal electric field that would be generated when the incident internal electric field is given by the related row of  $\mathbf{G}_{b,(s)}^{ext}$  and in presence of  $\tilde{\mathbf{c}}$ . Therefore, the rows of  $\mathbf{G}_{\tilde{\mathbf{c}},(s)}^{inh}$  can be efficiently computed by using the BiCGSTAB-FFT method. The computation of  $\hat{\mathbf{F}}_{\tilde{\mathbf{c}}}^{3D'}$  can be a serious bottleneck for the imaging technique. In fact, it needs that the BiCGSTAB-FFT method is run  $3SM + S$  times (computations of the inhomogeneous Green matrices and total internal electric fields for each view) in each outer iteration, which usually represents a significant workload. However,  $\mathbf{E}_{tot\tilde{\mathbf{c}},(s)}^{int}$  and  $\mathbf{G}_{\tilde{\mathbf{c}},(s)}^{inh}$  for  $s = 1, \dots, S$  can be computed in parallel. In our implementation, this has been accomplished by taking advantage of multi-core architectures and the OpenMP library [124].

### 3.6 2D Phaseless Scenario: Fréchet Derivative Computation

First of all, since in the phaseless case the data vector has real components only, it is useful to perform the following change of variable in order to work with real unknowns too [98]

$$\mathbf{c} = \mathbf{T}\mathbf{x} \quad (76)$$

where

$$\mathbf{T} = [\mathbf{I}_{N \times N} \quad j\mathbf{I}_{N \times N}] \quad \mathbf{x} = \begin{bmatrix} \text{Re}(\mathbf{c}) \\ \text{Im}(\mathbf{c}) \end{bmatrix} \quad (77)$$

where  $\mathbf{I}_{N \times N}$  is the identity matrix of dimensions  $N \times N$ . In order to get the Fréchet derivative for the 2D phaseless single-view scattering operator, the starting point is

$$\mathbf{F}_P^{2D}(\tilde{\mathbf{x}} + d\mathbf{x}) = [\mathbf{F}^{2D}(\tilde{\mathbf{x}} + d\mathbf{x}) + \mathbf{e}_{inc}^{ext}] \circ [\mathbf{F}^{2D}(\tilde{\mathbf{x}} + d\mathbf{x}) + \mathbf{e}_{inc}^{ext}]^* \quad (78)$$

where  $\tilde{\mathbf{x}}$  is a generic point of the unknowns space in which the Taylor expansion is performed. Analogously to the 3D case, the 2D full-data scattering operator admits the following Taylor expansion

$$\mathbf{F}^{2D}(\tilde{\mathbf{x}} + d\mathbf{x}) = \mathbf{F}^{2D}(\tilde{\mathbf{x}}) + \mathbf{F}_{\tilde{\mathbf{x}}}^{2D'} d\mathbf{x} + O[\text{diag}(\mathbf{T}d\mathbf{x})^2 \mathbf{e}_{inc}^{int}] \quad (79)$$

where

$$\mathbf{F}_{\tilde{\mathbf{x}}}^{2D'} = \mathbf{H}_b^{ext} [\mathbf{I} - \text{diag}(\mathbf{T}\tilde{\mathbf{x}}) \mathbf{H}_b^{int}]^{-1} \text{diag}(\mathbf{e}_{tot\tilde{\mathbf{x}}}^{int}) \mathbf{T} \quad (80)$$

where  $\mathbf{e}_{tot\tilde{\mathbf{x}}}^{int}$  is the total internal electric field in presence of the dielectric configuration indicated by  $\tilde{\mathbf{x}}$ . By inserting (79) in (78), the linear terms in  $d\mathbf{x}$  reduces to

$$2\text{Re}\{[\mathbf{F}^{2D}(\tilde{\mathbf{x}}) + \mathbf{e}_{inc}^{ext}]^* \circ \mathbf{F}_{\tilde{\mathbf{x}}}^{2D'} d\mathbf{x}\} \quad (81)$$

Therefore, the Fréchet derivative of the 2D phaseless single-view scattering operator is

$$\mathbf{F}_{P,\tilde{\mathbf{x}}}^{2D'} = 2\text{Re}\{\text{diag}[\mathbf{F}^{2D}(\tilde{\mathbf{x}}) + \mathbf{e}_{inc}^{ext}]^* \mathbf{F}_{\tilde{\mathbf{x}}}^{2D'}\} \quad (82)$$

The Fréchet derivative for the multi-view case is again obtained by stacking the terms corresponding to each view, i.e.,

$$\hat{\mathbf{F}}_{P,\tilde{\mathbf{x}}}^{2D'} = \begin{bmatrix} \mathbf{F}_{P,\tilde{\mathbf{x}},(1)}^{2D} \\ \vdots \\ \mathbf{F}_{P,\tilde{\mathbf{x}},(S)}^{2D} \end{bmatrix}' = \begin{bmatrix} 2\text{Re} \left\{ \text{diag} \left[ \mathbf{F}_{(1)}^{2D}(\tilde{\mathbf{x}}) + \mathbf{e}_{inc}^{ext,(1)} \right]^* \mathbf{F}_{\tilde{\mathbf{x}},(1)}^{2D} \right\} \\ \vdots \\ 2\text{Re} \left\{ \text{diag} \left[ \mathbf{F}_{(S)}^{2D}(\tilde{\mathbf{x}}) + \mathbf{e}_{inc}^{ext,(S)} \right]^* \mathbf{F}_{\tilde{\mathbf{x}},(S)}^{2D} \right\} \end{bmatrix} \quad (83)$$

Although the computational complexity of the 2D case is significantly lower than the 3D one, the BiCGSTAB-FFT method is exploited for the determination of the required inhomogeneous Green matrices and total internal electric fields in this case, too.

### 3.7 Frequency Hopping

In case measurements performed at  $F$  different working frequencies were available, it is possible to exploit these information in order to improve the quality of the inversion at single-frequency thanks to the frequency hopping technique [52], [125]. The following steps constitute the method (the angular frequencies are supposed to be sorted in ascending order, i.e.,  $\omega_1 < \omega_2 < \dots < \omega_F$ )

1. *Initialization.* Run the inversion algorithm on the data gathered at the lowest working angular frequency  $\omega_1$ . The resulting reconstructed dielectric image is indicated with  $\tilde{\mathbf{c}}_{\omega_1}$ . Transform this vector in the following starting guess

$$\tilde{\mathbf{c}}_{0,\omega_2} = \text{Re}(\tilde{\mathbf{c}}_{\omega_1}) + j \frac{\omega_1}{\omega_2} \text{Im}(\tilde{\mathbf{c}}_{\omega_1}) \quad (84)$$

2. *Loop.* For  $w = 2, \dots, F - 1$ , run the inversion algorithm on the data gathered at the working angular frequency  $\omega_w$  starting with the initial guess  $\tilde{\mathbf{c}}_{0,\omega_w}$ , obtaining the reconstructed dielectric image  $\tilde{\mathbf{c}}_{\omega_w}$ . Transform this solution in the starting guess

$$\tilde{\mathbf{c}}_{0,\omega_{w+1}} = \text{Re}(\tilde{\mathbf{c}}_{\omega_w}) + j \frac{\omega_w}{\omega_{w+1}} \text{Im}(\tilde{\mathbf{c}}_{\omega_w}) \quad (85)$$

3. *Output.* Run the inversion algorithm on the data gathered at the highest working angular frequency  $\omega_F$  with the starting guess  $\tilde{\mathbf{c}}_{0,\omega_F}$ . The reconstructed dielectric image is the final one  $\tilde{\mathbf{c}}$ .

## Chapter 4 Numerical and Experimental Validation: 3D Full-Vector Scenario

In this Chapter, the results concerning the 3D full-vector inversion schemes are reported. Both the truncated Landweber and the conjugate gradient methods have been considered [118], [119], [126]. In order to evaluate the performance of the algorithms, the following error metrics are used [118]

$$\begin{aligned}
 e_{inv} &= \frac{\|\tilde{\mathbf{c}} - \mathbf{c}\|_2}{\|\mathbf{c}\|_2} \\
 e_{obj} &= \frac{1}{N_{obj}} \sum_{\mathbf{r}_{obj}} \left| \frac{\tilde{c}(\mathbf{r}_{obj}) - c(\mathbf{r}_{obj})}{c(\mathbf{r}_{obj}) + 1} \right| \\
 e_b &= \frac{1}{N_b} \sum_{\mathbf{r}_b} \left| \frac{\tilde{c}(\mathbf{r}_b) - c(\mathbf{r}_b)}{c(\mathbf{r}_b) + 1} \right|
 \end{aligned} \tag{86}$$

where  $c$  and  $\tilde{c}$  are the actual and reconstructed contrast functions, respectively,  $\mathbf{r}_{obj}$  are the centers of the  $N_{obj}$  subdomains occupied by the target, and  $\mathbf{r}_b$  are the centers of the  $N_b$  subdomains occupied by the background medium only. In particular, the first metric in (86) is a normalized mean square error (NMSE) computed on the whole investigation domain, the second one is a relative mean error on the reconstruction of the target only, and the last one is a relative mean error on the reconstruction of the background only. In order to evaluate the performance versus the norm parameter  $p$ , this has been varied from 1.1 to 3 with a step of 0.1 for each test case. Finally, it is useful to define the following metrics for the outer and inner residuals vectors

$$r_i^{out} = \frac{\|\hat{\mathbf{E}}_{scat}^{ext} - \hat{\mathbf{F}}^{3D}(\mathbf{c}_i)\|_{\mathcal{D}}^2}{\|\hat{\mathbf{E}}_{scat}^{ext}\|_{\mathcal{D}}^2} \tag{87}$$

$$r_{i,k}^{in} = \frac{\|\hat{\mathbf{F}}_{\mathbf{c}_i}^{3D'} \mathbf{h}_k - [\hat{\mathbf{E}}_{scat}^{ext} - \hat{\mathbf{F}}^{3D}(\mathbf{c}_i)]\|_{\mathcal{D}}^2}{\|\hat{\mathbf{E}}_{scat}^{ext}\|_{\mathcal{D}}^2} \tag{88}$$



#### 4.1 Numerical Validation: Landweber-based Method

Let us start with the description of the illuminating and measurement simulated setup. The background medium is vacuum, which is characterized by the propagation constant  $k_0 = \omega\sqrt{\mu_0\epsilon_0}$ . The working frequency is  $f = 300$  MHz. In all cases,  $S = 6$  views are considered. The corresponding incident electric fields are given by the following unit-amplitude plane waves

$$\begin{aligned}\mathbf{E}_{inc,(s)}(\mathbf{r}) &= e^{-jk_0\hat{\mathbf{w}}_{(s)}\cdot\mathbf{r}}\hat{\mathbf{p}}_{(s)} \\ \hat{\mathbf{w}}_{(s)} &= \sin\theta_{(s)}\cos\phi_{(s)}\hat{\mathbf{x}} + \sin\theta_{(s)}\sin\phi_{(s)}\hat{\mathbf{y}} + \cos\theta_{(s)}\hat{\mathbf{z}} \\ \hat{\mathbf{p}}_{(s)} &= \cos\theta_{(s)}\cos\phi_{(s)}\hat{\mathbf{x}} + \cos\theta_{(s)}\sin\phi_{(s)}\hat{\mathbf{y}} - \sin\theta_{(s)}\hat{\mathbf{z}}\end{aligned}\tag{89}$$

where  $k_0\hat{\mathbf{w}}_{(s)}$  is the wave vector,  $\hat{\mathbf{p}}_{(s)}$  is the polarization vector, and  $\theta_{(s)}, \phi_{(s)}$  are the angles in the spherical coordinate system (as indicated in Figure 1), which has been set as follows

$$(\theta_{(s)}, \phi_{(s)}) = \begin{cases} (0,0) & s = 1 \\ \left(\frac{\pi}{2}, (s-2)\frac{\pi}{2}\right) & s = 2, \dots, 5 \\ (\pi, 0) & s = 6 \end{cases}\tag{90}$$

For every view, the total electric field is collected in  $M = 82$  measurement points uniformly distributed on a sphere of radius  $R_{V_{obs}} = 2\lambda_0$ , with  $\lambda_0 = 1$  m free-space wavelength. It is worth noting that the sampling condition derived from the 3D degrees of freedom theory for electric fields [114] is not accomplished. The domain  $V_{inv}$  is a cube of side  $L_{V_{inv}} = \lambda_0$ . Figure 6 shows the described configuration. The investigation volume has been partitioned with two different cube-based meshes for the forward and inverse problems, in order to avoid inverse crimes [85]: a coarse mesh with  $N = 8000$  voxels for the inverse problem and a fine mesh with  $N_{fwd} = 29791$  voxels for the forward one. The simulated electric field measurements have been numerically computed by using a custom code based on the MoM. Moreover, these synthetic data have been corrupted with an additive white Gaussian noise with zero mean and variance corresponding to a signal-to-noise ratio  $SNR = 25$  dB, in order to simulate real operating conditions. In particular, the standard deviation  $\sigma_\eta$  of the additive noise vector is related to the  $SNR$  by the following formula [127]

$$SNR = 10 \log_{10} \left( \frac{\|\hat{\mathbf{E}}_{tot}^{ext}\|_2^2}{2 \cdot 3SM\sigma_\eta^2} \right) \quad (91)$$

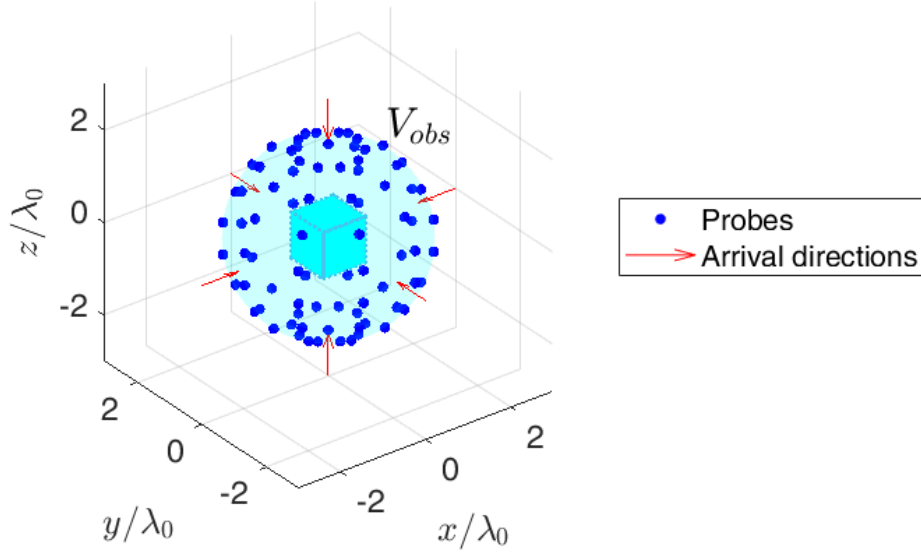


Figure 6. Measurement and illumination setup for the numerical validation of the 3D full-vector microwave imaging procedures.

Finally, the following stopping rules are adopted for the inexact-Newton scheme with truncated Landweber method

- Outer loop. Maximum number of iterations equals to  $I = 20$  or

$$r_i^{out} \leq \tau \frac{\|\delta\|_D^2}{\|\hat{\mathbf{E}}_{scat}^{ext}\|_D^2} \quad (92)$$

with  $\delta$  vector containing the values of the additive noise, and  $\tau \geq 1$ . This kind of stopping criterion derives from the Morozov's generalized discrepancy principle [85], [89]. The idea at the base of this criterion is to avoid an over-fitting behavior. In this section,  $\tau = 1$  is adopted.

- Inner loop. Maximum number of iterations equals to  $L = 10$  or

$$\frac{r_{i,k}^{in}}{r_i^{out}} \leq \tau_\mu \quad (93)$$

with  $\tau_\mu \in (0,1]$  [88], [89]. The value  $\tau_\mu = 0.5$  is selected.

#### 4.1.1 Reconstruction capabilities versus the scatterer dimension

Firstly, the reconstruction capabilities of the proposed microwave imaging algorithm have been evaluated by considering an investigation domain containing a single lossless sphere with center  $\mathbf{r}_c = (0.1, 0.1, 0.1)\lambda_0$  and relative dielectric permittivity  $\epsilon_r = 2.5$ . The radius of the sphere  $a_1$  has been varied in the range  $[0.15, 0.4]\lambda_0$ . The ground truth for the case  $a_1 = 0.2\lambda_0$  is shown in Figure 7.

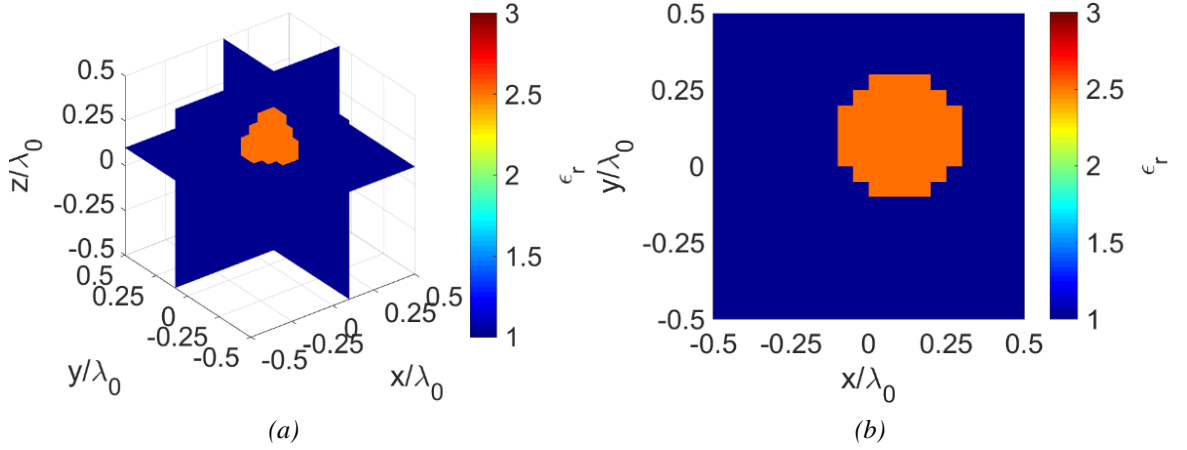


Figure 7. Actual distribution of the relative dielectric permittivity. (a) Three-dimensional view; (b)  $x - y$  cut ( $z = 0.1\lambda_0$ ). Single sphere with  $a_1 = 0.2\lambda_0$ .

Figure 8 shows the behavior of the NMSE for some of the considered values of the cylinder's radius.

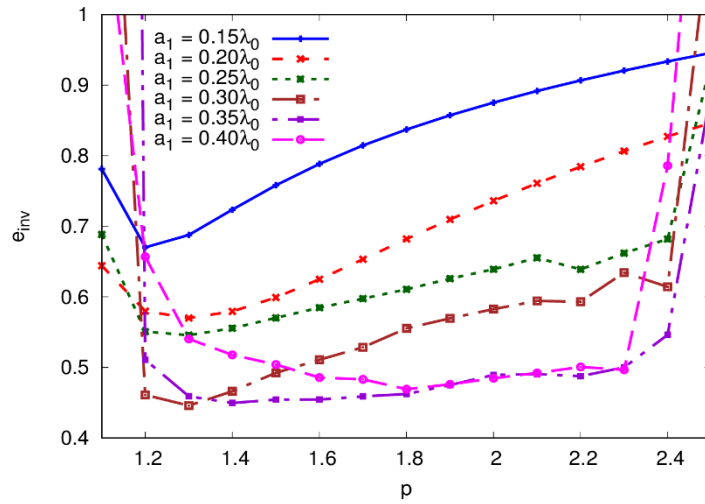


Figure 8. Behavior of  $e_{inv}$  versus the norm parameter  $p$  and for different values of the radius  $a_1$ . Single sphere.

Moreover, the values of the norm parameter  $p$  providing the NMSE-optimal reconstructions (indicated as  $p_{opt}$ ), the related mean relative errors, the final numbers of performed outer iterations  $i_f$ , and the total computational times  $T$  are reported in Table 1. The corresponding data for the Hilbert-space inversion (i.e., with  $p = 2$ ) are also reported for comparison purpose.

Table 1. Reconstruction errors, final number of outer iterations  $i_f$ , and computational times  $T$  versus  $a_1$  in correspondence of  $p = p_{opt}$  and  $p = 2$  (Hilbert space approach).

$a_1 [\lambda_0]$	$l^{p_{opt}}$					$l^2$ (Hilbert)			
	$p_{opt}$	$e_{obj}$	$e_b$	$i_f$	$T$ [s] <sup>(*)</sup>	$e_{obj}$	$e_b$	$i_f$	$T$ [s] <sup>(*)</sup>
0.15	1.2	0.36	0.017	1	46	0.47	0.065	1	46
0.2	1.3	0.28	0.042	2	230	0.33	0.11	2	222
0.25	1.3	0.26	0.063	2	262	0.29	0.13	2	174
0.3	1.3	0.14	0.11	4	748	0.16	0.21	4	791
0.35	1.4	0.18	0.14	5	1089	0.15	0.22	4	777
0.4	1.8	0.16	0.25	6	1534	0.16	0.27	5	1225

<sup>(\*)</sup> These refer to a PC equipped with a quad-core CPU Intel Core i5-2310 @2.9 GHz and 8 GB of RAM.

As can be seen, in all cases the optimal norm parameters are smaller than 2 (corresponding to the standard Hilbert-space algorithm), and the errors tend to increase above these values. As expected, the computational times  $T$  grow as  $a_1$  increases, since the scatterer becomes stronger. In fact, when the size and/or the dielectric contrast of the target become larger, an increasing number of Newton iterations are needed, since the inner linearization is locally less accurate in the first iterations. Moreover, the single outer iteration takes more time, too, since the BiCGSTAB-FFT used to compute the internal electric fields and the inhomogeneous Green's functions, as indicated in Section 3.5, requires more iterations to converge. For completeness, the outer residuals  $r_i^{out}$  versus the iteration number  $i$ , for the values of  $a_1$  and  $p_{opt}$  reported in Table 1, are shown in Figure 9, by which we can appreciate the different convergence rates for the various simulated spheres. An example of the reconstructed distributions of the relative dielectric permittivity is shown in Figure 10 for the case  $a_1 = 0.2\lambda_0$  with  $p = p_{opt} = 1.3$ . For comparison purposes, Figure 11 reports the reconstruction obtained on the same data but using the standard regularization scheme in Hilbert spaces ( $p = 2$ ). Although the object can be identified in both reconstruction, strong oversmoothing effects can be noticed when considering  $l^2$  spaces.

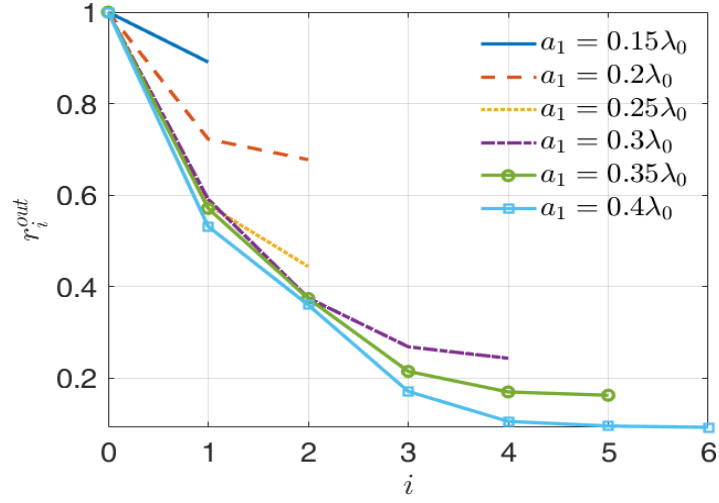


Figure 9. Behavior of  $r_i^{out}$  versus the iteration number for the values of  $a_1$  and  $p_{opt}$  reported in Table 1. Single sphere.

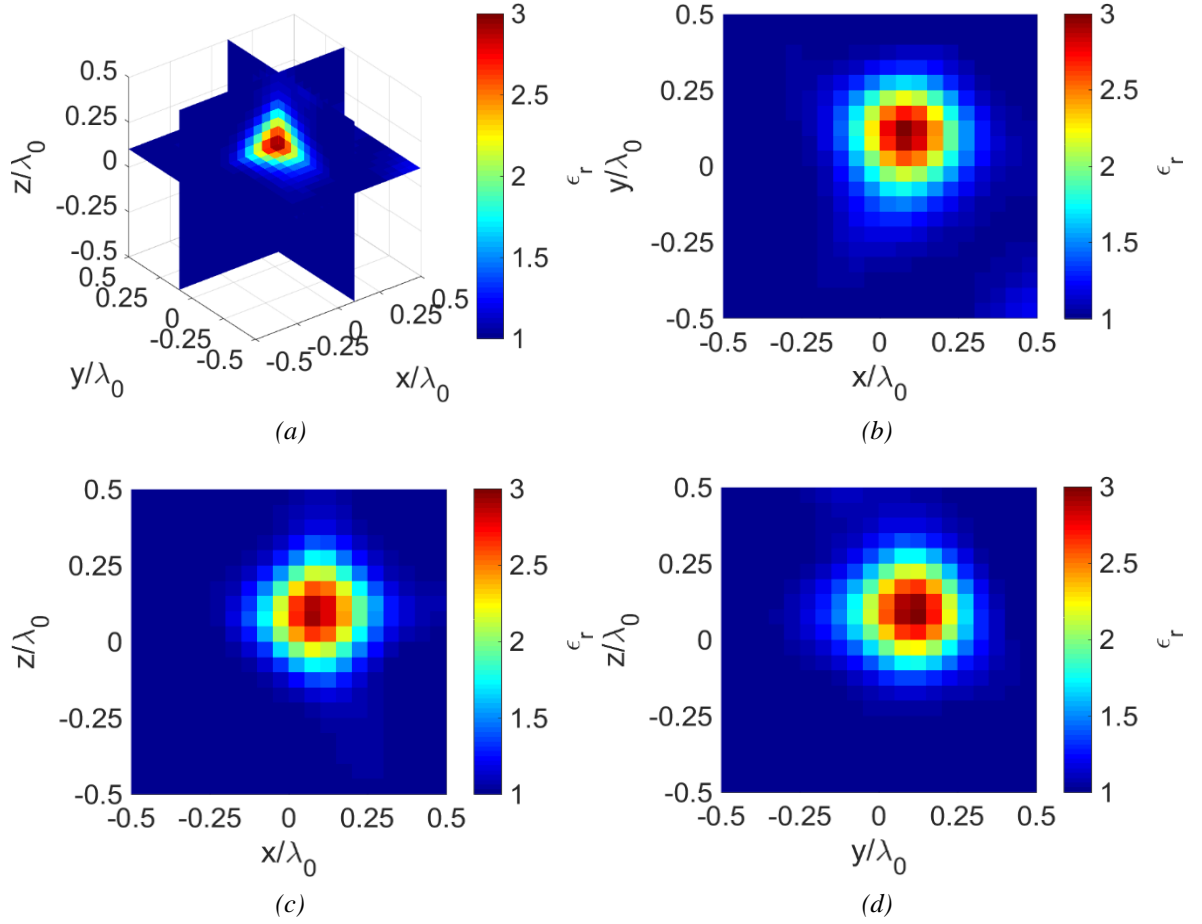


Figure 10. Reconstructed distribution of the dielectric permittivity with  $p = p_{opt} = 1.3$ . (a) Three-dimensional view; (b)  $x - y$  cut ( $z = 0.1\lambda_0$ ); (c)  $x - z$  cut ( $y = 0.1\lambda_0$ ); (d)  $y - z$  cut ( $x = 0.1\lambda_0$ ). Single sphere with  $a_1 = 0.2\lambda_0$ .

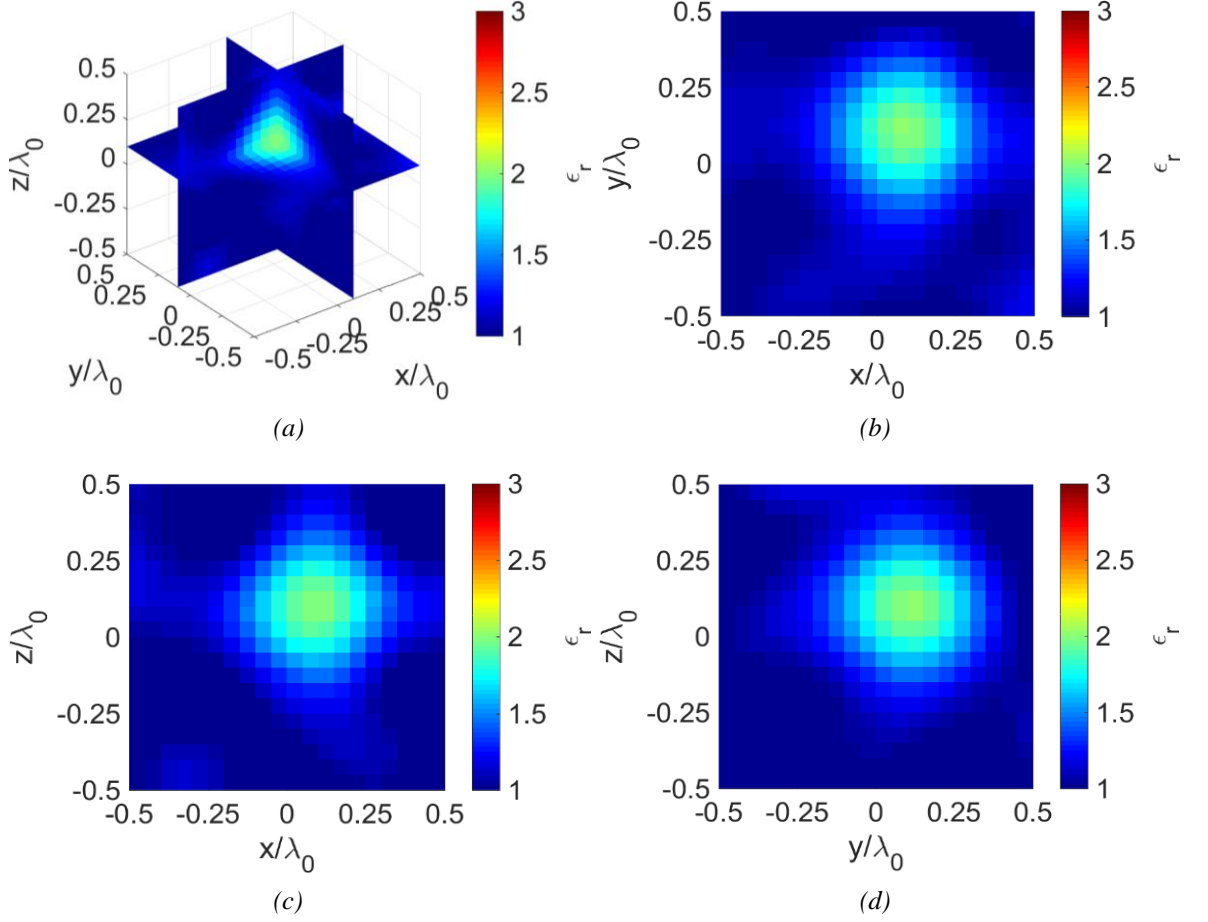


Figure 11. Reconstructed distribution of the dielectric permittivity with  $p = 2$  (Hilbert space approach). (a) Three-dimensional view; (b)  $x - y$  cut ( $z = 0.1\lambda_0$ ); (c)  $x - z$  cut ( $y = 0.1\lambda_0$ ); (d)  $y - z$  cut ( $x = 0.1\lambda_0$ ). Single sphere with  $a_1 = 0.2\lambda_0$ .

#### 4.1.2 Reconstruction capabilities in case of separate scatterers (two spheres)

In this Section, two separate spheres are considered. The first one has center  $\mathbf{r}_{c,1} = (0.15, 0.15, 0.15)\lambda_0$ , relative dielectric permittivity  $\epsilon_{r,1}$ , and radius  $a_1 = 0.2\lambda_0$ , whereas the second one has center  $\mathbf{r}_{c,2} = -\mathbf{r}_{c,1}$ , relative dielectric permittivity  $\epsilon_{r,2} = 2.5$ , and radius  $a_2 = a_1$ . The relative dielectric permittivity of the first sphere has been varied in the range  $[2, 6]$ . The ground truth for  $\epsilon_{r,1} = 4$  is shown in Figure 12. The trends of the NMSE versus the norm parameter  $p$  for different values of the simulated relative dielectric permittivity  $\epsilon_{r,1}$  are reported in Figure 13. Moreover, the mean relative errors, and the final numbers of performed outer iterations  $i_f$  in correspondence of  $p_{opt}$  and  $p = 2$  are reported in Table 2.

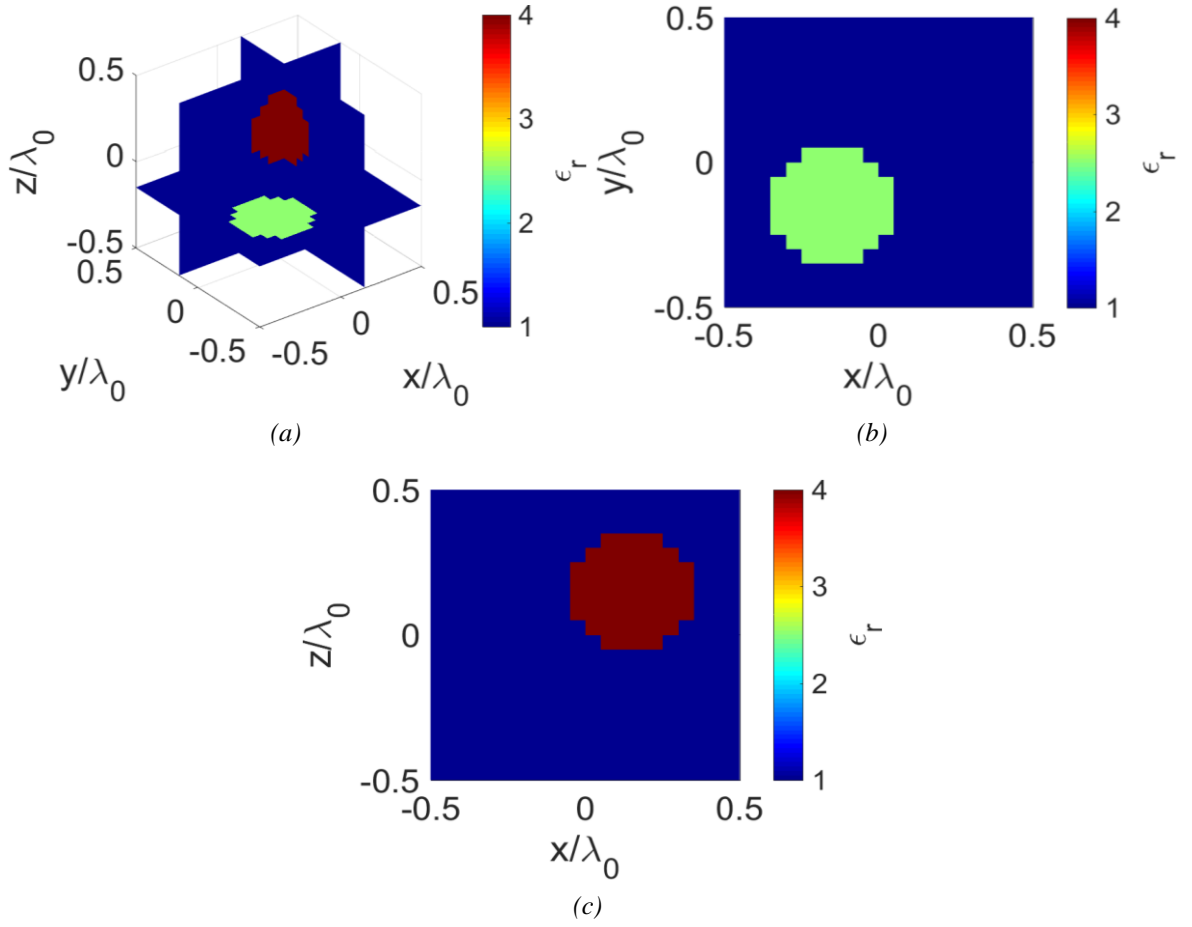


Figure 12. Actual distribution of the relative dielectric permittivity. (a) Three-dimensional view; (b)  $x - y$  cut ( $z = -0.15\lambda_0$ ); (c)  $x - z$  cut ( $y = 0.15\lambda_0$ ). Separate spheres with  $\epsilon_{r,1} = 4$ .

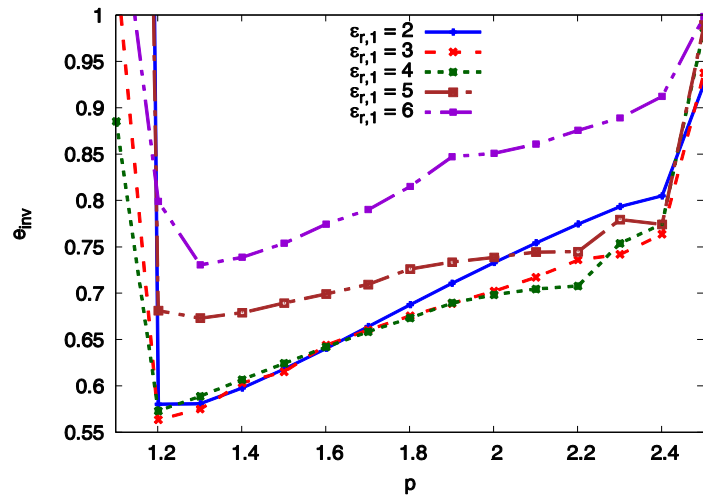


Figure 13. Behavior of  $e_{inv}$  versus the norm parameter  $p$  and for different values of the relative dielectric permittivity  $\epsilon_{r,1}$ . Separate spheres.

Table 2. Mean relative errors and final number of outer iterations  $i_f$  versus  $\epsilon_{r,1}$  in correspondence of  $p = p_{opt}$  and  $p = 2$  (Hilbert space approach).

$\epsilon_{r,1}$	$l^{p_{opt}}$				$l^2$ (Hilbert)		
	$p_{opt}$	$e_{obj}$	$e_b$	$i_f$	$e_{obj}$	$e_b$	$i_f$
2	1.2	0.27	0.043	2	0.31	0.13	2
3	1.2	0.3	0.057	3	0.36	0.15	2
4	1.2	0.31	0.077	3	0.37	0.20	3
5	1.3	0.37	0.17	5	0.40	0.28	5
6	1.3	0.39	0.27	8	0.45	0.45	9

Again, the more general Banach space approach is able to outperforms the classic Hilbert space one. However, the reconstruction accuracy gets worse as the dielectric permittivity of the first sphere increases, because of the lesser reliability of the inner linearization. Moreover, the outer residuals  $r_i^{out}$  versus the iteration number  $i$ , for the non-Hilbertian cases reported in Table 2, shown in Figure 14 allow us to better appreciate the slower convergence as  $\epsilon_{r,1}$  increases.

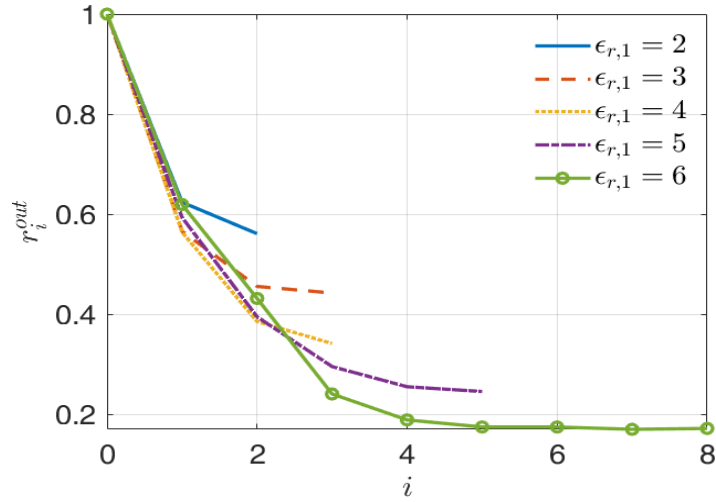


Figure 14. Behavior of  $r_i^{out}$  versus the iteration number for the values of  $\epsilon_{r,1}$  and  $p_{opt}$  reported in Table 2. Separate spheres.

Figure 15 shows the reconstructed distribution of the relative dielectric permittivity obtained with the optimal norm parameter  $p_{opt} = 1.2$  for  $\epsilon_{r,1} = 4$ , whereas the corresponding result obtained with  $p = 2$  (Hilbert space) is reported in Figure 16. As can be seen, the classic inexact-Newton shows a severe underestimation in the reconstructed relative dielectric permittivity distribution, which is significantly mitigated in  $l^{p_{opt}}$ .



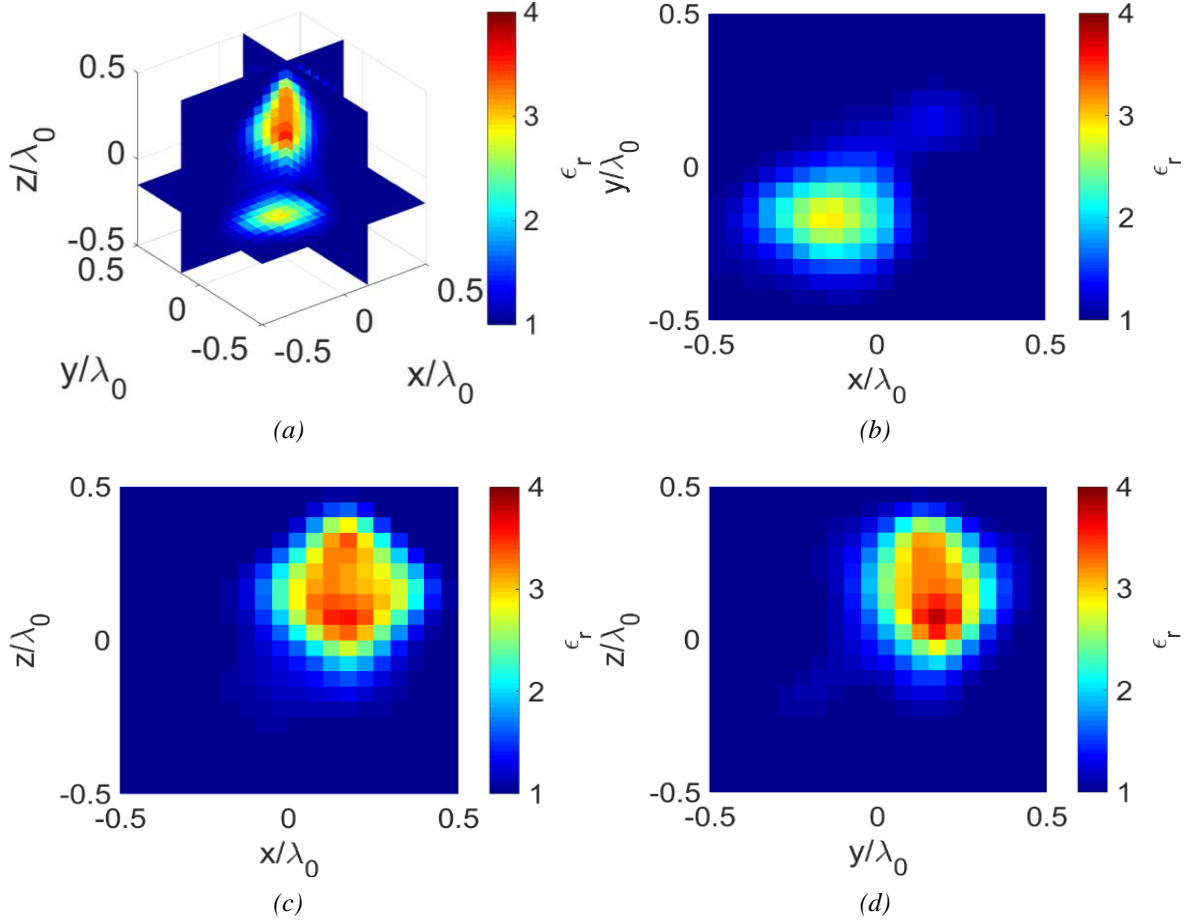


Figure 15. Reconstructed distribution of the dielectric permittivity with  $p = p_{opt} = 1.2$ . (a) Three-dimensional view; (b)  $x - y$  cut ( $z = -0.15\lambda_0$ ); (c)  $x - z$  cut ( $y = 0.15\lambda_0$ ); (d)  $y - z$  cut ( $x = 0.15\lambda_0$ ). Separate spheres with  $\epsilon_{r,1} = 4$ .

#### 4.1.3 Reconstruction capabilities versus the inner stopping threshold

The dependence of the reconstruction performance on the inner stopping threshold  $\tau_\mu$  is here assessed. The value of  $\tau_\mu$  has been varied in the admissible range  $(0,1]$ . The used investigation domain contains the separate targets introduced in Section 4.1.2 with relative dielectric permittivity of the first sphere fixed to  $\epsilon_{r,1} = 4$ . The norm parameter  $p$  has been set equal to  $p_{opt} = 1.2$ . Table 3 reports the obtained values of the reconstruction errors and the performed outer iterations. We can see that small values of  $\tau_\mu$  produce higher errors. In fact, when this threshold is excessively low, a proper early stopping of the inner loop rarely occurs, resulting in a weak regularization and so in an easier propagation of the noise. For values in the range  $[0.5,1]$  the errors exhibit only small variations, but the number of needed

outer iterations increases as  $\tau_\mu$  approaches 1, since a low number of inner iterations causes a slow update of the estimated contrast function.

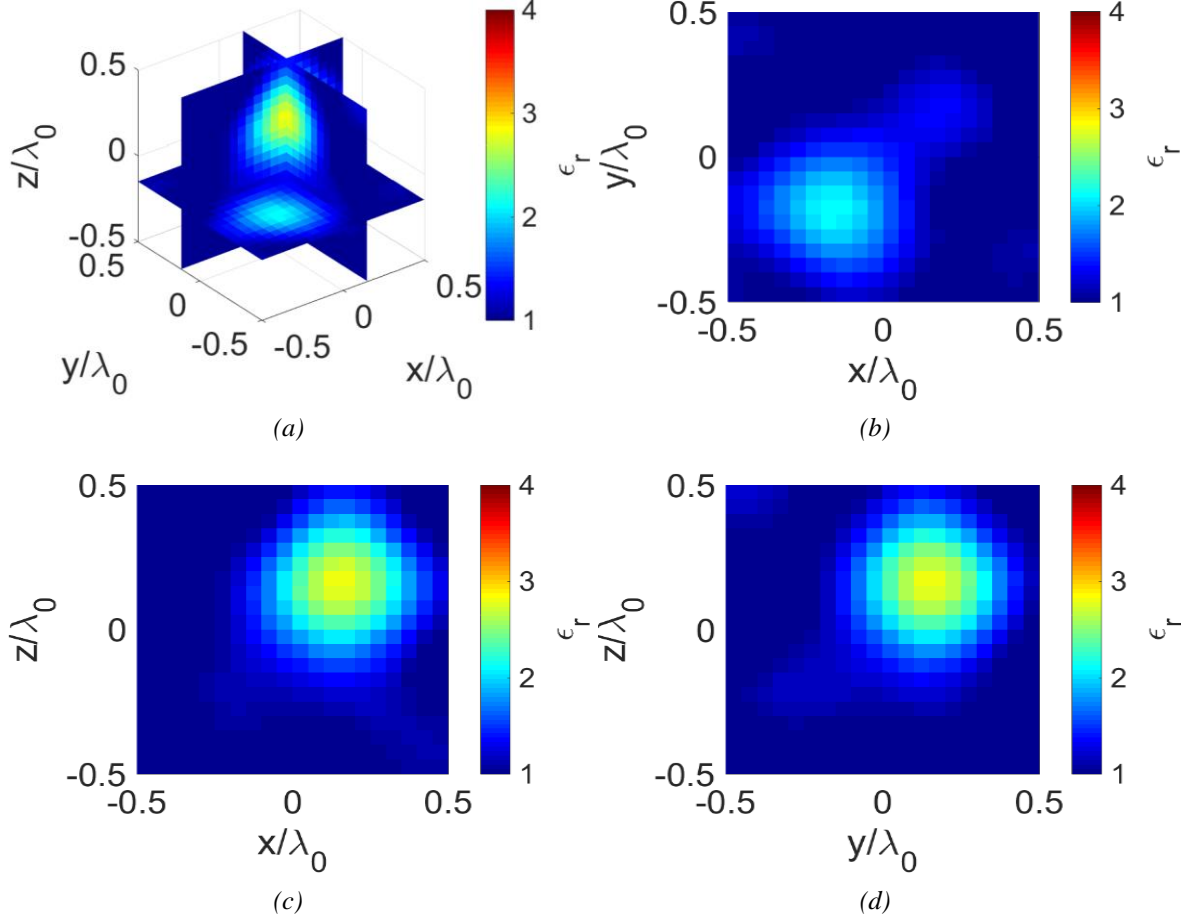


Figure 16. Reconstructed distribution of the dielectric permittivity with  $p = 2$  (Hilbert space approach). (a) Three-dimensional view; (b)  $x - y$  cut ( $z = -0.15\lambda_0$ ); (c)  $x - z$  cut ( $y = 0.15\lambda_0$ ); (d)  $y - z$  cut ( $x = 0.15\lambda_0$ ). Separate spheres with  $\epsilon_{r,1} = 4$ .

Table 3. Reconstruction errors and final number of outer iterations  $i_f$  versus  $\tau_\mu$  in correspondence of  $p = p_{opt} = 1.2$ . Separate spheres with  $\epsilon_{r,1} = 4$ .

$\tau_\mu$	$e_{inv}$	$e_{obj}$	$e_b$	$i_f$
0.25	0.60	0.34	0.087	3
0.5	0.57	0.31	0.077	3
0.75	0.57	0.32	0.078	5
0.95	0.58	0.32	0.078	9

#### 4.1.4 Reconstruction capabilities with inhomogeneous target and versus the signal-to-noise ratio

In this Section, the target consists in an inhomogeneous circular cylinder having height  $h = 0.6\lambda_0$ , radius  $R = 0.2\lambda_0$ , and center  $\mathbf{r}_c = (0.15, 0.15, 0)\lambda_0$ . The lowest half of this cylinder has relative dielectric permittivity  $\epsilon_{r,l} = 2$ , whereas the upper one has  $\epsilon_{r,u} = 3$  (Figure 17).

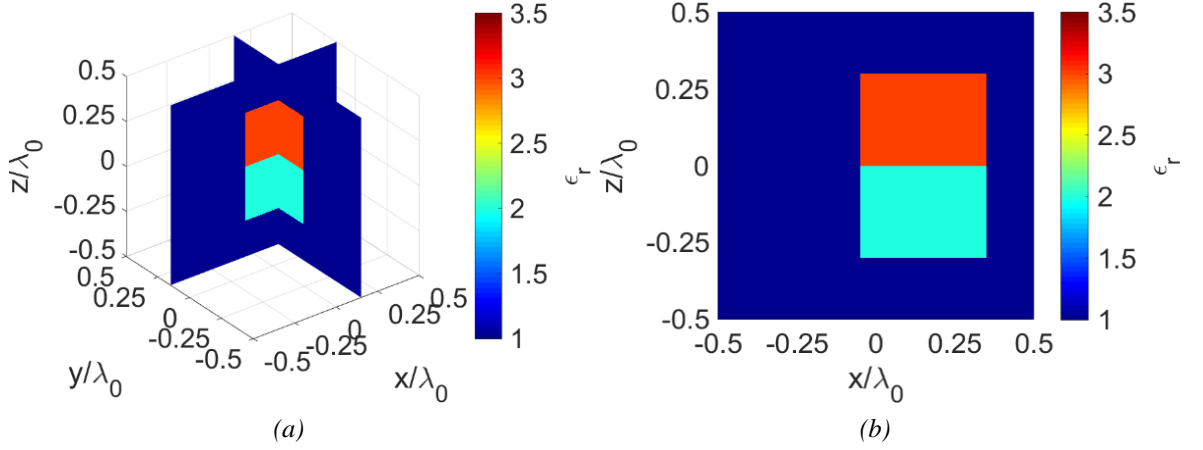


Figure 17. Actual distribution of the relative dielectric permittivity. (a) Three-dimensional view; (b)  $x - z$  cut ( $y = 0.15\lambda_0$ ). Inhomogeneous cylinder.

Moreover, in order to test the noise rejection capability of the proposed 3D microwave imaging technique, the  $SNR$  has been varied in the range  $[5, 50]$  dB. The behavior of the resulting NMSE versus the signal-to-noise ratio, obtained with both  $p = p_{opt}$  and  $p = 2$  (Hilbert-space case), is shown in Figure 18.

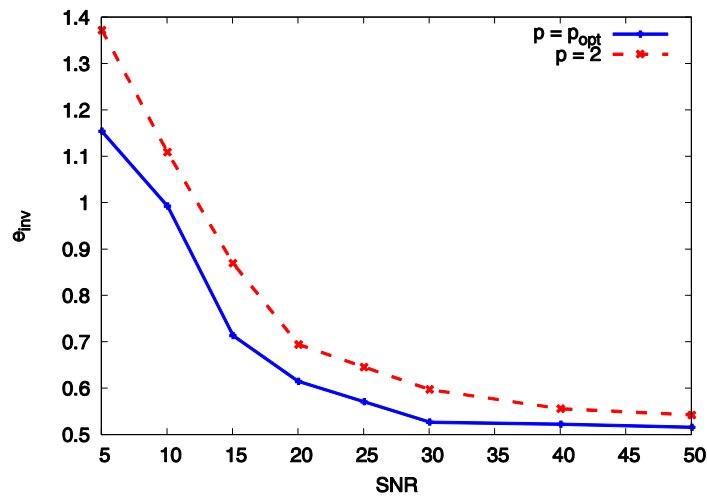


Figure 18. Behavior of  $e_{inv}$  versus the signal-to-noise ratio  $SNR$  for  $p = p_{opt}$  and  $p = 2$  (Hilbert space approach). Inhomogeneous cylinder.

The inexact-Newton scheme in  $l^{p_{opt}}$  presents a higher robustness to noise with respect to the standard Hilbert-space approach, as such behavior is also confirmed by the corresponding mean relative errors reported in Table 4, in which, although similar  $e_{obj}$  are achieved by the two methods, there is a significant gap on  $e_b$ .

Table 4. Mean relative errors and final number of outer iterations  $i_f$  versus SNR in correspondence of  $p = p_{opt}$  and  $p = 2$  (Hilbert space approach).

SNR [dB]	$l^{p_{opt}}$				$l^2$ (Hilbert)		
	$p_{opt}$	$e_{obj}$	$e_b$	$i_f$	$e_{obj}$	$e_b$	$i_f$
5	1.4	0.46	0.25	1	0.44	0.46	1
10	1.4	0.50	0.15	1	0.50	0.29	1
20	1.4	0.27	0.10	2	0.26	0.18	2
30	1.2	0.25	0.033	3	0.26	0.11	3
40	1.3	0.24	0.050	10	0.23	0.093	9
50	1.3	0.24	0.049	19	0.22	0.087	19

From this table, we can see also the action of the stopping rule in (92); in fact, the  $\|\delta\|_D^2$  term grows as the SNR decreases, and so the method is stopped earlier. Some examples of the reconstructed distributions of the relative dielectric permittivity are shown in Figure 19-21 for the values of SNR = 10 dB ( $p_{opt} = 1.4$ ), SNR = 20 dB ( $p_{opt} = 1.4$ ), and SNR = 30 dB ( $p_{opt} = 1.2$ ), respectively. In the same figures, the corresponding reconstructions obtained in Hilbert space are reported, too. As can be seen, in all cases, the advantages of using the Banach-space procedure are quite evident.

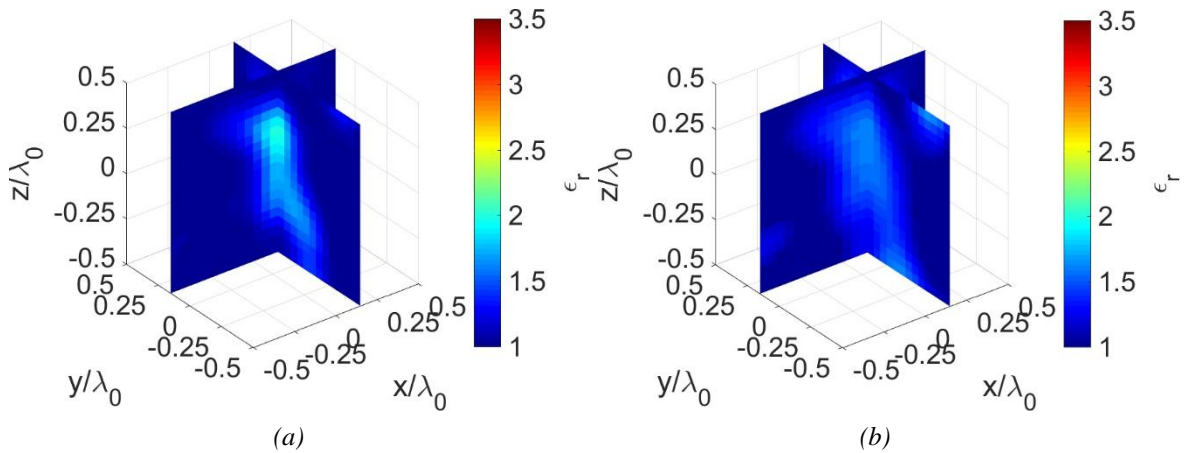


Figure 19. Reconstructed distribution of the dielectric permittivity for the signal-to-noise ratio SNR = 10 dB. (a)  $p_{opt} = 1.4$ ; (b)  $p = 2$ . Inhomogeneous cylinder.

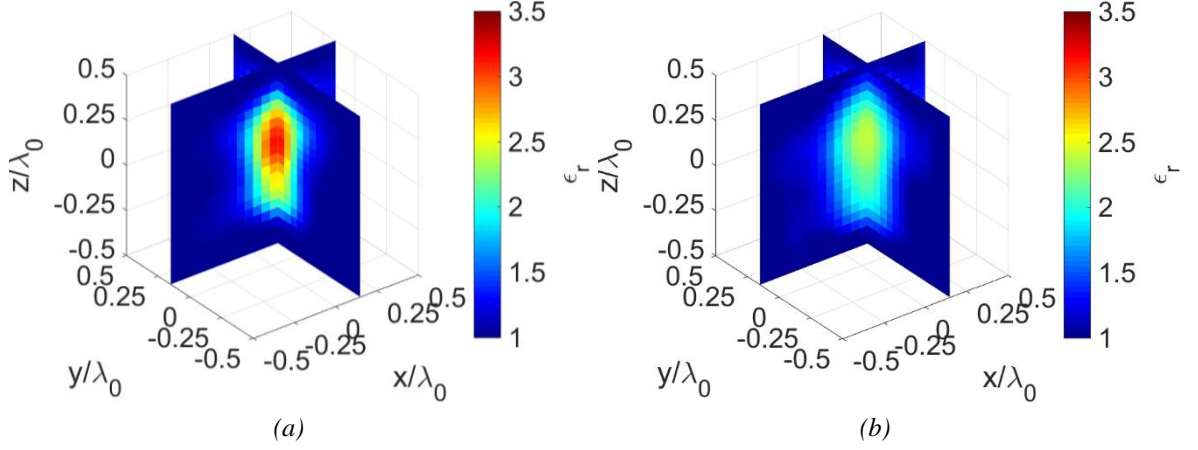


Figure 20. Reconstructed distribution of the dielectric permittivity for the signal-to-noise ratio  $SNR = 20$  dB. (a)  $p_{opt} = 1.4$ ; (b)  $p = 2$ . Inhomogeneous cylinder.

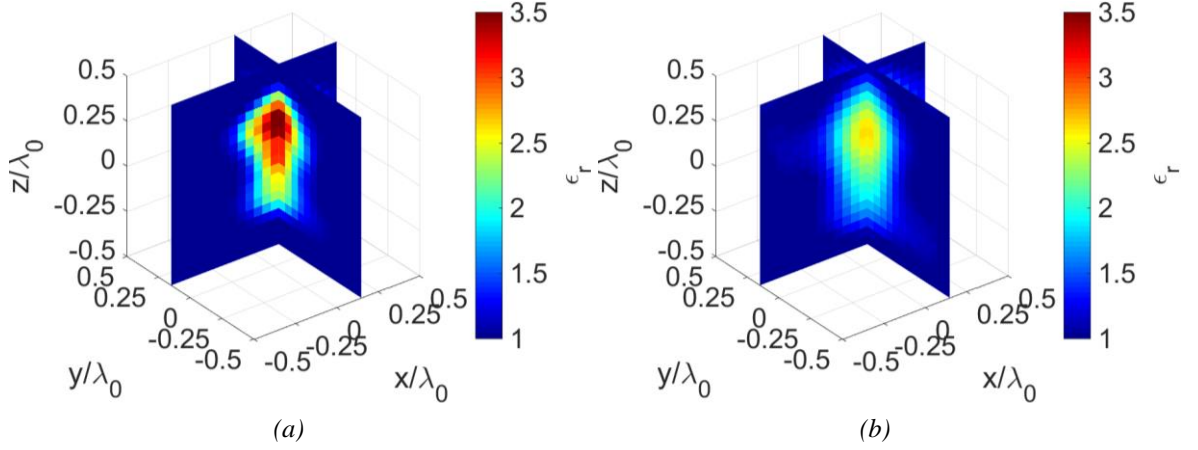


Figure 21. Reconstructed distribution of the dielectric permittivity for the signal-to-noise ratio  $SNR = 30$  dB. (a)  $p_{opt} = 1.2$ ; (b)  $p = 2$ . Inhomogeneous cylinder.

#### 4.1.5 Reconstruction capabilities against target with lossy inclusion

The simulated target is composed by a cube of side  $L = 0.7\lambda_0$ , centered in the origin, and with a spherical inclusion of radius  $R = 0.2\lambda_0$  and center  $\mathbf{r}_c = -(0.1, 0.1, 0.1)\lambda_0$ . The relative dielectric permittivity of the cube is  $\epsilon_{r,1} = 1.5$ , whereas the sphere is characterized by  $\epsilon_{r,2} = 3 - j1.2$ , that is a non-negligible electric conductivity  $\sigma_2 = 0.02$  S/m is present. The related ground truth is shown in Figure 22.

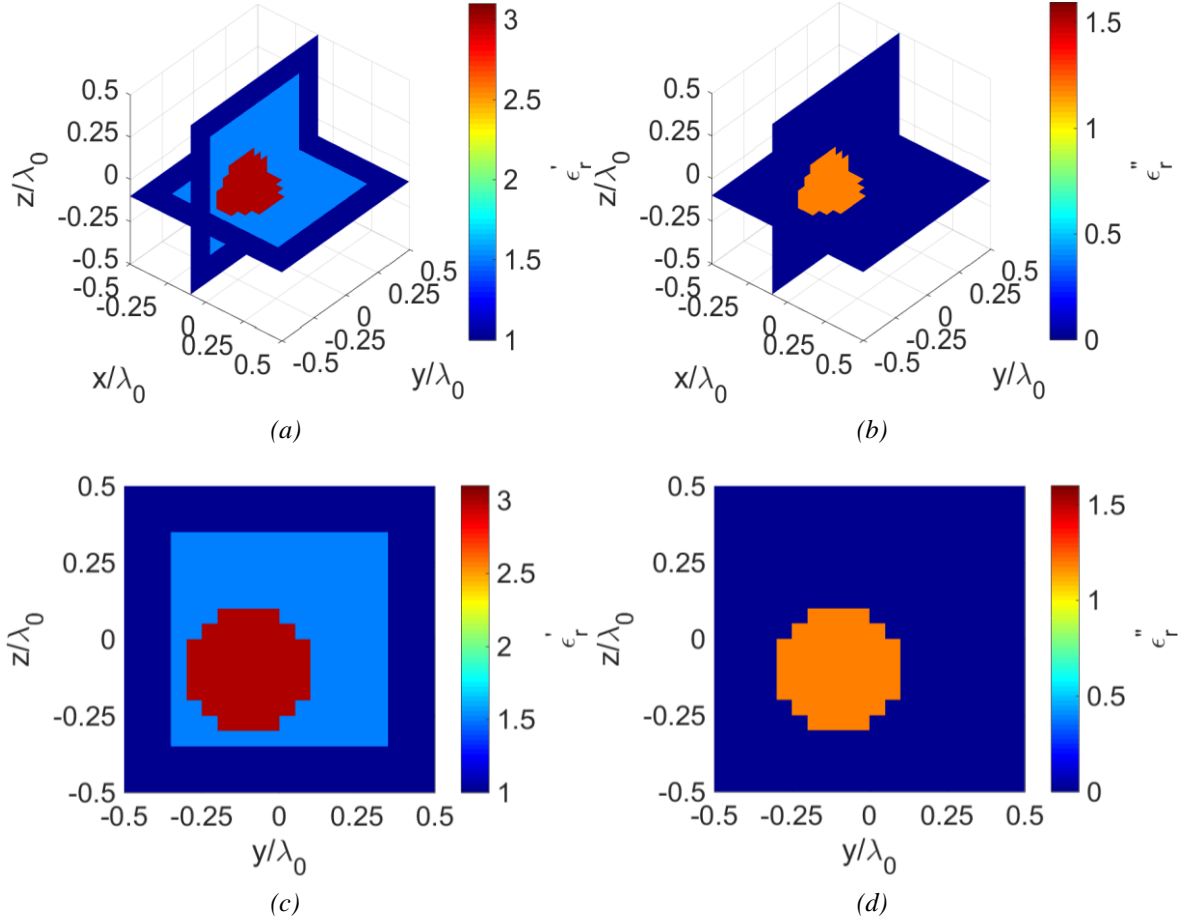


Figure 22. Actual distribution of the relative dielectric permittivity. Three-dimensional views of (a) real and (b) imaginary parts; cuts of (c) real and (d) imaginary parts ( $x = -0.1\lambda_0$ ). Target with lossy inclusion.

The reconstructed distributions of the real and imaginary parts of the complex dielectric permittivity obtained for  $p = p_{opt} = 1.3$  and  $p = 2$  (Hilbert space) are shown in Figure 23 and Figure 24, respectively. As can be seen, the inclusion and the host cube have been detected and the estimated values of the dielectric properties are fairly good in the result obtained in the space  $l^{1.3}$ . Instead, the real part of the dielectric permittivity is underestimated in the Hilbert-space solution.

#### 4.1.6 T-shaped target

Finally, an inhomogeneous T-shaped object is located in a larger investigation domain of side  $L_{V_{inv}} = 2\lambda_0$  and partitioned into  $N = 27000$  cubic voxels. The target is composed by two parallelepipeds: the upper one has center  $\mathbf{r}_{c,1} = (0,0,0.55)\lambda_0$ , and sides  $l_{x,1} = \lambda_0$ ,  $l_{y,1} = l_{z,1} = 0.3\lambda_0$ , whereas the lower one has center  $\mathbf{r}_{c,2} = (0,0,0)$ , and sides  $l_{x,2} = l_{y,2} = 0.3\lambda_0$ ,

$l_{z,2} = 0.8\lambda_0$ . The relative dielectric permittivities of the two parts are  $\epsilon_{r,1} = 3$  and  $\epsilon_{r,2} = 2$ . The ground truth is shown in Figure 25. The reconstructed distributions of the relative dielectric permittivity for the optimal value of the norm parameter  $p_{opt} = 1.2$  and  $p = 2$  (Hilbert space) are shown in Figure 26 and Figure 27, respectively. The two regions with different dielectric properties are clearly identified when  $p = p_{opt} = 1.2$ . On the contrary, a severe underestimation phenomenon affects the Hilbert space result, in which the parallelepipeds are barely distinguishable. For completeness, the resulting relative mean errors are  $e_{obj} = 0.28$ ,  $e_b = 0.02$  for  $p_{opt} = 1.2$ , and  $e_{obj} = 0.36$ ,  $e_b = 0.09$  for  $p = 2$ .

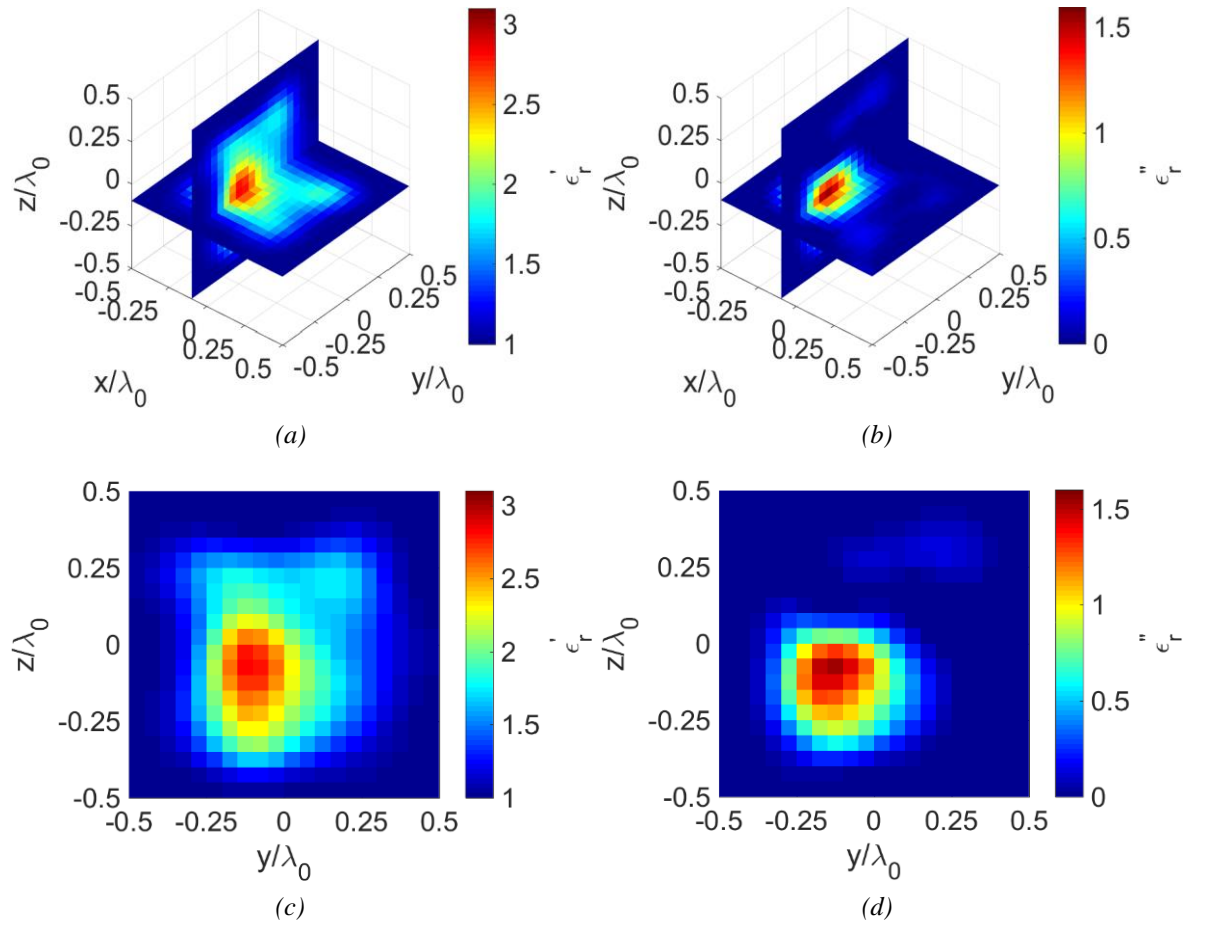


Figure 23. Reconstructed distribution of the dielectric permittivity with  $p = p_{opt} = 1.3$ . Three-dimensional views of (a) real and (b) imaginary parts; cuts of (c) real and (d) imaginary parts ( $x = -0.1\lambda_0$ ). Target with lossy inclusion.

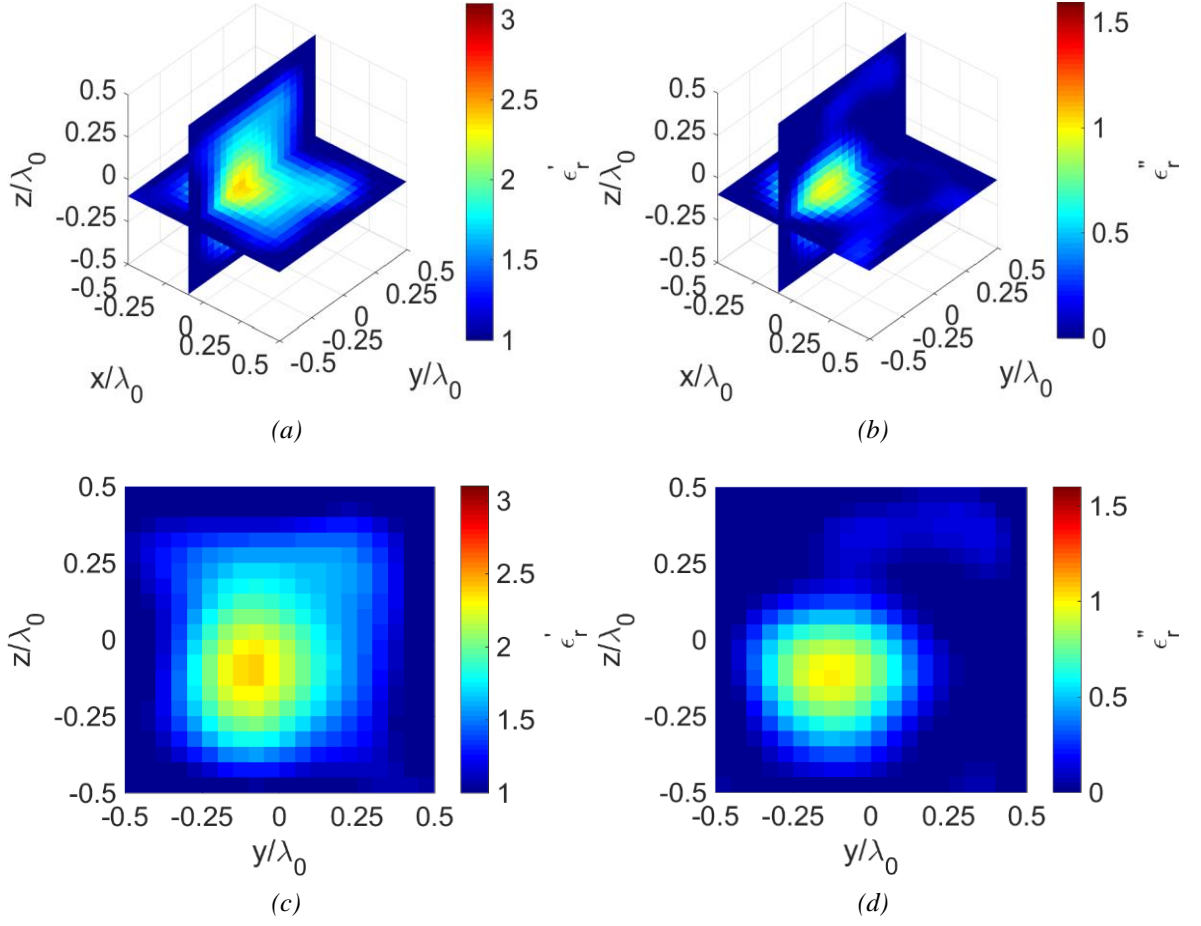


Figure 24. Reconstructed distribution of the dielectric permittivity with  $p = 2$  (Hilbert space approach). Three-dimensional views of (a) real and (b) imaginary parts; cuts of (c) real and (d) imaginary parts ( $x = -0.1\lambda_0$ ). Target with lossy inclusion.

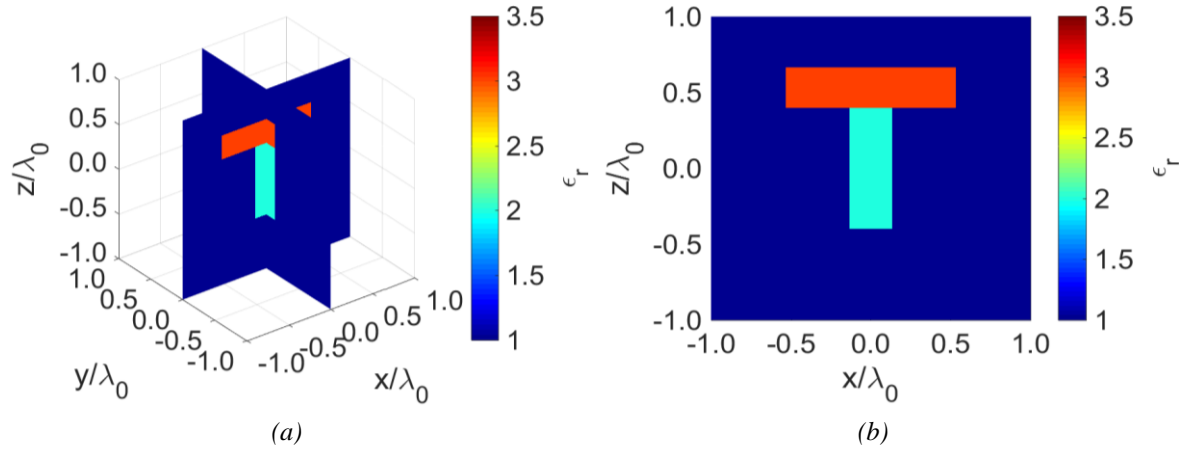


Figure 25. Actual distribution of the relative dielectric permittivity. (a) Three-dimensional view; (b)  $x - z$  cut ( $y = 0$ ). T-shaped target.



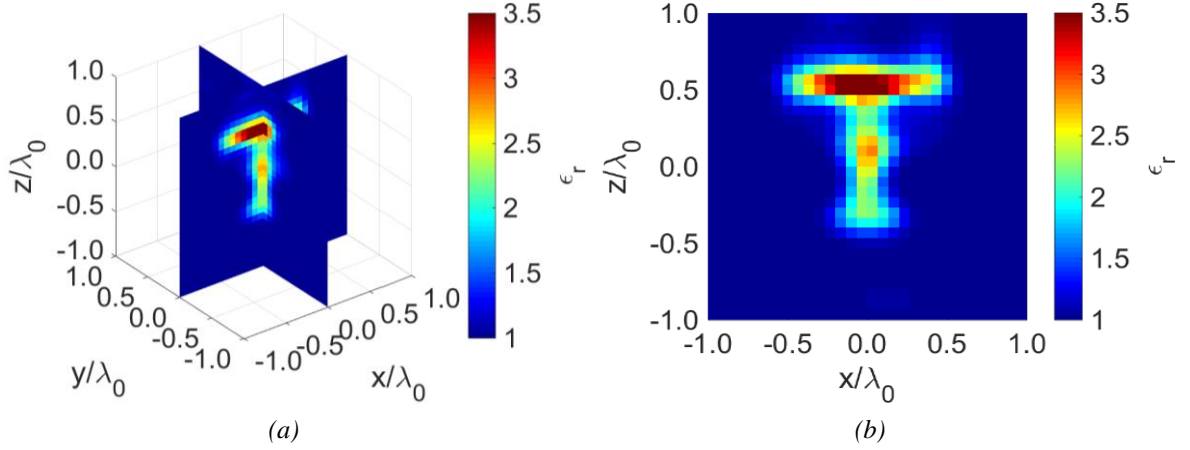


Figure 26. Reconstructed distribution of the dielectric permittivity with  $p = p_{opt} = 1.2$ . (a) Three-dimensional view; (b)  $x - z$  cut ( $y = 0$ ). T-shaped target.

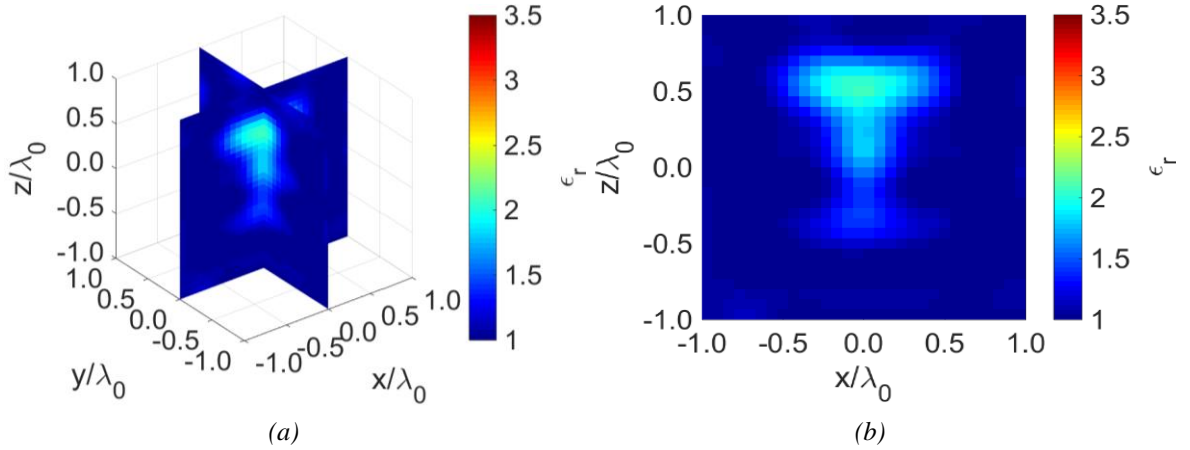


Figure 27. Reconstructed distribution of the dielectric permittivity with  $p = 2$  (Hilbert space approach). (a) Three-dimensional view; (b)  $x - z$  cut ( $y = 0$ ). T-shaped target.

## 4.2 Numerical Validation: Conjugate Gradient-based Method

In this Section, some preliminary results on synthetic data from the inexact-Newton scheme based on the conjugate gradient method applied in the 3D full-vector scenario are shown [126]. The same simulated illumination and measurement setup as reported in Section 4.1 is adopted here. The following stopping criteria are used

- Outer loop. Maximum number of iterations equals to  $I = 20$  or

$$\frac{r_i^{out} - r_{i+1}^{out}}{r_{i+1}^{out}} \leq \tau_I \quad (94)$$

with  $\tau_I = 0.01$  threshold on the relative outer residual variation [96].

- Inner loop. Maximum number of iterations equals to  $C = 10$  or

$$\frac{r_{i,k}^{in} - r_{i,k+1}^{in}}{r_{i,k+1}^{in}} \leq \tau_C \quad (95)$$

with  $\tau_C = 0.05$  threshold on the relative inner residual variation [126].

#### 4.2.1 Reconstruction capabilities versus the scatterer dimension

The reconstruction capabilities of the proposed conjugate gradient-based microwave imaging algorithm are here evaluated considering the investigation domain adopted in Section 4.1.1. Figure 28 shows the resulting NMSE behaviors versus the norm parameter  $p$  and for several radius of the sphere  $a_1$  in the range  $[0.15, 0.3]\lambda_0$ .

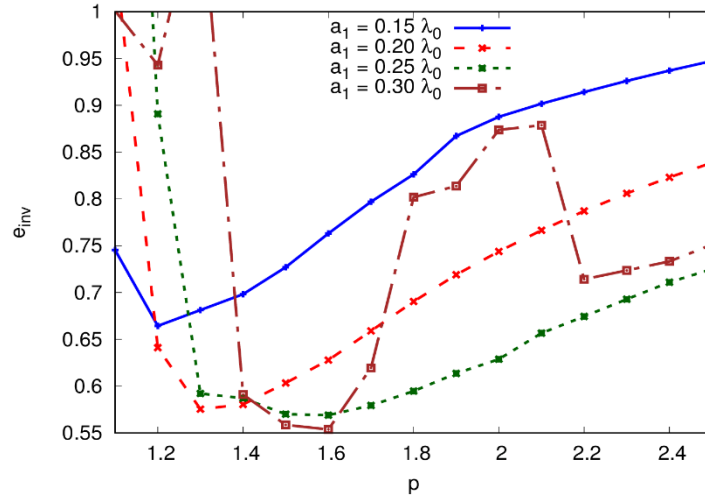


Figure 28. Behavior of  $e_{inv}$  versus the norm parameter  $p$  and for different values of the radius  $a_1$ . Single sphere. Conjugate gradient-based method.

Analogously to what we have seen in Section 4.1.1, the conjugate gradient-based inexact-Newton in Banach spaces is able to outperform the classic version of the algorithm in Hilbert spaces for values of the norm parameter  $p$  in the range (1,2). Figure 29 and Figure 30 report the reconstructed relative dielectric permittivity distributions obtained from the conjugate gradient-based method with  $p = p_{opt} = 1.3$  and  $p = 2$  (Hilbert space), respectively, for the case  $a_1 = 0.2\lambda_0$ .

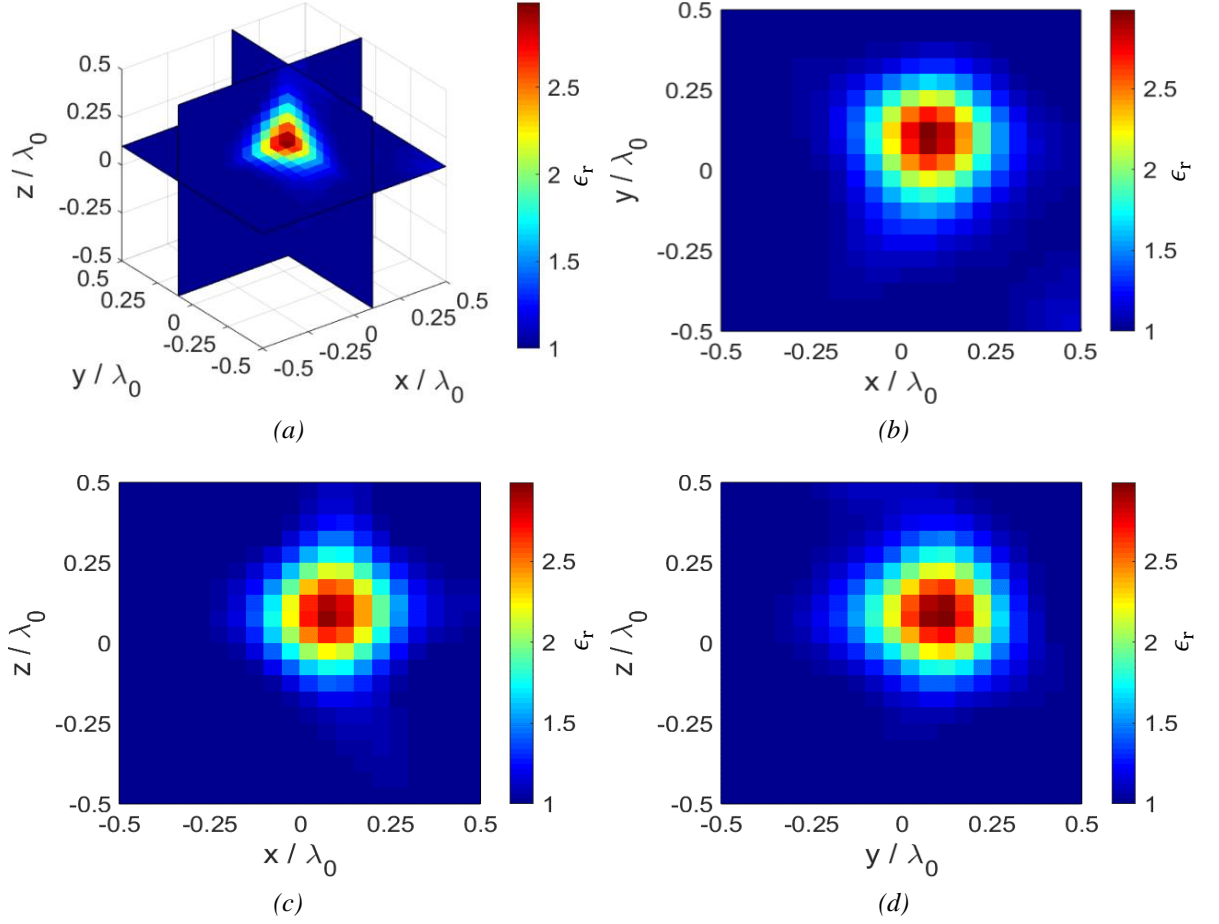


Figure 29. Reconstructed distribution of the dielectric permittivity with  $p = p_{opt} = 1.3$ . (a) Three-dimensional view; (b)  $x - y$  cut ( $z = 0.1\lambda_0$ ); (c)  $x - z$  cut ( $y = 0.1\lambda_0$ ); (d)  $y - z$  cut ( $x = 0.1\lambda_0$ ). Single sphere with  $a_1 = 0.2\lambda_0$ . Conjugate gradient-based method.

The same comments made for the reconstructions returned by the Landweber-based imaging method hold here similarly. Finally, a comparison about the convergence rates between the conjugate gradient-based inexact-Newton and the Landweber-based one is here made. In order to proper compare the two methods, the stopping criteria indicated in (94) and (95) are adopted also in the Landweber-based approach. For the case  $a_1 = 0.3\lambda_0$ , Figure 31 reports the behaviors of the inner and outer residuals metrics as defined in (87) and (88) versus the iteration number for both the compared methods in correspondence of their NMSE-optimal norm parameters ( $p_{opt} = 1.6$  and  $p_{opt} = 1.3$  for the conjugate gradient-based and Landweber-based methods, respectively). Moreover, Figure 32 shows the corresponding trends of the NMSE versus the iteration number.

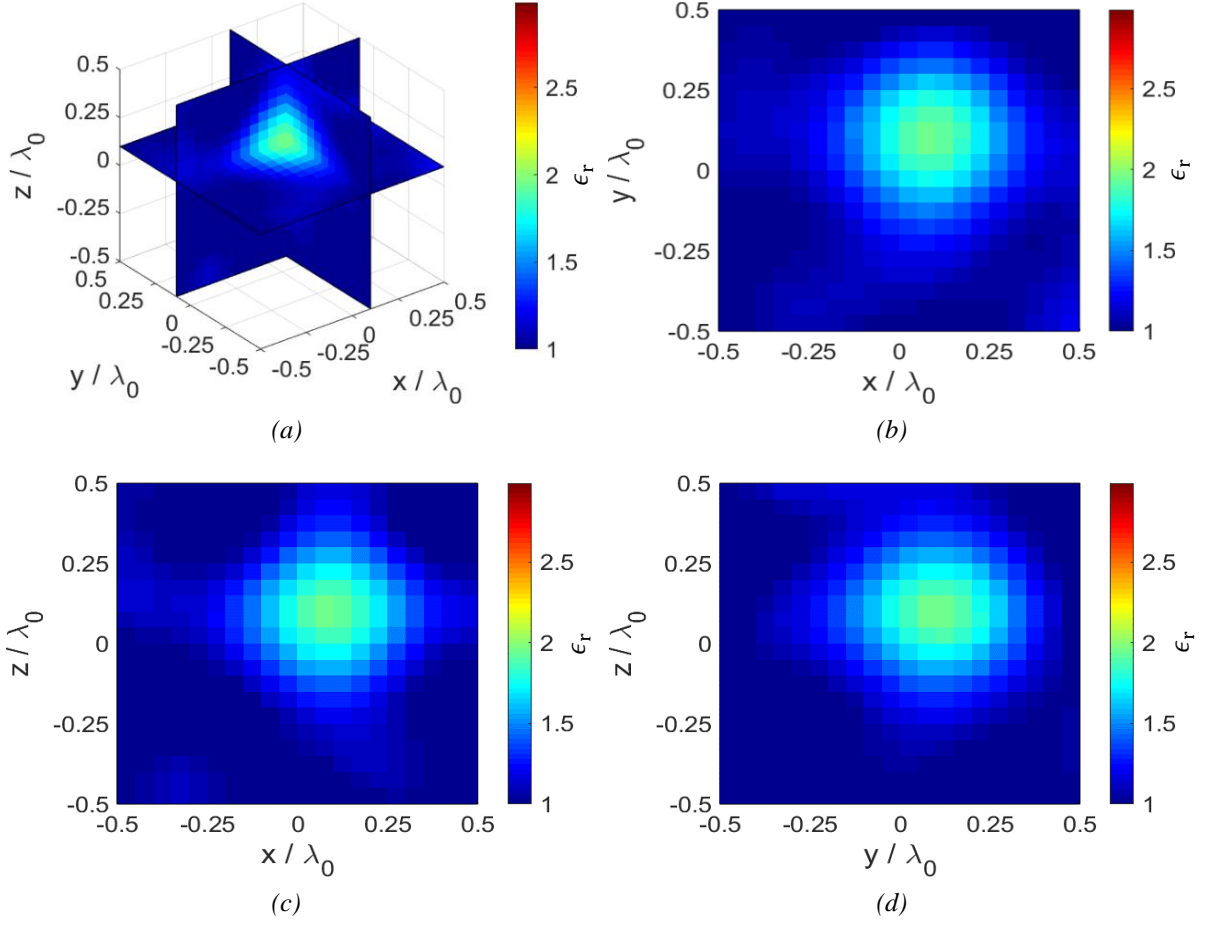


Figure 30. Reconstructed distribution of the dielectric permittivity with  $p = 2$  (Hilbert space approach). (a) Three-dimensional view; (b)  $x - y$  cut ( $z = 0.1\lambda_0$ ); (c)  $x - z$  cut ( $y = 0.1\lambda_0$ ); (d)  $y - z$  cut ( $x = 0.1\lambda_0$ ). Single sphere with  $a_1 = 0.2\lambda_0$ . Conjugate gradient-based method.

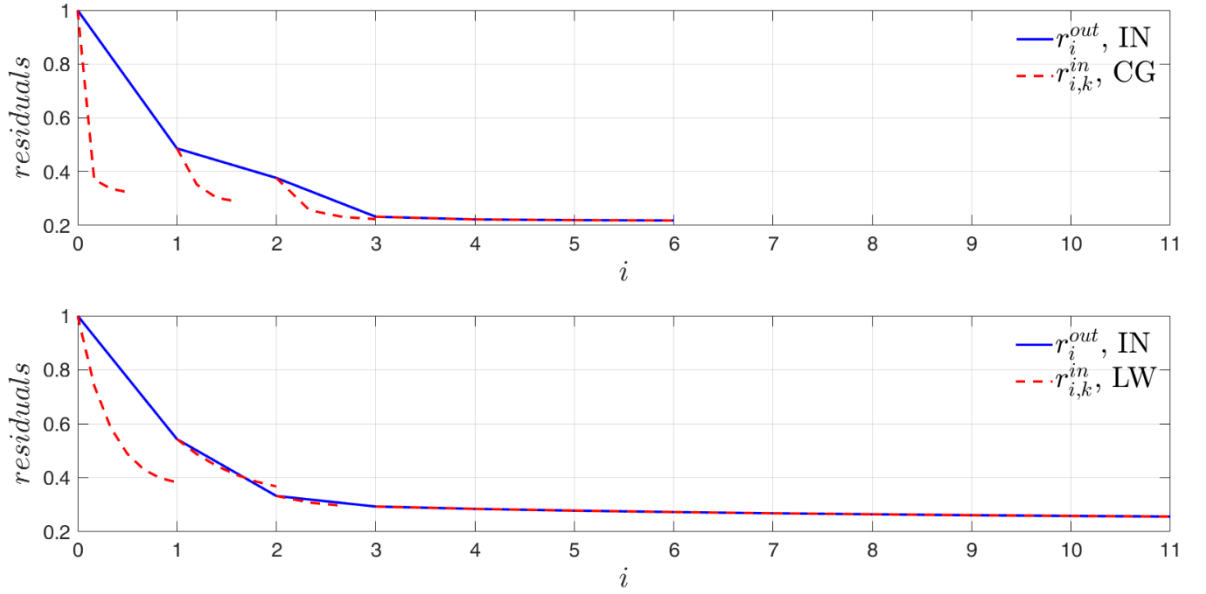


Figure 31. Behavior of  $r_i^{out}$  and  $r_{i,k}^{in}$  for the conjugate gradient-based ( $p_{opt} = 1.6$ ) and Landweber-based ( $p_{opt} = 1.3$ ) methods versus the iteration number. Single sphere with  $a_1 = 0.3\lambda_0$ .

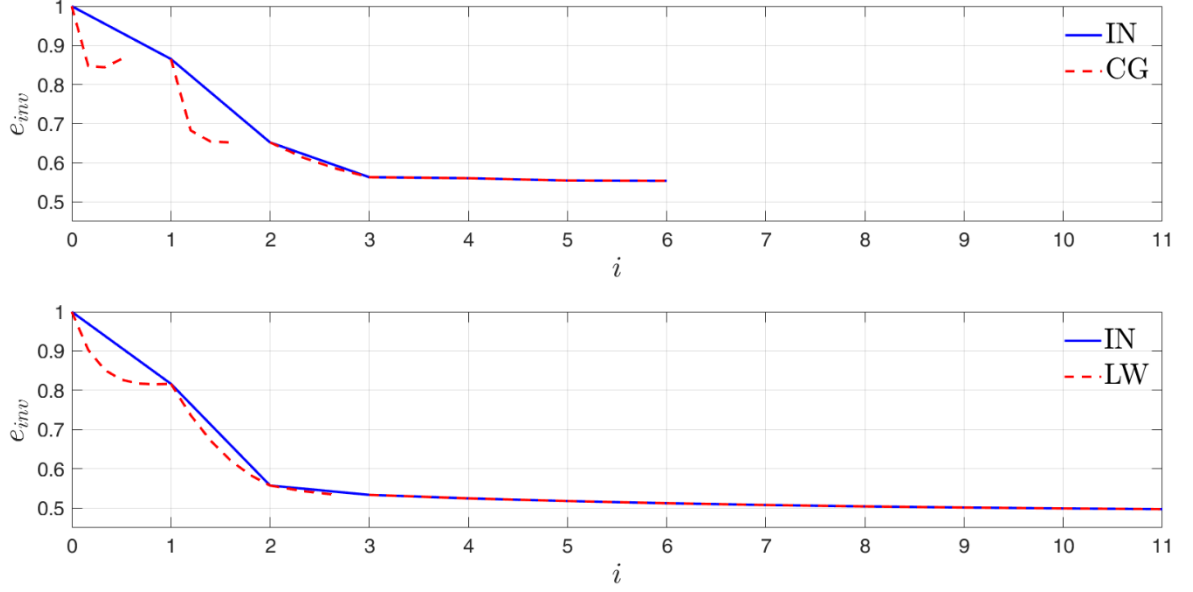


Figure 32. Behavior of  $e_{inv}$  for the conjugate gradient-based ( $p_{opt} = 1.6$ ) and Landweber-based ( $p_{opt} = 1.3$ ) methods versus the iteration number. Single sphere with  $a_1 = 0.3\lambda_0$ .

It can be seen that the adoption of the conjugate gradient method as inner linear solver for the inexact-Newton scheme allows a faster convergence in both the inner and outer loops than the Landweber algorithm. This result is in agreement with the numerical analysis theory in which the higher convergence rate of the classic conjugate gradient method with respect to the Landweber one has been proven, and that can be extended to the framework of the Banach spaces by continuity arguments [94]. On the other hand, in Figure 32 we see that the Landweber-based approach reaches a lower NMSE in the considered test case. However, Figure 33 shows that the two reconstructions are essentially equivalent.

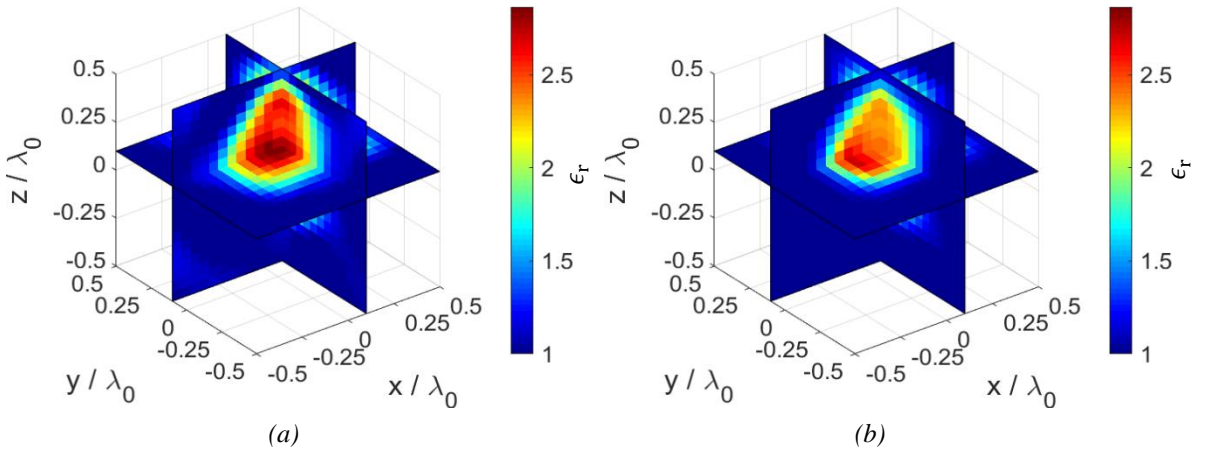


Figure 33. Reconstructed distributions of the dielectric permittivity. (a) Conjugate gradient-based method with  $p_{opt} = 1.6$ ; (b) Landweber-based method with  $p_{opt} = 1.3$ . Single sphere with  $a_1 = 0.3\lambda_0$ .

#### 4.2.2 Reconstruction capabilities in case of separate scatterers (sphere and cylinder)

In this Section, the conjugate gradient-based inexact-Newton imaging algorithm is tested against an investigation domain containing two objects. The first one is a sphere with center  $\mathbf{r}_{c,1} = (0.25, 0.25, 0)\lambda_0$ , diameter  $D_1 = 0.25\lambda_0$ , and relative dielectric permittivity  $\epsilon_{r,1}$ . The second object is a circular cylinder with center  $\mathbf{r}_{c,2} = -\mathbf{r}_{c,1}$ , diameter  $D_2 = 0.25\lambda_0$ , height  $H = 0.4\lambda_0$ , and relative dielectric permittivity  $\epsilon_{r,2} = 2$ . The relative dielectric permittivity of the sphere  $\epsilon_{r,1}$  has been varied in the range  $[2, 5]$ . The ground truth for  $\epsilon_{r,1} = 3$  is shown in Figure 34.

The behaviors of the NMSE versus the norm parameter  $p$  for different values of the simulated relative dielectric permittivity  $\epsilon_{r,1}$  are reported in Figure 35.

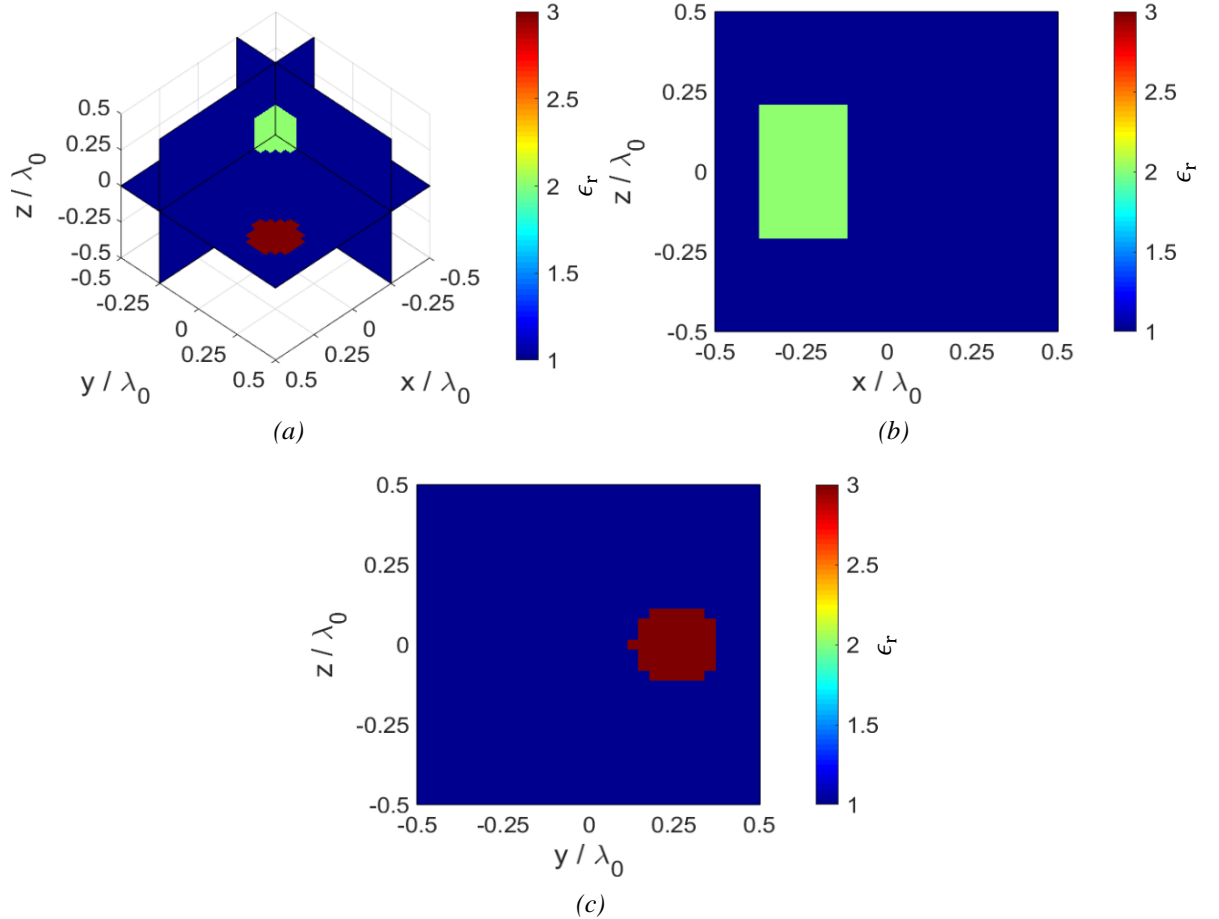


Figure 34. Actual distribution of the relative dielectric permittivity. (a) Three-dimensional view; (b)  $x - z$  cut ( $y = -0.25\lambda_0$ ); (c)  $y - z$  cut ( $x = 0.25\lambda_0$ ). Sphere and cylinder with  $\epsilon_{r,1} = 3$ .

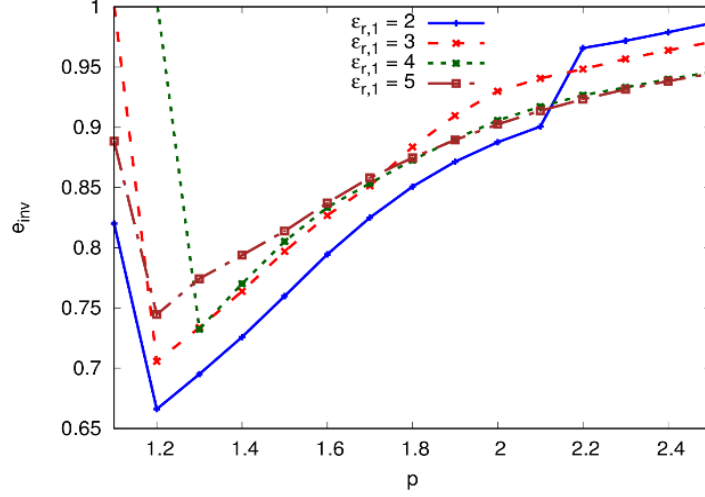


Figure 35. Behavior of  $e_{\text{inv}}$  versus the norm parameter  $p$  and for different values of the relative dielectric permittivity  $\epsilon_{r,1}$ . Sphere and cylinder. Conjugate gradient-based method.

Table 5. Mean relative errors and final number of outer iterations  $i_f$  versus  $\epsilon_{r,1}$  in correspondence of  $p = p_{\text{opt}}$  and  $p = 2$  (Hilbert space approach). Conjugate gradient-based method.

$\epsilon_{r,1}$	$l^{p_{\text{opt}}}$				$l^2$ (Hilbert)		
	$p_{\text{opt}}$	$e_{\text{obj}}$	$e_b$	$i_f$	$e_{\text{obj}}$	$e_b$	$i_f$
2	1.2	0.20	0.04	3	0.35	0.07	3
3	1.2	0.28	0.04	3	0.39	0.10	2
4	1.3	0.31	0.05	3	0.40	0.10	2
5	1.2	0.31	0.06	5	0.42	0.11	3

Moreover, the mean relative errors and the final numbers of performed outer iterations  $i_f$  in correspondence of  $p = p_{\text{opt}}$  and  $p = 2$  are reported in Table 5.

Similarly to Section 4.1.2, the reconstruction accuracy gets worse as the relative dielectric permittivity of the sphere increases, because, with strong scatterers, the first-order Taylor expansion in (58) has a smaller neighborhood of the current estimated solution in which the linearization is a good approximation of the underlying non-linear function. However, the Banach-space approach shows to better tackle such situation than the Hilbert-space one. Figure 36 reports the reconstructed distribution of the relative dielectric permittivity obtained with  $p_{\text{opt}} = 1.2$  for the case  $\epsilon_{r,1} = 3$ , whereas the corresponding result returned with  $p = 2$  (Hilbert space) is reported in Figure 37. Although the scatterers are visible in both reconstructions, the solution belonging to  $l^{p_{\text{opt}}}$  has a higher fidelity to the actual dielectric distribution than the one of  $l^2$ .

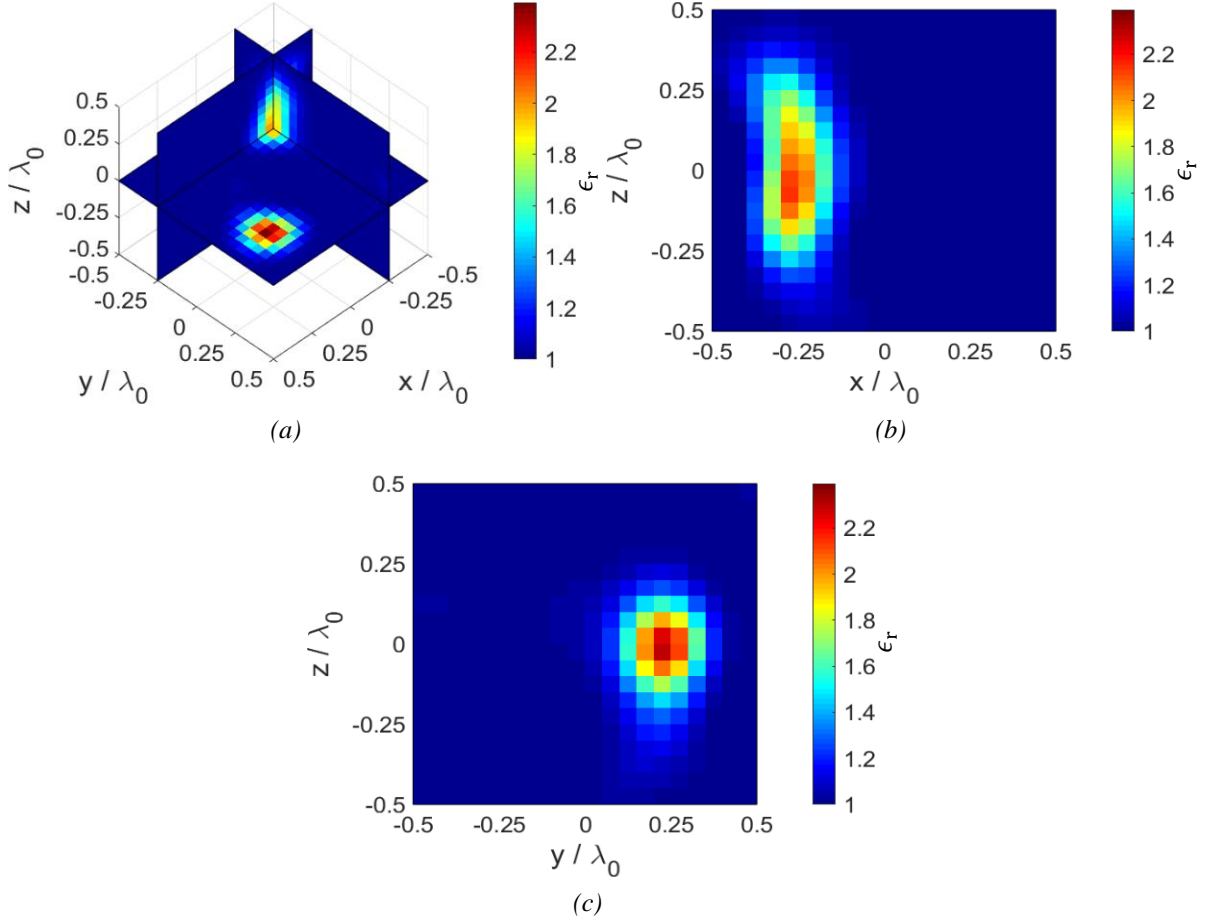


Figure 36. Reconstructed distribution of the dielectric permittivity with  $p = p_{opt} = 1.2$ . (a) Three-dimensional view; (b)  $x - z$  cut ( $y = -0.25\lambda_0$ ); (c)  $y - z$  cut ( $x = 0.25\lambda_0$ ). Sphere and cylinder with  $\epsilon_{r,1} = 3$ . Conjugate gradient-based method.

#### 4.2.3 Reconstruction capabilities with inhomogeneous target and versus the signal-to-noise ratio

In this Section, the same target adopted in Section 4.1.4 is used. Moreover, the same variation of the signal-to-noise ratio is here considered, namely  $SNR \in [5, 50]$  dB. The behavior of the resulting NMSE versus the signal-to-noise ratio, obtained with both  $p = p_{opt}$  and  $p = 2$  (Hilbert-space case), is shown in Figure 38. We see that the reconstructions obtained in non-Hilbertian spaces are able to outperform the standard Hilbertian one. Such finding is also supported by the corresponding mean relative errors reported in Table 6.



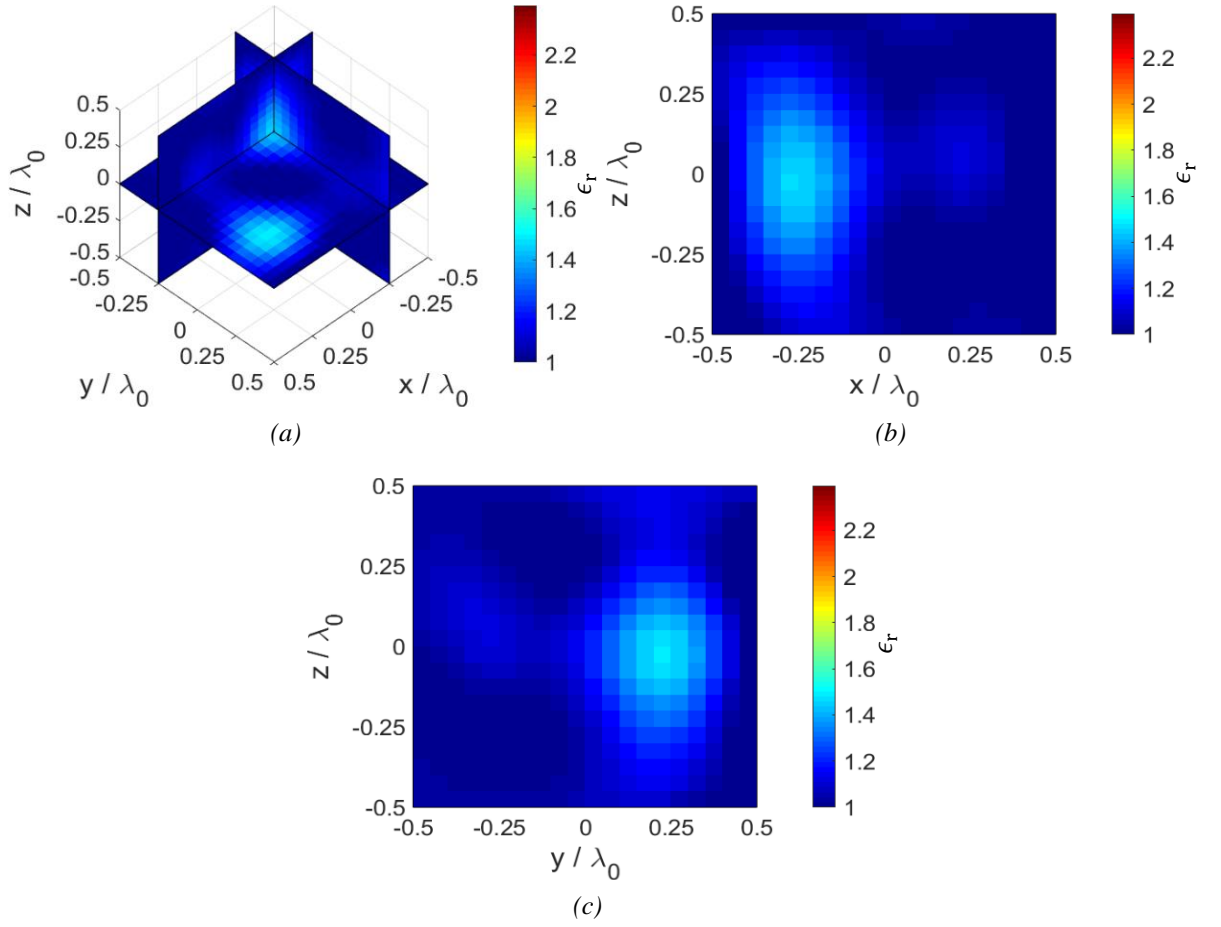


Figure 37. Reconstructed distribution of the dielectric permittivity with  $p = 2$  (Hilbert space approach). (a) Three-dimensional view; (b)  $x - z$  cut ( $y = -0.25\lambda_0$ ); (c)  $y - z$  cut ( $x = 0.25\lambda_0$ ). Sphere and cylinder with  $\epsilon_{r,1} = 3$ . Conjugate gradient-based method.

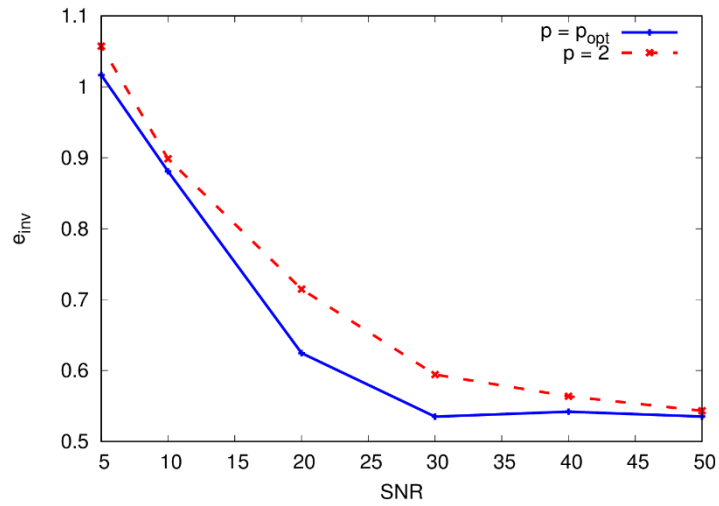


Figure 38. Behavior of  $e_{inv}$  versus the signal-to-noise ratio SNR for  $p = p_{opt}$  and  $p = 2$  (Hilbert space approach). Inhomogeneous cylinder. Conjugate gradient-based method.

Table 6. Mean relative errors and final number of outer iterations  $i_f$  versus SNR in correspondence of  $p = p_{opt}$  and  $p = 2$  (Hilbert space approach). Conjugate gradient-based method.

SNR [dB]	$\mathcal{I}^{p_{opt}}$				$\mathcal{I}^2$ (Hilbert)		
	$p_{opt}$	$e_{obj}$	$e_b$	$i_f$	$e_{obj}$	$e_b$	$i_f$
5	1.1	0.58	0.02	1	0.37	0.32	3
10	1.6	0.41	0.18	3	0.42	0.20	3
20	1.5	0.26	0.13	4	0.26	0.18	4
30	1.5	0.23	0.08	4	0.22	0.14	4
40	1.7	0.23	0.09	7	0.22	0.13	8
50	1.8	0.22	0.09	6	0.22	0.11	6

In Section 4.1.4, we saw that the stopping rule for the outer loop based on the Morozov's generalized discrepancy principle caused the method to be stopped earlier as the signal-to-noise ratio decreased. In the present test case, although the adopted stopping criterion for the outer loop does not descend from the generalized discrepancy principle, Table 6 shows that also the action of this stopping rule induces the method to be stopped earlier as the SNR decreases. Some examples of the reconstructed distributions of the relative dielectric permittivity are shown in Figure 39-41 for the values of SNR = 10 dB ( $p_{opt} = 1.6$ ), SNR = 20 dB ( $p_{opt} = 1.5$ ), and SNR = 30 dB ( $p_{opt} = 1.5$ ), respectively. In the same figures, the corresponding reconstructions obtained in Hilbert space are reported, too. The advantages of using the Banach-space procedure are quite evident in all the presented cases.

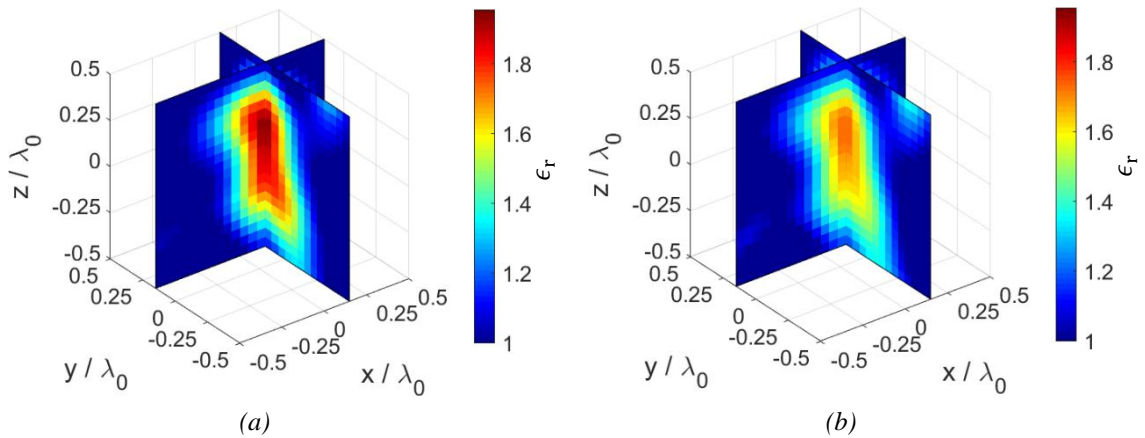


Figure 39. Reconstructed distribution of the dielectric permittivity for the signal-to-noise ratio SNR = 10 dB. (a)  $p_{opt} = 1.6$ ; (b)  $p = 2$ . Inhomogeneous cylinder. Conjugate gradient-based method.

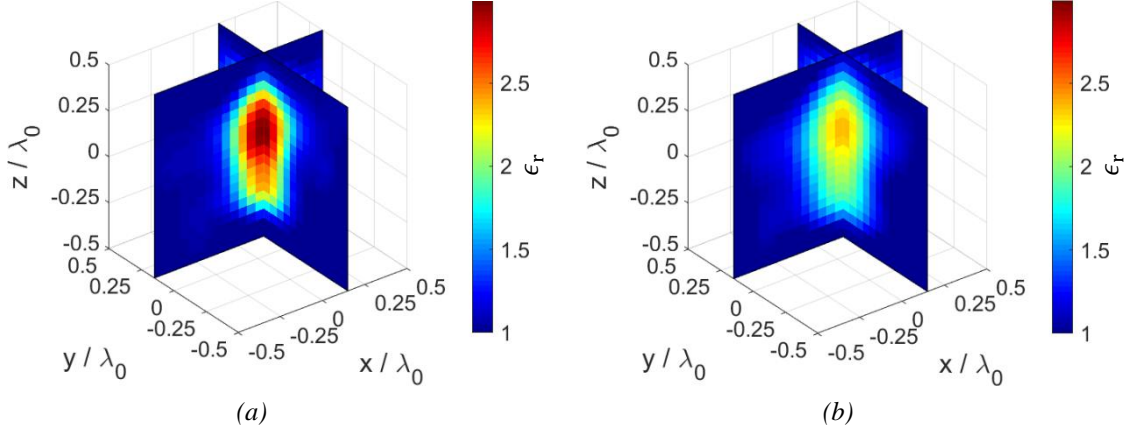


Figure 40. Reconstructed distribution of the dielectric permittivity for the signal-to-noise ratio  $SNR = 20$  dB. (a)  $p_{opt} = 1.5$ ; (b)  $p = 2$ . Inhomogeneous cylinder. Conjugate gradient-based method.

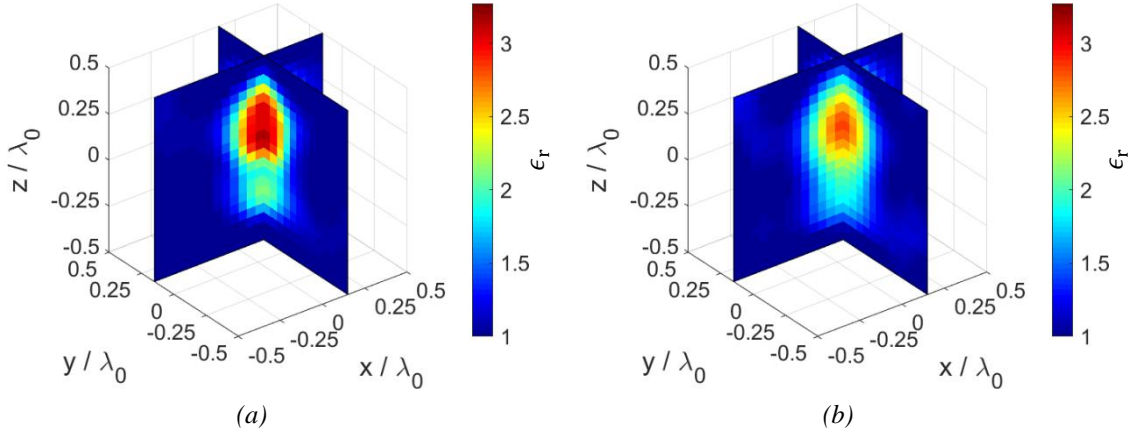


Figure 41. Reconstructed distribution of the dielectric permittivity for the signal-to-noise ratio  $SNR = 30$  dB. (a)  $p_{opt} = 1.5$ ; (b)  $p = 2$ . Inhomogeneous cylinder. Conjugate gradient-based method.

#### 4.2.4 Reconstruction capabilities versus the inner stopping threshold

The dependence of the reconstruction performance on the inner stopping threshold  $\tau_C$  is here assessed. The value of  $\tau_C$  is varied in the range  $[0.001, 0.3]$ . The adopted investigation domain contains the inhomogeneous cylinder used in Section 4.2.3. The norm parameter  $p_{opt} = 1.4$  that is resulted to be optimal for the reference parameters  $\tau_C = 0.05$  and  $SNR = 25$  dB is here adopted for each tested value of  $\tau_C$ . Table 7 reports the obtained values of the reconstruction errors and the performed outer iterations. We see that small values of  $\tau_C$  cause an improper stopping of the inner loop, resulting in a weak regularization and so in higher errors. For tested values higher than the reference  $\tau_C = 0.05$ , the errors exhibit only small

variations, but the number of needed outer iterations increases as  $\tau_C$  grows, since a low number of inner iterations causes a slow update of the estimated contrast function.

Table 7. Reconstruction errors and final number of outer iterations  $i_f$  versus  $\tau_C$  in correspondence of  $p = 1.4$ . Conjugate gradient-based method.

$\tau_C$	$e_{inv}$	$e_{obj}$	$e_b$	$i_f$
0.001	1.20	0.32	0.33	4
0.005	0.67	0.29	0.13	4
0.01	0.65	0.28	0.12	4
0.05	0.59	0.26	0.09	4
0.1	0.58	0.26	0.09	5
0.15	0.58	0.26	0.09	5
0.20	0.58	0.26	0.09	5
0.30	0.59	0.27	0.08	6

#### 4.2.5 T-shaped target

The same inhomogeneous T-shaped target introduced in Section 4.1.6 is considered here. Figure 42 and Figure 43 show the reconstructed relative dielectric permittivity distributions returned with  $p_{opt} = 1.4$  and  $p = 2$  (Hilbert space). Although the image in Figure 42 does not fully replicate the actual shape of the target, anyway the Banach-space conjugated gradient approach outperforms the Hilbert-space one again. For completeness, the resulting relative mean errors are  $e_{obj} = 0.28$ ,  $e_b = 0.07$  for  $p_{opt} = 1.4$ , and  $e_{obj} = 0.32$ ,  $e_b = 0.12$  for  $p = 2$ .

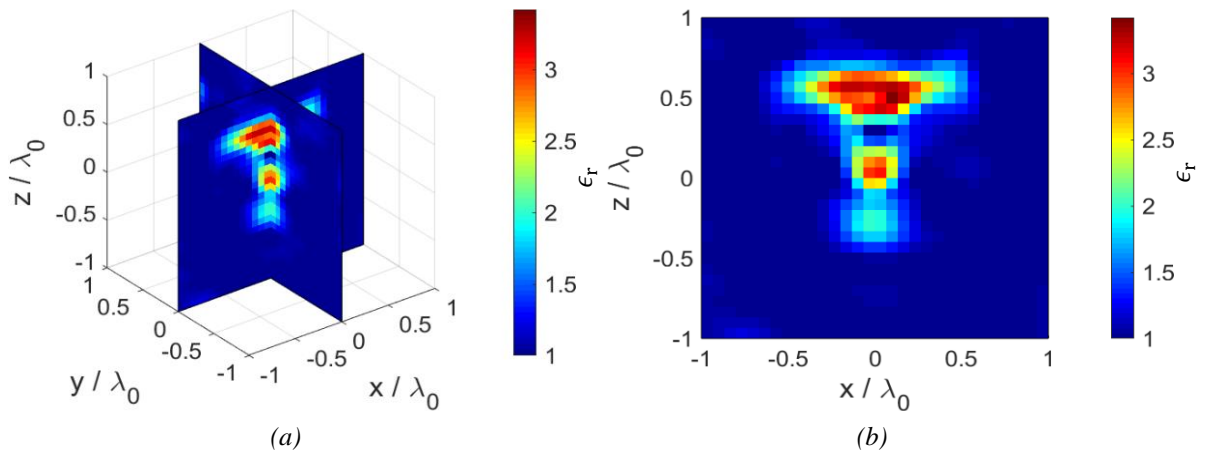


Figure 42. Reconstructed distribution of the dielectric permittivity with  $p = p_{opt} = 1.4$ . (a) Three-dimensional view; (b)  $x - z$  cut ( $y = 0$ ). T-shaped target. Conjugate gradient-based method.

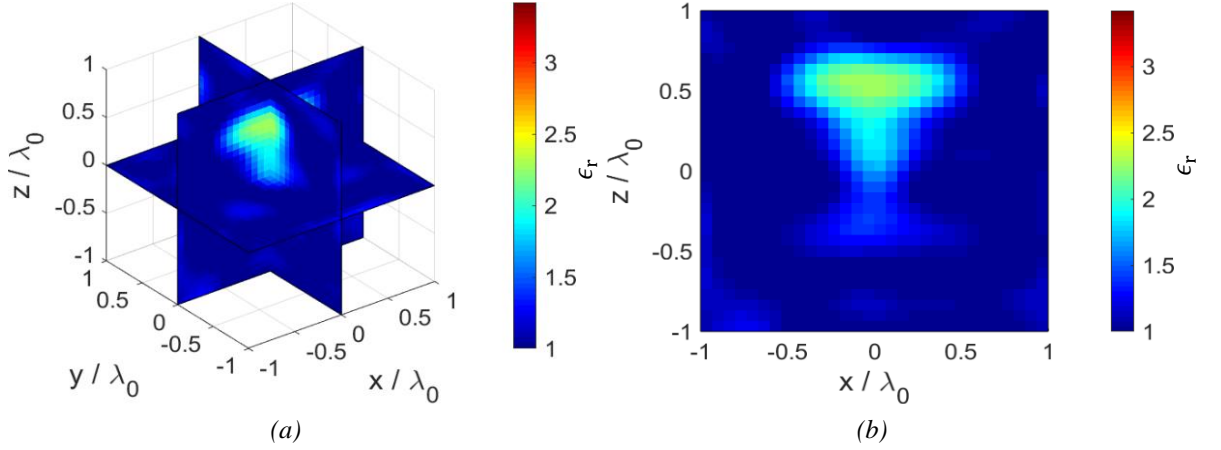


Figure 43. Reconstructed distribution of the dielectric permittivity with  $p = 2$  (Hilbert space approach). (a) Three-dimensional view; (b)  $x - z$  cut ( $y = 0$ ). T-shaped target. Conjugate gradient-based method.

### 4.3 Experimental Validation: Landweber-based Method

The developed Landweber-based approach has been also validated by considering the measured dataset provided by the Institut Frénel [128]. The dataset provides data in the range 3 – 8 GHz but, in order to work in the resonant regime with respect to the targets described in the following,  $f = 3$  GHz is selected, which correspond to a free-space wavelength  $\lambda_0 = 10$  cm. The experimental system in which these measurements have been gathered consists in two moving antennas able to collect multi-view data. The transmitting antenna moves in  $S_{tot} = 81$  locations on a sphere of radius  $R_{V_S} = 1.796$  m and radiates sequentially with both vertical and horizontal polarizations, whereas the receiving one moves in  $M = 27$  positions (for each view) on a circumference of radius  $R_{V_{obs}} = 1.796$  m placed on the  $x - y$  plane and records the vertical electric field component only. However, only a subset of  $S = 25$  evenly spaced vertically polarized sources has been considered here; this number has been found to be a good compromise between the need of increasing the available data as much as possible and the reduction of computational requirements. Since only the vertical component of the measured field is available, the transverse components of the data vector and of the predicted one have been set equal to zero, in order to exclude their role from the inversion process. Figure 44 shows the used illumination and measurement configuration. For deeper technical insights in the experimental apparatus, the reader is referred to [128].

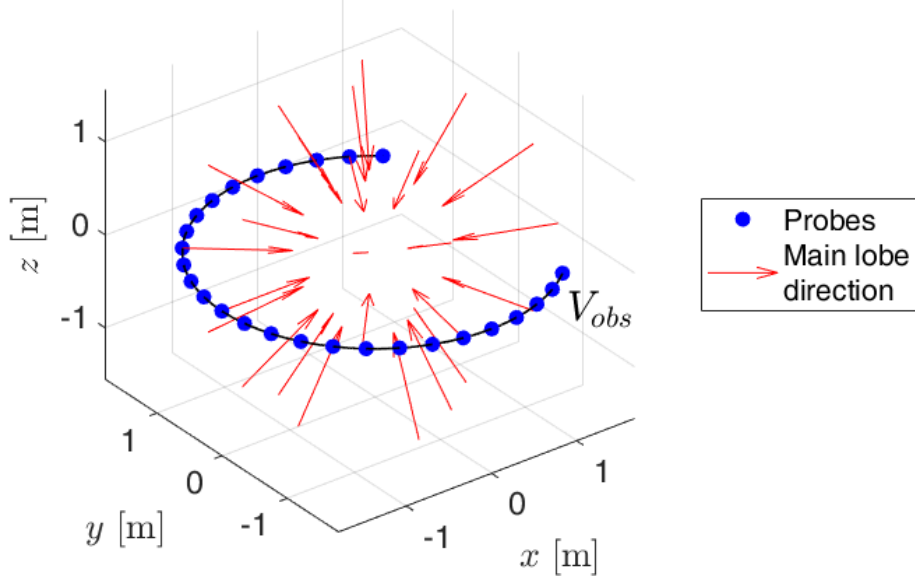


Figure 44. Illumination and measurement setup for the experimental validation of the 3D full-vector microwave imaging procedures. The red arrows symbolize the direction of the transmitting antenna's main lobe.

The stopping rules presented in the Section 4.1 are here adopted too. However, although the Morozov's generalized discrepancy principle prescribes  $\tau \geq 1$ , here  $\tau = 0.75$  is used in order to mitigate the over-regularization that the generalized discrepancy principle often causes in practice [129]. The following two different targets are considered

1. TwoSpheres. Two spheres with centers  $\mathbf{r}_{c,1} = (-2.5, 0, 0)$  cm and  $\mathbf{r}_{c,2} = (2.5, 0, 0)$  cm, radii  $R_1 = R_2 = 2.5$  cm, and relative dielectric permittivities  $\epsilon_{r,1} = \epsilon_{r,2} = 2.6$  (Figure 45). The investigation domain  $V_{inv}$  is a cube of side  $L_{V_{inv}} = 15$  cm, center in the axes origin, and partitioned in  $N = 8000$  cubic voxels.
2. TwoCubes. Two cubes with centers  $\mathbf{r}_{c,1} = (1.25, -1.25, 3.75)$  cm and  $\mathbf{r}_{c,2} = (-1.25, 1.25, 6.25)$  cm, sides  $L_1 = L_2 = 2.5$  cm, and relative dielectric permittivities  $\epsilon_{r,1} = \epsilon_{r,2} = 2.35$  (Figure 46). The investigation volume  $V_{inv}$  is a cube of side  $L_{V_{inv}} = 15$  cm, centered at  $(0, 0, 5)$  cm, and partitioned in  $N = 8000$  cubic voxels.

The behaviors of the resulting error metrics defined in (86) versus the norm parameter  $p$  for both the TwoSpheres and TwoCubes targets are given in Figure 47. As it already happened with synthetic data, also here small values of the norm parameter  $p$  allow to obtain significantly better results than the standard Hilbert-space inversion approach. The distributions of the relative dielectric permittivity reconstructed with the NMSE-optimal

norm parameter  $p_{opt} = 1.2$  and  $p = 2$  (Hilbert space case) for both targets visually support this assertion (Figure 48-51).

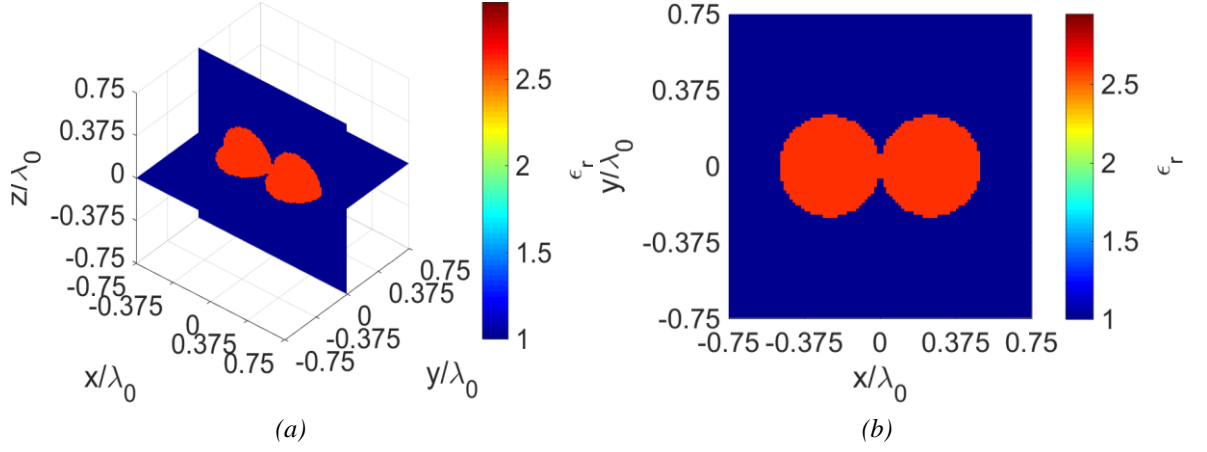


Figure 45. Actual distribution of the relative dielectric permittivity. (a) Three-dimensional view; (b)  $x - y$  cut ( $z = 0$ ). TwoSpheres target.

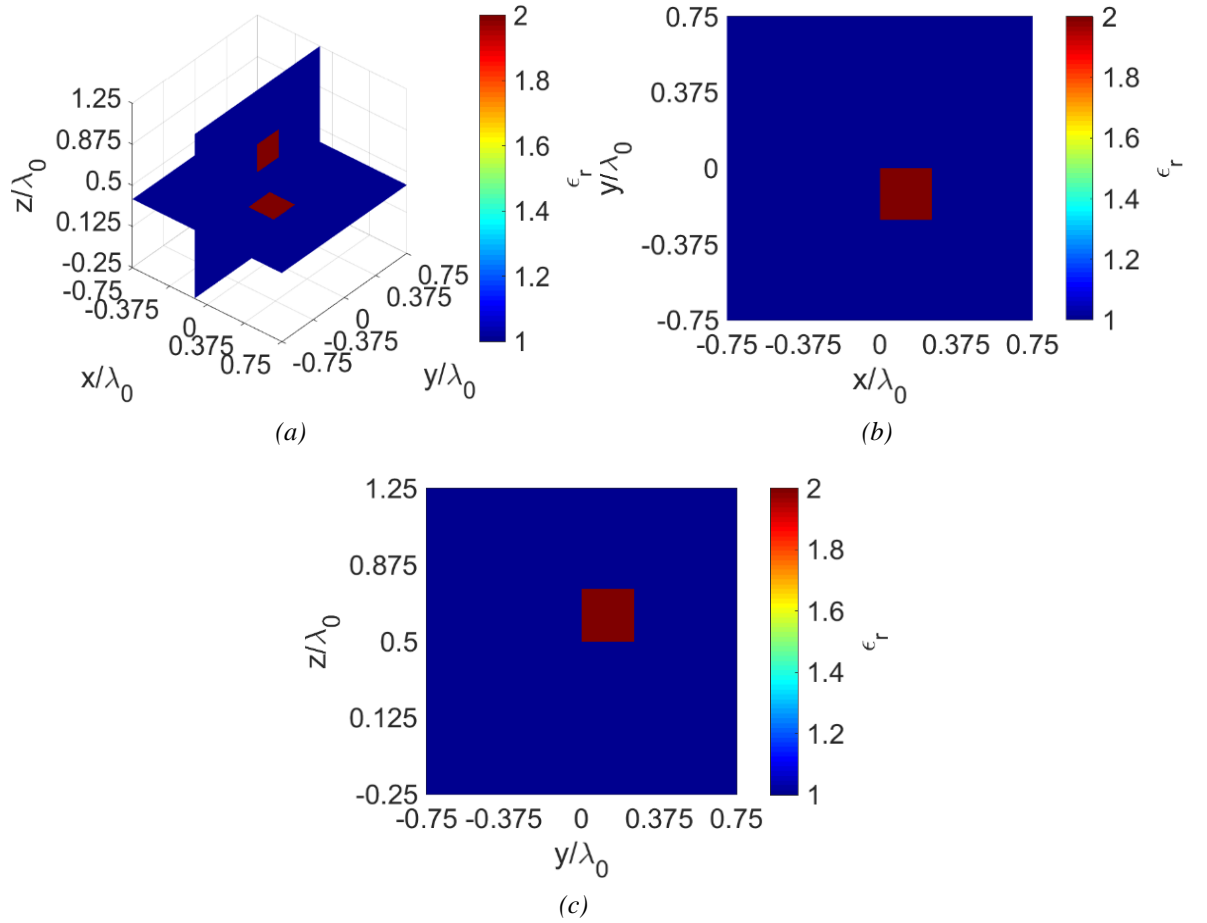


Figure 46. Actual distribution of the relative dielectric permittivity. (a) Three-dimensional view; (b)  $x - y$  cut ( $z = 0.375\lambda_0$ ); (c)  $y - z$  cut ( $x = -0.125\lambda_0$ ). TwoCubes target.

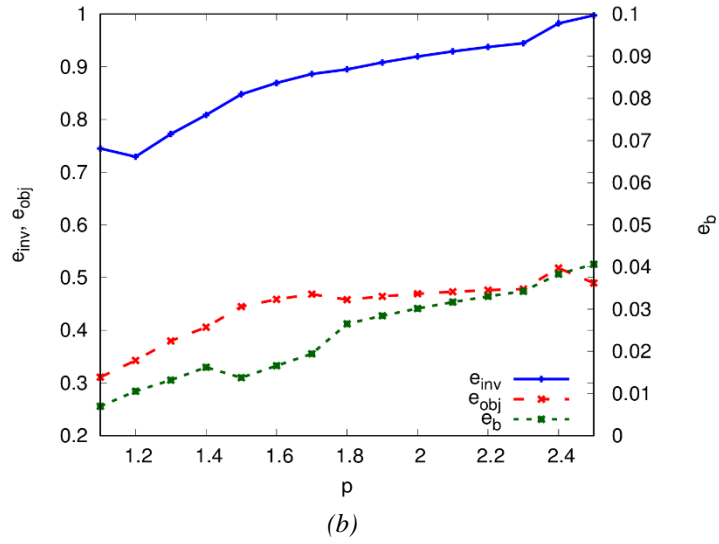
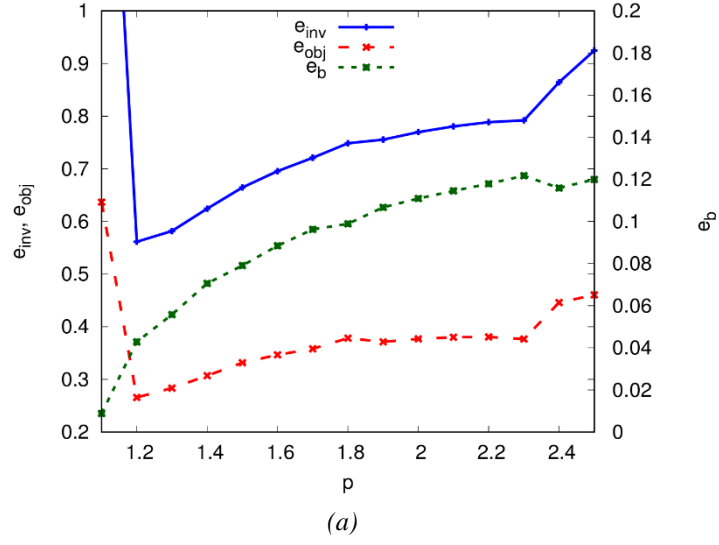


Figure 47. Behavior of  $e_{inv}$ ,  $e_{obj}$ , and  $e_b$  versus the norm parameter  $p$ . (a) TwoSpheres and (b) TwoCubes targets.

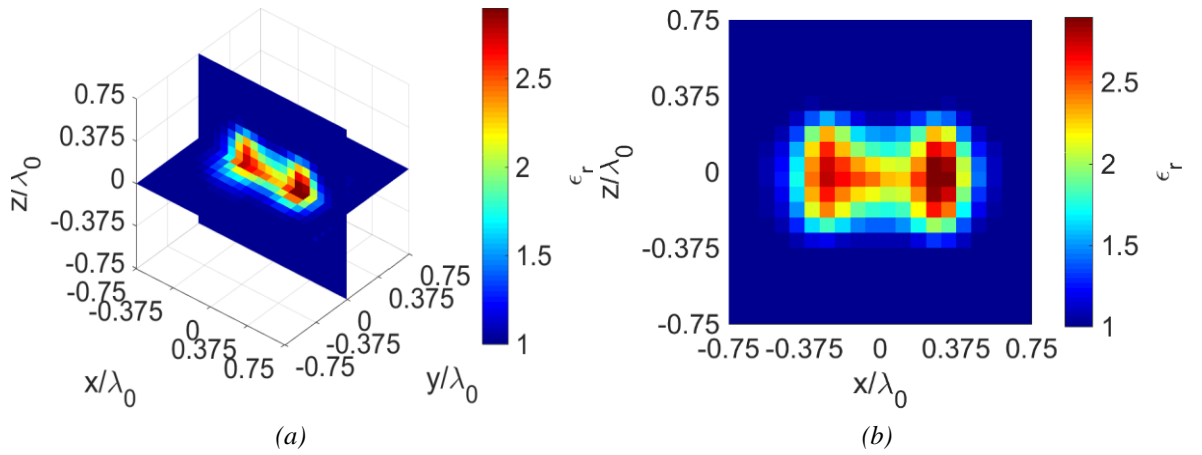


Figure 48. Reconstructed distribution of the dielectric permittivity with  $p = p_{opt} = 1.2$ . (a) Three-dimensional view; (b)  $x - z$  cut ( $y = 0$ ). TwoSpheres target.



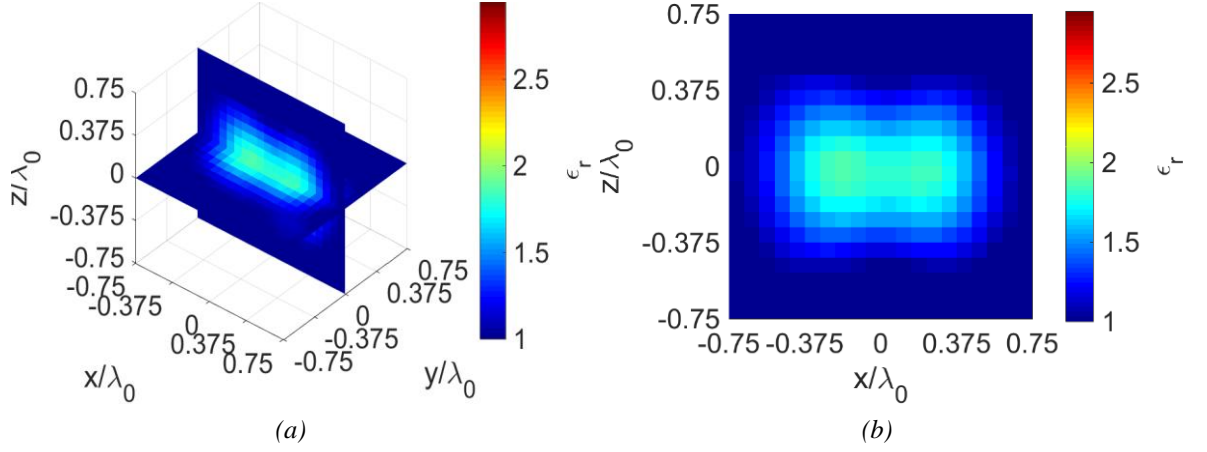


Figure 49. Reconstructed distribution of the dielectric permittivity with  $p = 2$  (Hilbert space approach). (a) Three-dimensional view; (b)  $x - z$  cut ( $y = 0$ ). TwoSpheres target.

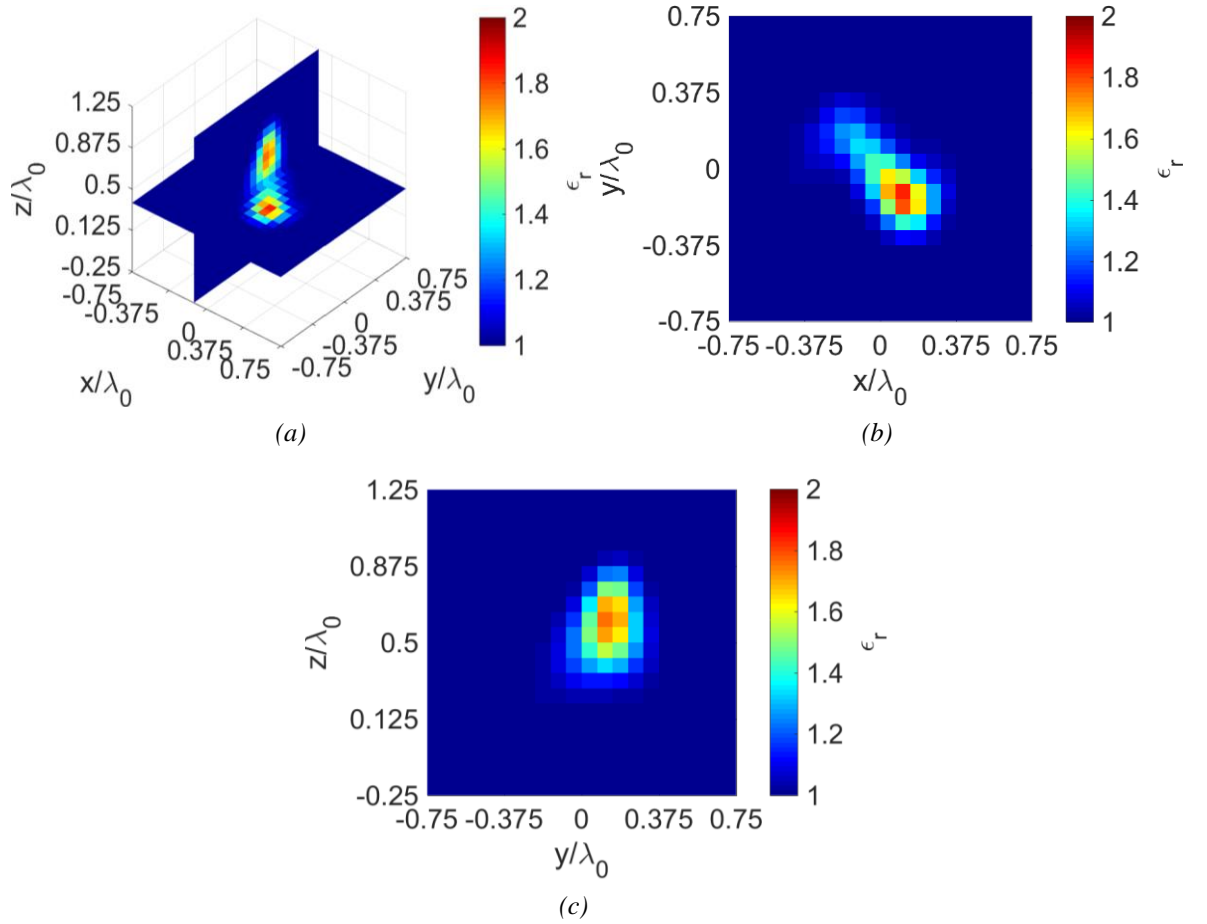


Figure 50. Reconstructed distribution of the dielectric permittivity with  $p = p_{\text{opt}} = 1.2$ . (a) Three-dimensional view; (b)  $x - y$  cut ( $z = 0.375\lambda_0$ ); (c)  $y - z$  cut ( $x = -0.125\lambda_0$ ). TwoCubes target.

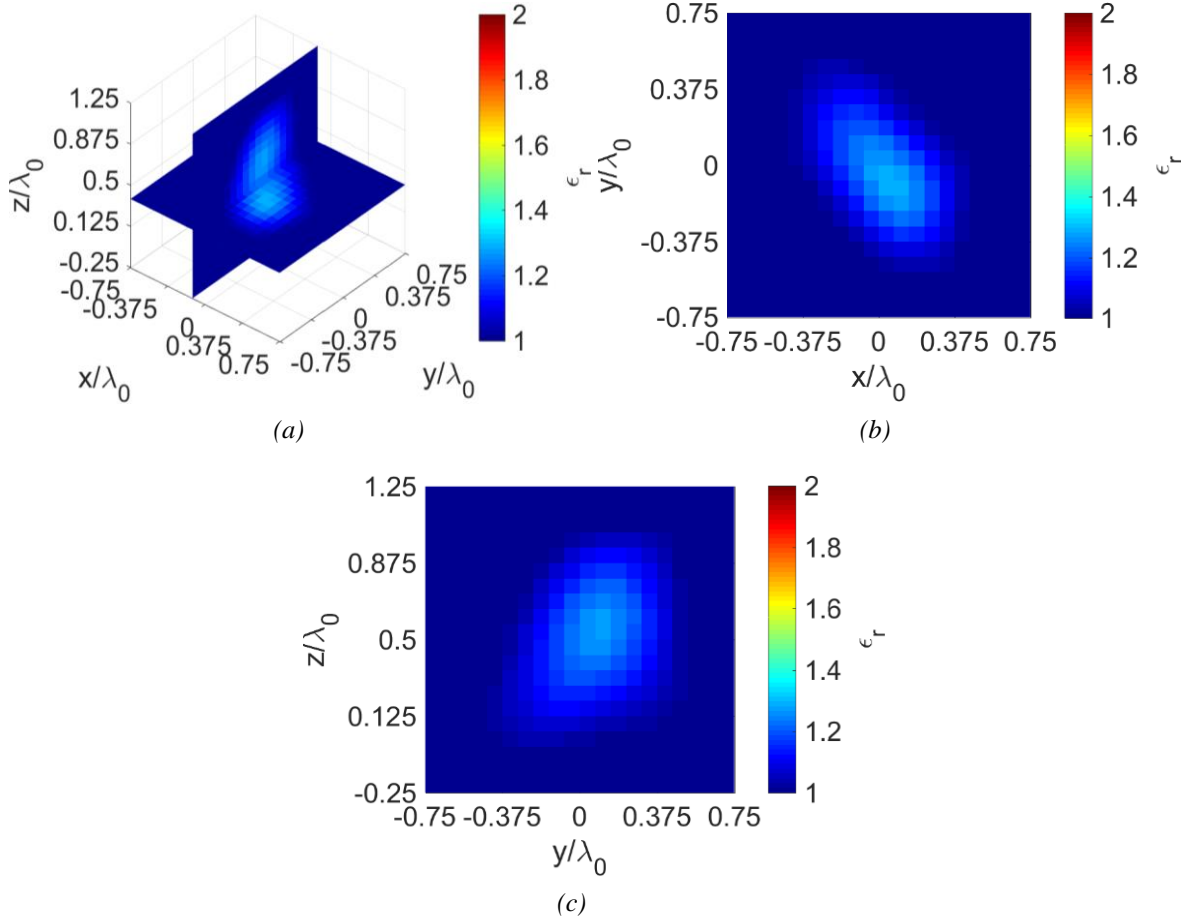


Figure 51. Reconstructed distribution of the dielectric permittivity with  $p = 2$  (Hilbert space approach). (a) Three-dimensional view; (b)  $x - y$  cut ( $z = 0.375\lambda_0$ ); (c)  $y - z$  cut ( $x = -0.125\lambda_0$ ). TwoCubes target.

The standard Hilbert-space inversion method produces smoothed images, where the separation between the two objects is not clear. On the contrary, the results returned working in  $l^{1,2}$  allow to clearly identify the two different objects.

#### 4.4 Experimental Validation: Conjugate Gradient-based Method

In this Section, the inexact-Newton scheme based on the conjugated gradient method is tested on the same experimental data and setup reported in Section 4.3. Moreover, the stopping rules described in Section 4.2 are here adopted, too. The resulting trends of the reconstruction errors versus the norm parameter  $p$  for both the TwoSpheres and TwoCubes targets are given in Figure 52.

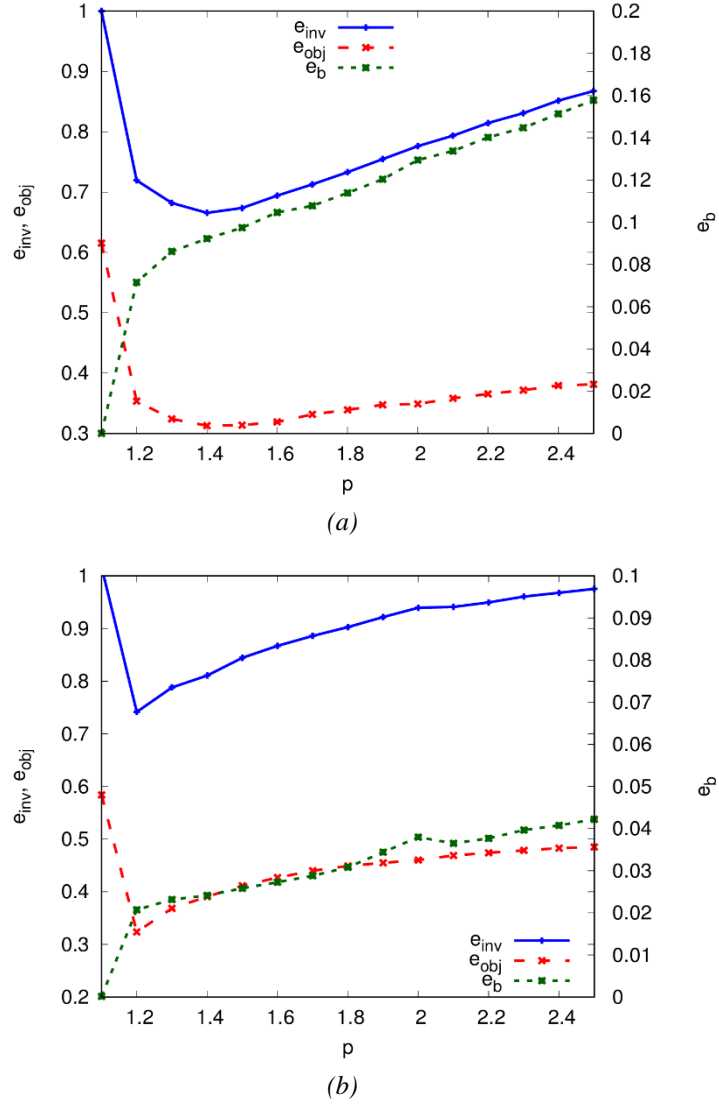


Figure 52. Behavior of  $e_{inv}$ ,  $e_{obj}$ , and  $e_b$  versus the norm parameter  $p$ . (a) TwoSpheres and (b) TwoCubes targets. Conjugate gradient-based method.

Also with the conjugate gradient method as inner linear solver, the Hilbert-space solution is the optimal one in no case; only small values of the norm parameter  $p$  result to be the best. The reconstructed distributions of the relative dielectric permittivity given by  $p_{opt} = 1.4$  and  $p_{opt} = 1.2$  for the TwoSpheres and TwoCubes targets, respectively, are shown in Figure 53 and Figure 54. The corresponding images obtained in the Hilbert-space framework are shown in Figure 55 and Figure 56. The same conclusions made for the Landweber-based approach hold here for the images returned by the conjugate gradient-based one.

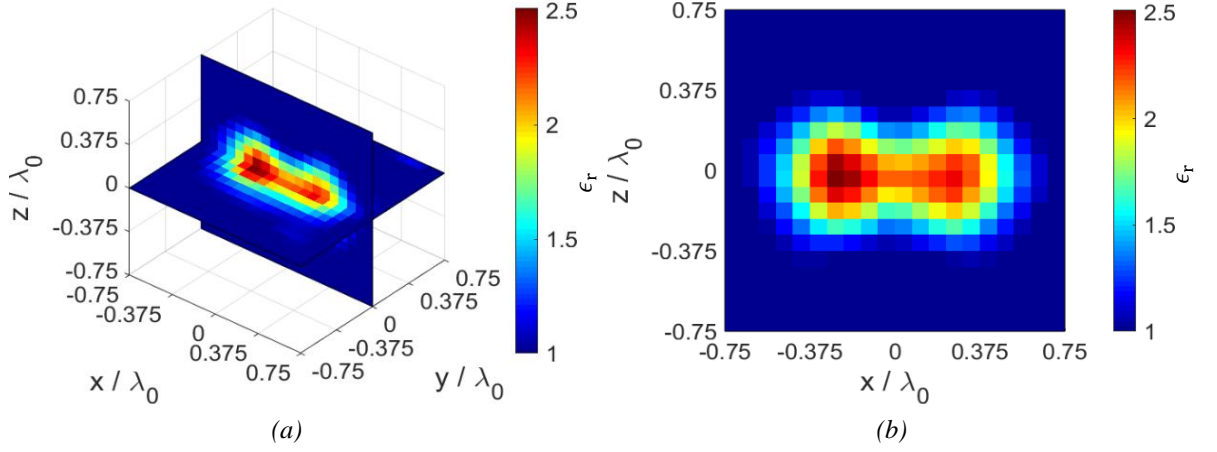


Figure 53. Reconstructed distribution of the dielectric permittivity with  $p = p_{opt} = 1.4$ . (a) Three-dimensional view; (b)  $x - z$  cut ( $y = 0$ ). TwoSpheres target. Conjugate gradient-based method.

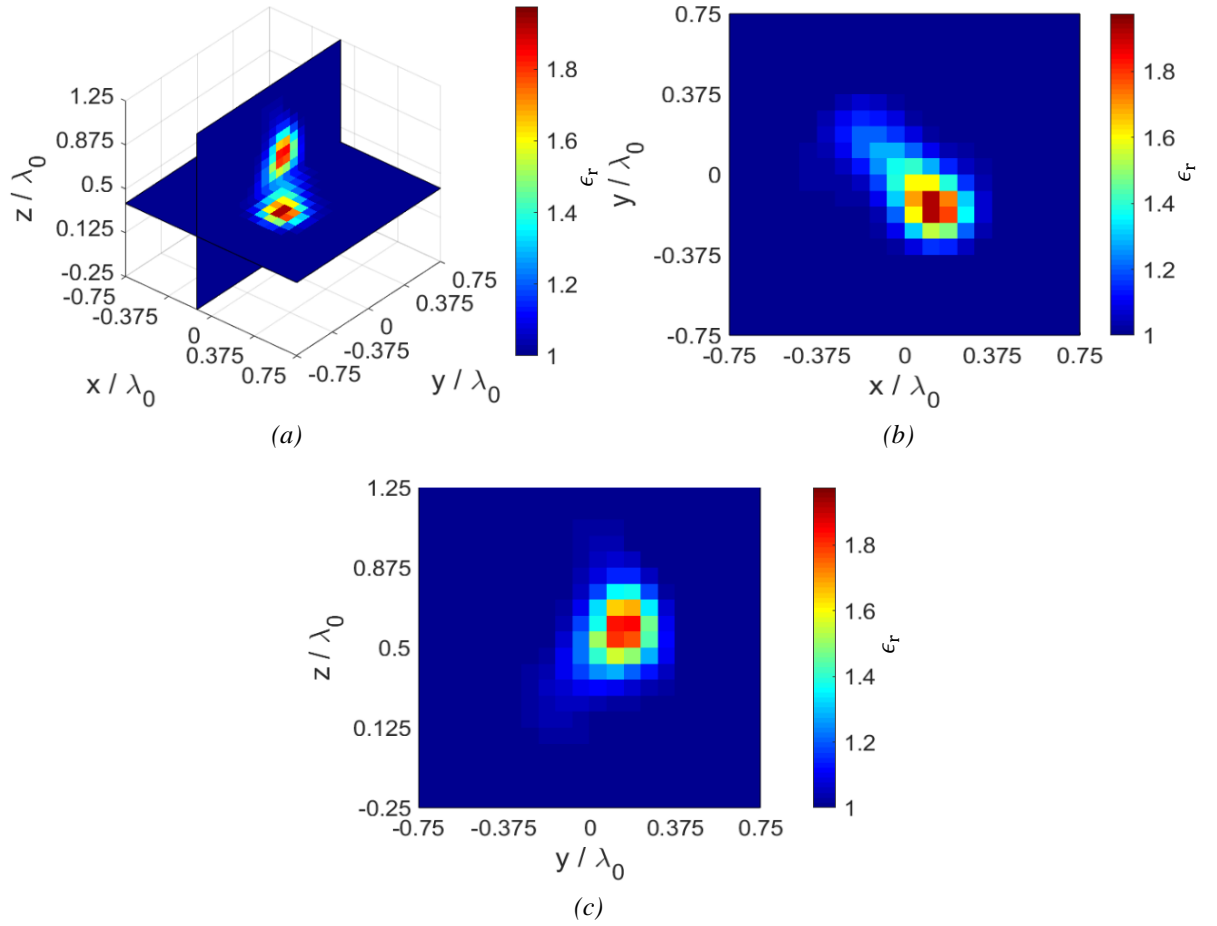


Figure 54. Reconstructed distribution of the dielectric permittivity with  $p = p_{opt} = 1.2$ . (a) Three-dimensional view; (b)  $x - y$  cut ( $z = 0.375\lambda_0$ ); (c)  $y - z$  cut ( $x = -0.125\lambda_0$ ). TwoCubes target. Conjugate gradient-based method.

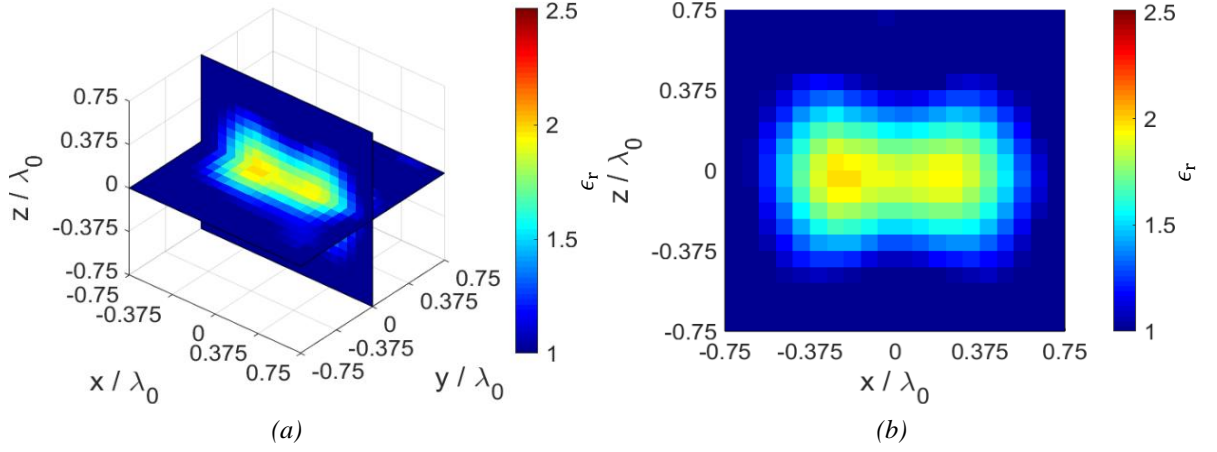


Figure 55. Reconstructed distribution of the dielectric permittivity with  $p = 2$  (Hilbert space approach). (a) Three-dimensional view; (b)  $x - z$  cut ( $y = 0$ ). TwoSpheres target. Conjugate gradient-based method.

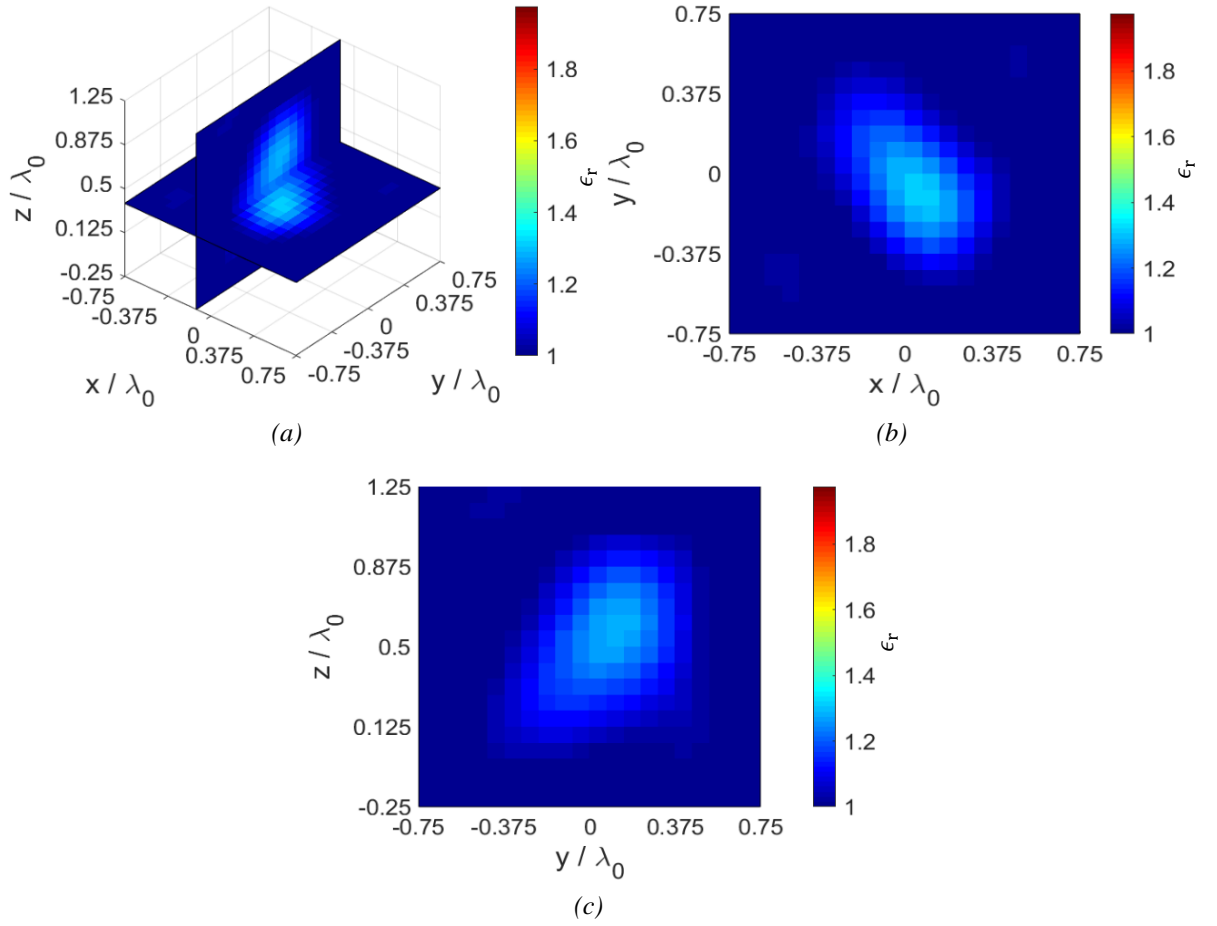


Figure 56. Reconstructed distribution of the dielectric permittivity with  $p = 2$  (Hilbert space approach). (a) Three-dimensional view; (b)  $x - y$  cut ( $z = 0.375\lambda_0$ ); (c)  $y - z$  cut ( $x = -0.125\lambda_0$ ). TwoCubes target. Conjugate gradient-based method.

## Chapter 5 Numerical and Experimental Validation: 2D Phaseless Scenario

In this Chapter a numerical and experimental validation of the inexact-Newton scheme with truncated Landweber method in  $l^p$  Banach spaces applied to the 2D phaseless setting is reported. To evaluate the reconstruction performance, the same error metrics defined in (86) are here adopted, too. Moreover, it is useful to define the following metrics for the residuals vectors

$$r_i^{PL} = \frac{\|\hat{\mathbf{p}}_{tot}^{ext} - \hat{\mathbf{F}}_P^{2D}(\mathbf{x}_i)\|_{\mathcal{D}}^2}{\|\hat{\mathbf{p}}_{tot}^{ext} - [\text{abs}(\hat{\mathbf{e}}_{inc}^{ext})]^2\|_{\mathcal{D}}^2} \quad (96)$$

$$r_{i,k}^{PL} = \frac{\|\hat{\mathbf{F}}_{P,\mathbf{x}_i}^{2D'} \mathbf{h}_k - [\hat{\mathbf{p}}_{tot}^{ext} - \hat{\mathbf{F}}_P^{2D}(\mathbf{x}_i)]\|_{\mathcal{D}}^2}{\|\hat{\mathbf{p}}_{tot}^{ext} - [\text{abs}(\hat{\mathbf{e}}_{inc}^{ext})]^2\|_{\mathcal{D}}^2} \quad (97)$$

$$r_i^{FD} = \frac{\|\hat{\mathbf{e}}_{scat}^{ext} - \hat{\mathbf{F}}^{2D}(\mathbf{c}_i)\|_{\mathcal{D}}^2}{\|\hat{\mathbf{e}}_{scat}^{ext}\|_{\mathcal{D}}^2} \quad (98)$$

where the superscripts  $PL$  and  $FD$  are referred to the phaseless and full-data inversions, respectively, and  $\text{abs}(\cdot)$  is the element-wise absolute value. For both kind of validation, the following stopping rules are used for the inversion procedure

- Outer loop. Maximum number of iterations equals to  $I = 100$  or

$$\frac{r_i^{PL} - r_{i+1}^{PL}}{r_{i+1}^{PL}} \leq \tau_I \quad (99)$$

with  $\tau_I = 0.01$  threshold on the relative outer residual variation [96].

- Inner loop. Maximum number of iterations equals to  $L = 10$  or

$$\frac{r_{i,k}^{PL} - r_{i,k+1}^{PL}}{r_{i,k+1}^{PL}} \leq \tau_L \quad (100)$$

with  $\tau_L = 0.01$  threshold on the relative inner residual variation [96].

## 5.1 Numerical Validation with Synthetic Data

The numerical validation has been performed by considering a working frequency  $f = 300$  MHz and assuming a void background. The investigation domain  $D_{inv}$  is a square of side  $L_{D_{inv}} = 1.5\lambda_0$ , whereas the observation one  $D_{obs}$  is a circumference with radius  $R_{D_{obs}} = 1.5\lambda_0$ . In order to properly sample the square amplitude of the total external electric field, the following total number of samples is needed [73]

$$SM \geq \text{ceil} \left( \max \left\{ (4k_0 R_{D_{obs}})^2, \left[ 2k_0 \left( R_{D_{obs}} + \frac{L_{D_{inv}}}{\sqrt{2}} \right) \right]^2 \right\} \right) = 1423 \quad (101)$$

where  $\text{ceil}(\cdot)$  indicates a round to the next integer and  $L_{D_{inv}}/\sqrt{2}$  is the radius of the circle that strictly encloses the investigation domain. This requirement can be satisfied by choosing  $S = 40$  sources uniformly distributed on  $D_{obs}$  and  $M = 39$  measurement points for each view. In particular, when one of the sources is active, the positions of the remaining inactive sources are occupied by the probes. The sources are unit-amplitude current lines and the incident electric field generated by each one is given by

$$\mathbf{E}_{inc,(s)}(\mathbf{r}_t) = -\frac{\omega\mu_0}{4} H_0^{(2)}(k_0 |\mathbf{r}_t - \mathbf{r}_{t,(s)}|) \hat{\mathbf{z}} \quad (102)$$

where  $\mathbf{r}_{t,(s)} = 1.5\lambda_0 \left[ \cos\left(\frac{2\pi}{S}(s-1)\right) \quad \sin\left(\frac{2\pi}{S}(s-1)\right) \right]^T$  with  $s = 1, \dots, S$ . Figure 57 shows the adopted configuration for the first view. In order to avoid inverse crimes [85], the investigation domain has been partitioned with a square-based mesh having  $N = 1600$  sub-domains for the inverse problem solution, whereas  $N_{fwd} = 5329$  has been used in the discretization adopted for computing the simulated measurements. This latter problem is solved with a numerical implementation of the MoM or, when the investigation domain contains a single circular cylinder only, by an analytical solver [101]. In order to simulate real operating conditions, an additive white Gaussian noise with zero mean and variance corresponding to a signal-to-noise ratio  $SNR = 25$  dB has been used to corrupt the full

(modulus and phase) synthetic data. In particular, the standard deviation  $\sigma_\eta$  of the additive noise is related to the  $SNR$  by [127]

$$SNR = 10 \log_{10} \left( \frac{\|\hat{\mathbf{e}}_{tot}^{ext}\|_2^2}{2SM\sigma_\eta^2} \right) \quad (103)$$

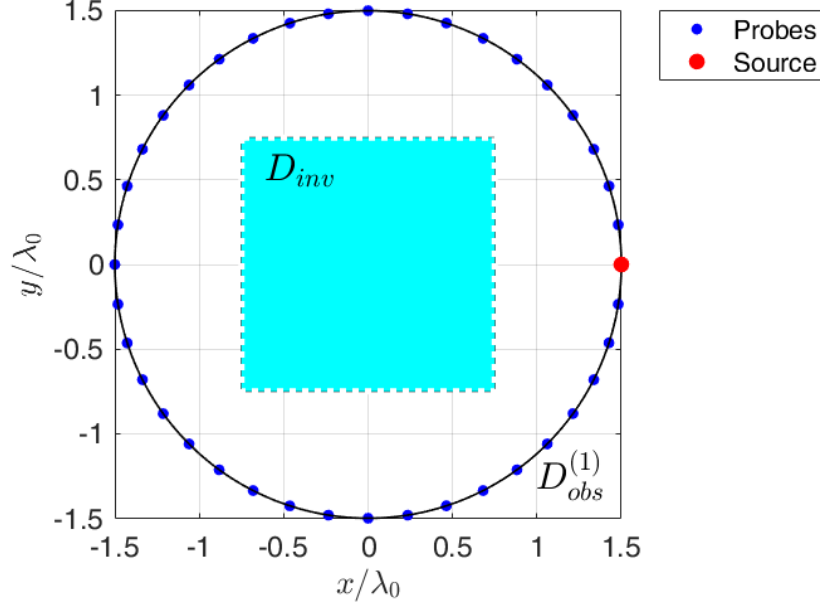


Figure 57. Illumination and measurement setup for the numerical validation of the 2D phaseless microwave imaging procedure. First view.

### 5.1.1 Reconstruction capabilities versus the scatterer dimension

Firstly, the reconstruction capabilities of the developed approach have been evaluated by considering a dielectric circular cylinder with center  $\mathbf{r}_c = (0.1, 0.1)\lambda_0$  and relative dielectric permittivity  $\epsilon_r = 2$ . Its diameter  $D$  has been varied in the range  $[0.2, 0.6]\lambda_0$ . Figure 58 shows the behaviors of the reconstruction errors defined in (86) versus the norm parameter  $p$  and the cylinder's diameter. The Banach-space approach allows in all cases to obtain reconstructions characterized by lower errors with respect to the standard Hilbert-space method (corresponding to  $p = 2$ ). In particular, the best values of  $p$  are in the range  $[1.2, 1.6]$ .



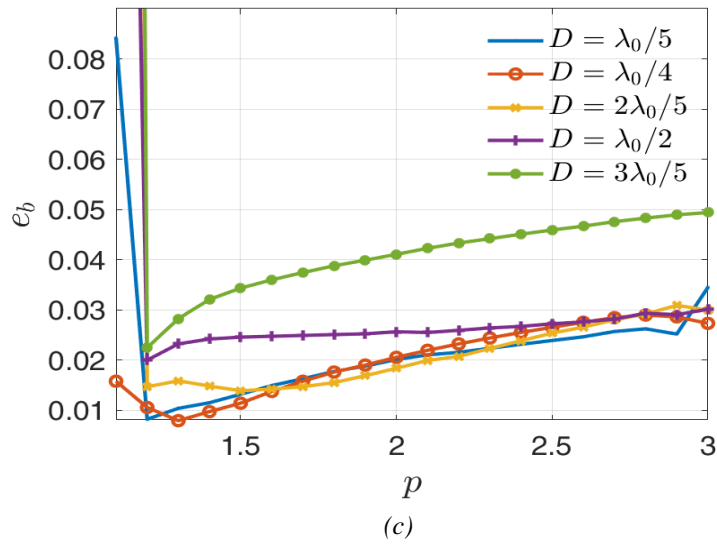
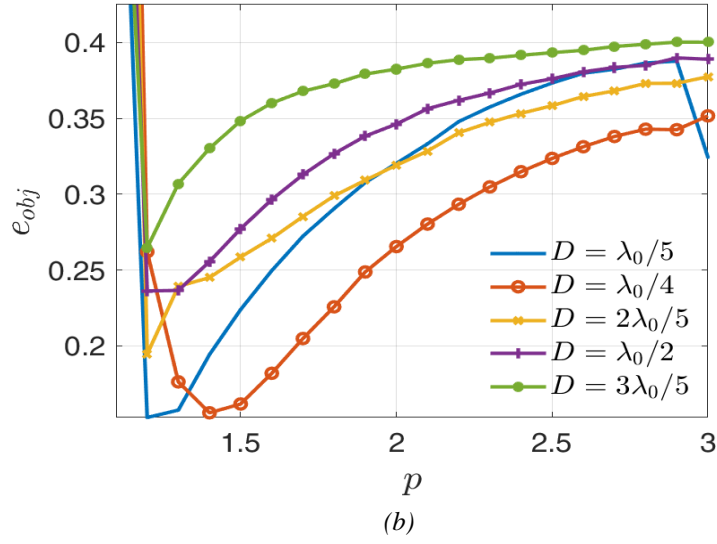
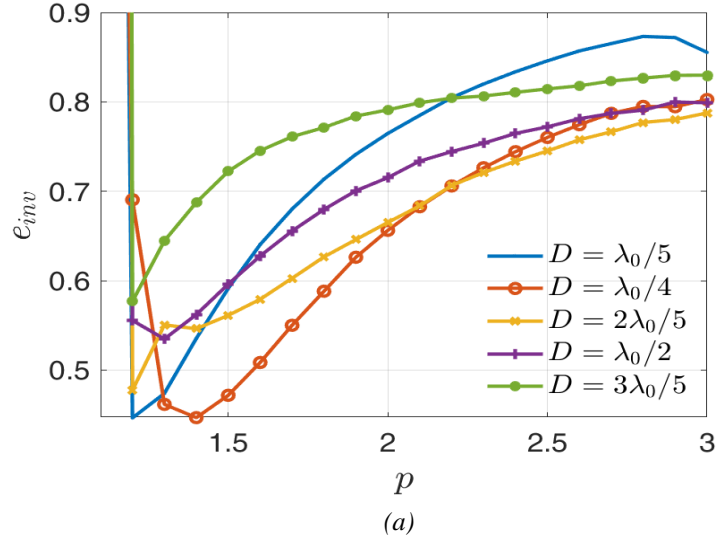


Figure 58. Behavior of (a)  $e_{inv}$ , (b)  $e_{obj}$ , and (c)  $e_b$  versus the norm parameter  $p$  and for different values of the diameter  $D$ . Single circular cylinder.

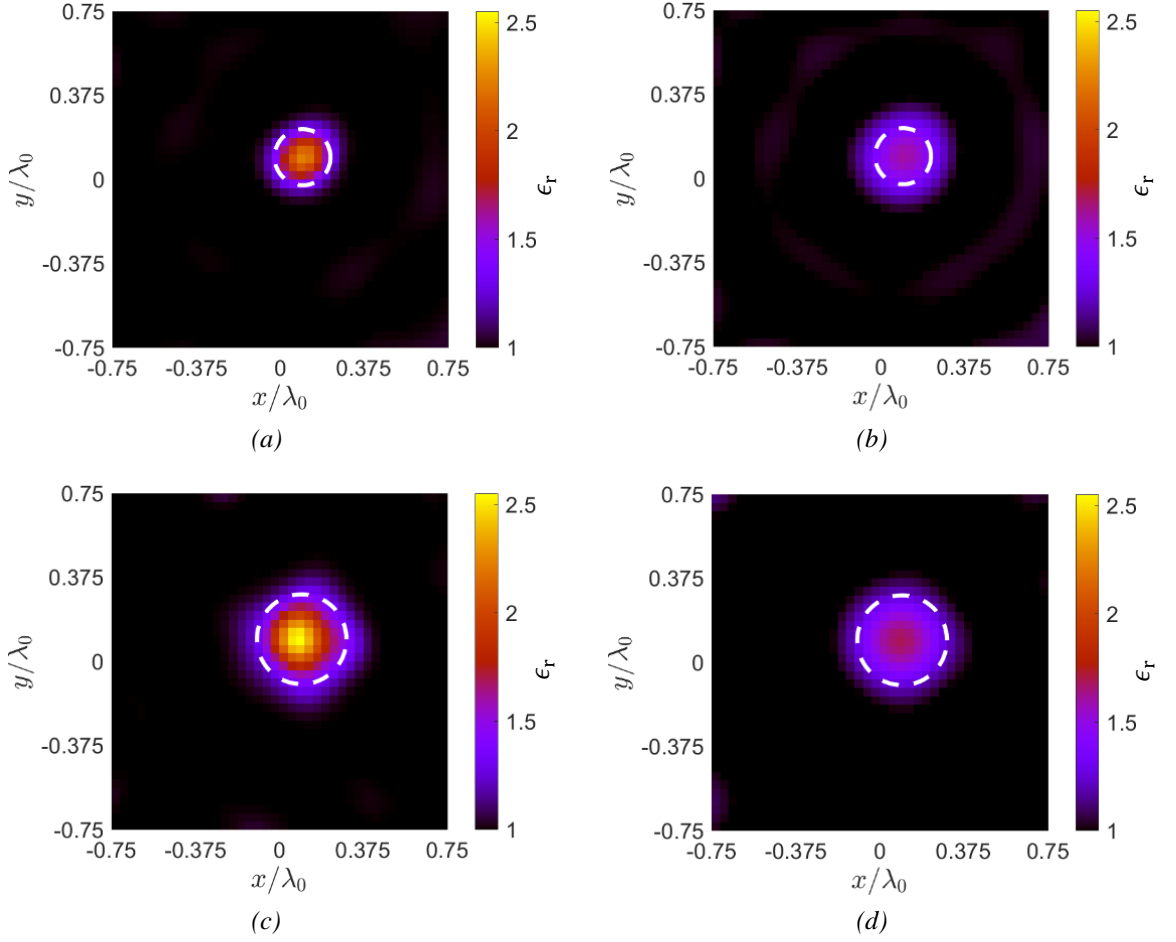


Figure 59. Reconstructed distribution of the dielectric permittivity for the single cylinder. (a)  $p_{opt} = 1.4$ ,  $D = 0.25\lambda_0$ ; (b)  $p = 2$ ,  $D = 0.25\lambda_0$ ; (c)  $p_{opt} = 1.2$ ,  $D = 0.4\lambda_0$ ; (d)  $p = 2$ ,  $D = 0.4\lambda_0$ . The white dashed circles indicate the actual profiles.

This is also visually supported by the images in Figure 59, which shows the reconstructed distributions of the relative dielectric permittivity corresponding to  $D = 0.25\lambda_0$  and  $D = 0.4\lambda_0$  for  $p_{opt} = 1.4$  and  $p_{opt} = 1.2$ , respectively, together with the corresponding Hilbert-space solutions. The proposed approach is able to properly detect the contour of the cylinder and its relative dielectric permittivity is averagely well estimated (only few pixels in the center of the cylinder having  $D = 0.4\lambda_0$  are overestimated). On the other hand, the classic inexact-Newton suffers of a significant underestimation of the dielectric permittivity, and a slight ringing effect is visible around the cylinder in the reconstruction for  $D = 0.25\lambda_0$ . To better see these drawbacks, slices at  $y = 0.1\lambda_0$  of Figure 59(a), Figure 59(b), and the actual profile are shown in Figure 60; in such figure,  $\langle \tilde{\epsilon}_r \rangle_a$  is the reconstructed relative dielectric permittivity averaged over the cylinder's profile.

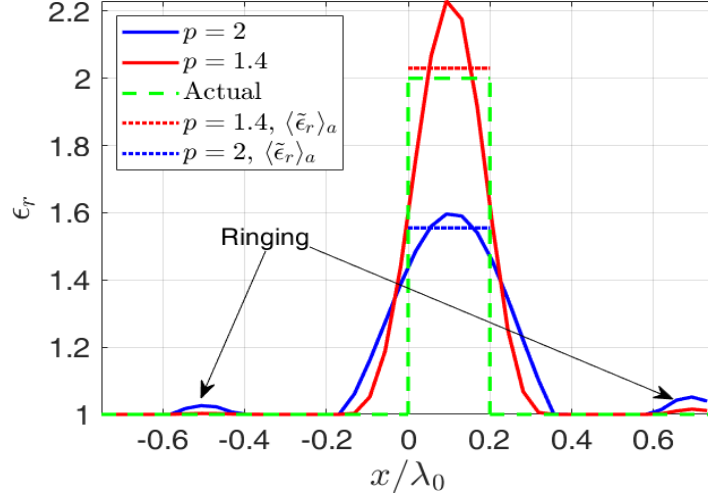


Figure 60. Slices at  $y = 0.1\lambda_0$  of Figure 59(a), Figure 59(b), and the actual profile.

### 5.1.2 Reconstruction capabilities versus the scatterer density

In this Section, the cylinder given in Section 5.1.1 with fixed diameter  $D = \lambda_0/4$  is considered and its relative dielectric permittivity is varied in the range  $[2,4]$  to evaluate the behavior of the proposed method on this variation. Figure 61 shows the behaviors of the reconstruction errors versus the norm parameter  $p$  and the cylinder's dielectric permittivity. The three plots exhibit essentially the same trends, that is the errors reach their minima in the interval  $(1,1.5)$  and then rapidly grow as  $p$  increases. It is interesting to compare the phaseless and full-data performance. In particular, Figure 62 illustrates the best NMSE values achieved by the phaseless and full-data approaches versus  $\epsilon_r$ . As can be seen, comparable errors are obtained. Moreover, the estimated relative dielectric permittivity distributions for  $\epsilon_r = 4$  with  $p = p_{opt} = 1.2$  (phaseless data) and  $p_{opt} = 1.3$  (full-data) are shown in Figure 63. For completeness, the result obtained with  $p = 2$  in the phaseless case is also provided. As expected, the full-data imaging performs better than its phaseless counterpart, and, with focus on the cases in Figure 63, this last suffers of erroneous estimation of the dielectric properties. However, cylinder's boundaries are still clearly visible for  $p = p_{opt}$  and phaseless measurements.

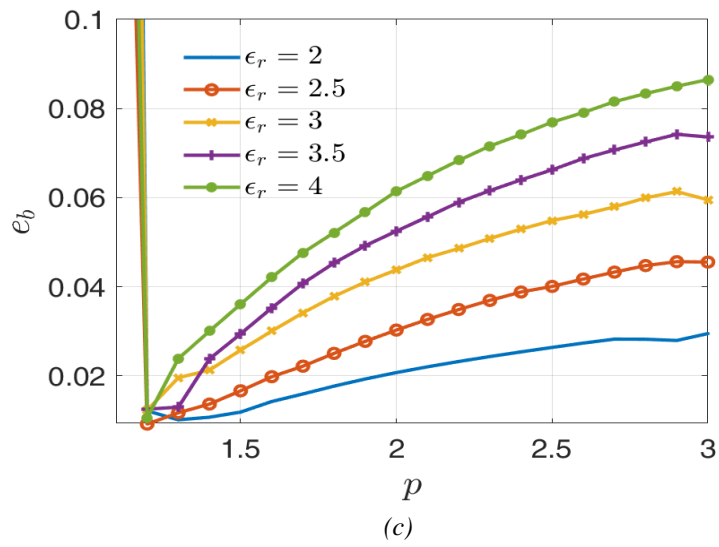
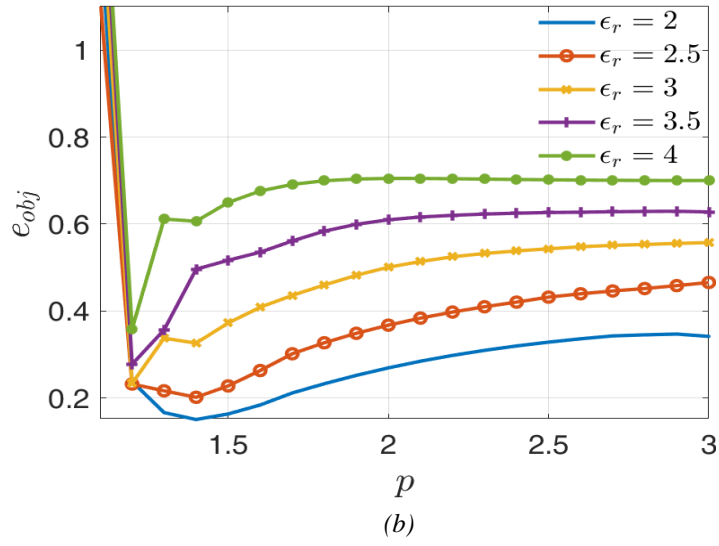
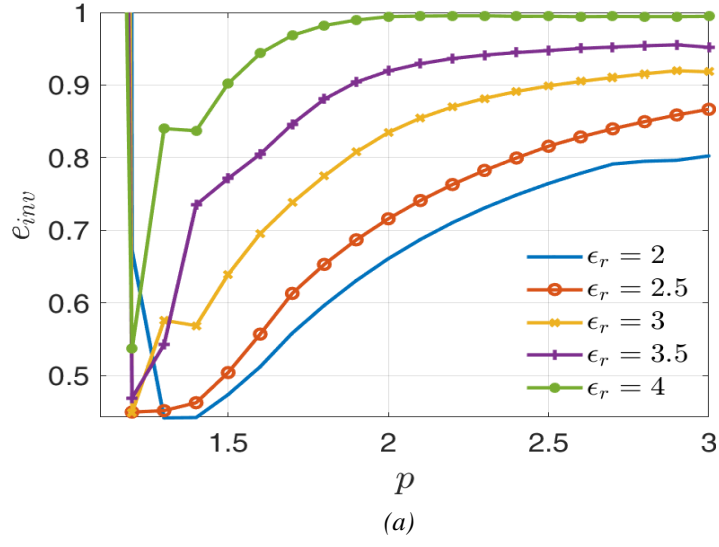


Figure 61. Behavior of (a)  $e_{inv}$ , (b)  $e_{obj}$ , and (c)  $e_b$  versus the norm parameter  $p$  and for different values of the relative dielectric permittivity  $\epsilon_r$ . Single circular cylinder.

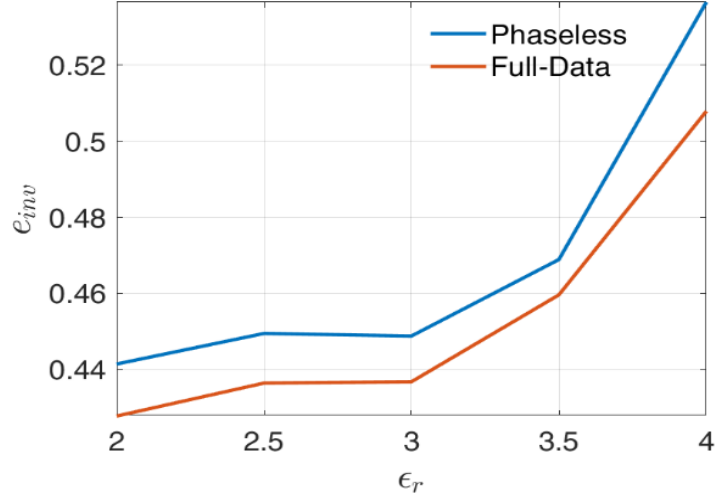


Figure 62. Best  $e_{inv}$  versus  $\epsilon_r$  for both phaseless and full-data inversions. Single circular cylinder.

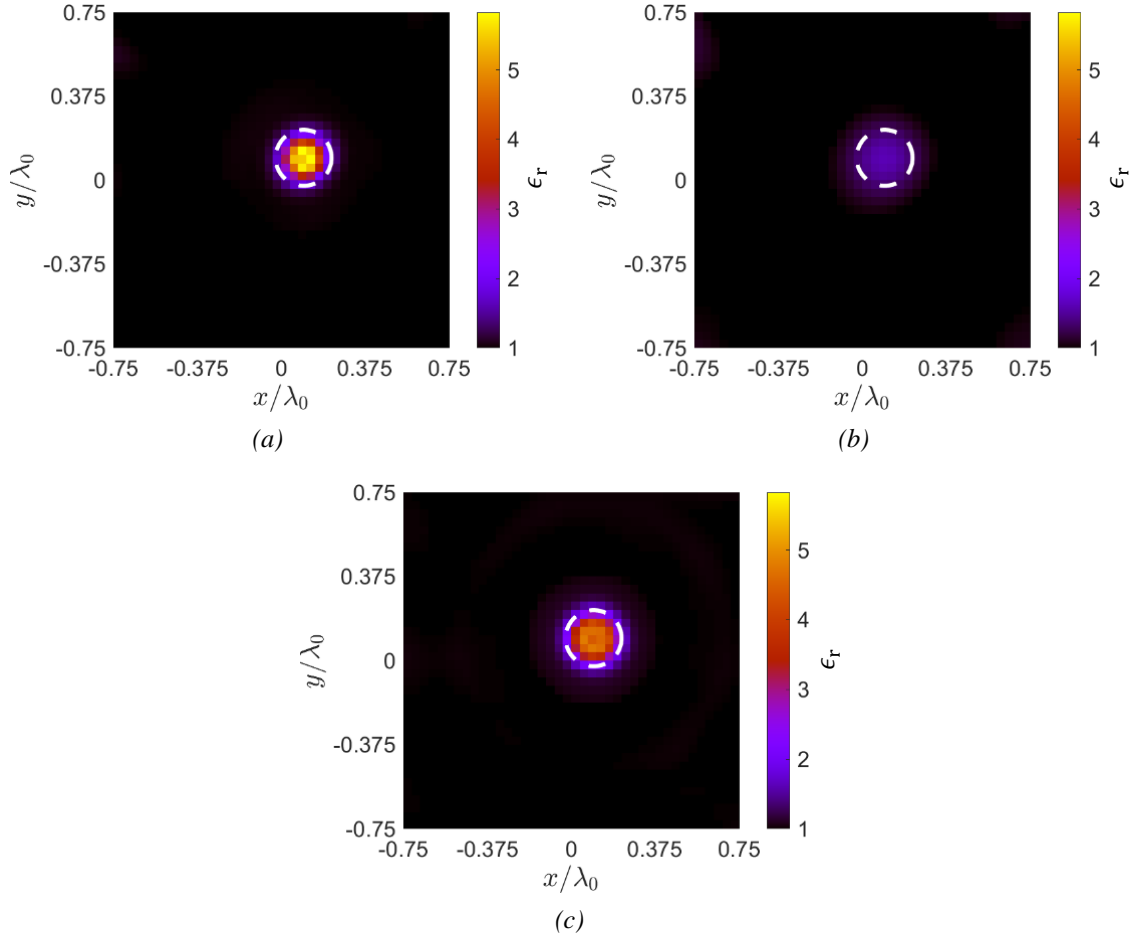


Figure 63. Reconstructed distribution of the dielectric permittivity for the single cylinder with  $\epsilon_r = 4$ . (a)  $p_{opt} = 1.2$ , phaseless; (b)  $p = 2$ , phaseless; (c)  $p_{opt} = 1.3$ , full-data. The white dashed circles indicate the actual profiles.

### 5.1.3 Reconstruction capabilities versus the signal-to-noise ratio

The noise rejection capability of the developed microwave imaging algorithm is here tested by varying the intensity of the additive white Gaussian noise whereby the simulated measurements are corrupted. In particular, the signal-to-noise ratio  $SNR$  is varied in the range  $[5, 25]$  dB. The considered target is a circular cylinder with center  $\mathbf{r}_c = (0.1, 0.1)\lambda_0$ , diameter  $D = \lambda_0/4$ , and relative dielectric permittivity  $\epsilon_r = 2$ . Table 8 reports the values of the error metrics defined in (86) and the final number of outer iterations  $i_f$  for each of the simulated  $SNR$  in correspondence of  $p = p_{opt}$ . For comparison, the same data are reported for the Hilbert-space case too.

Table 8. Reconstruction errors and final number of outer iterations  $i_f$  versus  $SNR$  in correspondence of  $p = p_{opt}$  and  $p = 2$  (Hilbert space approach).

$SNR$ [dB]	$p_{opt}$					$l^2$ (Hilbert)			
	$p_{opt}$	$e_{inv}$	$e_{obj}$	$e_b$	$i_f$	$e_{inv}$	$e_{obj}$	$e_b$	$i_f$
5	1.4	0.73	0.26	0.02	2	0.87	0.33	0.05	3
10	1.2	0.60	0.24	0.01	3	0.79	0.36	0.03	2
15	1.4	0.53	0.19	0.02	3	0.73	0.31	0.03	3
20	1.3	0.48	0.17	0.01	3	0.71	0.30	0.03	3
25	1.4	0.43	0.15	0.01	4	0.65	0.26	0.02	3

We see that a proper selection of the norm parameter allows to obtain better noise rejection capabilities with respect to the classic inexact-Newton approach. Figure 64 shows a comparison between the NMSE achieved by the phaseless algorithm and the ones obtained by inverting full-data synthetic measurements (considering the optimal value of the parameter  $p$ ). Moreover, the estimated relative dielectric permittivity distributions for  $SNR = 15$  dB in the phaseless case with  $p_{opt} = 1.4$  and  $p = 2$  (Hilbert-space) are plotted in Figure 65. For comparison purposes, the result obtained with the full-data and  $p_{opt} = 1.3$  is also shown. As expected, we see from Figure 64 that the full-data approach provides better NMSE values. However, as can be noticed from Figure 65, in a rather noisy environment the phaseless technique with  $p_{opt}$  is able to maintain a reconstruction quality comparable to the full-data setting, as opposed to the classic Hilbert space-based procedure that presents a significant underestimation of the dielectric permittivity and several artefacts in the background. These assertions are also supported by the plots cuts along the line  $x = 0.1\lambda_0$  shown in Figure 66.

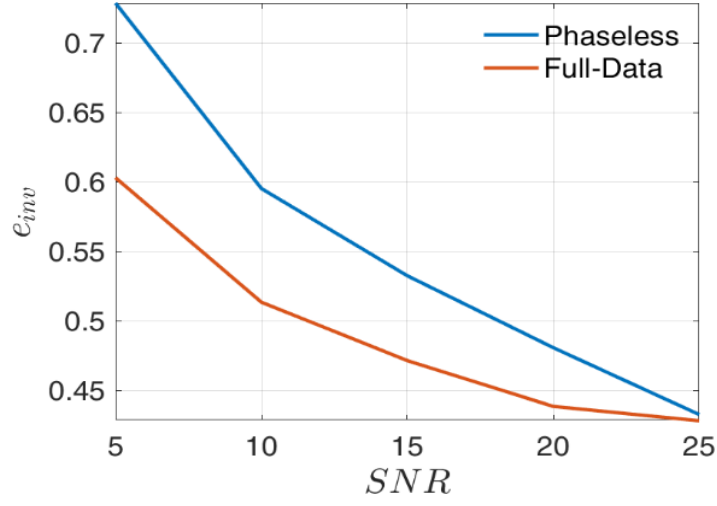


Figure 64. Best  $e_{inv}$  versus SNR for both phaseless and full-data inversions.

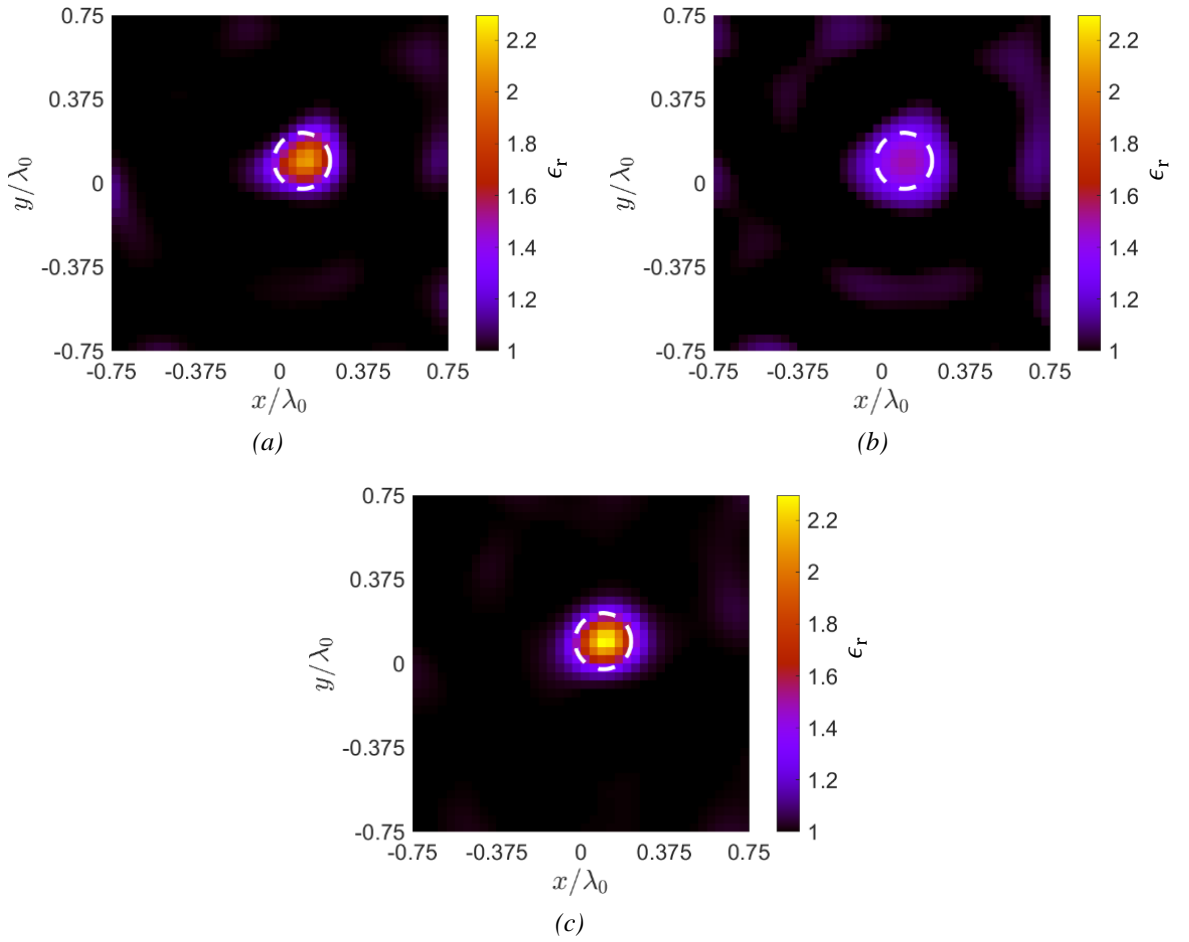


Figure 65. Reconstructed distribution of the dielectric permittivity for SNR = 15 dB. (a)  $p_{opt} = 1.4$ , phaseless; (b)  $p = 2$ , phaseless; (c)  $p_{opt} = 1.3$ , full-data. The white dashed circles indicate the actual profiles.

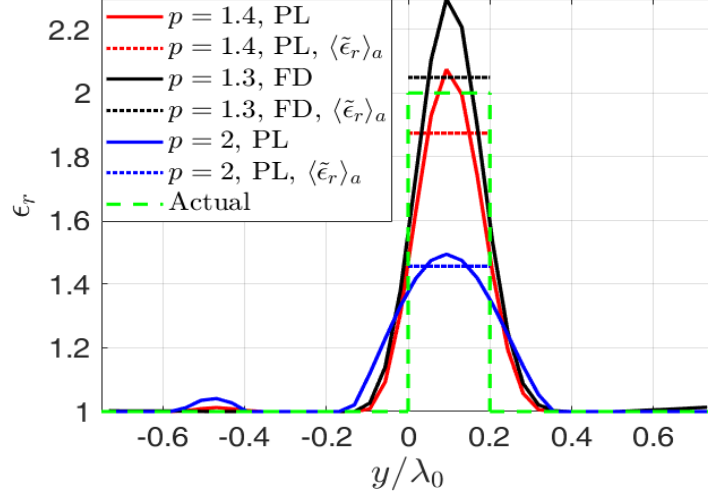


Figure 66. Slices at  $x = 0.1\lambda_0$  of Figure 65(a)-(c), and the actual profile.

#### 5.1.4 Reconstruction capabilities versus the outer stopping threshold

In this Section, the influence of the outer stopping criteria on the reconstruction performance is assessed. To this end, the outer stopping threshold on the relative residuals variation  $\tau_I$  has been varied in the range  $[10^{-4}, 10^{-2}]$ . The investigation domain contains the same cylindrical target used in Section 5.1.3, and  $SNR = 15$  dB. Figure 67 shows the trends of the resulting optimal NMSE values versus  $\tau_I$  for both the phaseless and full-data inversions.

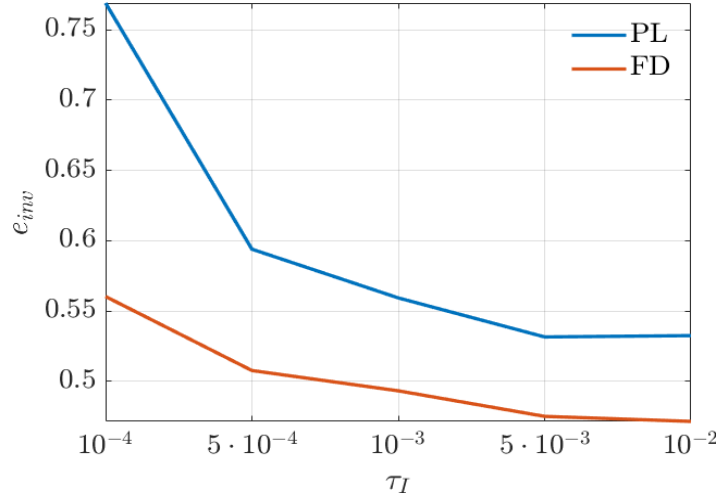


Figure 67. Behavior of  $e_{inv}$  versus  $\tau_I$  for both the phaseless and full-data inversions.

We can see that small values of  $\tau_I$  produce higher errors. Figure 68 and Figure 69 show how this happens; in particular, the first image reports the behaviors of  $r_i^{PL}$  and  $e_{inv}$  versus the



iteration number when  $\tau_I = 10^{-4}$  and  $p_{opt} = 1.5$ , whereas the second one concerns  $\tau_I = 10^{-2}$  (this is the reference value adopted in this Chapter) and  $p_{opt} = 1.4$ .

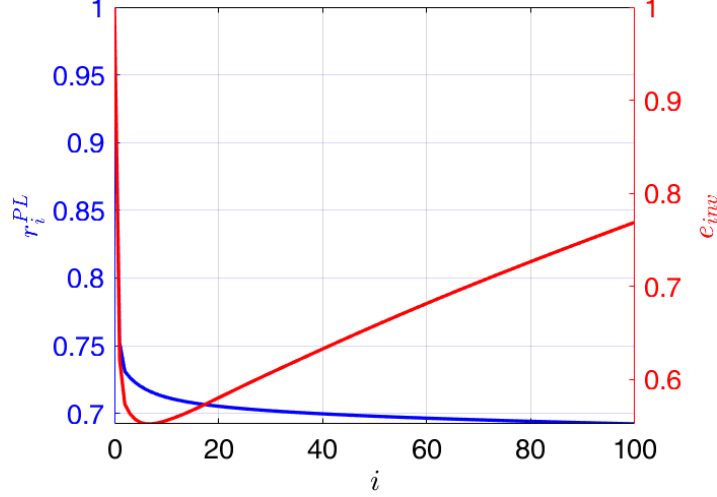


Figure 68. Behavior of  $r_i^{PL}$  and  $e_{inv}$  versus the iteration number when  $\tau_I = 10^{-4}$  and  $p_{opt} = 1.5$ .

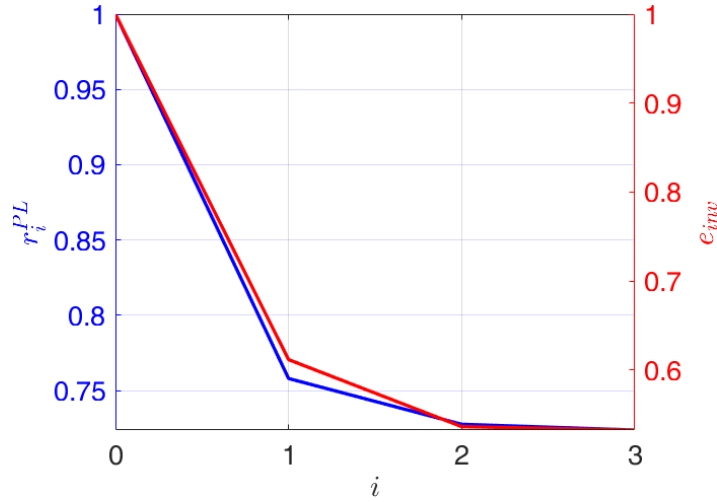


Figure 69. Behavior of  $r_i^{PL}$  and  $e_{inv}$  versus the iteration number when  $\tau_I = 10^{-2}$  and  $p_{opt} = 1.4$ .

In Figure 68, although the residual decreases in each iteration, the NMSE grows significantly after the achievement of a minimum. This is a typical property of the iterative methods in presence of noisy data and it is known as semiconvergence [86]; its degrading effect on the reconstruction quality is caused by a delayed stopping of the method. In this particular case, the low threshold  $\tau_I$  causes the improper stopping. On the other hand, in Figure 69 the higher  $\tau_I$  limits the semiconvergence effects, since it causes the outer loop to be stopped before that the NMSE started to increase significantly. However, as expected, Figure 67 shows that the

phaseless inversion is more seriously affected by the degrading effect of the semiconvergence than the full-data one.

### 5.1.5 Reconstruction capabilities in case of lossy scatterer

The circular cylinder used as target in Section 5.1.3 is endowed here with a non-null electric conductivity  $\sigma$ , which has been varied in the range  $[10^{-4}, 10^{-2}]$  S/m. The resulting NMSE, relative mean errors and final number of outer iterations  $i_f$  are reported in Table 9 for several values of  $\sigma$  (for the values of the norm parameter providing the minimum NMSE). The same data are reported for the  $l^2$  case too.

Table 9. Reconstruction errors and final number of outer iterations  $i_f$  versus  $\sigma$  in correspondence of  $p = p_{opt}$  and  $p = 2$  (Hilbert space approach).

$\sigma$ [S/m]	$l^{p_{opt}}$					$l^2$ (Hilbert)			
	$p_{opt}$	$e_{inv}$	$e_{obj}$	$e_b$	$i_f$	$e_{inv}$	$e_{obj}$	$e_b$	$i_f$
$10^{-4}$	1.4	0.44	0.16	0.01	3	0.66	0.27	0.02	3
$5 \cdot 10^{-4}$	1.4	0.44	0.16	0.01	3	0.66	0.27	0.02	3
$10^{-3}$	1.3	0.44	0.17	0.01	4	0.67	0.27	0.02	3
$5 \cdot 10^{-3}$	1.3	0.42	0.16	0.01	4	0.70	0.31	0.02	3
$10^{-2}$	1.3	0.41	0.15	0.01	4	0.71	0.35	0.02	3

For  $\sigma = 10^{-2}$  S/m, the reconstructed distributions of the relative dielectric permittivity's real part and of the electric conductivity provided by the phaseless approach in the cases of  $p = p_{opt} = 1.3$  and  $p = 2$  are shown in Figure 70. Moreover, the results obtained by considering the full complex data are also provided. We can see that the classic phaseless approach (i.e., with  $p = 2$ ) suffers of a significant ringing in the reconstructed electric conductivity and of an underestimation of the relative dielectric permittivity's real part. Such effects are mitigated with  $p_{opt} = 1.3$ . To better compare the quality of the images reported in Figure 70, cuts along the line  $x = 0.1\lambda_0$  are shown in Figure 71; in such figure,  $\langle \tilde{\epsilon}'_r \rangle_a$  and  $\langle \tilde{\sigma} \rangle_a$  are the reconstructed relative dielectric permittivity's real part and electric conductivity averaged over the cylinder's profile, respectively.

### 5.1.6 Reconstruction capabilities versus the amount of data

The reconstruction performance has been evaluated here against a variable amount of available data. In particular, the number of views  $S$  has been varied in the range  $[10, 40]$ .

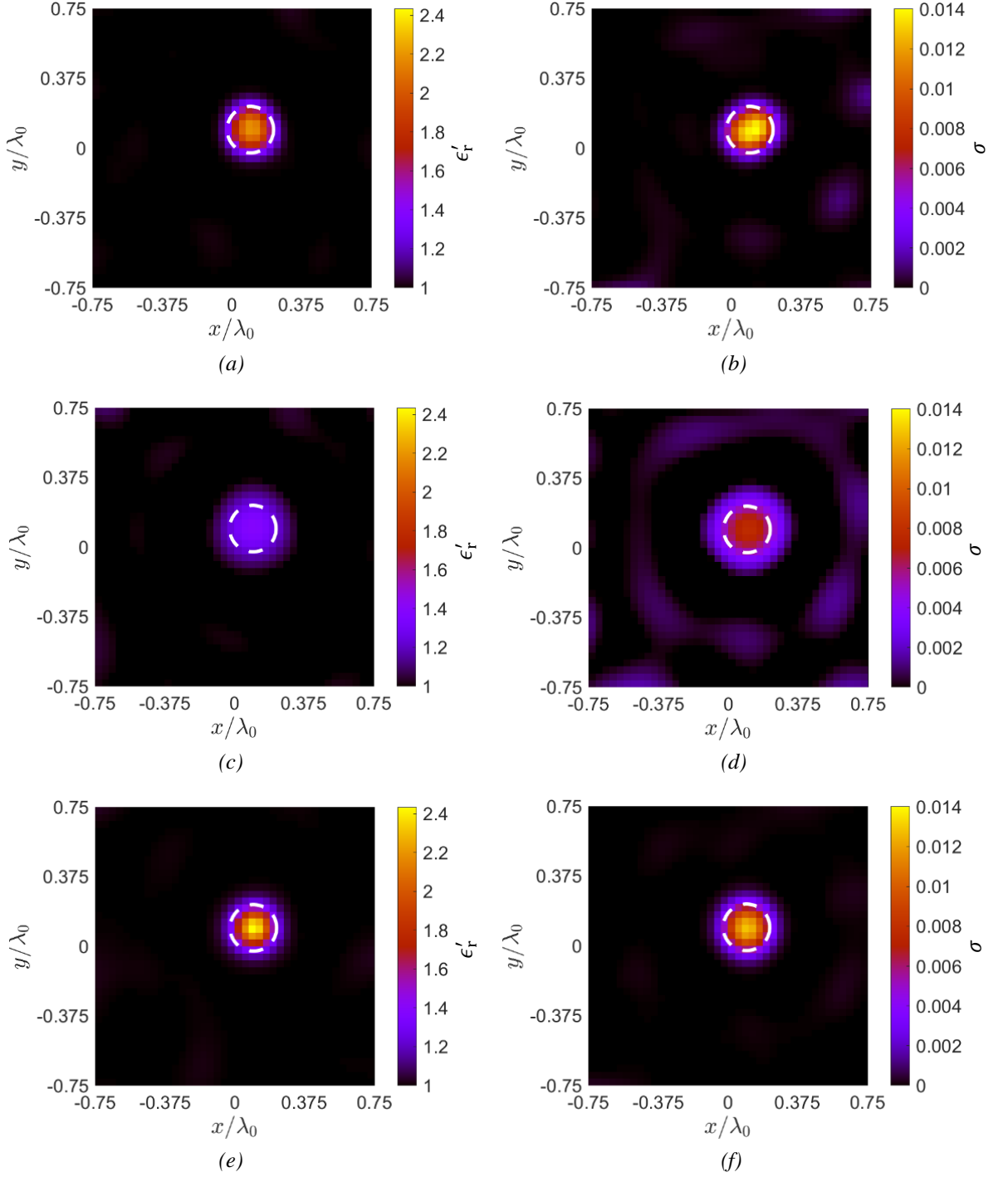


Figure 70. Reconstructed distribution of the dielectric permittivity for  $\sigma = 10^{-2}$  S/m. Case  $p_{opt} = 1.3$ , phaseless: (a)  $\epsilon'_r$ , (b)  $\sigma$ . Case  $p = 2$ , phaseless: (c)  $\epsilon'_r$ , (d)  $\sigma$ . Case  $p_{opt} = 1.3$ , full-data: (e)  $\epsilon'_r$ , (f)  $\sigma$ . The white dashed circles indicate the actual profiles.

Because of  $M = S - 1$ , the number of measurement points varies accordingly. It is important to note that in some of these cases an under-sampling condition subsists. The adopted target is the circular cylinder described in Section 5.1.3.

Table 10 reports the resulted values of the reconstruction errors, the final number of outer iterations  $i_f$ , and the total computational times  $T$  for each of the simulated  $S$  values in correspondence of  $p_{opt}$  and  $p = 2$  (Hilbert space case).

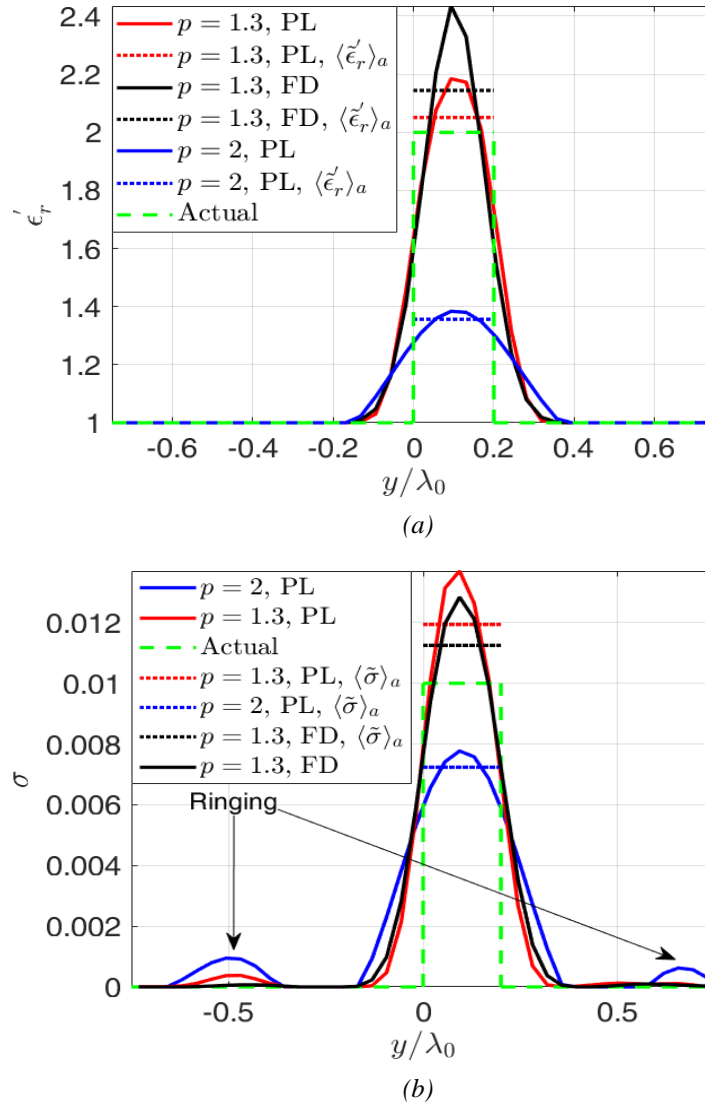


Figure 71. Slices at  $x = 0.1\lambda_0$  of Figure 70(a)-(f), and the actual profile. (a)  $\epsilon'_r$ , (b)  $\sigma$ .

Table 10. Reconstruction errors, final number of outer iterations  $i_f$ , and computational times  $T$  versus  $S$  in correspondence of  $p = p_{opt}$  and  $p = 2$  (Hilbert space approach).

$S$	$\mathcal{I}^{p_{opt}}$						$\mathcal{I}^2$ (Hilbert)				
	$p_{opt}$	$e_{inv}$	$e_{obj}$	$e_b$	$i_f$	$T$ [s] <sup>(*)</sup>	$e_{inv}$	$e_{obj}$	$e_b$	$i_f$	$T$ [s] <sup>(*)</sup>
10	1.3	0.57	0.23	0.01	4	8	0.81	0.35	0.04	3	6
20	1.4	0.46	0.16	0.01	4	17	0.67	0.25	0.03	3	15
30	1.4	0.45	0.15	0.01	4	42	0.66	0.25	0.02	3	33
40	1.4	0.45	0.15	0.01	4	75	0.66	0.27	0.02	3	67

<sup>(\*)</sup> These refer to a PC equipped with a quad-core CPU Intel Core i5-2310 @2.9 GHz and 8 GB of RAM.

As expected, a smaller amount of data lowers the computational times but causes performance degradation. However, the classic algorithm suffers more the data reduction. This fact is also confirmed by the reconstructed distributions of the relative dielectric permittivity shown in Figure 72 corresponding to the case  $S = 10$  with  $p = p_{opt} = 1.3$  and  $p = 2$ . For comparison purposes, the full-data inversion result for  $p_{opt} = 1.3$  is reported too.

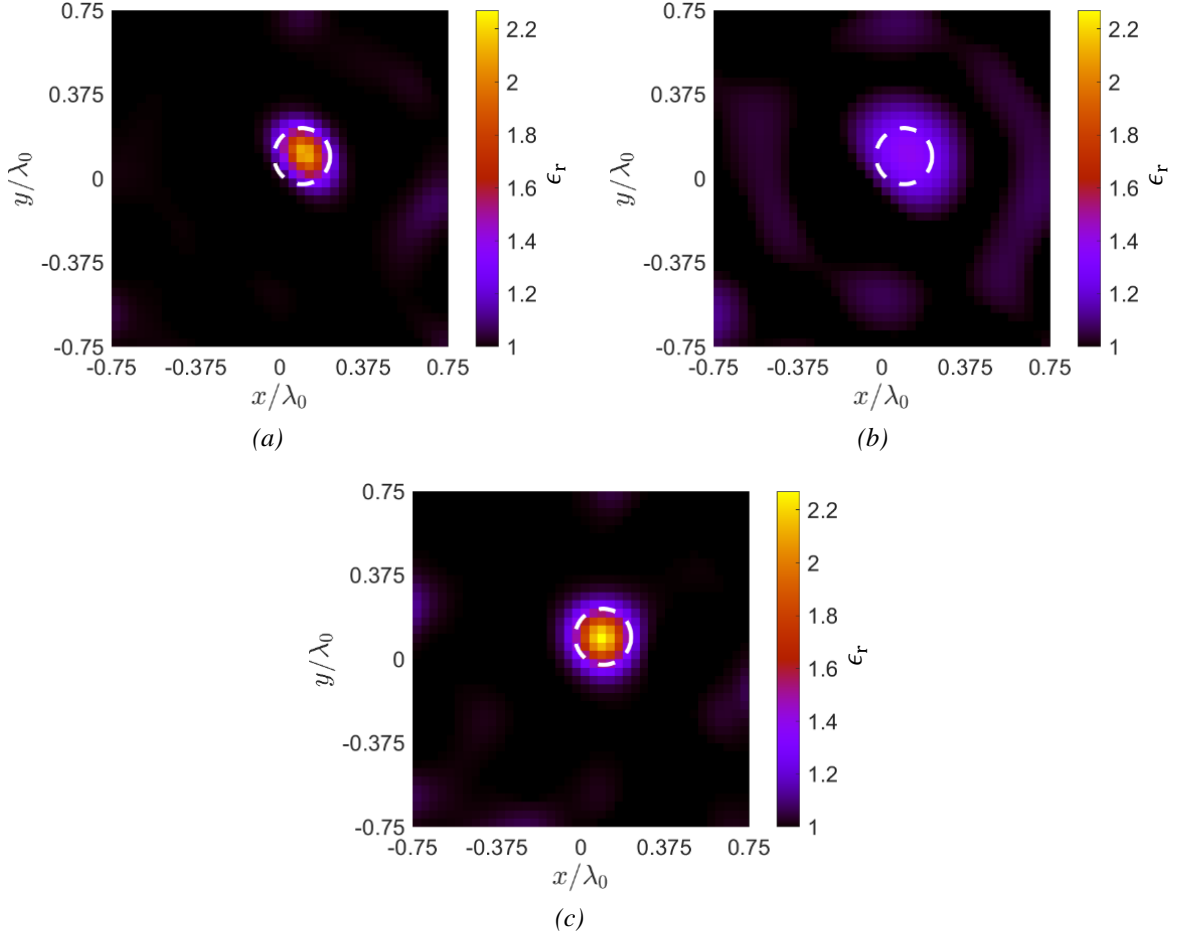


Figure 72. Reconstructed distribution of the dielectric permittivity for  $S = 10$ . (a)  $p_{opt} = 1.3$ , phaseless; (b)  $p = 2$ , phaseless; (c)  $p_{opt} = 1.3$ , full-data. The white dashed circles indicate the actual profiles.

Moreover, cuts at  $y = 0.1\lambda_0$  of the images in Figure 72 are shown in Figure 73. The inexact-Newton in  $l^2$  presents both underestimation and ringing phenomena. Such problems are reduced considering the  $l^{p_{opt}}$  setting. Moreover, in this latter case the reconstruction is similar to the one provided by the full-data approach, although, as expected, the full-data method is more robust to the decrease in the amount of information, as can be seen in Figure 74.



$$\begin{aligned}
\zeta_o &= \frac{1}{2} \left( \left| \frac{\tilde{x}_c - x_c}{x_c} \right| + \left| \frac{\tilde{y}_c - y_c}{y_c} \right| \right) \\
\zeta_D &= \frac{|\tilde{D} - D|}{D} \\
\zeta_{\epsilon\sigma} &= \frac{|\check{\epsilon} - \check{\sigma}|}{\check{\epsilon}}
\end{aligned} \tag{104}$$

where  $(\tilde{x}_c, \tilde{y}_c)$  and  $\tilde{D}$  are the estimated center and diameter of the cylinder, respectively, whereas  $(x_c, y_c)$  and  $D$  are the actual ones. Moreover,  $\check{\epsilon}$  and  $\check{\sigma}$  are defined as

$$\begin{aligned}
\check{\epsilon} &= \left| (\langle \tilde{\epsilon}'_r \rangle_r - 1)^2 - j \frac{\langle \tilde{\sigma} \rangle_r}{\omega \epsilon_0} \right| \\
\check{\sigma} &= \left| (\langle \epsilon'_r \rangle_a - 1)^2 - j \frac{\langle \sigma \rangle_a}{\omega \epsilon_0} \right|
\end{aligned} \tag{105}$$

with  $\langle \cdot \rangle_r$  and  $\langle \cdot \rangle_a$  average operator on the recognized and actual cylinder's domain, respectively. The centers, diameters, and relative dielectric permittivities of the inspected cylinders are estimated on the basis of the reconstructed dielectric distribution by an automatic recognition tool, whose details are given in Appendix A.

The error metrics defined in (104) for the cases  $p = 1.3$ ,  $p = 2$  in the phaseless approach and  $p = 1.5$  in the full-data one are shown in Figure 75. As can be seen, the Hilbert-space framework almost always provides higher errors than its Banach-space counterpart. Moreover, at least in this test, the phaseless technique is not far in terms of reconstruction errors from the full-data one. These assertions are also confirmed by the reconstructed distributions of the relative dielectric permittivity reported in Figure 76 and by the corresponding cuts along the line  $x = y$  shown in Figure 77. Finally, for the reconstructions obtained in non-Hilbertian spaces shown in Figure 76, the behaviors of the quantities in (96), (98) versus the iteration number are reported in Figure 78 and the corresponding trends of the NMSE are shown in Figure 79. We see that both the residuals and the errors are monotonically decreasing and reach an almost flat slope in few iterations. However, as expected, the full-data inversion reaches lower final values of residuals and NMSE.

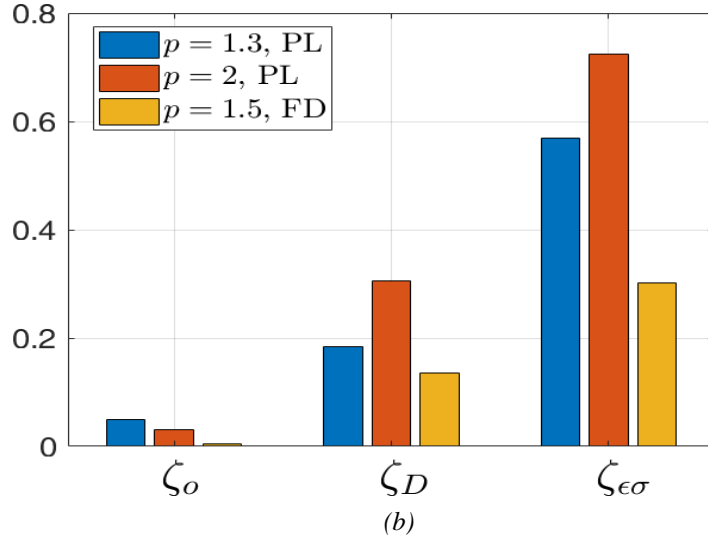
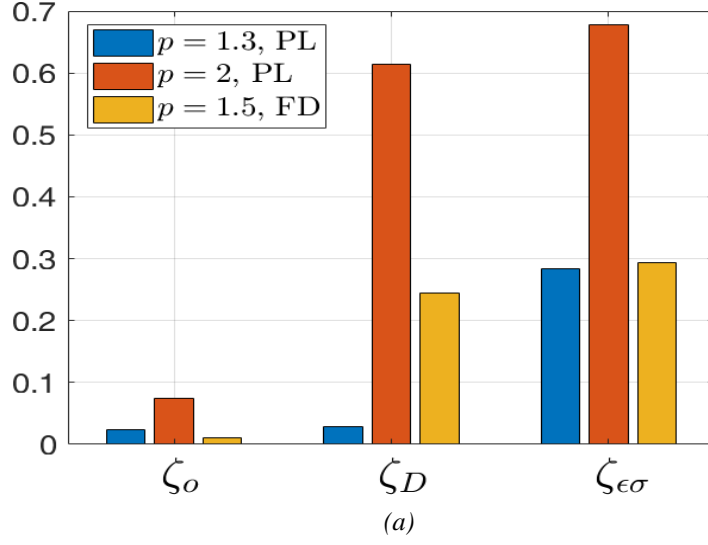


Figure 75. Behavior of the error metrics  $\zeta_o$ ,  $\zeta_D$ , and  $\zeta_{\epsilon\sigma}$  for (a) cylinder n.1 and (b) cylinder n. 2.

### 5.1.8 T-shaped target

The reconstruction capabilities of the developed approach have been evaluated here by considering a T-shaped target made of two cylinders having rectangular cross-section. The first one has center  $\mathbf{r}_{c,1} = (0.25,0)\lambda_0$ , width  $w_1 = \lambda_0/2$ , and height  $h_1 = \lambda_0/4$ , whereas the second one has center  $\mathbf{r}_{c,2} = (-0.125,0)\lambda_0$ , width  $w_2 = \lambda_0/4$ , and height  $h_2 = \lambda_0/2$ . The behaviors of the NMSE and of the relative mean errors versus  $p$  are reported in Figure 80.



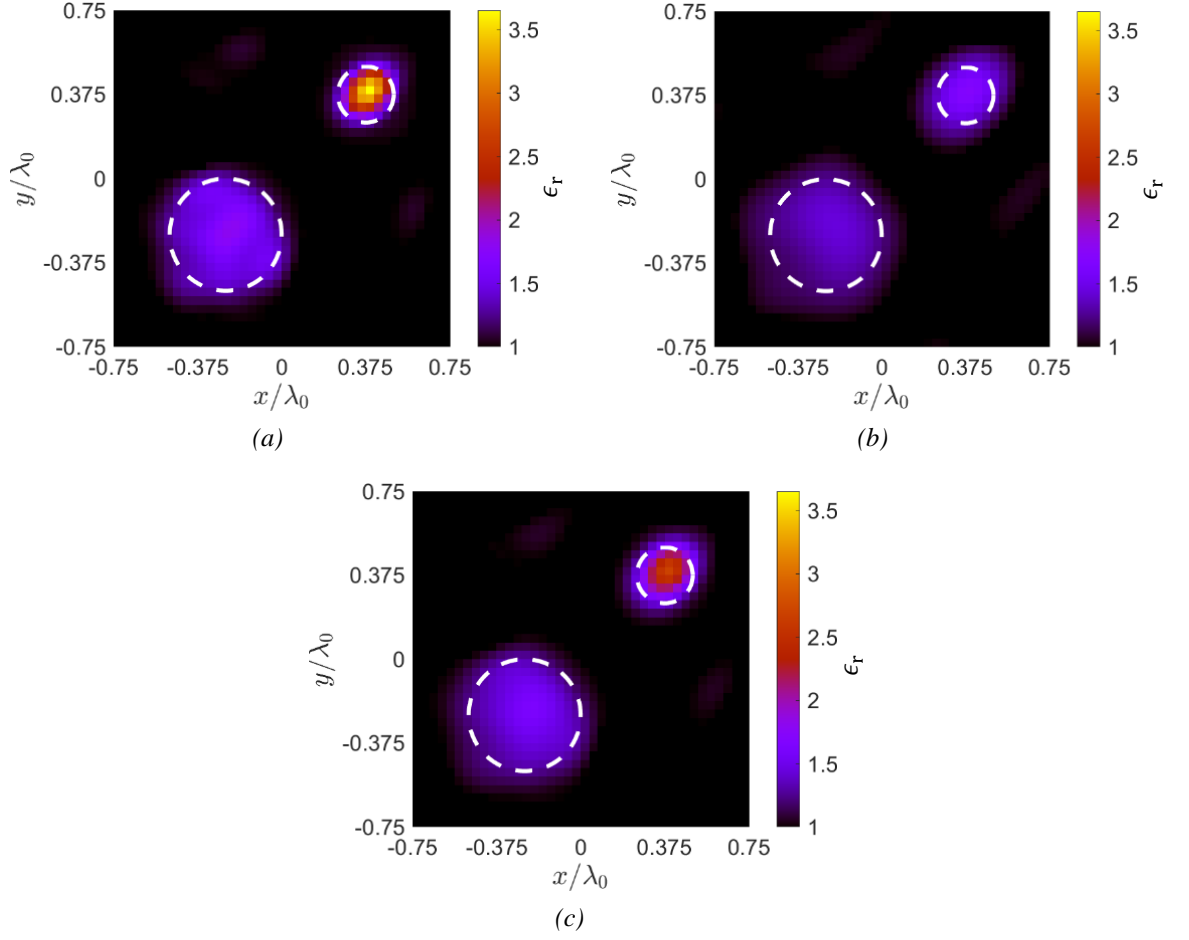


Figure 76. Reconstructed distribution of the dielectric permittivity for the two cylinders case. (a)  $p = 1.3$ , phaseless; (b)  $p = 2$ , phaseless; (c)  $p = 1.5$ , full-data. The white dashed lines indicate the actual profiles.

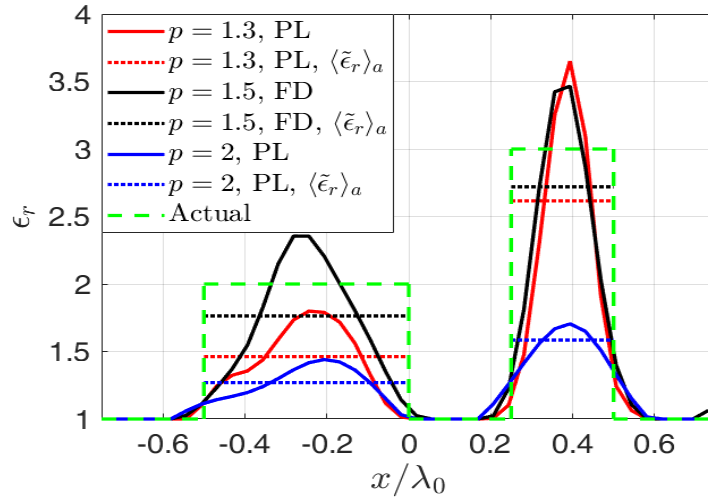


Figure 77. Slices at  $x = y$  of Figure 76(a)-(c), and the actual profile.

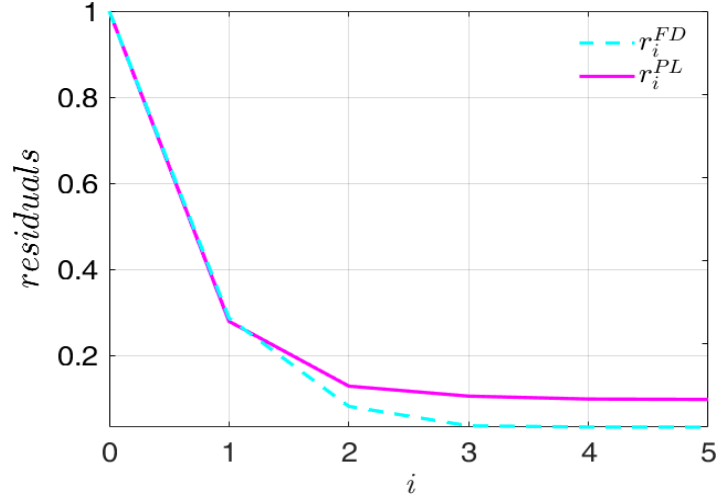


Figure 78. Behavior of  $r_i^{PL}$  and  $r_i^{FD}$  versus the iteration number. Two circular cylinders.

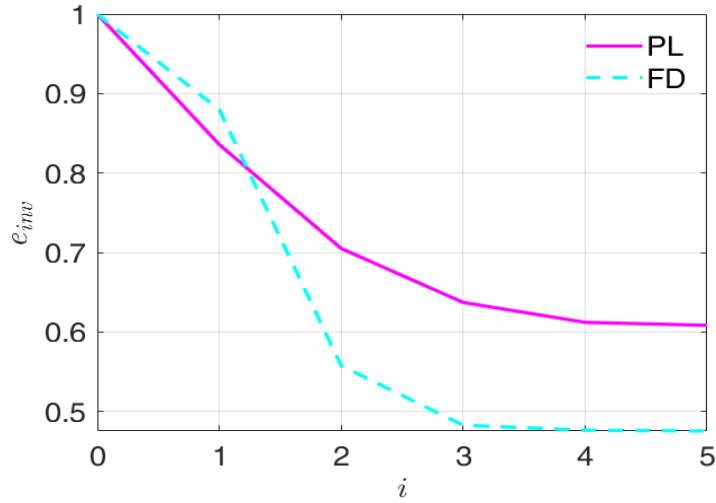


Figure 79. Behavior of  $e_{inv}$  versus the iteration number. Two circular cylinders.

As usual, the traces have their minima for values of  $p$  largely smaller than 2. The images related to  $p_{opt} = 1.2$ ,  $p = 2$ , and for the full-data inversion with  $p_{opt} = 1.5$  are shown in Figure 81. The higher performance in  $l^{1,2}$  with respect to  $l^2$  is quite evident, although the full-data result has a higher fidelity to the shape of the actual target. Finally, for the reconstructions obtained in non-Hilbertian spaces shown in Figure 81, the behaviors of the residuals metrics in (96), (98) versus the iteration number are reported in Figure 82, and the corresponding trends of the NMSE are shown in Figure 83. As it happened in Section 5.1.7, both the methods monotonically reach a stationary point in few iterations, with the full-data inversion getting lower final values.

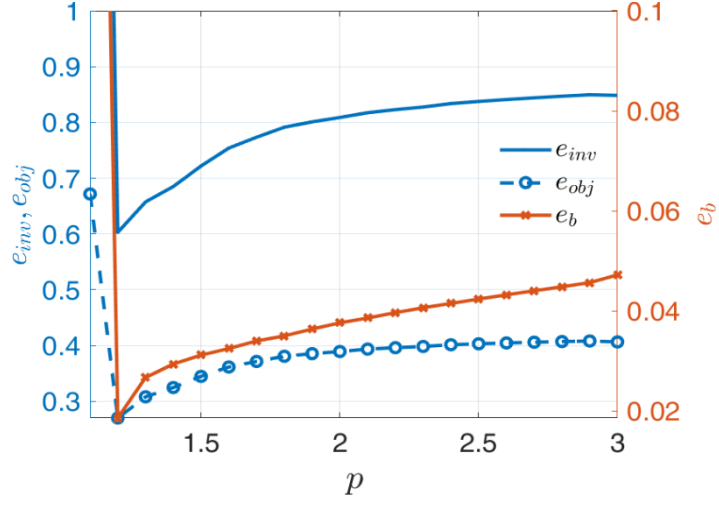


Figure 80. Behavior of  $e_{inv}$ ,  $e_{obj}$ , and  $e_b$  versus the norm parameter  $p$ . T-shaped target.

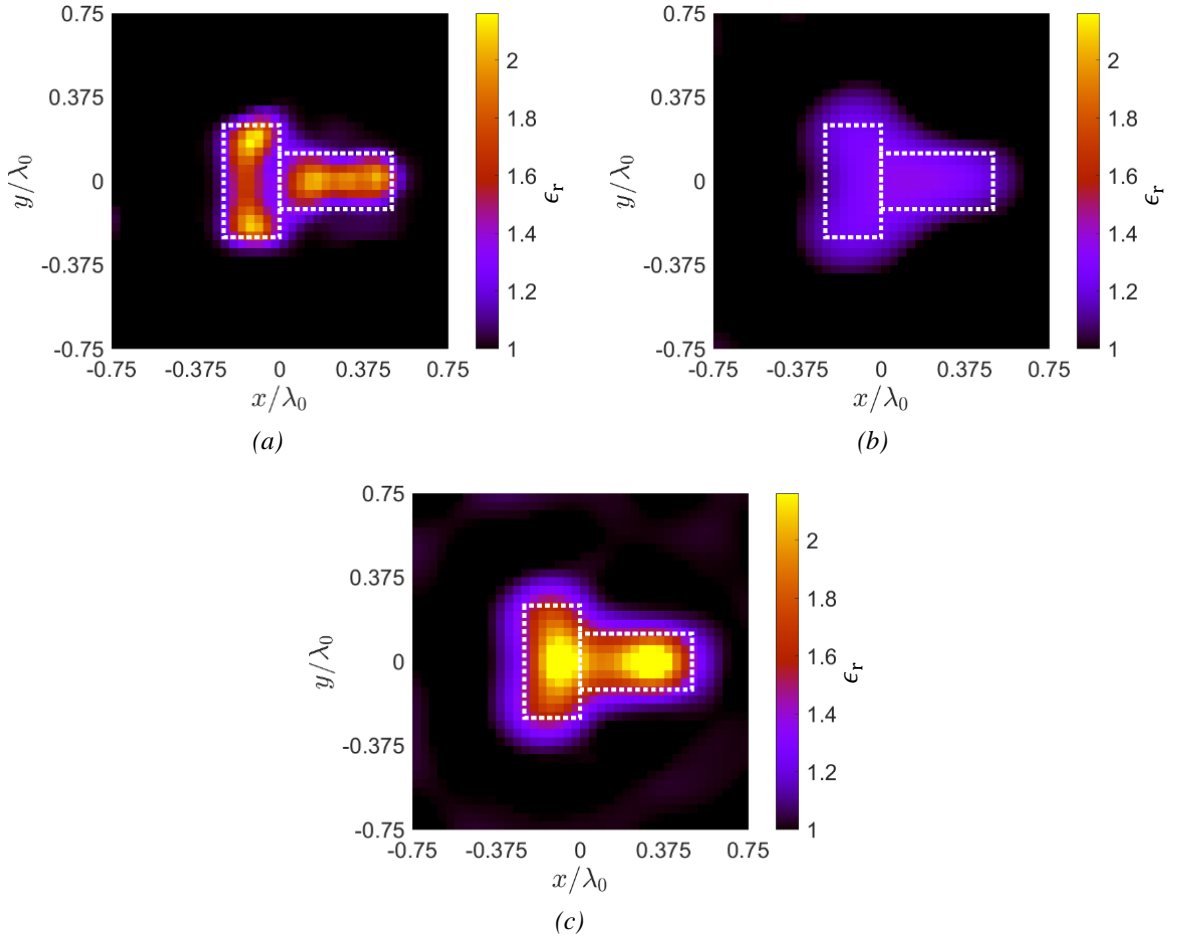


Figure 81. Reconstructed distribution of the dielectric permittivity for the T-shaped target. (a)  $p_{opt} = 1.2$ , phaseless; (b)  $p = 2$ , phaseless; (c)  $p_{opt} = 1.5$ , full-data. The white dashed lines indicate the actual profiles.

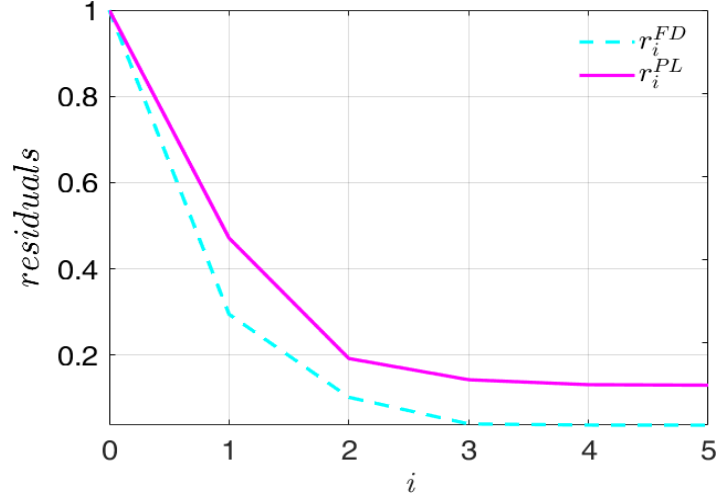


Figure 82. Behavior of  $r_i^{PL}$  and  $r_i^{FD}$  versus the iteration number. T-shaped target.

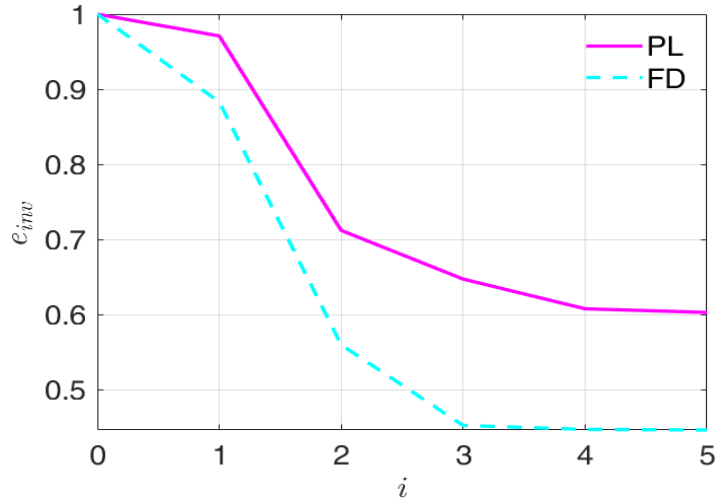


Figure 83. Behavior of  $e_{inv}$  versus the iteration number. T-shaped target.

## 5.2 Experimental Validation

The developed inversion procedure has been validated by using experimental data too. In particular, two different datasets have been used. The first one is made freely available by the Institut Frénel [130], [131] and consists of two databases of data. Moreover, a microwave tomograph has been developed at the University of Applied Sciences and Arts of Southern Switzerland (SUPSI) in collaboration with the Applied Electromagnetics (AEM) research unit of the University of Genoa, and the proposed approach is validated on a dataset from this system, too [132], [133]. Since the incident electric fields in  $D_{inv}$  are computed by

assuming line currents as sources, instead of the more complex real antennas, these sets of data are calibrated as follows

$$\mathbf{p}_{tot}^{ext,(s)} = |\gamma_{(s)}|^2 \mathbf{p}_{tot,meas}^{ext,(s)} \quad (106)$$

with

$$\frac{E_{inc,(s)}^{calc}(\mathbf{r}_{md}^{(s)})}{E_{inc,(s)}^{meas}(\mathbf{r}_{md}^{(s)})} = \gamma_{(s)} \quad (107)$$

where  $\mathbf{p}_{tot,meas}^{ext,(s)}$  contains the square measured amplitude of the total external electric field for the  $s$ th view,  $E_{inc,(s)}^{calc}$  is the incident electric field given by a line current with equal placement of the  $s$ th transmitting antenna,  $E_{inc,(s)}^{meas}$  is the experimentally measured incident electric field for the  $s$ th view, and  $\mathbf{r}_{md}^{(s)}$  is the position of the measurement point farthest away from the  $s$ th source.

A void background is adopted by both systems and the same stopping criteria introduced at the beginning of this Chapter are here applied, too.

### 5.2.1 Institut Frénel Dataset: First Experimental Database

The first experimental setup [130] has  $S = 36$  transmitting antenna uniformly distributed on a circumference of radius  $R_{D_S} = 72$  cm. For each view,  $M = 49$  probing points are considered on an arc of circumference with radius  $R_{D_{obs}} = 76$  cm and aperture  $240^\circ$ . The active transmitting antenna is located in the middle of the empty arc of the circumference. A square investigation domain  $D_{inv}$  of side  $L_{D_{inv}} = 18$  cm and discretized in  $N = 3969$  square pixels is considered in the inversion procedure. Figure 84 shows the illuminating and measurement configuration with reference to the first view.

The following two different targets are considered

1. DielTM. One cylinder with center  $\mathbf{r}_c = (0, 2.7)$  cm, radius  $R = 1.5$  cm, and relative dielectric permittivity  $\epsilon_r = 3$ .
2. TwoDielTM. Two cylinders with centers  $\mathbf{r}_{c,1} = (-0.3, 4.8)$  cm and  $\mathbf{r}_{c,2} = (-1.2, -4.3)$  cm, radii  $R_1 = R_2 = 1.5$  cm, and dielectric permittivities  $\epsilon_{r,1} = \epsilon_{r,2} = 3$ .

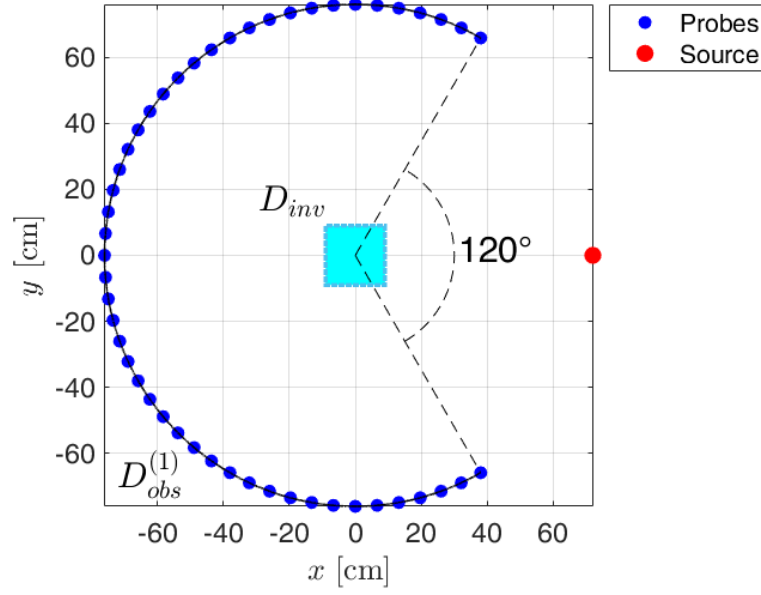


Figure 84. Illumination and measurement setup adopted in the first experimental database of the Institut Frésnel. First view.

The data at the working frequency  $f = 2$  GHz has been used. The reconstruction errors versus the norm parameter are reported in Figure 85 for both the considered targets. As can be seen, all the metrics achieve their minima for values of the norm parameter  $p$  largely minor than  $p = 2$  (corresponding to the classic Hilbert-space approach). In Figure 86 and Figure 87 the reconstructed distributions of the relative dielectric permittivity with  $p_{opt} = 1.2$  and  $p = 2$  for the first and second target are shown. Moreover, the optimal reconstructions obtained when considering the full complex data are reported, too ( $p_{opt} = 1.1$  for DielTM and  $p_{opt} = 1.2$  for TwoDielTM). It is clear that the proposed phaseless approach with  $p_{opt} = 1.2$  outperforms the classic one in Hilbert space in terms of both dielectric permittivity and shape retrieval. Moreover, its results are similar to the full-data ones. Finally, Figure 88 shows the experimental and simulated (with a MoM solver) amplitude of the scattered electric fields in the measurement points for the target TwoDielTM. The electric fields corresponding to the optimal reconstructions provided by the phaseless and full-data inversion procedures are also plotted. As can be seen, there is a quite good agreement.

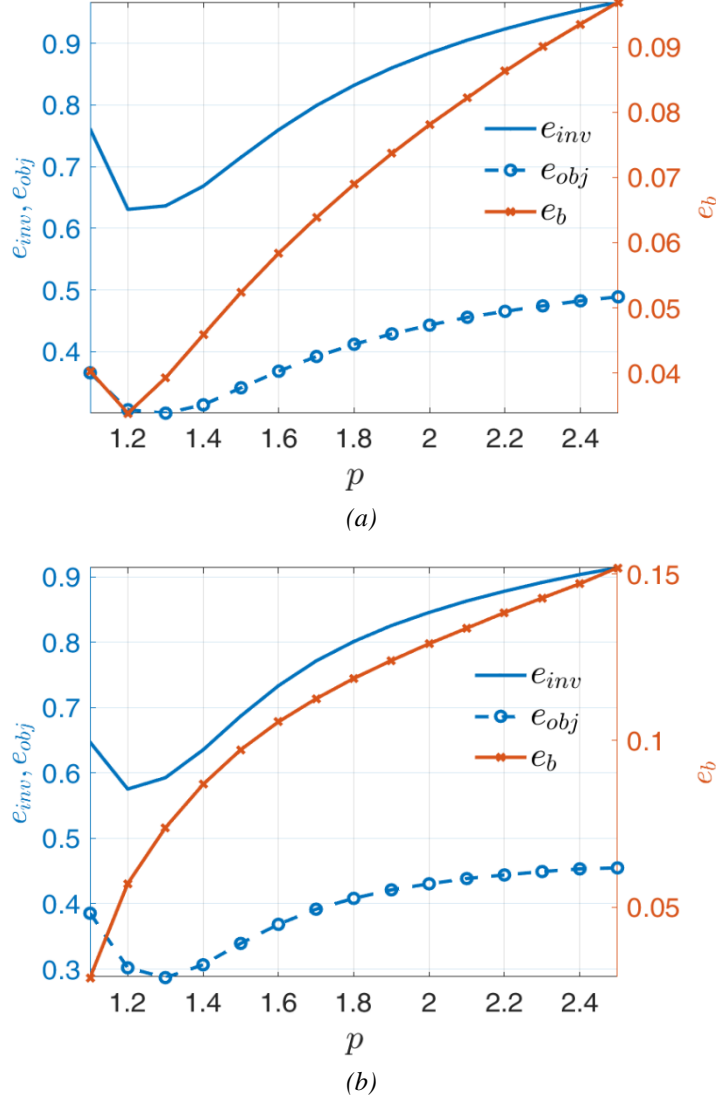


Figure 85. Behavior of  $e_{inv}$ ,  $e_{obj}$ , and  $e_b$  versus the norm parameter  $p$  for the (a) DielTM and (b) TwoDielTM targets.

### 5.2.2 Institut Frénel Dataset: Second Experimental Database

In the second experimental setup [131] the transmitting antennas are uniformly distributed on a circumference of radius  $R_{D_S} = 167$  cm. Their number varies with the target type and so it will be specified at occurrence. For each view,  $M = 241$  probing points are considered on an arc of circumference with radius  $R_{D_{obs}} = 167$  cm and aperture  $240^\circ$ . The transmitting antenna is located in the middle of the empty  $120^\circ$  arc. A square investigation domain  $D_{inv}$  of side  $L_{D_{inv}} = 18$  cm and discretized in  $N = 3969$  square pixels is considered. Figure 89 shows the illuminating and measurement configuration for the first view.

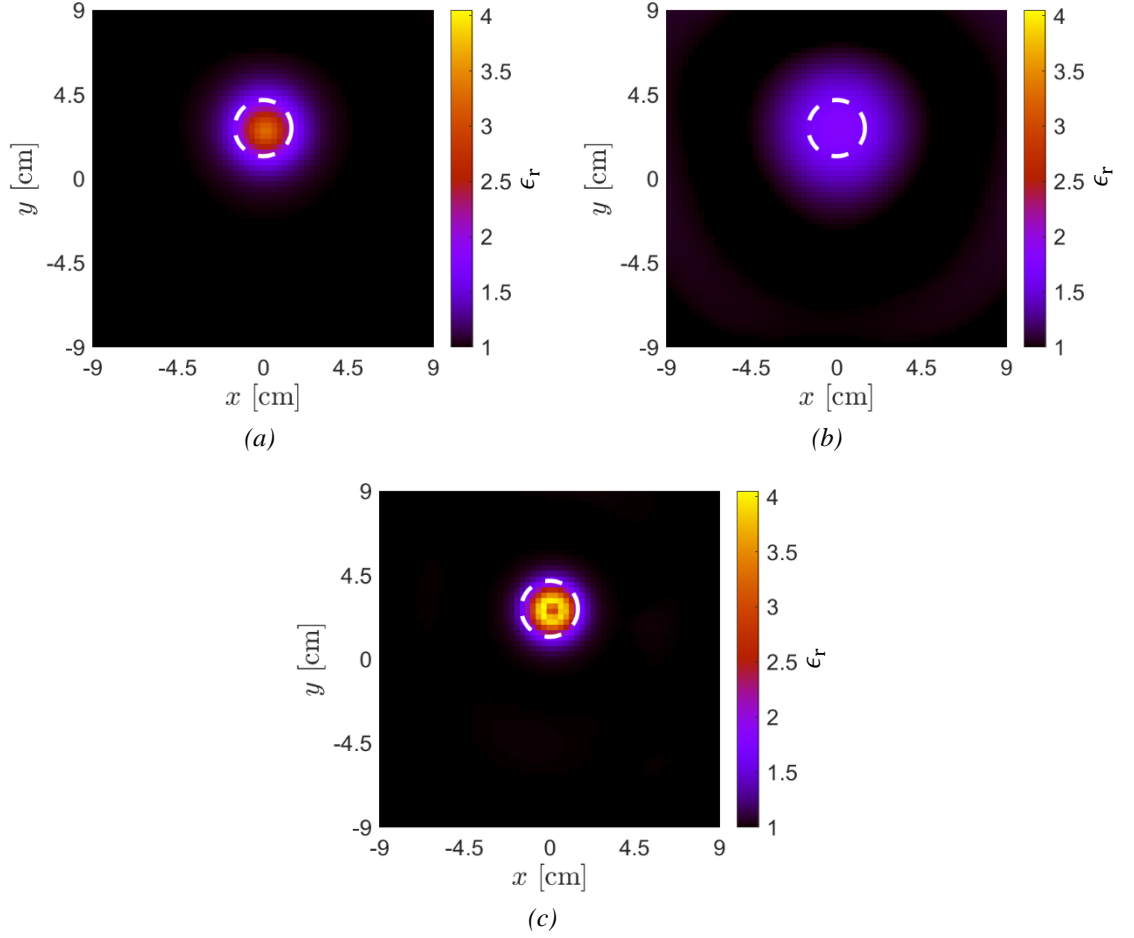


Figure 86. Reconstructed distribution of the dielectric permittivity for the DielTM target. (a)  $p_{opt} = 1.2$ , phaseless; (b)  $p = 2$ , phaseless; (c)  $p_{opt} = 1.1$ , full-data. The white dashed circles indicate the actual profiles.

The following three different targets are considered

1. FoamDielExtTM. Two cylinders with centers  $\mathbf{r}_{c,1} = (0,0)$  cm and  $\mathbf{r}_{c,2} = (-5.55,0)$  cm, radii  $R_1 = 4$  cm and  $R_2 = 1.55$  cm, dielectric permittivities  $\epsilon_{r,1} = 1.45$  and  $\epsilon_{r,2} = 3$ . Working frequency  $f = 3$  GHz and number of views  $S = 8$ .
2. FoamDielIntTM. Two cylinders with centers  $\mathbf{r}_{c,1} = (0,0)$  cm and  $\mathbf{r}_{c,2} = (-0.5,0)$  cm, radii  $R_1 = 4$  cm and  $R_2 = 1.55$  cm, dielectric permittivities  $\epsilon_{r,1} = 1.45$  and  $\epsilon_{r,2} = 3$ . Working frequency  $f = 3$  GHz and number of views  $S = 8$ .
3. FoamTwinDielTM. Three cylinders with centers  $\mathbf{r}_{c,1} = (0,0)$  cm,  $\mathbf{r}_{c,2} = (-5.55,0)$  cm, and  $\mathbf{r}_{c,3} = (-0.5,0)$  cm, radii  $R_1 = 4$  cm, and  $R_2 = R_3 = 1.55$  cm, dielectric permittivities  $\epsilon_{r,1} = 1.45$  and  $\epsilon_{r,2} = \epsilon_{r,3} = 3$ . Working frequency  $f = 2$  GHz and number of views  $S = 18$ .



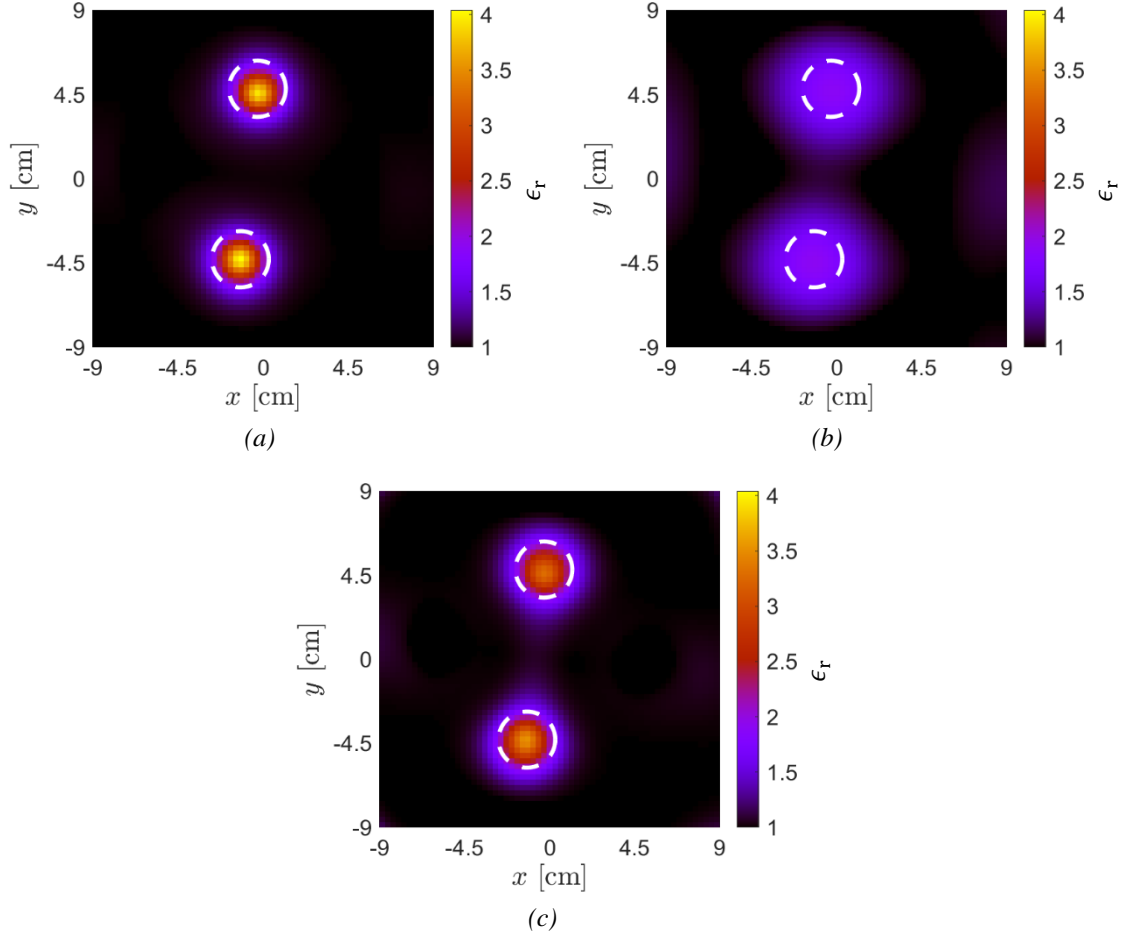


Figure 87. Reconstructed distribution of the dielectric permittivity for the TwoDielTM target. (a)  $p_{opt} = 1.2$ , phaseless; (b)  $p = 2$ , phaseless; (c)  $p_{opt} = 1.2$ , full-data. The white dashed circles indicate the actual profiles.

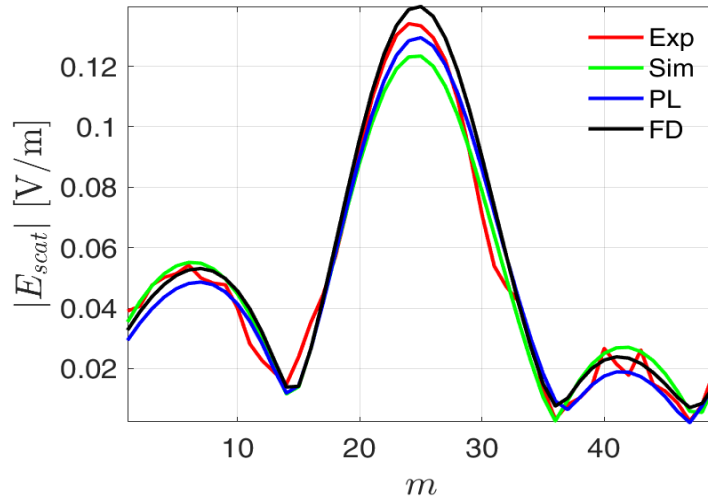


Figure 88. Amplitude of the scattered electric fields in the measurement points given by the experimental data (“Exp” in legend), the actual dielectric distribution (“Sim” in legend), and the optimal reconstructed ones obtained by phaseless and full-data inversions (“PL” and “FD” in legend, respectively). TwoDielTM target.

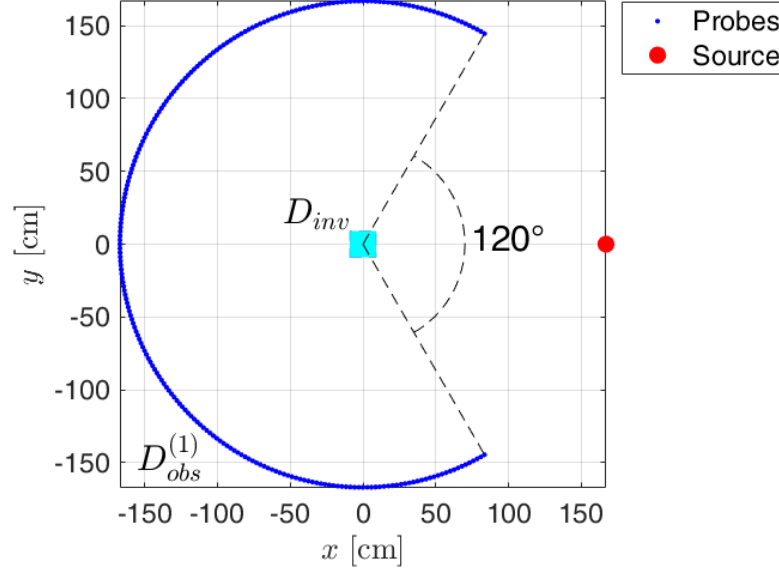


Figure 89. Illumination and measurement setup adopted in the second experimental database of the Institut Frénel. First view.

The NMSE and relative mean errors on the reconstruction results obtained by the developed procedure are shown in Figure 90 versus the value of the norm parameter  $p$ . As it happens for the first experimental database, the best reconstructions are not achieved with the classic Hilbert-space approach, but for lower values of  $p$ . The images related to the targets FoamDielExtTM, FoamDielIntTM, and FoamTwinDielTM obtained with  $p_{opt} = 1.2$ ,  $p_{opt} = 1.4$ , and  $p_{opt} = 1.1$ , respectively, are shown in Figure 91-93. For comparison purpose, the results of the phaseless inexact-Newton in  $l^2$  and of the optimal full-data inversions are reported in the same figures. Moreover, the cuts along a line at  $y = 0$  cm are also shown in Figure 94. The higher performance of the proposed phaseless technique with respect to the Hilbert one can be appreciated in all the test cases. Moreover, the results are comparable to the one obtained when considering the full complex data. Finally, the amplitude of the scattered electric fields in the measurement points for the experimental data, the actual dielectric distributions, and the optimal reconstructed ones are reported in Figure 95. The electric fields in presence of the actual and reconstructed dielectric distributions are simulated with a MoM solver. A good agreement is observed in all the reported cases.

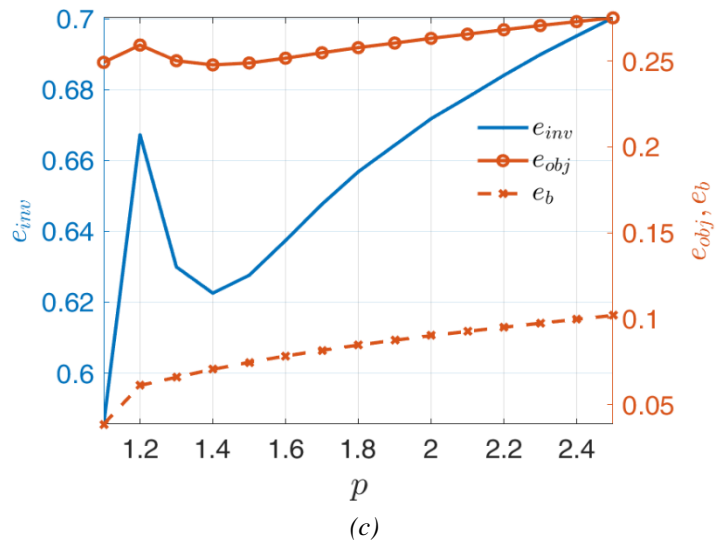
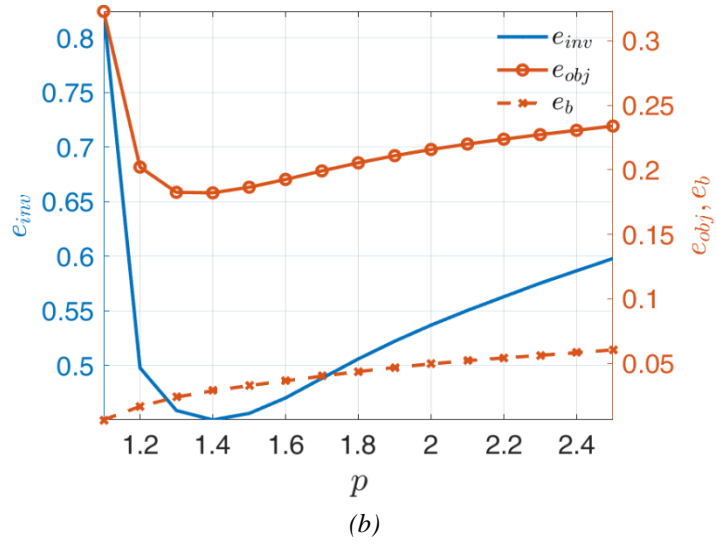
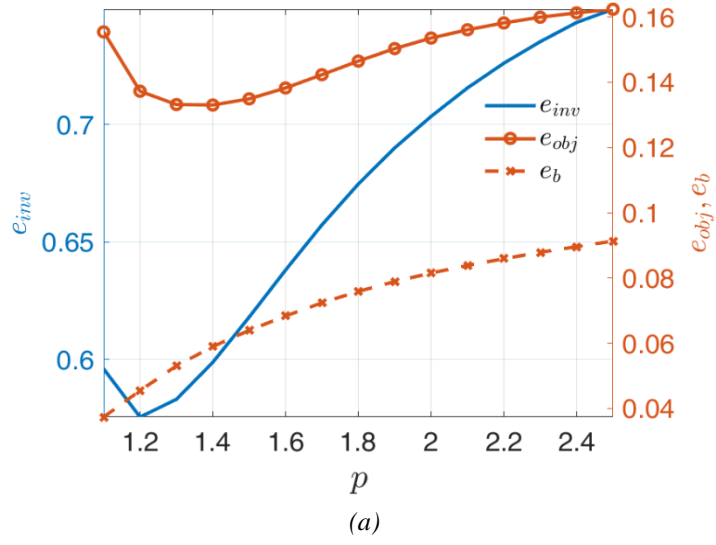


Figure 90. Behavior of  $e_{inv}$ ,  $e_{obj}$ , and  $e_b$  versus the norm parameter  $p$  for the (a) *FoamDielExtTM*, (b) *FoamDielIntTM*, and (c) *FoamTwinDielTM* targets.

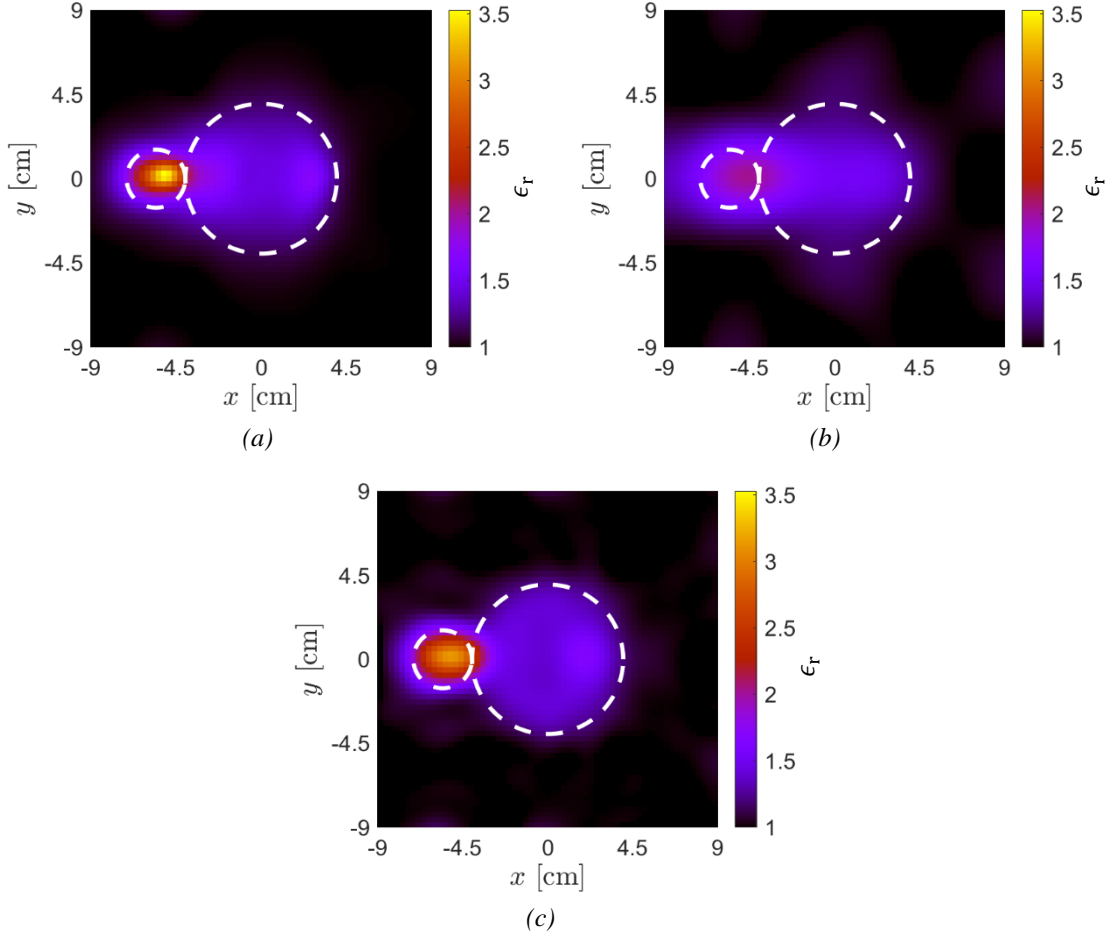


Figure 91. Reconstructed distribution of the dielectric permittivity for the FoamDieExtTM target. (a)  $p_{opt} = 1.2$ , phaseless; (b)  $p = 2$ , phaseless; (c)  $p_{opt} = 1.3$ , full-data. The white dashed circles indicate the actual profiles.

### 5.2.3 SUPSI Experimental Dataset

The experimental setup [132], [133] consists of  $S = 8$  sources and  $M = 55$  measurement points for each view. The probes are located on an arc of circumference having radius  $R_{D_{obs}}$  and aperture  $270^\circ$ , and the active transmitting antenna is in the middle of the remaining sector of  $90^\circ$ . The radius of the circle  $R_{D_{obs}}$  varies with the working frequency as indicated in Table 11. The investigation domain  $D_{inv}$  is a square of side  $L_{D_{inv}} = 0.3$  m and it is discretized in  $N = 3969$  square pixels. A schematic representation of the considered configuration, related to the first view and  $f = 1$  GHz, is reported in Figure 96.

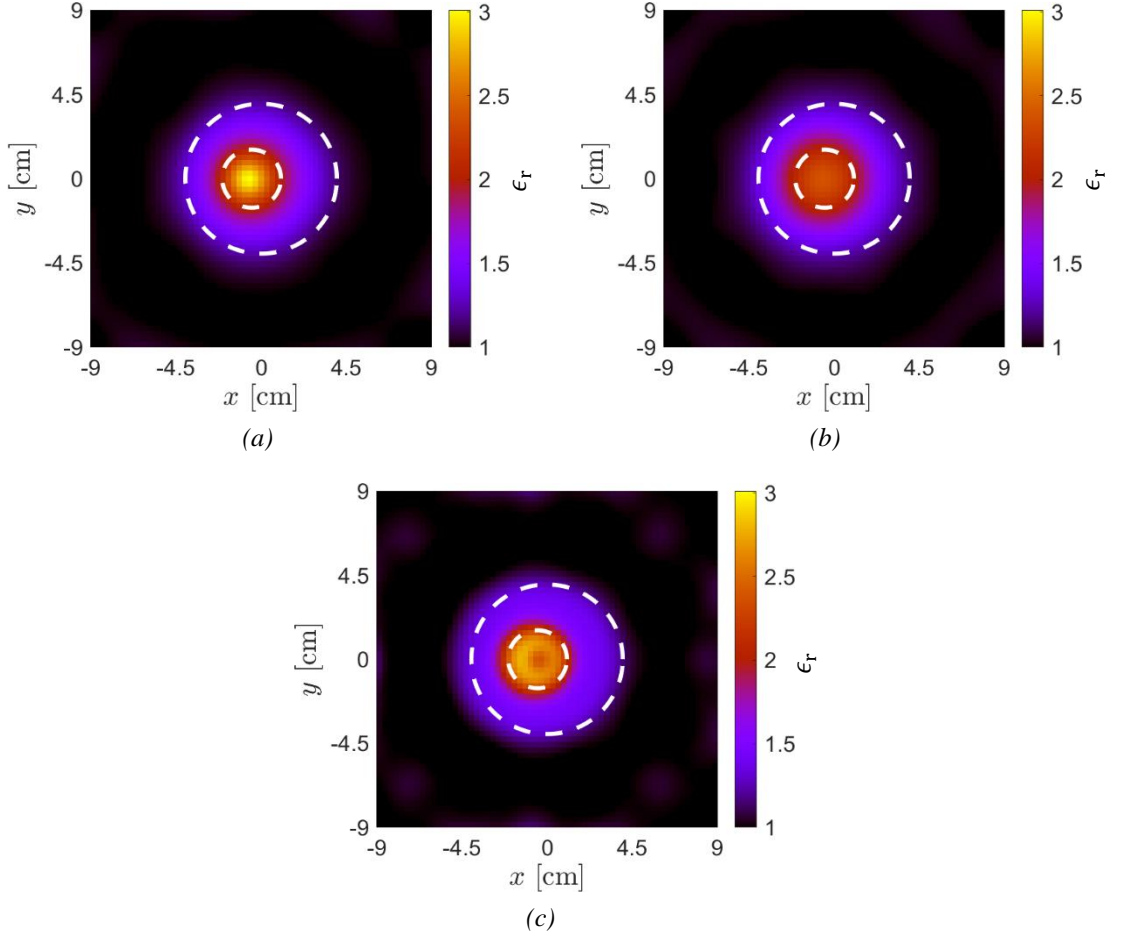


Figure 92. Reconstructed distribution of the dielectric permittivity for the FoamDielIntTM target. (a)  $p_{opt} = 1.4$ , phaseless; (b)  $p = 2$ , phaseless; (c)  $p_{opt} = 1.3$ , full-data. The white dashed circles indicate the actual profiles.

Table 11. Radius of the observation domain  $R_{D_{obs}}$  for each working frequency.

$f$ [GHz]	$R_{D_{obs}}$ [m]
1	0.5
2	0.42
3	0.395
4	0.381
5	0.372

In order to further mitigate the occurrence of false solutions, the available multi-frequency data are exploited thanks to the frequency hopping approach described in Section 3.7. The investigation domain contains two slabs of wood. The first one has circular cross-section of diameter  $D_1 = 5$  cm, relative dielectric permittivity  $\epsilon_{r,1} = 3.5$ , and center  $\mathbf{r}_{c,1} = (1.4, -5.5)$  cm. The second cylinder has rectangular cross-section of width  $w_2 = 11.5$  cm, height  $h_2 = 7.5$  cm, relative dielectric permittivity  $\epsilon_{r,2} = 1.8$ , and center  $\mathbf{r}_{c,2} = (0.3, 8)$  cm.

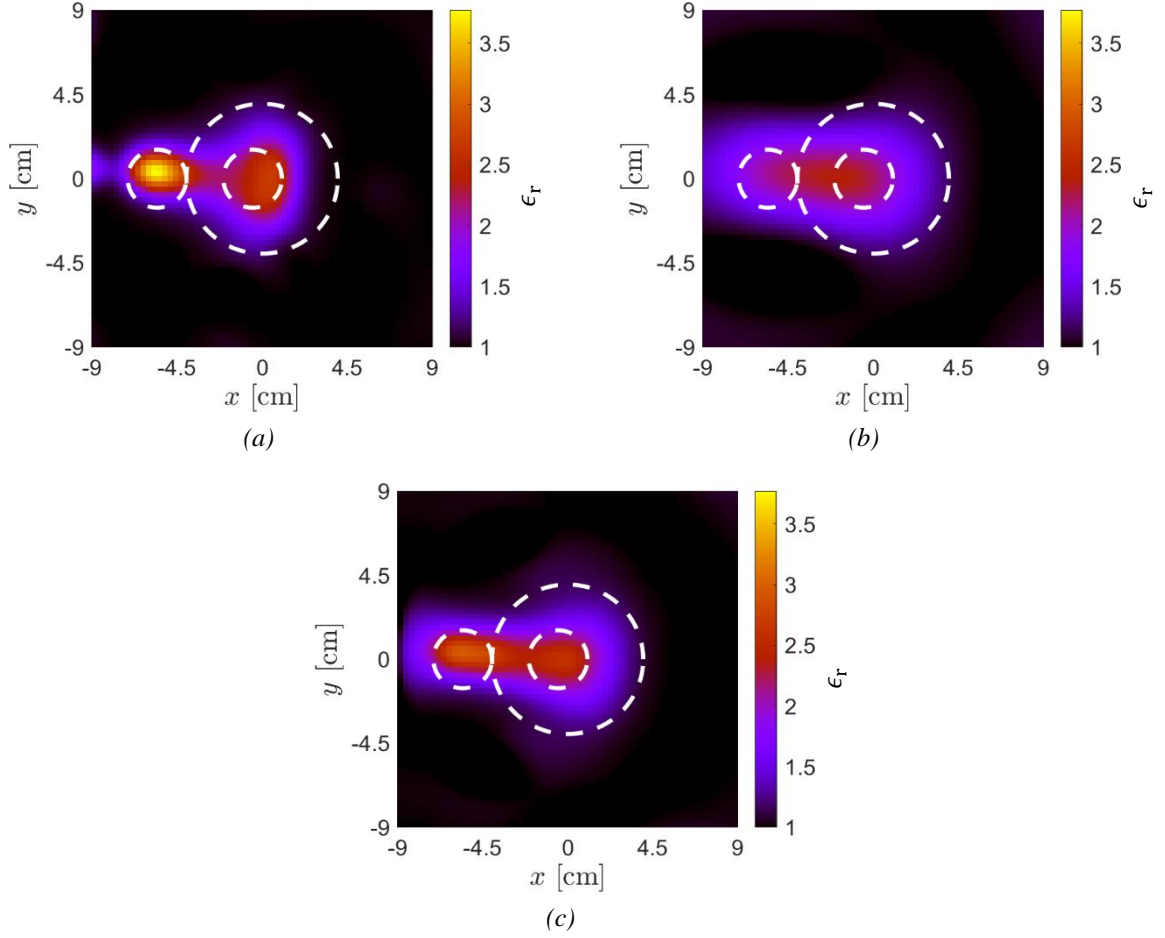


Figure 93. Reconstructed distribution of the dielectric permittivity for the FoamTwinDielTM target. (a)  $p_{opt} = 1.1$ , phaseless; (b)  $p = 2$ , phaseless; (c)  $p_{opt} = 1.3$ , full-data. The white dashed circles indicate the actual profiles.

Moreover, this latter has a central hole of width  $w_3 = 5.5$  cm and height  $h_3 = 3.5$  cm. Figure 97 gives the reconstructed distributions of the relative dielectric permittivity obtained with  $p = 1.5$  for both phaseless and full-data approaches. Moreover, the cuts along the line  $x = 1.4$  cm are also presented in Figure 98. As can be seen, the scatterers are reconstructed by both techniques, and the hole in the rectangular slab is correctly identified. However, in the full-data case, the dielectric properties of the circular cylinder and the hole in the rectangular slab are better retrieved. Finally, the behavior of the NMSE in each step of the frequency-hopping technique for the phaseless and full-data cases, both with  $p = 1.5$ , are shown in Figure 99 and Figure 100, respectively. In these plots we see the benefits of the frequency-hopping approach; in fact, each set of measurement (one for each working frequency) contributes to improve the accuracy of the reconstructions.

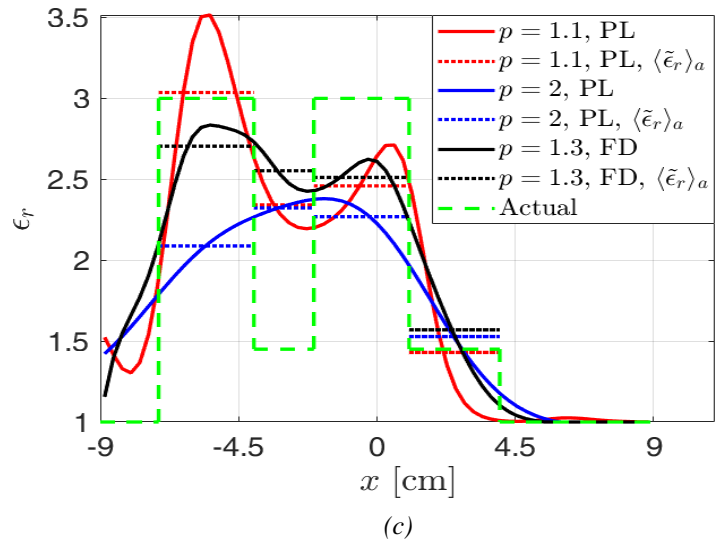
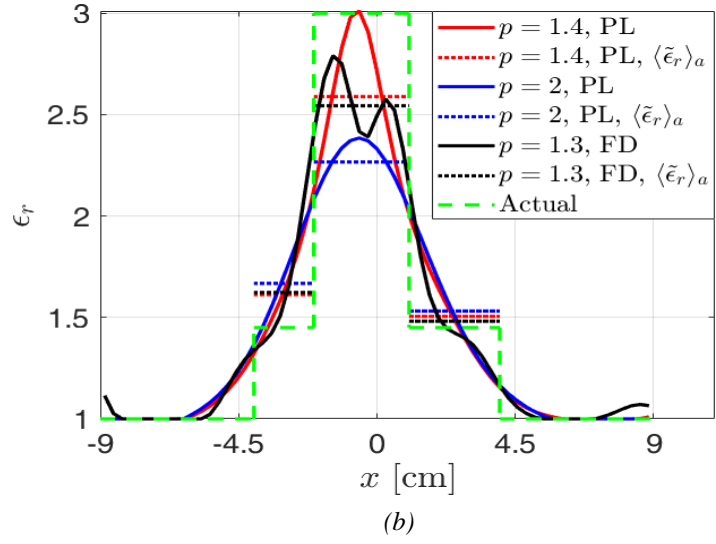
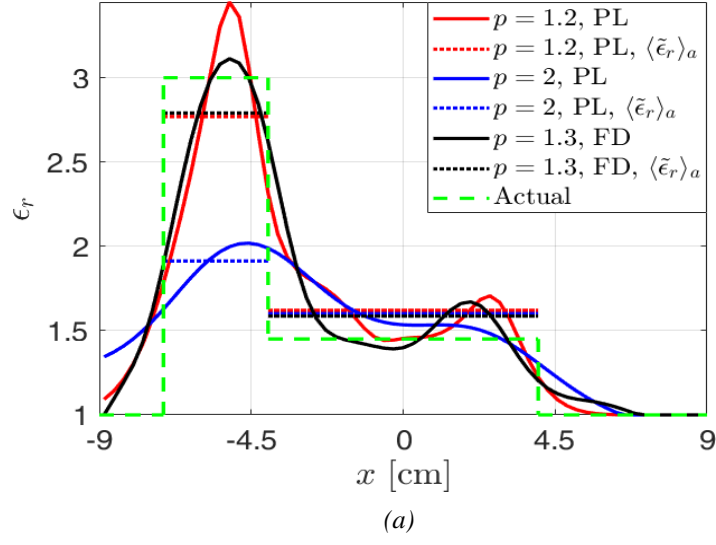
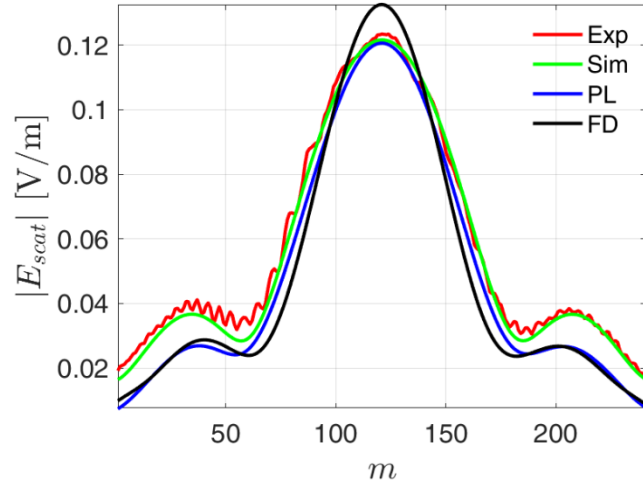
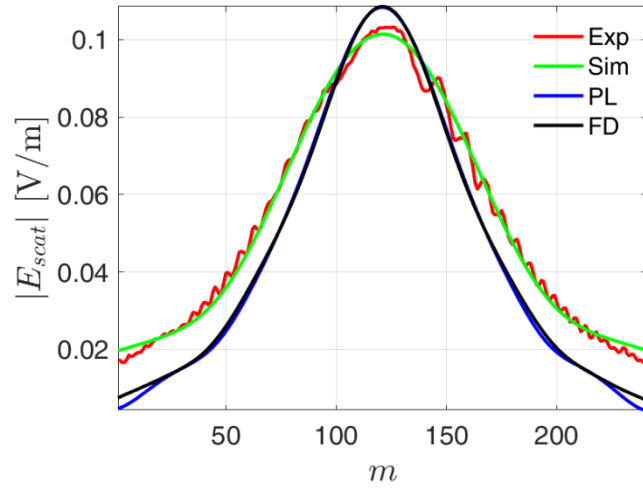


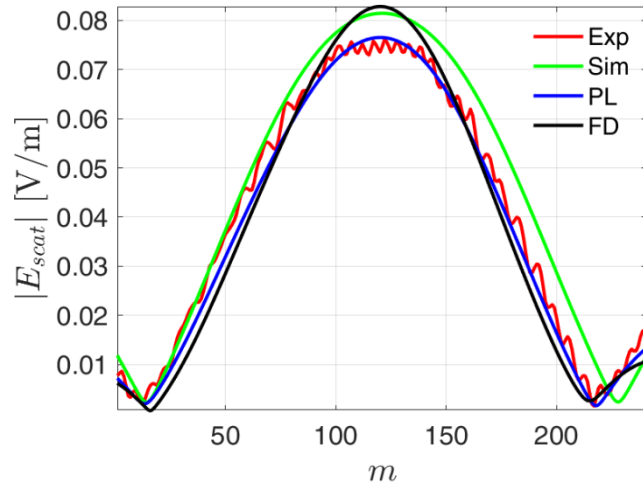
Figure 94. Cuts along the line  $y = 0$  cm of (a) Figure 91(a)-(c), (b) Figure 92(a)-(c), (c) Figure 93(a)-(c), and the actual profiles.



(a)



(b)



(c)

Figure 95. Amplitude of the scattered electric fields in the measurement points given by the experimental data (“Exp” in legend), the actual dielectric distributions (“Sim” in legend), and the optimal reconstructed ones obtained by the phaseless and full-data inversion techniques (“PL” and “FD” in legend, respectively). (a) FoamDielExtTM, (b) FoamDielIntTM, (c) FoamTwinDielTM.



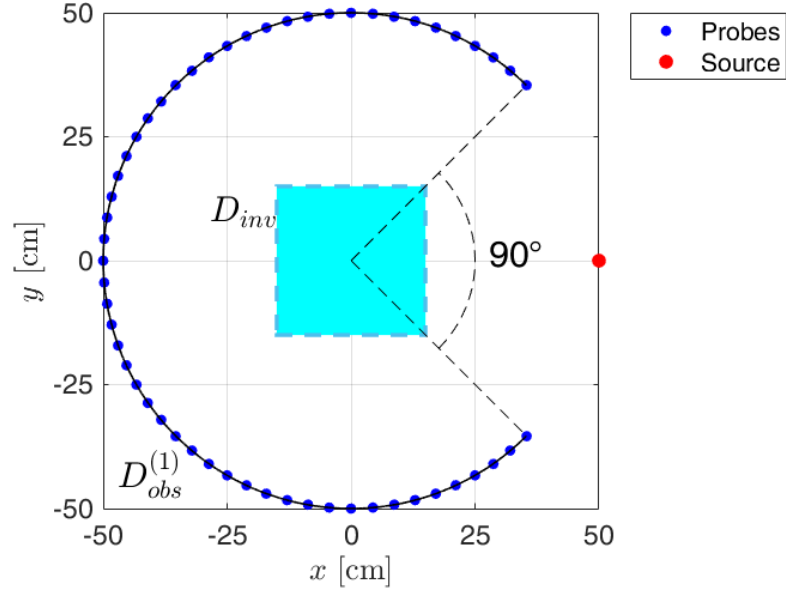


Figure 96. Illumination and measurement setup adopted in the SUPSI experimental dataset. First view and  $f = 1$  GHz.

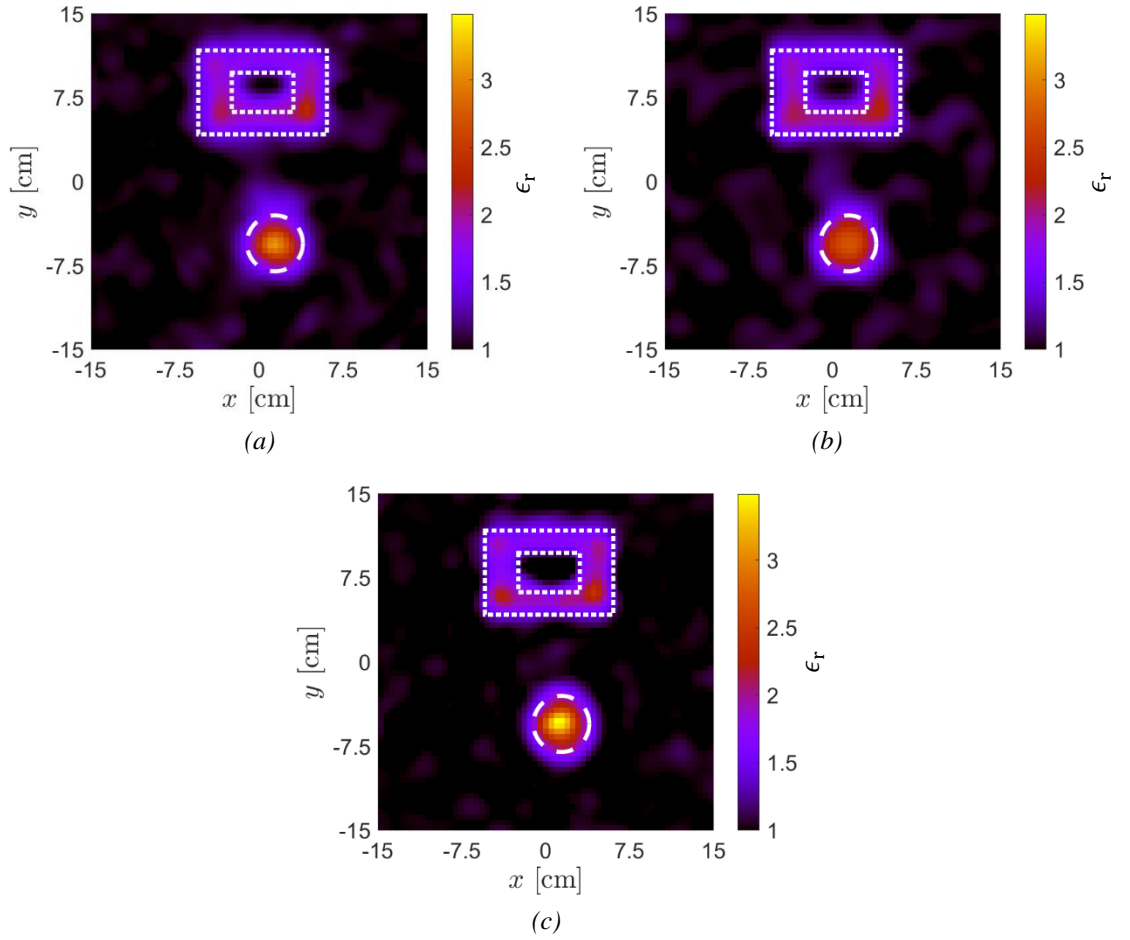


Figure 97. Reconstructed distribution of the dielectric permittivity for the SUPSI target. (a)  $p = 1.5$ , phaseless; (b)  $p = 2$ , phaseless; (c)  $p = 1.5$ , full-data. The white dashed lines indicate the actual profiles.

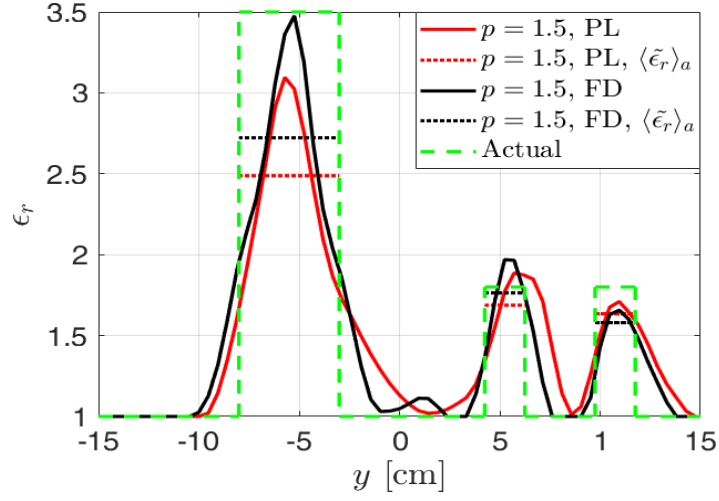


Figure 98. Slices at  $x = 1.4$  cm of Figure 97(a), Figure 97(c), and the actual profile.

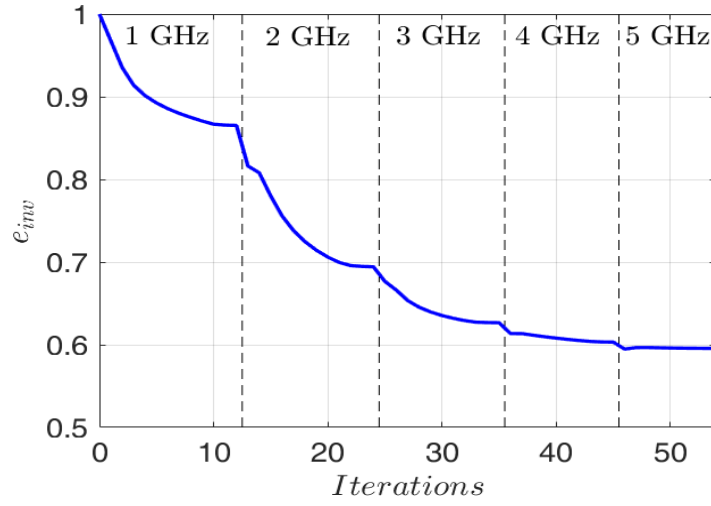


Figure 99. Behavior of  $e_{inv}$  in each step of the frequency-hopping phaseless inversion with  $p = 1.5$ .

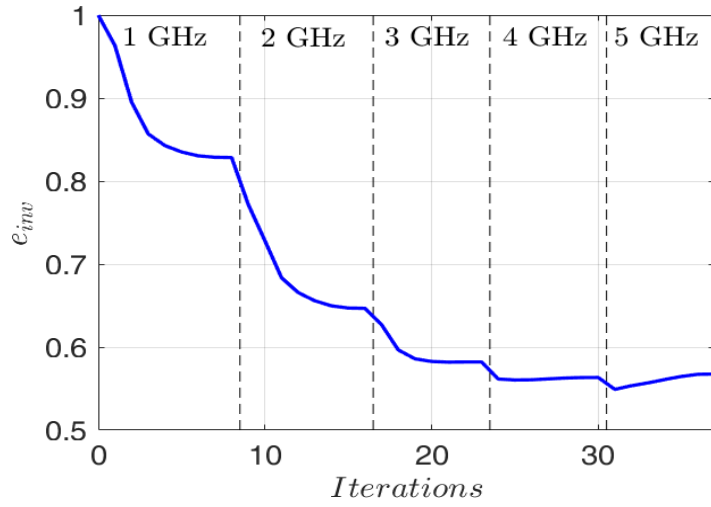


Figure 100. Behavior of  $e_{inv}$  in each step of the frequency-hopping full-data inversion with  $p = 1.5$ .

## Conclusions

In this Thesis, an approach for solving microwave imaging problems in the 3D full-vector and 2D phaseless scenarios has been developed. The considered method employs an inexact-Newton strategy with regularization performed in the framework of the  $l^p$  Banach spaces, in contrast to the classic  $l^2$  Hilbert spaces. In particular, the Banach-space versions of the truncated Landweber and conjugate gradient methods have been alternatively adopted as inner linear solvers in the Newton iterations. The performance of the developed microwave imaging method in both 3D full-vector and 2D phaseless scenarios has been validated by several simulations involving both synthetic and experimental data. Analyzing the obtained results in the 3D full-vector scenario, the Landweber-based inexact-Newton algorithm in Banach spaces has been able to outperform the Hilbert-based counterpart in all the cases. Also the preliminary results returned by the conjugate gradient-based method have supported the choice of working in the more general Banach spaces framework. About the 2D phaseless scenario, the results obtained with new Landweber-based approach have shown to be not only superior to the Hilbert-based ones, but also to have quality not so far from the corresponding full-data inversions. Among the various future research activities that will be devoted to the advancement in the microwave imaging techniques, a strong effort will be dedicated in the development of a reliable strategy for the automatic selection of the optimal norm parameter  $p$ .

## Appendix A: Automatic Detection of Circular Cylinders in Reconstructed Contrast Function

This Appendix describes a simple algorithm able to search for a known number  $N_{cyl}$  of circular cylinders in a reconstructed contrast function and to estimate their centers and diameters. Cylinders with void inclusions are allowed. The implementation of the algorithm described in the following and used in Section 5.1.7 is based on the OpenCV [134] and Armadillo [135] libraries. The following steps constitute the algorithm

1. Compute the following indicator vector

$$\mathbf{f} = \begin{bmatrix} f_1 \\ \vdots \\ f_N \end{bmatrix} \quad f_n = \begin{cases} 1, & \tilde{d}(\mathbf{r}_n^{inv}) \geq \tau_t \\ 0, & otherwise \end{cases} \quad (108)$$

where  $\tilde{d} = |\tilde{c}|/\|\tilde{c}\|_\infty$ , and  $0 < \tau_t < 1$ . The value  $\tau_t = 0.25$  has been selected.

2. Run the  $k$ -means method [136] (function in Armadillo) with  $k = N_{cyl}$  on the clusters of points in the binary image given by the indicator vector  $\mathbf{f}$ . The returned centers are indicated with  $\tilde{\mathbf{r}}_{c,k}$ ,  $k = 1, \dots, N_{cyl}$ .
3. For  $k = 1, \dots, N_{cyl}$ , scan the rings of pixels with center  $\tilde{\mathbf{r}}_{c,k}$ , starting from the closer one to this point, until a peak of  $\tilde{d}$  is detected. The position vectors of these peaks are indicated with  $\tilde{\mathbf{r}}_{s,k}$ .
4. For  $k = 1, \dots, N_{cyl}$ , generate a binary mask that identifies the connected region whose the seed point  $\tilde{\mathbf{r}}_{s,k}$  belongs to. This is done by running the Flood Fill algorithm [137] (function in OpenCV) with the seed point  $\tilde{\mathbf{r}}_{s,k}$  and assigning a candidate pixel  $\tilde{\mathbf{r}}'$  to the connected region if the following condition is satisfied

$$\tilde{d}(\tilde{\mathbf{r}}') - (1 - \tau_t)\tilde{d}(\tilde{\mathbf{r}}_{s,k}) \leq \tilde{d}(\tilde{\mathbf{r}}_{s,k}) \leq \tilde{d}(\tilde{\mathbf{r}}') + (1 - \tau_t)\tilde{d}(\tilde{\mathbf{r}}_{s,k}) \quad (109)$$

The centers of the  $N_{1,k}$  pixels in the binary mask belonging to the  $k$ th connected domain are indicated with the set  $\{\mathbf{m}_{i,k}\}_{i=1}^{N_{1,k}}$ .

5. For  $k = 1, \dots, N_{cyl}$ , run the 1-means on the mask of the  $k$ th connected region. The returned refined centers are indicated with  $\hat{\mathbf{r}}_{c,k}$ .

6. For  $k = 1, \dots, N_{cyl}$ , estimate the diameter  $\tilde{D}_k$  of the  $k$ th cylinder as follows

$$\tilde{D}_k = 2 \cdot \max_{i=1, \dots, N_{1,k}} |\mathbf{m}_{i,k} - \hat{\mathbf{r}}_{c,k}| \quad (110)$$

## References

- [1] M. Pastorino, *Microwave Imaging*. Hoboken, N.J.: Wiley, 2010.
- [2] M. Pastorino and A. Randazzo, *Microwave Imaging Methods and Applications*. Boston, MA: Artech House, 2018.
- [3] N. D. Nikolova, *Introduction to Microwave Imaging*. Cambridge: Cambridge University Press, 2017.
- [4] R. Zoughi, *Microwave non-destructive testing and evaluation*. Dordrecht: Kluwer Academic Publishers, 2000.
- [5] M. T. Ghasr, M. J. Horst, M. R. Dvorsky, and R. Zoughi, “Wideband Microwave Camera for Real-Time 3-D Imaging,” *IEEE Trans. Antennas Propag.*, vol. 65, no. 1, pp. 258–268, Jan. 2017.
- [6] M. G. Amin, Ed., *Through-the-wall radar imaging*. Boca Raton, FL: CRC Press, 2011.
- [7] C.-C. Chen, J. T. Johnson, M. Sato, and A. G. Yarovoy, “Special Issue on Subsurface Sensing Using Ground-Penetrating Radar (GPR),” *IEEE Trans. Geosci. Remote Sens.*, vol. 45, no. 8, pp. 2419–2573, Aug. 2007.
- [8] G. Gennarelli, I. Catapano, and F. Soldovieri, “Reconstruction capabilities of down-looking airborne GPRs: The single frequency case,” *IEEE Trans. Comput. Imaging*, pp. 1–1, 2017.
- [9] R. Persico, *Introduction to ground penetrating radar: inverse scattering and data processing*. Hoboken, New Jersey: Wiley, 2014.
- [10] D. Colton, H. Haddar, and M. Piana, “The linear sampling method in inverse electromagnetic scattering theory,” *Inverse Probl.*, vol. 19, no. 6, pp. S105–S137, Dec. 2003.
- [11] R. Solimene, G. Leone, and A. Dell’Aversano, “MUSIC algorithms for rebar detection,” *J. Geophys. Eng.*, vol. 10, no. 6, p. 064006, 2013.
- [12] W. C. Chew and Y. M. Wang, “Reconstruction of two-dimensional permittivity distribution using the distorted Born iterative method,” *IEEE Trans. Med. Imaging*, vol. 9, no. 2, pp. 218–225, Jun. 1990.
- [13] D. J. Brenner and E. J. Hall, “Computed Tomography — An Increasing Source of Radiation Exposure,” *N. Engl. J. Med.*, vol. 357, no. 22, pp. 2277–2284, Nov. 2007.

- [14] C. R. Paul, *Introduction to electromagnetic compatibility*, 2nd ed. Hoboken, N.J: Wiley-Interscience, 2006.
- [15] A. T. Mobashsher, A. Mahmoud, and A. M. Abbosh, "Portable Wideband Microwave Imaging System for Intracranial Hemorrhage Detection Using Improved Back-projection Algorithm with Model of Effective Head Permittivity," *Sci. Rep.*, vol. 6, p. 20459, Feb. 2016.
- [16] I. Bisio *et al.*, "Brain stroke microwave imaging by means of a Newton-conjugate-gradient method in Lp Banach spaces," *IEEE Trans. Microw. Theory Tech.*, vol. 66, no. 8, pp. 3668–3682, Aug. 2018.
- [17] J. Ljungqvist, S. Candefjord, M. Persson, L. Jönsson, T. Skoglund, and M. Elam, "Clinical Evaluation of a Microwave-Based Device for Detection of Traumatic Intracranial Hemorrhage," *J. Neurotrauma*, vol. 34, no. 13, pp. 2176–2182, Feb. 2017.
- [18] L. M. Neira, B. D. Van Veen, and S. C. Hagness, "High-resolution microwave breast imaging using a 3-D inverse scattering algorithm with a variable-strength spatial prior constraint," *IEEE Trans. Antennas Propag.*, vol. 65, no. 11, pp. 6002–6014, Nov. 2017.
- [19] M. T. Bevacqua and R. Scapaticci, "A compressive sensing approach for 3D breast cancer microwave imaging with magnetic nanoparticles as contrast agent," *IEEE Trans. Med. Imaging*, vol. 35, no. 2, pp. 665–673, Feb. 2016.
- [20] F. Gao, B. D. Van Veen, and S. C. Hagness, "Sensitivity of the distorted born iterative method to the initial guess in microwave breast imaging," *IEEE Trans. Antennas Propag.*, vol. 63, no. 8, pp. 3540–3547, Aug. 2015.
- [21] Z. Meng, "An adaptive reconstruction algorithm in concrete diagnosis," in *2016 Progress in Electromagnetic Research Symposium (PIERS)*, Shanghai, China, 2016, pp. 3949–3953.
- [22] J. Laviada, B. Wu, M. T. Ghasr, and R. Zoughi, "Nondestructive Evaluation of Microwave-Penetrable Pipes by Synthetic Aperture Imaging Enhanced by Full-Wave Field Propagation Model," *IEEE Trans. Instrum. Meas.*, pp. 1–8, 2018.
- [23] F. Boero *et al.*, "Microwave tomography for the inspection of wood materials: imaging system and experimental results," *IEEE Trans. Microw. Theory Tech.*, vol. 66, no. 7, pp. 3497–3510, Jul. 2018.

- [24] R. Obermeier and J. A. Martinez-Lorenzo, "Sensing matrix design via mutual coherence minimization for electromagnetic compressive imaging applications," *IEEE Trans. Comput. Imaging*, vol. 3, no. 2, pp. 217–229, Jun. 2017.
- [25] H.-Y. Liu, D. Liu, H. Mansour, P. T. Boufounos, L. Waller, and U. S. Kamilov, "SEAGLE: Sparsity-driven image reconstruction under multiple scattering," *IEEE Trans. Comput. Imaging*, pp. 1–1, 2017.
- [26] M. Thiel and D. Omeragic, "High-fidelity real-time imaging with electromagnetic logging-while-drilling measurements," *IEEE Trans. Comput. Imaging*, vol. 3, no. 2, pp. 369–378, Jun. 2017.
- [27] M. T. Bevacqua, L. Crocco, L. D. Donato, and T. Isernia, "Non-linear inverse scattering via sparsity regularized contrast source inversion," *IEEE Trans. Comput. Imaging*, vol. 3, no. 2, pp. 296–304, Jun. 2017.
- [28] R. Palmeri, M. T. Bevacqua, L. Crocco, T. Isernia, and L. Di Donato, "Microwave imaging via distorted iterated virtual experiments," *IEEE Trans. Antennas Propag.*, vol. 65, no. 2, pp. 829–838, Feb. 2017.
- [29] D. K. Ghodgaonkar, O. P. Gandhi, and M. J. Hagmann, "Estimation of complex permittivities of three-dimensional inhomogeneous biological bodies," *IEEE Trans. Microw. Theory Tech.*, vol. 31, no. 6, pp. 442–446, Jun. 1983.
- [30] T. C. Guo, W. W. Guo, S. J. Dwyer III, and R. H. Schneider, "Physics of image formation by microwave scattering," *Proc SPIE*, vol. 0767, pp. 30–39, Jan. 1987.
- [31] S. Caorsi, G. L. Gragnani, and M. Pastorino, "Electromagnetic vision-oriented numerical solution to three-dimensional inverse scattering," *Radio Sci.*, vol. 23, no. 6, pp. 1094–1106, Nov. 1988.
- [32] C. Curtis, B. R. Lavoie, and E. Fear, "An analysis of the assumptions inherent to near field beamforming for biomedical applications," *IEEE Trans. Comput. Imaging*, pp. 1–1, 2017.
- [33] A. T. Mobashsher, A. M. Abbosh, and Y. Wang, "Microwave system to detect traumatic brain injuries using compact unidirectional antenna and wideband transceiver with verification on realistic head phantom," *IEEE Trans. Microw. Theory Tech.*, vol. 62, no. 9, pp. 1826–1836, Sep. 2014.



- [34] M. D. Hossain and A. S. Mohan, "Cancer detection in highly dense breasts using coherently focused time-reversal microwave imaging," *IEEE Trans. Comput. Imaging*, vol. 3, no. 4, pp. 928–939, Dec. 2017.
- [35] A. Shahzad, M. O'Halloran, E. Jones, and M. Glavin, "Prefiltered beamforming for early-stage breast cancer detection," *IEEE Antennas Wirel. Propag. Lett.*, vol. 12, pp. 500–503, 2013.
- [36] M. A. Elahi, A. Shahzad, M. Glavin, E. Jones, and M. O'Halloran, "Hybrid artifact removal for confocal microwave breast imaging," *IEEE Antennas Wirel. Propag. Lett.*, vol. 13, pp. 149–152, 2014.
- [37] M. Sarafianou, I. J. Craddock, and T. Henriksson, "Towards enhancing skin reflection removal and image focusing using a 3-D breast surface reconstruction algorithm," *IEEE Trans. Antennas Propag.*, vol. 61, no. 10, pp. 5343–5346, Oct. 2013.
- [38] M. T. Ghasr, J. T. Case, and R. Zoughi, "Novel reflectometer for millimeter-wave 3-D holographic imaging," *IEEE Trans. Instrum. Meas.*, vol. 63, no. 5, pp. 1328–1336, May 2014.
- [39] R. K. Amineh, M. Ravan, A. Khalatpour, and N. K. Nikolova, "Three-dimensional near-field microwave holography using reflected and transmitted signals," *IEEE Trans. Antennas Propag.*, vol. 59, no. 12, pp. 4777–4789, Dec. 2011.
- [40] R. K. Amineh, M. Ravan, A. Khalatpour, and N. K. Nikolova, "Errata to 'Three-Dimensional Near-Field Microwave Holography Using Reflected and Transmitted Signals' [Dec 11 4777-4789]," *IEEE Trans. Antennas Propag.*, vol. 60, no. 1, pp. 425–425, Jan. 2012.
- [41] R. K. Amineh, J. McCombe, and N. K. Nikolova, "Microwave holographic imaging using the antenna phaseless radiation pattern," *IEEE Antennas Wirel. Propag. Lett.*, vol. 11, pp. 1529–1532, 2012.
- [42] M. R. Eskandari, R. Safian, and M. Dehmollaian, "Three-dimensional near-field microwave imaging using hybrid linear sampling and level set methods in a medium with compact support," *IEEE Trans. Antennas Propag.*, vol. 62, no. 10, pp. 5117–5125, Oct. 2014.
- [43] G. Gennarelli, I. Catapano, F. Soldovieri, and R. Persico, "On the achievable imaging performance in full 3D linear inverse scattering," *IEEE Trans. Antennas Propag.*, vol. 63, no. 3, pp. 1150–1155, Mar. 2015.

- [44] S. Jun, Z. Xiaoling, X. Gao, and J. Jianyu, "Signal processing for microwave array imaging: TDC and sparse recovery," *IEEE Trans. Geosci. Remote Sens.*, vol. 50, no. 11, pp. 4584–4598, Nov. 2012.
- [45] N. Ghavami, G. Tiberi, D. J. Edwards, and A. Monorchio, "UWB microwave imaging of objects with canonical shape," *IEEE Trans. Antennas Propag.*, vol. 60, no. 1, pp. 231–239, Jan. 2012.
- [46] G. Gennarelli, R. Solimene, F. Soldovieri, and M. G. Amin, "Three-dimensional through-wall sensing of moving targets using passive multistatic radars," *IEEE J. Sel. Top. Appl. Earth Obs. Remote Sens.*, vol. 9, no. 1, pp. 141–148, Jan. 2016.
- [47] C. Yu, M. Yuan, and Q. H. Liu, "Reconstruction of 3D objects from multi-frequency experimental data with a fast DBIM-BCGS method," *Inverse Probl.*, vol. 25, no. 2, 2009.
- [48] A. Abubakar, T. M. Habashy, G. Pan, and M.-K. Li, "Application of the multiplicative regularized Gauss-Newton algorithm for three-dimensional microwave imaging," *IEEE Trans. Antennas Propag.*, vol. 60, no. 5, pp. 2431–2441, May 2012.
- [49] A. Abubakar, T. M. Habashy, and G. Pan, "Microwave data inversions using the source-receiver compression scheme," *IEEE Trans. Antennas Propag.*, vol. 60, no. 6, pp. 2853–2864, Jun. 2012.
- [50] C. Estatico, M. Pastorino, and A. Randazzo, "Microwave imaging of three-dimensional targets by means of an inexact-Newton-based inversion algorithm," *Int. J. Antennas Propag.*, vol. 2013, Art. ID 407607, 2013.
- [51] E. Kilic, F. Akleman, B. Esen, D. M. Ozaltin, O. Ozdemir, and A. Yapar, "3-D imaging of inhomogeneous materials loaded in a rectangular waveguide," *IEEE Trans. Microw. Theory Tech.*, vol. 58, no. 5, pp. 1290–1296, May 2010.
- [52] D. Franceschini, M. Donelli, R. Azaro, and A. Massa, "Dealing with multifrequency scattering data through the IMSA," *IEEE Trans. Antennas Propag.*, vol. 55, no. 8, pp. 2412–2417, Aug. 2007.
- [53] M. Salucci *et al.*, "Three-dimensional electromagnetic imaging of dielectric targets by means of the multiscaling inexact-Newton method," *J. Opt. Soc. Am. A*, vol. 34, no. 7, p. 1119, Jul. 2017.
- [54] M. Donelli, D. Franceschini, P. Rocca, and A. Massa, "Three-dimensional microwave imaging problems solved through an efficient multiscaling particle swarm

- optimization,” *IEEE Trans. Geosci. Remote Sens.*, vol. 47, no. 5, pp. 1467–1481, May 2009.
- [55] M. Brignone, G. Bozza, A. Randazzo, M. Piana, and M. Pastorino, “A hybrid approach to 3D microwave imaging by using linear sampling and ACO,” *IEEE Trans. Antennas Propag.*, vol. 56, no. 10, pp. 3224–3232, Oct. 2008.
- [56] M. Pastorino, “Stochastic optimization methods applied to microwave imaging: A review,” *IEEE Trans. Antennas Propag.*, vol. 55, no. 3, pp. 538–548, Mar. 2007.
- [57] M. A. Ali and M. Moghaddam, “3D nonlinear super-resolution microwave inversion technique using time-domain data,” *IEEE Trans. Antennas Propag.*, vol. 58, no. 7, pp. 2327–2336, Jul. 2010.
- [58] T. U. Gürbüz, B. Aslanyürek, A. Yapar, H. Şahintürk, and I. Akduman, “A nonlinear microwave breast cancer imaging approach through realistic body-breast modeling,” *IEEE Trans. Antennas Propag.*, vol. 62, no. 5, pp. 2596–2605, May 2014.
- [59] C. Eyraud, J.-M. Geffrin, and A. Litman, “3D-aggregate quantitative imaging: experimental results and polarization effects,” *IEEE Trans. Antennas Propag.*, vol. 59, no. 4, pp. 1237–1244, Apr. 2011.
- [60] Q. Fang, P. M. Meaney, and K. D. Paulsen, “Viable three-dimensional medical microwave tomography: theory and numerical experiments,” *IEEE Trans. Antennas Propag.*, vol. 58, no. 2, pp. 449–458, Feb. 2010.
- [61] M. Asefi, A. Zakaria, and J. LoVetri, “Microwave imaging using normal electric-field components inside metallic resonant chambers,” *IEEE Trans. Microw. Theory Tech.*, vol. 65, no. 3, pp. 923–933, Mar. 2017.
- [62] M. Asefi and J. LoVetri, “Use of field-perturbing elements to increase nonredundant data for microwave imaging systems,” *IEEE Trans. Microw. Theory Tech.*, vol. 65, no. 9, pp. 3172–3179, Sep. 2017.
- [63] R. G. Yaccarino and Y. Rahmat-Samii, “Phaseless bi-polar planar near-field measurements and diagnostics of array antennas,” *IEEE Trans. Antennas Propag.*, vol. 47, no. 3, pp. 574–583, Mar. 1999.
- [64] F. Las-Heras and T. K. Sarkar, “A direct optimization approach for source reconstruction and NF-FF transformation using amplitude-only data,” *IEEE Trans. Antennas Propag.*, vol. 50, no. 4, pp. 500–510, Apr. 2002.

- [65] C. D. Reeve and J. F. Wombwell, "Novel space-integrating acousto-optic correlator: amplitude and phase information from intensity only measurements," *IEE Proc. F Radar Signal Process.*, vol. 136, no. 4, p. 185, 1989.
- [66] R. G. Yaccarino and Y. Rahmat-Samii, "A comparison of conventional and phaseless planar near-field antenna measurements: the effect of probe position errors," in *Proceedings 2000 IEEE International Conference on Phased Array Systems and Technology (Cat. No.00TH8510)*, Dana Point, CA, USA, 2000, pp. 525–528.
- [67] M. F. Akay, S. N. Kharkovsky, and U. C. Hasar, "An automated amplitudes-only measurement system for permittivity determination using free-space method," in *IMTC 2001. Proceedings of the 18th IEEE Instrumentation and Measurement Technology Conference. Rediscovering Measurement in the Age of Informatics (Cat. No.01CH 37188)*, Budapest, Hungary, 2001, vol. 1, pp. 503–506.
- [68] M. Lambert and D. Lesselier, "Binary-constrained inversion of a buried cylindrical obstacle from complete and phaseless magnetic fields," *Inverse Probl.*, vol. 16, no. 3, pp. 563–576, Jun. 2000.
- [69] T. Takenaka, D. J. N. Wall, H. Harada, and M. Tanaka, "Reconstruction algorithm of the refractive index of a cylindrical object from the intensity measurements of the total field," *Microw. Opt. Technol. Lett.*, vol. 14, no. 3, pp. 182–188, Feb. 1997.
- [70] L. Crocco, M. D'Urso, and T. Isernia, "Inverse scattering from phaseless measurements of the total field on a closed curve," *J. Opt. Soc. Am. A*, vol. 21, no. 4, p. 622, Apr. 2004.
- [71] O. M. Bucci, L. Crocco, M. D'Urso, and T. Isernia, "Inverse scattering from phaseless measurements of the total field on open lines," *J. Opt. Soc. Am. A*, vol. 23, no. 10, p. 2566, Oct. 2006.
- [72] L. Crocco, M. D'Urso, and T. Isernia, "Faithful non-linear imaging from only-amplitude measurements of incident and total fields," *Opt. Express*, vol. 15, no. 7, p. 3804, 2007.
- [73] M. D'Urso, K. Belkebir, L. Crocco, T. Isernia, and A. Litman, "Phaseless imaging with experimental data: Facts and challenges," *J. Opt. Soc. Am. A*, vol. 25, no. 1, p. 271, Jan. 2008.

- [74] L. Pan, X. Chen, and S. P. Yeo, "A Compressive-Sensing-Based Phaseless Imaging Method for Point-Like Dielectric Objects," *IEEE Trans. Antennas Propag.*, vol. 60, no. 11, pp. 5472–5475, Nov. 2012.
- [75] G. Franceschini, M. Donelli, R. Azaro, and A. Massa, "Inversion of Phaseless Total Field Data Using a Two-Step Strategy Based on the Iterative Multiscaling Approach," *IEEE Trans. Geosci. Remote Sens.*, vol. 44, no. 12, pp. 3527–3539, Dec. 2006.
- [76] L. Pan, Y. Zhong, X. Chen, and S. P. Yeo, "Subspace-based optimization method for inverse scattering problems utilizing phaseless data," *IEEE Trans. Geosci. Remote Sens.*, vol. 49, no. 3, pp. 981–987, Mar. 2011.
- [77] L. Li, H. Zheng, and F. Li, "Two-dimensional contrast source inversion method with phaseless data: TM case," *IEEE Trans. Geosci. Remote Sens.*, vol. 47, no. 6, pp. 1719–1736, Jun. 2009.
- [78] W. Zhang, L. Li, and F. Li, "Multifrequency Imaging From Intensity-Only Data Using the Phaseless Data Distorted Rytov Iterative Method," *IEEE Trans. Antennas Propag.*, vol. 57, no. 1, pp. 290–295, Jan. 2009.
- [79] S. Caorsi, A. Massa, M. Pastorino, and A. Randazzo, "Electromagnetic detection of dielectric scatterers using phaseless synthetic and real data and the memetic algorithm," *IEEE Trans. Geosci. Remote Sens.*, vol. 41, no. 12, pp. 2745–2753, Dec. 2003.
- [80] S. Costanzo, G. Di Massa, M. Pastorino, and A. Randazzo, "Hybrid microwave approach for phaseless imaging of dielectric targets," *IEEE Geosci. Remote Sens. Lett.*, vol. 12, no. 4, pp. 851–854, Apr. 2015.
- [81] S. Costanzo, G. Di Massa, and M. D. Migliore, "A novel hybrid approach for far-field characterization from near-field amplitude-only measurements on arbitrary scanning surfaces," *IEEE Trans. Antennas Propag.*, vol. 53, no. 6, pp. 1866–1874, Jun. 2005.
- [82] O. Yurduseven, T. Fromenteze, D. L. Marks, J. N. Gollub, and D. R. Smith, "Frequency-Diverse Computational Microwave Phaseless Imaging," *IEEE Antennas Wirel. Propag. Lett.*, vol. 16, pp. 2808–2811, 2017.
- [83] O. Yurduseven, T. Fromenteze, and D. R. Smith, "Relaxation of Alignment Errors and Phase Calibration in Computational Frequency-Diverse Imaging using Phase Retrieval," *IEEE Access*, vol. 6, pp. 14884–14894, 2018.
- [84] Y. Álvarez *et al.*, "Inverse Scattering for Monochromatic Phaseless Measurements," *IEEE Trans. Instrum. Meas.*, vol. 66, no. 1, pp. 45–60, Jan. 2017.

- [85] D. Colton and R. Kress, *Inverse Acoustic and Electromagnetic Scattering Theory*, vol. 93. New York, NY: Springer New York, 2013.
- [86] M. Bertero and P. Boccacci, *Introduction to Inverse Problems in Imaging*. Bristol, UK ; Philadelphia, Pa: Institute of Physics Pub, 1998.
- [87] W. C. Chew, *Waves and fields in inhomogeneous media*. Piscataway, NY: IEEE Press, 1995.
- [88] R. S. Dembo, S. C. Eisenstat, and T. Steihaug, "Inexact Newton methods," *SIAM J. Numer. Anal.*, vol. 19, no. 2, pp. 400–408, Apr. 1982.
- [89] A. Rieder, "On the regularization of nonlinear ill-posed problems via inexact Newton iterations," *Inverse Probl.*, vol. 15, no. 1, pp. 309–327, Feb. 1999.
- [90] B. Kaltenbacher, A. Neubauer, and O. Scherzer, *Iterative regularization methods for nonlinear ill-posed problems*. Berlin, Boston: De Gruyter, 2008.
- [91] T. Schuster, B. Kaltenbacher, B. Hofmann, and K. S. Kazimierski, *Regularization methods in Banach spaces*. Berlin: De Gruyter, 2012.
- [92] F. Schöpfer, A. K. Louis, and T. Schuster, "Nonlinear iterative methods for linear ill-posed problems in Banach spaces," *Inverse Probl.*, vol. 22, no. 1, pp. 311–329, Feb. 2006.
- [93] F. Lenti, F. Nunziata, C. Estatico, and M. Migliaccio, "On the Spatial Resolution Enhancement of Microwave Radiometer Data in Banach Spaces," *IEEE Trans. Geosci. Remote Sens.*, vol. 52, no. 3, pp. 1834–1842, Mar. 2014.
- [94] C. Estatico, S. Gratton, F. Lenti, and D. Titley-Peloquin, "A conjugate gradient like method for p-norm minimization in functional spaces," *Numer. Math.*, vol. 137, no. 4, pp. 895–922, Dec. 2017.
- [95] F. Lenti, F. Nunziata, C. Estatico, and M. Migliaccio, "Conjugate Gradient Method in Hilbert and Banach Spaces to Enhance the Spatial Resolution of Radiometer Data," *IEEE Trans. Geosci. Remote Sens.*, vol. 54, no. 1, pp. 397–406, Jan. 2016.
- [96] C. Estatico, M. Pastorino, and A. Randazzo, "A novel microwave imaging approach based on regularization in  $L_p$  Banach spaces," *IEEE Trans. Antennas Propag.*, vol. 60, no. 7, pp. 3373–3381, Jul. 2012.
- [97] C. Estatico, A. Fedeli, M. Pastorino, and A. Randazzo, "Buried object detection by means of a  $L_p$  Banach-space inversion procedure," *Radio Sci.*, vol. 50, no. 1, pp. 41–51, Jan. 2015.

- [98] C. Estatico, A. Fedeli, M. Pastorino, and A. Randazzo, "A multifrequency inexact-Newton method in  $L_p$  Banach spaces for buried objects detection," *IEEE Trans. Antennas Propag.*, vol. 63, no. 9, pp. 4198–4204, Sep. 2015.
- [99] J. D. Jackson, *Classical electrodynamics*, 3rd ed. New York: Wiley, 1999.
- [100] S. J. Orfanidis, *Electromagnetic Waves and Antennas*. Available online: <http://www.ece.rutgers.edu/~orfanidi/ewa/>, 2016.
- [101] J. van Bladel, *Electromagnetic fields*, 2nd ed. Hoboken, NJ: IEEE, 2007.
- [102] C. Tai, *Dyadic Green's Functions in Electromagnetic Theory*. Scranton, PA: International Textbook Company, 1971.
- [103] R. F. Harrington, *Field Computation by Moment Methods*. Piscataway, NJ: IEEE, 1993.
- [104] D. B. Davidson, *Computational electromagnetics for RF and microwave engineering*, 2nd ed. Cambridge: Cambridge University Press, 2010.
- [105] D. E. Livesay and K. Chen, "Electromagnetic fields induced inside arbitrarily shaped biological bodies," *IEEE Trans. Microw. Theory Tech.*, vol. 22, no. 12, pp. 1273–1280, Dec. 1974.
- [106] J. Van Bladel, "Some remarks on green's dyadic for infinite space," *IRE Trans. Antennas Propag.*, vol. 9, no. 6, pp. 563–566, Nov. 1961.
- [107] G. Gao, C. Torres-Verdin, and T. M. Habashy, "Analytical techniques to evaluate the integrals of 3D and 2D spatial dyadic Green's functions," *Prog. Electromagn. Res.*, vol. 52, pp. 47–80, 2005.
- [108] C. A. Balanis, *Advanced engineering electromagnetics*, 2nd ed. Hoboken, NJ: Wiley, 2012.
- [109] M. Abramowitz and I. A. Stegun, Eds., *Handbook of mathematical functions: with formulas, graphs, and mathematical tables*, 9. Dover print. New York, NY: Dover Publ, 2013.
- [110] E. R. Pike and P. C. Sabatier, Eds., *Scattering: scattering and inverse scattering in pure and applied science*. San Diego, Calif: Academic Press, 2002.
- [111] J. Richmond, "Scattering by a dielectric cylinder of arbitrary cross section shape," *IEEE Trans. Antennas Propag.*, vol. 13, no. 3, pp. 334–341, May 1965.

- [112] T. Isernia, V. Pascazio, and R. Pierri, “On the local minima in a tomographic imaging technique,” *IEEE Trans. Geosci. Remote Sens.*, vol. 39, no. 7, pp. 1596–1607, Jul. 2001.
- [113] O. M. Bucci and G. Franceschetti, “On the degrees of freedom of scattered fields,” *IEEE Trans. Antennas Propag.*, vol. 37, no. 7, pp. 918–926, Jul. 1989.
- [114] O. M. Bucci and T. Isernia, “Electromagnetic inverse scattering: retrievable information and measurement strategies,” *Radio Sci.*, vol. 32, no. 6, pp. 2123–2137, Nov. 1997.
- [115] J. N. Franklin, “On Tikhonov’s Method for Ill-Posed Problems,” *Math. Comput.*, vol. 28, no. 128, p. 889, Oct. 1974.
- [116] P. C. Hansen, *Rank-Deficient and Discrete Ill-Posed Problems: Numerical Aspects of Linear Inversion*. Society for Industrial and Applied Mathematics, 1998.
- [117] G. H. Golub and C. F. Van Loan, *Matrix computations*, Fourth edition. Baltimore: The Johns Hopkins University Press, 2013.
- [118] C. Estatico, M. Pastorino, A. Randazzo, and E. Tavanti, “Three-dimensional microwave imaging in  $L_p$  Banach spaces: Numerical and experimental results,” *IEEE Trans. Comput. Imaging*, vol. 4, no. 4, pp. 609–623, Dec. 2018.
- [119] E. Tavanti, C. Estatico, A. Fedeli, M. Pastorino, and A. Randazzo, “Nonlinear electromagnetic inverse scattering in via Frozen or Broyden update of the Fréchet derivative,” *J. Phys. Conf. Ser.*, vol. 657, p. 012008, Nov. 2015.
- [120] A. W. Knap, *Basic real analysis*. Boston: Birkhäuser, 2005.
- [121] W. Rudin, *Functional analysis*, 2. ed. New Delhi: Tata McGraw Hill Education, 2006.
- [122] J. F. Epperson, *An introduction to numerical methods and analysis*. Hoboken, N.J.: Wiley-Interscience, 2007.
- [123] X. M. Xu, Q. H. Liu, and Z. Q. Zhang, “The stabilized biconjugate gradient fast Fourier transform method for electromagnetic scattering,” *J. Appl. Comput. Electromagn. Soc.*, vol. 17, no. 1, pp. 97–103, Mar. 2002.
- [124] R. Chandra, Ed., *Parallel programming in OpenMP*. San Francisco, CA: Morgan Kaufmann Publishers, 2001.



- [125] M. Salucci, G. Oliveri, and A. Massa, “GPR Prospecting Through an Inverse-Scattering Frequency-Hopping Multifocusing Approach,” *IEEE Trans. Geosci. Remote Sens.*, vol. 53, no. 12, pp. 6573–6592, Dec. 2015.
- [126] C. Estatico, A. Fedeli, M. Pastorino, A. Randazzo, and E. Tavanti, “A Newton-Conjugate-Gradient Method in Lp Banach Spaces for Three-Dimensional Microwave Imaging,” in *IEEE International Conference on Imaging Systems and Techniques (IST)*, Kraków (Poland), 2018.
- [127] I. T. Rekanos, S. M. Panas, and T. D. Tsiboukis, “Microwave imaging using the finite-element method and a sensitivity analysis approach,” *IEEE Trans. Med. Imaging*, vol. 18, no. 11, pp. 1108–1114, Nov. 1999.
- [128] J. M. Geffrin and P. Sabouroux, “Continuing with the Fresnel database: experimental setup and improvements in 3D scattering measurements,” *Inverse Probl.*, vol. 25, no. 2, p. 024001, Feb. 2009.
- [129] P. C. Hansen and D. P. O’Leary, “The Use of the L-Curve in the Regularization of Discrete Ill-Posed Problems,” *SIAM J. Sci. Comput.*, vol. 14, no. 6, pp. 1487–1503, Nov. 1993.
- [130] K. Belkebir and M. Saillard, “Special section: Testing inversion algorithms against experimental data,” *Inverse Probl.*, vol. 17, no. 6, pp. 1565–1571, Dec. 2001.
- [131] J.-M. Geffrin, P. Sabouroux, and C. Eyraud, “Free space experimental scattering database continuation: experimental set-up and measurement precision,” *Inverse Probl.*, vol. 21, no. 6, pp. S117–S130, Dec. 2005.
- [132] A. Salvade, M. Pastorino, R. Monleone, G. Bozza, and A. Randazzo, “A new microwave axial tomograph for the inspection of dielectric materials,” *IEEE Trans. Instrum. Meas.*, vol. 58, no. 7, pp. 2072–2079, Jul. 2009.
- [133] A. Fedeli, M. Pastorino, A. Randazzo, M. Lanini, M. Maffongelli, and R. Monleone, “Wood characterization by using microwave inverse scattering: Experimental results,” in *2017 IEEE MTT-S International Microwave Workshop Series on Advanced Materials and Processes for RF and THz Applications (IMWS-AMP)*, Pavia, 2017, pp. 1–3.
- [134] K. Pulli, A. Baksheev, K. Korniyakov, and V. Eruhimov, “Real-time computer vision with OpenCV,” *Commun. ACM*, vol. 55, no. 6, p. 61, Jun. 2012.

- [135] C. Sanderson and R. Curtin, “Armadillo: a template-based C++ library for linear algebra,” *J. Open Source Softw.*, vol. 1, no. 2, p. 26, Jun. 2016.
- [136] G. A. F. Seber, *Multivariate observations*. Hoboken, N.J: Wiley-Interscience, 2004.
- [137] S. Torbert, *Applied computer science*. New York, NY: Springer Science+Business Media, 2016.